

Using Biomass-derived Carbon Catalysts for Electrochemical CO₂ Reduction

Fu, S.

DOI

[10.4233/uuid:19232f14-6765-417e-8bb6-198f91a4a8a6](https://doi.org/10.4233/uuid:19232f14-6765-417e-8bb6-198f91a4a8a6)

Publication date

2023

Document Version

Final published version

Citation (APA)

Fu, S. (2023). *Using Biomass-derived Carbon Catalysts for Electrochemical CO₂ Reduction*. [Dissertation (TU Delft), Delft University of Technology]. <https://doi.org/10.4233/uuid:19232f14-6765-417e-8bb6-198f91a4a8a6>

Important note

To cite this publication, please use the final published version (if applicable).
Please check the document version above.

Copyright

Other than for strictly personal use, it is not permitted to download, forward or distribute the text or part of it, without the consent of the author(s) and/or copyright holder(s), unless the work is under an open content license such as Creative Commons.

Takedown policy

Please contact us and provide details if you believe this document breaches copyrights.
We will remove access to the work immediately and investigate your claim.

The background of the cover features a stylized illustration of green leaves on the left side, with a hexagonal pattern resembling a carbon lattice or honeycomb structure extending from the leaves towards the center. The overall color palette is various shades of green, from light lime to dark forest green, set against a pale yellow-green gradient background.

Using Biomass-derived Carbon Catalysts for Electrochemical CO₂ Reduction

Shilong Fu

Using Biomass-derived Carbon Catalysts for Electrochemical CO₂ Reduction

Shilong Fu

Using Biomass-derived Carbon Catalysts for Electrochemical CO₂ Reduction

Dissertation

for the purpose of obtaining the degree of doctor

at Delft University of Technology

by the authority of the Rector Magnificus, prof.dr.ir. T.H.J.J. van der Hagen,

Chair of the Board for Doctorates

to be defended publicly on

Monday 18 December 2023 at 10:00 o'clock

by

Shilong FU

Master of Science in New Energy Science and Engineering,

Huazhong University of Science and Technology, China

born in Luoyang, Henan Province, China

This dissertation has been approved by the promotor.

Composition of the doctoral committee:

Rector Magnificus	chairperson
Prof. dr. ir. W. de Jong	Delft University of Technology, promotor
Dr. R. Kortlever	Delft University of Technology, copromotor

Independent members:

Prof. dr. M.M. Titirici	Imperial College London, United Kingdom
Prof. dr. ir. J.R. van Ommen	Delft University of Technology
Prof. dr. G. Mul	University of Twente
Dr. L. Botto	Delft University of Technology
Dr. M. Costa Figueiredo	Eindhoven University of Technology
Prof. dr. ir. J.T. Padding	Delft University of Technology, reserve member



The research described in this thesis was conducted in the Large-Scale Energy Storage section of the Process and Energy Department, Faculty of Mechanical, Maritime and Materials Engineering (3mE) of the Delft University of Technology, and co-financed by the China Scholarship Council (CSC).

Keywords: Electrochemical CO₂ reduction, Electrocatalyst, N-doped Carbon, Biomass

Printed by: Ridderprint | www.ridderprint.nl

Copyright © 2023 by Shilong Fu

Cover design by Shilong Fu & Bing Image Creator.

ISBN 978-94-6384-515-1

An electronic version of this dissertation is available at

<http://repository.tudelft.nl/>.

To Family

Contents

Summary	v
Samenvatting	ix
1. Introduction	1
1.1 Background	3
1.2 What is the electrochemical CO ₂ reduction reaction (CO ₂ RR)?	4
1.3 The electrocatalyst: the cornerstone for efficient CO ₂ RR	5
1.4 Why use biomass-derived carbon?	7
1.5 Main challenges of using N-doped biomass-derived carbon as catalysts for CO ₂ RR	9
1.6 Research questions and thesis outline	10
References	12
2. Recent Progress of Biomass-derived Nitrogen-doped Carbon Materials as Electrocatalysts	17
2.1 Introduction	19
2.2 Carbonization, functionalization and characterization of biomass-derived carbon materials	21
2.2.1 Carbonization	21
2.2.1.1 Pyrolysis	22
2.2.1.2 Gasification	23
2.2.1.3 Hydrothermal carbonization	23
2.2.2 Functionalization	24
2.2.2.1 Activation	25
2.2.2.2 Nitrogen doping	29
2.2.3 Characterization	35
2.3 Biomass-derived carbon as electrocatalysts	36
2.3.1 Hydrogen evolution reaction (HER)	36

2.3.2 Oxygen reduction reaction (ORR)	38
2.3.3 Carbon dioxide reduction reaction (CO ₂ RR)	41
2.3.4 Similarities and differences.....	44
2.4 Conclusions and future perspectives.....	46
References	49
3. Unravelling the effect of activators used in the synthesis of biomass-derived carbon electrocatalysts on the electrocatalytic performance for CO₂ reduction	71
3.1 Introduction	73
3.2 Experimental Section.....	75
3.2.1 Materials and chemicals	75
3.2.2 Catalyst preparation	75
3.2.3 Catalyst characterization	76
3.2.4 Electrochemical measurements	76
3.3 Results and Discussions	78
3.3.1 Characterization of the biomass-derived materials.....	78
3.3.2 Understanding the effect of activators	84
3.3.3 Electrochemical performance.....	85
3.3.4 Understanding the structure-activity relationship	89
3.4 Conclusions	91
3.5 Supporting Information	93
References	103
4. Tuning the properties of N-doped biochar for selective CO₂ electroreduction to CO	113
4.1 Introduction	115
4.2 Experimental.....	117
4.2.1 Synthesis of catalysts	117
4.2.2 Catalyst characterization	118

4.2.3 Electrode preparation	118
4.2.4 Electrochemical measurements	119
4.3 Results and Discussions	120
4.3.1 Effect of carbonization temperature.....	120
4.3.2 Effect of N-doping level	127
4.3.3 Understanding the correlation between physicochemical properties and electrochemical performance.....	135
4.4 Conclusions	138
4.5 Supporting Information	139
References	161
5. Electrochemical CO₂ Reduction in the Presence of SO₂ Impurities on a Nitrogen-doped Carbon Electrocatalyst.....	167
5.1 Introduction	169
5.2 Experimental Methods	169
5.3 Results and Discussions	172
5.4 Conclusions	181
5.5 Supporting Information	182
References	193
6. Ni-N-C catalysts for CO₂ electrochemical reduction to CO: The effects of carbon support.....	197
6.1 Introduction	199
6.2 Experimental Section	200
6.2.1 Synthesis of catalysts	201
6.2.2 Characterization.....	202
6.2.3 Electrode preparation.....	202
6.2.4 Electrochemical measurement	203
6.3 Results and Discussions	204
6.3.1 Catalyst characterization	204

6.3.2 Electrocatalytic performance.....	207
6.3.3 Factors behind the performance differences	211
6.4 Conclusions	215
6.5 Supporting Information	216
References	229
7. Conclusions and Recommendations	237
7.1 Conclusions	239
7.2 Recommendations	241
Acknowledgements.....	245
Curriculum vitae.....	249
List of Publications	251

Summary

Integrating clean and renewable energy with electrochemical CO₂ reduction reaction (CO₂RR) is a promising approach to solve CO₂-related environmental issues. The CO₂ reduction reaction (CO₂RR) converts waste CO₂ into various chemicals and fuels, meanwhile storing excessive and intermittent electricity into chemical bonds. Owing to the thermodynamic stability of CO₂, sluggish reaction kinetics and the competitive hydrogen evolution reaction, an active and robust catalyst for CO₂RR is highly desired to overcome the inherent energy barrier, improve the product selectivity and reaction activity. To date, metal-free nitrogen-doped (N-doped) carbon materials have been demonstrated as efficient catalysts for electrochemical CO₂ reduction to CO, which exhibit comparable performance to the state-of-the-art metal-based catalysts. Using renewable biomass as carbon precursor to substitute fossil-based feedstocks provides a more sustainable, cost-effective, and environmental friendly solution for the production of N-doped carbon catalysts.

Chapter 1 serves as introduction and presents the fundamental knowledge of electrochemical CO₂ reduction, introduces the motivation and main challenges of using biomass-derived N-doped carbon for CO₂RR, and lists the research questions and the outline of this dissertation.

Chapter 2 summarizes the most used methods for N-doped biochar production, including carbonization, activation, and N-doping strategies. The differences of each method are discussed. Moreover, the commonly used characterization methods for revealing the textural properties and chemical compositions of N-doped biochar catalysts are introduced. Furthermore, **Chapter 2** carefully scrutinizes the recent progress of using N-doped biochar catalysts for the hydrogen evolution reaction, oxygen reduction reaction and CO₂ reduction reaction. The correlations between synthesis – structure – performance of N-doped biochar catalysts for different reactions are highlighted.

Chapter 3 assesses different types of activators (KOH, NaOH, KHCO₃, NaHCO₃, K₂CO₃) used for the preparation of N-doped biochar. The different activation mechanisms of various activators influence the N-doping level, porosity, specific surface area, and the degree of graphitization of as-prepared N-doped biochar catalysts, which significantly influence their electrochemical CO₂RR performances. Sodium hydroxide (NaOH) is one of the most efficient activators, endowing the N-doped biochar catalyst with a proper N-doping content (3.85 at%), large surface area (1278 m²/g), abundant pores with relatively higher mesoporosity (17%) and relatively higher degree of graphitization ($I_D/I_G = 0.88$). The sample activated by NaOH exhibits a good CO₂RR performance with 80% faradaic efficiency toward CO (FE_{CO}) at -0.93 V vs. RHE.

Chapter 4 evaluates the structure-performance relationship of N-doped biochar catalysts for the CO₂RR via tuning the carbonization temperature and the addition of nitrogen dopant. The prepared catalysts exhibit substantial differences in maximum faradaic efficiency to CO varying from 26.8 to 94.9% at around -0.8 to -0.9 V vs. RHE. A multivariate correlation analysis is established to elucidate the correlation between physicochemical properties and electrochemical performance of N-doped biochar catalysts. The results demonstrate that increasing the N-doping content and specific surface area are not efficient approaches to enhance the CO₂RR performance of N-doped biochar catalysts, whereas boosting the surface hydrophobicity, the abundance of defects, and optimizing the porosity distribution of N-doped carbon can significantly improve the overall catalytic performance for CO₂RR. The results highlight the importance of the synergistic effect of all physicochemical properties for CO₂RR, rather than overemphasizing the contribution from high N-doping contents and large specific surface areas.

Chapter 5 investigates the performance of N-doped biochar catalyst for electrochemical CO₂RR in the presence of 100 to 10000 ppm SO₂ impurities, which often present in the downstream industrial flue gas. The overall CO₂RR performance is co-dependent on the SO₂ concentrations and applied potentials. The N-doped biochar catalyst outperforms a benchmark silver foil electrode, exhibits higher faradaic efficiency and partial current density to CO, stronger tolerance to SO₂ impurities, longer stability and better robustness than silver foil electrode. The catalyst maintains over 90% faradaic efficiency toward CO during an 8-hour stability measurement at -1.0 V vs. RHE with 100 ppm SO₂ and shows a strong tolerance to the gas feed changes (concentrations of SO₂ fluctuating from 0 to 100 ppm) with negligible changes of the faradaic efficiency and current density toward CO. SEM and XPS results indicate the absence of sulfur-containing species resulting from SO₂ reduction on the surface of N-doped biochar catalyst, suggesting that the SO₂ reduction reaction is the main reason for the losses of faradaic efficiency on N-doped biochar catalysts. On the contrary, silver reacts with SO₂ impurities and leads to the reconfiguration of the electrode surface, which results in the further deactivation of the silver foil catalyst.

Chapter 6 reports a strategy for using N-doped biochar as a carbon support to synthesize a nickel-nitrogen-carbon (Ni-N-C) catalyst for the CO₂RR. A series of Ni-N-C catalysts are synthesized by using carbon black (CB), multi-walled carbon nanotubes (CNT), and activated nitrogen-doped biochar (ANBC) as carbon support via a ligand mediated method. The Ni-N-ANBC catalyst shows a maximum of 97% faradaic efficiency to CO at -0.93 V vs. RHE, which is better than Ni-N-CB catalyst (maximum 88% FE_{CO} at -0.8 V vs. RHE) and comparable to Ni-N-CNT catalyst (maximum 95% FE_{CO} at -0.7 V vs. RHE). The porosity of carbon supports and the distribution of Ni-N_x active sites of Ni-N-C catalysts are main factors that govern the differences of CO₂RR performance. The hierarchical structure of N-doped biochar confines a part of the Ni-N_x active sites into deeper and narrower pores, enabling

that the Ni-N-ANBC catalyst to maintain over 90% FE_{CO} even at more negative potentials. This chapter provides new insights for utilizing N-doped biochar materials for more efficient electrochemical CO_2 reduction.

Chapter 7 provides the overall conclusions of the studies reported in this dissertation and lists a few recommendations for future investigations.

Samenvatting

Het gebruik van hernieuwbare energie voor de elektrochemische CO₂ reductie reactie (CO₂RR) is een veelbelovende oplossing voor CO₂-gerelateerde milieuproblemen. Hierbij wordt uitgestoten CO₂ in verschillende chemicaliën en brandstoffen omgezet, zodat overmatige hernieuwbare elektriciteit wordt opgeslagen in chemische verbindingen. Vanwege de thermodynamische stabiliteit van CO₂, de trage reactiekinetiek en de concurrerende waterstofevolutiereactie, is een robuuste en actieve katalysator voor de CO₂RR nodig om de inherente energiebarrière te overkomen en de productselectiviteit en reactieactiviteit te verbeteren. Eerder onderzoek heeft aangetoond dat stikstof-gedoopte (N-gedoopte) koolstofmaterialen efficiënte katalysatoren zijn voor elektrochemische CO₂ reductie naar CO. Deze katalysatoren tonen vergelijkbare prestaties als de state-of-the-art metaal gebaseerde katalysatoren. Het gebruik van hernieuwbare biomassa als koolstofbron voor de katalysatoren, in plaats van fossiele grondstoffen, biedt een duurzamer, kosten effectiever, en milieuvriendelijker alternatief voor de productie van N-gedoopte koolstofkatalysatoren.

Hoofdstuk 1 dient als inleiding van het onderwerp, waarin de fundamentele kennis van elektrochemische CO₂-reductie wordt gepresenteerd, de motivatie en belangrijkste uitdagingen van het gebruik van biomassa-afgeleide N-gedoopte koolstof voor de CO₂RR worden geïntroduceerd. Als laatste worden de onderzoeksvragen en hoofdlijnen van dit proefschrift uiteengezet.

Hoofdstuk 2 geeft een overzicht van de meest gebruikte methoden voor de productie van N-gedoopte biochar, waaronder verschillende carbonisatie-, activerings- en N-doperingsstrategieën. De verschillen tussen deze methoden worden besproken. Ook worden de meest gebruikte karakterisatie methoden om de morfologieën en chemische samenstellingen van N-gedoopte biochar katalysatoren te bepalen, geïntroduceerd. Bovendien wordt in **hoofdstuk 2** de recente literatuur over stikstof-gedoopte biochar katalysatoren voor de waterstof evolutie reactie, zuurstof reductie reactie en CO₂ reductie reactie behandeld. Ook worden de correlaties tussen de synthese methode, de structuur van de katalysator en de katalytische prestaties van stikstof-gedoteerde biochar katalysatoren voor verschillende reacties verder belicht.

In **hoofdstuk 3** worden verschillende soorten activators die worden gebruikt voor de bereiding van N-gedoteerde biochar behandeld. De verschillende activeringsmechanismen van de verschillende activators beïnvloeden het N-dopingniveau, de porositeit, het specifieke oppervlak, en de mate van grafitisering van de gemaakte N-gedoopte biochar-katalysatoren. Elk van deze variabelen heeft een sterke invloed op de elektrochemische

CO₂RR prestatie van de katalysator. Natriumhydroxide (NaOH) is een van de meest efficiënte activatoren, die het N-gedoopte biochar voorziet van een juiste N-dopingniveau (3.85 at%), een groot oppervlak (1278 m²/g), veel poriën met een relatief hogere mesoporositeit (17%) en een relatief hogere grafitiseringsgraad ($I_D/I_G = 0.88$). Het met NaOH geactiveerde monster vertoont een goede CO₂RR-prestatie met faradische efficiëntie van 80% naar CO (FE_{CO}) bij -0.93 V vs. RHE.

Hoofdstuk 4 evalueert de structuurprestaties van N-gedoopte biochar katalysatoren voor de CO₂RR door het afstemmen van de carbonisatietemperatuur en de toevoeging van stikstofdopering. De geteste katalysatoren vertonen grote verschillen in maximale faradische efficiëntie naar CO, van 26.8 tot 94.9% bij een potentiaal tussen ongeveer -0.8 en -0.9 V vs. RHE. Een multivariate correlatieanalyse is uitgevoerd om de correlatie tussen de fysisch-chemische eigenschappen en elektrochemische prestaties van N-gedoopte biochar katalysatoren te bepalen. De resultaten laten zien dat het verbeteren van het N-dopinggehalte en het specifieke oppervlak geen efficiënte manieren zijn om de CO₂RR-prestaties van N-gedoopte biochar-katalysatoren te verbeteren. Echter, het verhogen van de hydrofobiciteit van het oppervlak, de overvloed aan defecten en het optimaliseren van de porositeitsdistributie van N-gedoteerde koolstof verbeteren de algemene katalytische prestaties voor elektrochemische CO₂ reductie aanzienlijk. De resultaten benadrukken het belang van het synergetische effect van alle fysisch-chemische eigenschappen voor de CO₂RR, in plaats van te veel nadruk te leggen op slechts de bijdrage van hoge N-dopinggehalten en grote specifieke oppervlakten.

Hoofdstuk 5 onderzoekt de prestaties van N-gedoopte biochar katalysatoren voor de elektrochemische CO₂RR in de aanwezigheid van 100 tot 10000 ppm SO₂. De algemene CO₂RR-prestaties zijn afhankelijk van zowel de SO₂-concentraties als de toegepaste potentialen. De N-gedoopte biochar katalysator presteert beter dan een benchmark zilver elektrode. Bovendien vertoont de biochar een hogere faradische efficiëntie en partiële stroomdichtheid naar CO, sterkere tolerantie voor SO₂-onzuiverheden, langere stabiliteit en betere robuustheid dan de zilver elektrode. De katalysator behoudt meer dan 90% faradische efficiëntie naar CO na een 8 uur durende stabiliteitsmeting bij -1.0 V vs. RHE met 100 ppm SO₂ en toont een sterke tolerantie voor veranderingen in de gastoevoer (waarbij de concentratie SO₂ fluctueert van 0 tot 100 ppm) met verwaarloosbare veranderingen in de faradische efficiëntie en stroomdichtheid van CO. SEM- en XPS-resultaten laten geen zwavelhoudende soorten zien als gevolg van SO₂ reductie op het oppervlak van de N-gedoopte biochar katalysator. Dit resultaat suggereert dat de SO₂ reductie reactie de belangrijkste reden is voor het verlies van faradische efficiëntie op N-gedoteerde biochar katalysatoren. Zilver daarentegen reageert met SO₂-onzuiverheden wat leidt tot herconfiguratie van het elektrodeoppervlak met de deactivatie van de zilverfolie-katalysator als gevolg.

Hoofdstuk 6 beschrijft een strategie voor het gebruik van N-gedoopt biochar als koolstofdrager voor de synthese van een nikkel-stikstof-koolstof (Ni-N-C) katalysator voor de CO₂RR. Een reeks Ni-N-C katalysatoren wordt gesynthetiseerd via een ligand mediated methode met carbon black (CB), carbon nanotubes (CNT) en geactiveerde stikstof-gedoopte biochar (ANBC) als support. De Ni-N-ANBC katalysator toont maximaal 97% faradische efficiëntie naar CO bij -0.93 V vs. RHE, wat hoger is dan de Ni-N-CB katalysator (maximaal 88% FE_{CO} bij -0.8 V vs. RHE) en vergelijkbaar met de Ni-N-CNT katalysator (maximaal 95% FE_{CO} bij -0.7 V vs. RHE). De porositeit van de koolstof support en de verdeling van Ni-N_x active sites zijn de belangrijkste factoren voor het bepalen van de CO₂RR-prestaties. De hiërarchische structuur van N-gedoopt biochar sluit een deel van de Ni-N_x actieve sites op in diepere en smallere poriën, waardoor de Ni-N-ANBC katalysator meer dan 90% FE_{CO} behoudt, zelfs bij negatievere potentialen. Dit onderzoek biedt nieuwe inzichten voor het gebruik van N-gedoopte biochar materialen voor efficiëntere elektrochemische CO₂-reductie.

Hoofdstuk 7 geeft de algemene conclusies van de in dit proefschrift gerapporteerde onderzoeken en noemt enkele aanbevelingen voor toekomstig onderzoek.

1

Introduction

1.1 Background

With an increasing world population and overwhelming development of urbanization and industrialization, the excessive emission of carbon dioxide (CO₂) due to human activity has led to serious environmental problems, including global warming, climate change and extreme weather events.^{1,2} According to major scientific reports, taking actions to mitigate climate change, accelerating the energy transition, and reducing CO₂ emissions are ever more urgent.^{3,4} In Paris and Glasgow, many countries have committed to ambitious plans, namely nationally determined contributions (NDCs), to reduce their greenhouse gas (GHG) emissions and limit the temperature increase to 1.5 °C above the pre-industrial levels (Figure 1.1). To achieve these objectives, greenhouse gas emissions must reach to their peak before 2025 and decline by 43% before 2030.⁵

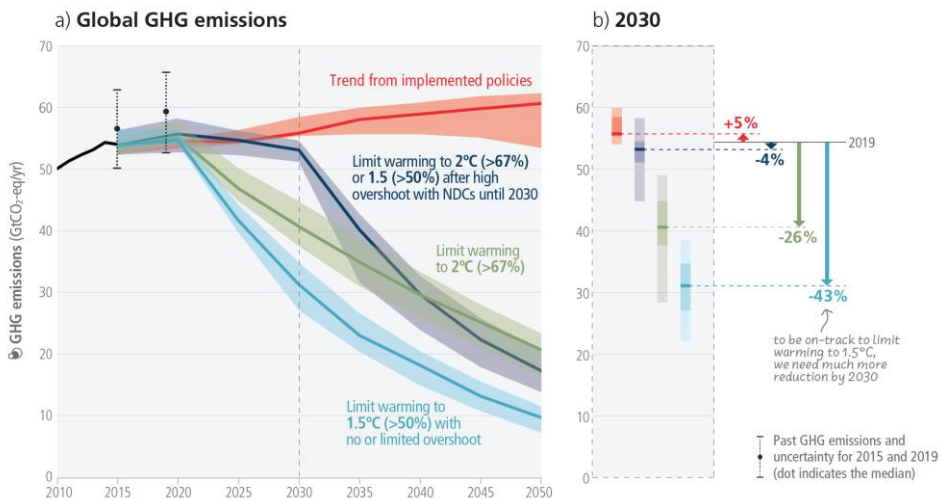


Figure 1.1 (a) Global GHG emissions of modelled pathways; (b) projected emission outcomes from near-term policy assessments for 2030. Reprinted from IPCC6.⁵

In addition to developing renewable energy and improving energy efficiency for industrial processes, carbon capture, utilization and storage (CCUS) has also been deemed as an essential strategy for climate change mitigation.⁶ CCUS is used to capture CO₂ from industrial flue gases or directly from the air, and then transport the CO₂ for further utilization or permanent storage.⁷ Importantly, CO₂ is no longer considered as a waste but a resource to produce high-value added products. Regarding to this issue, the study of CO₂ conversion has triggered tremendous interest in the past decades. Several strategies have been developed for CO₂ conversion, including biological, thermochemical, photochemical, and

electrochemical.⁸ Among them, electrochemical CO₂ reduction is very attractive due to its moderate operation conditions and controllable products by varying applied potentials.⁹

1.2 What is the electrochemical CO₂ reduction reaction (CO₂RR)?

The electrochemical CO₂ reduction reaction (CO₂RR) is a promising pathway to close the carbon cycle. It uses clean and renewable electricity (solar, wind, etc.) to convert CO₂ and H₂O into valuable products. The process can be operated at ambient temperature, atmospheric pressure and neutral pH, and can convert waste CO₂ into various chemicals and fuels whilst storing intermittent renewable and off-peak electricity into chemical bonds.¹⁰ In a typical CO₂ electrolyzer, the CO₂ reduction reaction occurs on the cathode, whereas water is oxidized on the anode. Cathode and anode are located in two chambers separated by an ion exchange membrane (Figure 1.2a).

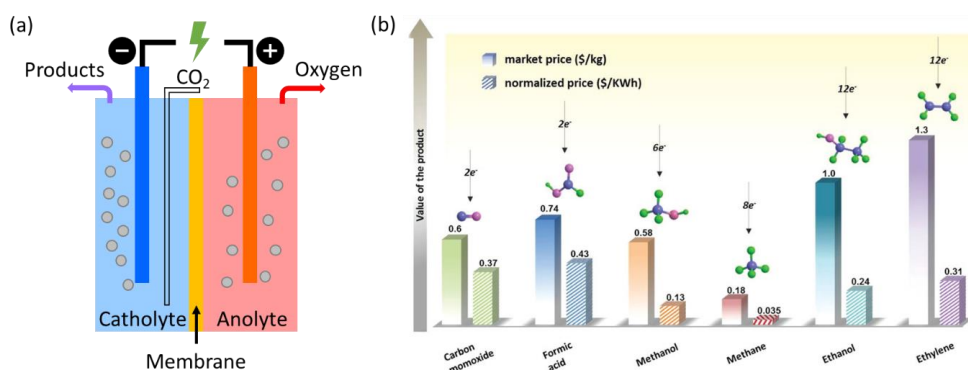


Figure 1.2 (a) Schematic illustration of a typical CO₂ electrolyzer; (b) Comparison of the values of different CO₂RR products in terms of their market prices (\$/kg) and added values per kWh electrical energy input (\$/kWh), reprinted from ref.12 with permission from Wiley.

Depending on the reaction pathway, CO₂ can be reduced to approximately 16 products, including carbon monoxide (CO), methane (CH₄), formate, methanol, ethylene and ethanol.¹¹ The main cathodic reactions and their equilibrium potentials are summarized in Table 1.1. Among these products, C₂ or C₃ hydrocarbons are desirable due to their higher market prices than CO and formate. However, the product selectivity of hydrocarbon products (~60% for ethylene, ~40% for acetate, ~15% for n-propanol) are much lower than CO and formate (~100%).¹² In addition, considering the energy consumption, and

downstream separation costs, CO is so far the most profitable target for large-scale applications (Figure 1.2b).^{13,14}

Table 1.1 Standard electrochemical potentials for some CO₂ electrolysis related reactions (pH 7 in aqueous solution vs. standard hydrogen electrode (SHE), 25 °C, 1 atm).

Reaction	E ⁰ (V vs. SHE)
$\text{CO}_2 + 2\text{H}^+ + 2\text{e}^- \rightarrow \text{HCOOH}$	-0.61
$\text{CO}_2 + 2\text{H}^+ + 2\text{e}^- \rightarrow \text{CO} + \text{H}_2\text{O}$	-0.52
$\text{CO}_2 + 4\text{H}^+ + 4\text{e}^- \rightarrow \text{HCHO} + \text{H}_2\text{O}$	-0.51
$\text{CO}_2 + 6\text{H}^+ + 6\text{e}^- \rightarrow \text{CH}_3\text{OH} + \text{H}_2\text{O}$	-0.38
$\text{CO}_2 + 8\text{H}^+ + 8\text{e}^- \rightarrow \text{CH}_4 + 2\text{H}_2\text{O}$	-0.24
$2\text{CO}_2 + 12\text{H}^+ + 12\text{e}^- \rightarrow \text{C}_2\text{H}_4 + 4\text{H}_2\text{O}$	-0.34
$2\text{H}^+ + 2\text{e}^- \rightarrow \text{H}_2$	-0.42

Due to the low solubility, thermodynamic stability, and low electron affinity of CO₂, electrochemical CO₂ reduction reaction processes are still facing multiple challenges, such as the high energy barriers, sluggish reaction kinetics and the competition reaction of hydrogen evolution reaction (HER).^{15,16} Therefore, developing an efficient electrocatalyst with a high selectivity and activity to preferred products is highly desired.

1.3 The electrocatalyst: the cornerstone for efficient CO₂RR

To date, the most commonly used catalysts for the CO₂RR can be divided into three categories: molecular catalysts, metallic catalysts, and non-metallic catalysts (Figure 1.3).¹⁷ Since the 1970s, several molecular catalysts, such as cobalt and nickel phthalocyanines, were reported as active catalysts for CO₂ electrochemical reduction.¹⁸ The advantages of molecular catalysts include their tunability and electronic characteristics, which give access to a large variety of catalysts with high selectivity, activity, and durability.¹⁹ Additionally, molecular catalysts can be used as homogeneous catalysts or heterogeneous catalysts, which have attracted a considerable attention in recent years.

For metallic catalysts, Hori et al. systemically studied the electrochemical CO₂RR performance over various bulk metal catalysts since the 1980s and summarized their

characteristics.²⁰ The monometallic electrodes can be classified according to their product distribution into four subgroups, including formate selective metals (e.g. Pb, Sn, Bi), CO selective metals (e.g. Au, Ag, Zn), H₂ selective metals (Pt, Ni, Fe), and hydrocarbon selective metal (Cu). In the past decades, several metal oxide, metal sulfide, metal nitride, bimetallic alloys, and high entropy alloys have been demonstrated as efficient catalysts for the CO₂RR.²¹ In addition, the CO₂RR performance of metal-based catalysts can be effectively improved by optimizing the morphology, defects, facets, and surface microenvironment of applied catalysts.^{22,23}

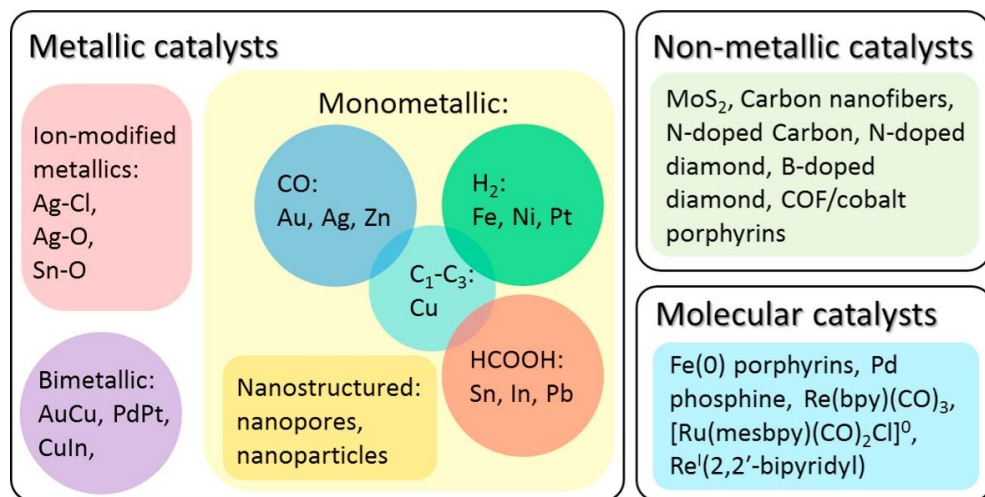


Figure 1.3 Three major categories of electrocatalysts for electrochemical CO₂ reduction.

Reprinted from ref.17 with permission from Elsevier.

Metal-free carbon-based materials are emerging catalysts for the CO₂RR with remarkable selectivity, activity and long durability.²⁴ Compared with metal-based catalysts, carbon-based catalysts exhibit several advantages, such as natural abundance, relatively low price, large specific surface area, abundant pore structure and resistance to acids and bases.²⁵ However, pure carbon materials possess poor activity for the CO₂RR and mainly produce H₂.²⁶ Heteroatom doping is one of the commonly used strategies to impart catalytic activity to carbon materials. The most doped heteroatoms include boron (B), nitrogen (N), sulfur (S), phosphor (P), fluorine (F), etc.²⁷ By introducing one or more heteroatoms into the carbon skeleton, the charge distribution on carbon catalysts will be modulated owing to the different electronegativity of heteroatoms, which further influences the adsorption and activation of reactants and intermediates.²⁸ These changes of charge distribution on the carbon framework, derived from heteroatom(s) doping, are usually considered to be the

active sites for the CO₂RR. N-doping is one of the most investigated strategies for the preparation of metal-free carbon-based catalyst for the CO₂RR. N-doped carbon materials (e.g. carbon fiber, carbon nanotubes, graphene, carbon nanosheets) have been demonstrated as efficient catalysts for electrochemical CO₂ reduction to CO, in some cases exhibiting better performances than Ag and Au.^{29,30}

With the development of green chemistry, there are higher expectations for the selection and investigation of catalysts for the CO₂RR. The pursuit of catalysts with high selectivity, activity and stability needs to be balanced with cost-effectiveness, sustainability and environmental friendliness. For metallic catalysts, mining and metallurgical processes damage the natural environment and increase their carbon footprint. Although N-doped carbon materials can be used as feasible substitutes, most of them are derived from fossil feedstocks. Moreover, the low yield, harsh synthesis conditions and intensive energy processes also hinder the large-scale utilization of these catalysts.³¹

1.4 Why use biomass-derived carbon?

Apart from solar and wind energy, biomass is the only renewable energy source that can close the carbon cycle. Biomass captures CO₂ from the air, converts CO₂ into organic material by photosynthesis, and stores CO₂ into the biomass-derived carbon during carbonization.³² Therefore, using renewable biomass as feedstocks to manufacture biomass-derived carbon is a more sustainable approach for the production of functional carbon materials. Additionally, the wide distribution and earth abundance of biomass shows the potential for large-scale application of biomass-derived carbon.

Depending on the characteristics of different biomass type, they can be converted into biochar through pyrolysis, gasification, torrefaction and hydrothermal conversion. The specific surface area, porosity, surface wettability, and surface functional groups can be easily modulated by simply adjusting the synthetic conditions. Benefitting from these tunable physicochemical properties, biomass-derived carbon has been widely investigated as adsorbent for wastewater treatment, air purification, and soil remediation (Figure 1.4).³³

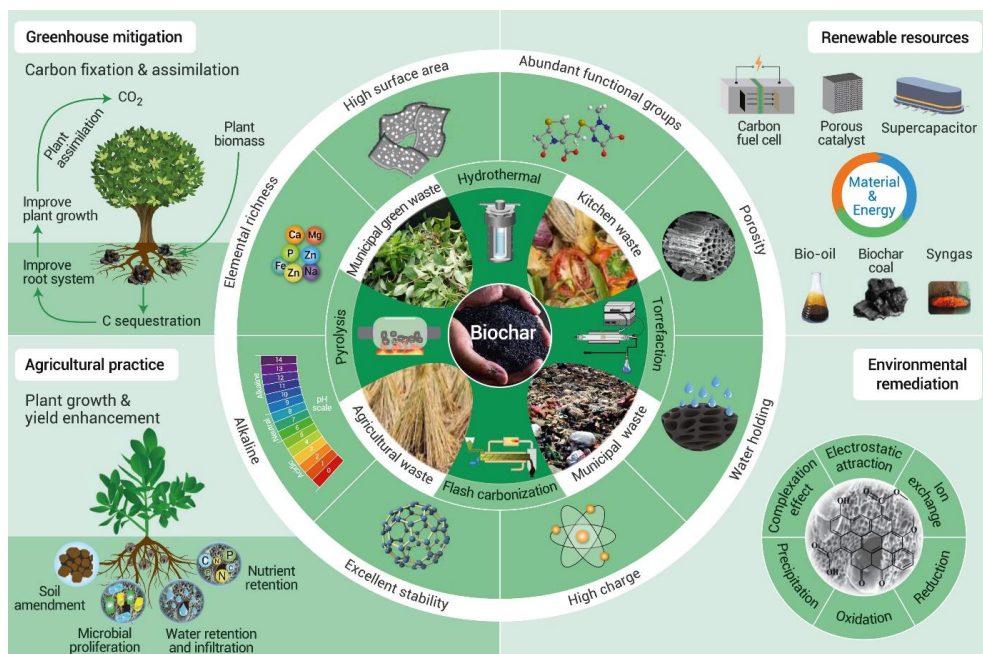


Figure 1.4 Biochar as a carbon-neutral tool for sustainable development. Reprinted from ref.33 with permission from Elsevier.

Owing to its tailorable porous structure, large specific surface area, inherent functional groups, abundant defects and electronic conductivity, biomass-derived carbon shows potential as a viable substitute to replace unsustainable fossil-based carbon catalysts for electrochemical energy conversion processes.³⁴ In addition, the pristine protein and inorganic salts in biomass feedstocks are helpful for the self-doping and pore generation, respectively, which could further improve the electrochemical performance of biomass-derived carbon.^{35,36} Some pioneering studies have demonstrated that the N-doped biochar catalysts exhibit comparable CO₂RR performances as advanced fossil-based carbon catalysts.^{37–39}

Using biomass-derived carbon as electrocatalysts for CO₂RR shows multiple merits. It converts waste biomass into functional carbon materials and improves its added value, while also providing a sustainable and efficient catalyst for the electrochemical CO₂ reduction to close the CO₂ cycle. Despite the fact that many challenges associated with the use of N-doped biomass-derived carbon as catalysts for electrochemical CO₂RR remain, there are great opportunities to achieve practical applications in the future.

1.5 Main challenges of using N-doped biomass-derived carbon as catalysts for CO₂RR

Although considerable progress has been made in using N-doped biochar as catalysts for CO₂RR, some critical issues should still be addressed in future work. First, the selection of biomass feedstock should follow the discipline of ethics. Studies using animal-derived materials (e.g. butterfly, silk cocoon, etc.) and edible food (e.g. egg, flour, etc.) as feedstock to prepare biomass-derived carbon materials should not be encouraged, even if they show better electrochemical performances.^{40,41} The ideal biomass feedstock should be waste or by-products from industrial processes, with large yields and should be easily collected and transported.

Second, the relationship between synthesis conditions and physicochemical properties of N-doped biochar is unclear. Due to the diversity of biomass, dopant, activator and operation conditions (carbonization temperature, heating rate, atmosphere), it is impossible to summarize the correlation between synthesis conditions and properties of N-doped biochar from numerous published studies. However, it is important to understand the influence of each single variable of the synthesis procedure, such as the carbonization temperature, heating rate, type of activator and amount of N-dopant, to the final properties of the N-doped biochar.

Third, the relationship between physicochemical properties and electrochemical CO₂RR performances of N-doped biochar is unclear. Countless N-doped carbon catalysts with impressive CO₂RR catalytic performances were reported. However, the excellent performances were always simply attributed to a certain type of N-containing species (e.g. pyridinic N, graphitic N, etc.) or a large specific surface area.^{42–44} However, studies with contradicting conclusions have also widely been reported.^{45,46} This controversy stems from the differences of structural properties, surface wettability, defect abundance of various N-doped carbon materials. Therefore, a systematical investigation with consideration of the contribution from different properties, rather than overemphasizing the function of N-containing species and specific surface area, is critical to reveal the correlation between physicochemical properties and electrochemical CO₂RR performances of N-doped biochar.

Fourth, the excellent CO₂RR performances of N-doped biochar were reported using ideal laboratory conditions with high purity CO₂. In a practice, the industrial CO₂ streams can contain trace amounts of gaseous impurities. Understanding the CO₂RR performance of N-doped biochar in the presence of gaseous impurities is meaningful for the future application using CO₂-rich industrial flue gas.

Last but not least, the faradaic efficiency toward CO of N-doped biochar is comparable to the advanced catalysts for electrochemical CO₂ reduction to CO. However, the partial

current density of CO of N-doped biochar catalyst, namely catalytic activity, is still worse than the state-of-the-art metal-based catalysts. Therefore, improving the catalytic activity of N-doped biochar is still facing challenges.

1.6 Research questions and thesis outline

According to the above discussion about current challenges, this thesis aims to address the following research questions (RQ):

- RQ1: What is the recent progress for the preparation of N-doped biochar via carbonization, activation and functionalization? (Chapter 2)
- RQ2: Can we get transferable knowledge about the preparation and characterization of N-doped biochar catalysts from other electrocatalytic reactions, such as the hydrogen evolution reaction and oxygen reduction reaction? (Chapter 2)
- RQ3: How does the type of activator used for the preparation of N-doped biochar influence the structural properties and further influence the electrochemical CO₂RR performance? (Chapter 3)
- RQ4: Is improving the N-doping content and specific surface area helpful to enhance the CO₂RR performance of N-doped biochar catalyst? (Chapter 4)
- RQ5: How do we comprehensively understand the contributions of various physicochemical properties to the CO₂RR performance of N-doped biochar catalyst? (Chapter 4)
- RQ6: What is the performance of N-doped biochar catalyst for electrochemical CO₂ reduction in the presence of SO₂ impurities? (Chapter 5)
- RQ7: Is N-doped biochar a feasible alternative as carbon support to fabricate metal-nitrogen-carbon catalysts for CO₂RR with better performance? (Chapter 6)
- RQ8: How do the characteristics of carbon supports affect the CO₂RR performances of metal-nitrogen-carbon catalysts? (Chapter 6)

These research questions are addressed throughout the thesis with the following approach (Figure 1.5). **Chapter 2** summarizes the most commonly used strategies for carbonization, activation, and functionalization of the preparation of N-doped biochar.

Additionally, the recent progress of using N-doped biochar catalysts for the hydrogen evolution reaction, oxygen reduction reaction and CO₂ reduction reaction are carefully scrutinized. **Chapter 3** tests six different types of activators used for the preparation of N-doped biochar and evaluates the structural properties and electrochemical CO₂RR performances of these as-prepared N-doped biochar catalysts. **Chapter 4** assesses the effect of N-doping content and specific surface area of N-doped biochar catalysts for CO₂RR performance via controlling the carbonization temperature and the addition of nitrogen dopant. A multivariate correlation analysis is made to elucidate the correlation between physicochemical properties and electrochemical performance of N-doped biochar catalysts. **Chapter 5** evaluates the performance of a N-doped biochar catalyst and a benchmark silver foil electrode for electrochemical CO₂ reduction in the presence of 100 to 10000 ppm SO₂ impurities. The changes of surface morphology and chemical composition of N-doped biochar catalyst and silver foil are reported as well. **Chapter 6** investigates the feasibility of using N-doped biochar as carbon support to prepare metal-nitrogen-carbon catalyst and scrupulously assesses the importance of carbon supports for the CO₂RR performance of metal-nitrogen-carbon catalysts. **Chapter 7** includes conclusions and recommendations for future research.

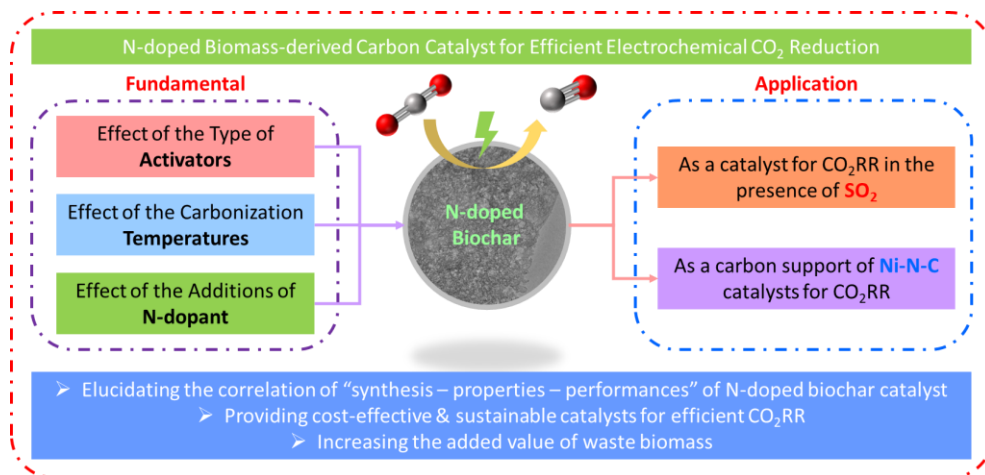


Figure 1.5 Scope and objectives of this thesis.

References

- (1) Obama, B. The Irreversible Momentum of Clean Energy. *Science*. **2017**, 355 (6321), 126–129.
- (2) Chu, S.; Cui, Y.; Liu, N. The Path towards Sustainable Energy. *Nat. Mater.* **2017**, 16 (1), 16–22.
- (3) Carley, S.; Konisky, D. M. The Justice and Equity Implications of the Clean Energy Transition. *Nat. Energy* 2020 58 **2020**, 5 (8), 569–577.
- (4) Hoegh-Guldberg, O.; Jacob, D.; Taylor, M.; Guillén Bolaños, T.; Bindi, M.; Brown, S.; Camilloni, I. A.; Diedhiou, A.; Djalante, R.; Ebi, K.; Engelbrecht, F.; Guiot, J.; Hijikata, Y.; Mehrotra, S.; Hope, C. W.; Payne, A. J.; Pörtner, H. O.; Seneviratne, S. I.; Thomas, A.; Warren, R.; Zhou, G. The Human Imperative of Stabilizing Global Climate Change at 1.5°C. *Science*. **2019**, 365, 6459.
- (5) Nicholls, Z.; Meinshausen, M.; Lewis, J.; Smith, C. J.; Forster, P. M.; Fuglestad, J. S.; Rogelj, J.; Kikstra, J. S.; Riahi, K.; Byers, E. Changes in IPCC Scenario Assessment Emulators Between SR1.5 and AR6 Unraveled. *Geophys. Res. Lett.* **2022**, 49 (20), e2022GL099788.
- (6) Chen, S.; Liu, J.; Zhang, Q.; Teng, F.; McLellan, B. C. A Critical Review on Deployment Planning and Risk Analysis of Carbon Capture, Utilization, and Storage (CCUS) toward Carbon Neutrality. *Renew. Sustain. Energy Rev.* **2022**, 167, 112537.
- (7) Jiang, K.; Ashworth, P.; Zhang, S.; Liang, X.; Sun, Y.; Angus, D. China's Carbon Capture, Utilization and Storage (CCUS) Policy: A Critical Review. *Renew. Sustain. Energy Rev.* **2020**, 119, 109601.
- (8) Saravanan, A.; Vo, D.-V. N.; Jeevanantham, S.; Bhuvaneswari, V.; Narayanan, V. A.; Yaashikaa, P. R.; Swetha, S.; Reshma, B. A Comprehensive Review on Different Approaches for CO₂ Utilization and Conversion Pathways. *Chem. Eng. Sci.* **2021**, 236, 116515.
- (9) Sullivan, I.; Goryachev, A.; Digdaya, I. A.; Li, X.; Atwater, H. A.; Vermaas, D. A.; Xiang, C. Coupling Electrochemical CO₂ Conversion with CO₂ Capture. *Nat. Catal.* **2021**, 4 (11), 952–958.
- (10) Kortlever, R.; Shen, J.; Schouten, K. J. P.; Calle-Vallejo, F.; Koper, M. T. M. Catalysts and Reaction Pathways for the Electrochemical Reduction of Carbon Dioxide. *J. Phys. Chem. Lett.* **2015**, 6 (20), 4073–4082.
- (11) Kuhl, K. P.; Cave, E. R.; Abram, D. N.; Jaramillo, T. F. New Insights into the Electrochemical Reduction of Carbon Dioxide on Metallic Copper Surfaces. *Energy Environ. Sci.* **2012**, 5 (5), 7050–7059.

- (12) Han, N.; Ding, P.; He, L.; Li, Y.; Li, Y. Promises of Main Group Metal-Based Nanostructured Materials for Electrochemical CO₂ Reduction to Formate. *Adv. Energy Mater.* **2020**, *10* (11), 1902338.
- (13) Jin, S.; Hao, Z.; Zhang, K.; Yan, Z.; Chen, J. Advances and Challenges for the Electrochemical Reduction of CO₂ to CO: From Fundamentals to Industrialization. *Angew. Chemie* **2021**, *133* (38), 20795–20816.
- (14) Debergh, P.; Gutiérrez-Sánchez, O.; Khan, M. N.; Birdja, Y. Y.; Pant, D.; Bulut, M. The Economics of Electrochemical Syngas Production via Direct Air Capture. *ACS Energy Lett.* **2023**, *8* (8), 3398–3403.
- (15) Birdja, Y. Y.; Pérez-Gallent, E.; Figueiredo, M. C.; Göttle, A. J.; Calle-Vallejo, F.; Koper, M. T. M. Advances and Challenges in Understanding the Electrocatalytic Conversion of Carbon Dioxide to Fuels. *Nat. Energy* **2019**, *4* (9), 732–745.
- (16) Sun, Z.; Ma, T.; Tao, H.; Fan, Q.; Han, B. Fundamentals and Challenges of Electrochemical CO₂ Reduction Using Two-Dimensional Materials. *Chem* **2017**, *3* (4), 560–587.
- (17) Lu, Q.; Jiao, F. Electrochemical CO₂ Reduction: Electrocatalyst, Reaction Mechanism, and Process Engineering. *Nano Energy* **2016**, *29*, 439–456.
- (18) Meshitsuka, S.; Ichikawa, M.; Tamaru, K. Electrocatalysis by Metal Phthalocyanines in the Reduction of Carbon Dioxide. *J. Chem. Soc. Chem. Commun.* **1974**, *5*, 158–159.
- (19) Elouarzaki, K.; Kannan, V.; Jose, V.; Sabharwal, H. S.; Lee, J. M. Recent Trends, Benchmarking, and Challenges of Electrochemical Reduction of CO₂ by Molecular Catalysts. *Adv. Energy Mater.* **2019**, *9* (24), 1900090.
- (20) HoriYoshio; KikuchiKatsuhei; SuzukiShin. PRODUCTION OF CO AND CH₄ IN ELECTROCHEMICAL REDUCTION OF CO₂ AT METAL ELECTRODES IN AQUEOUS HYDROGENCARBONATE SOLUTION. **2006**, *14* (11), 1695–1698.
- (21) Franco, F.; Rettenmaier, C.; Jeon, H. S.; Roldan Cuenya, B. Transition Metal-Based Catalysts for the Electrochemical CO₂ Reduction: From Atoms and Molecules to Nanostructured Materials. *Chem. Soc. Rev.* **2020**, *49* (19), 6884–6946.
- (22) Reske, R.; Mistry, H.; Behafarid, F.; Roldan Cuenya, B.; Strasser, P. Particle Size Effects in the Catalytic Electroreduction of CO₂ on Cu Nanoparticles. *J. Am. Chem. Soc.* **2014**, *136* (19), 6978–6986.
- (23) Mistry, H.; Varela, A. S.; Kühl, S.; Strasser, P.; Cuenya, B. R. Nanostructured Electrocatalysts with Tunable Activity and Selectivity. *Nat. Rev. Mater.* **2016**, *1* (4), 1–14.

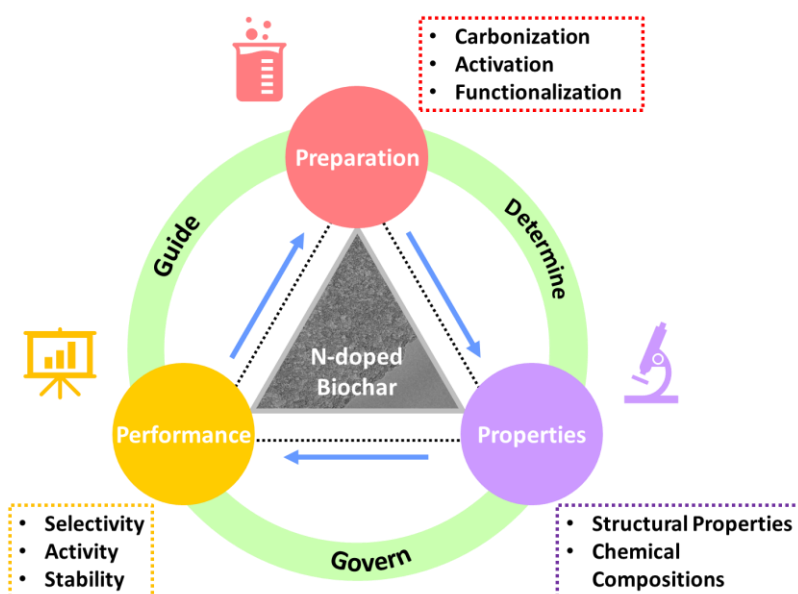
- (24) Paul, R.; Dai, Q.; Hu, C.; Dai, L. Ten Years of Carbon-based Metal-free Electrocatalysts. *Carbon Energy* **2019**, *1* (1), 19–31.
- (25) Hu, C.; Xiao, Y.; Zou, Y.; Dai, L. Carbon-Based Metal-Free Electrocatalysis for Energy Conversion and Storage. *Electrochem. Energy Rev.* **2018**, *1* (1), 84–112.
- (26) Vasileff, A.; Zheng, Y.; Qiao, S. Z. Carbon Solving Carbon's Problems: Recent Progress of Nanostructured Carbon-Based Catalysts for the Electrochemical Reduction of CO₂. *Adv. Energy Mater.* **2017**, *7* (21), 1–21.
- (27) Hu, C.; Dai, L. Doping of Carbon Materials for Metal-Free Electrocatalysis. *Adv. Mater.* **2019**, *31* (7), 1–17.
- (28) Duan, X.; Xu, J.; Wei, Z.; Ma, J.; Guo, S.; Wang, S.; Liu, H.; Dou, S. Metal-Free Carbon Materials for CO₂ Electrochemical Reduction. *Adv. Mater.* **2017**, *29* (41), 1701784.
- (29) Kumar, B.; Asadi, M.; Pisasale, D.; Sinha-Ray, S.; Rosen, B. A.; Haasch, R.; Abiade, J.; Yarin, A. L.; Salehi-Khojin, A. Renewable and Metal-Free Carbon Nanofibre Catalysts for Carbon Dioxide Reduction. *Nat. Commun.* **2013**, *4* (1), 1–8.
- (30) Sharma, P. P.; Wu, J.; Yadav, R. M.; Liu, M.; Wright, C. J.; Tiwary, C. S.; Yakobson, B. I.; Lou, J.; Ajayan, P. M.; Zhou, X. D. Nitrogen-Doped Carbon Nanotube Arrays for High-Efficiency Electrochemical Reduction of CO₂: On the Understanding of Defects, Defect Density, and Selectivity. *Angew. Chemie - Int. Ed.* **2015**, *54* (46), 13701–13705.
- (31) Liu, W.-J.; Jiang, H.; Yu, H.-Q. Emerging Applications of Biochar-Based Materials for Energy Storage and Conversion. *Energy Environ. Sci.* **2019**, *12* (6), 1751–1779.
- (32) Barrio, J.; Pedersen, A.; Favero, S.; Luo, H.; Wang, M.; Sarma, S. C.; Feng, J.; Ngoc, L. T. T.; Kellner, S.; Li, A. Y.; Jorge Sobrido, A. B.; Titirici, M. M. Bioinspired and Bioderived Aqueous Electrocatalysis. *Chem. Rev.* **2023**, *123* (5), 2311–2348.
- (33) Wang, F.; Harindintwali, J. D.; Yuan, Z.; Wang, M.; Wang, F.; Li, S.; Yin, Z.; Huang, L.; Fu, Y.; Li, L.; Chang, S. X.; Zhang, L.; Rinklebe, J.; Yuan, Z.; Zhu, Q.; Xiang, L.; Tsang, D. C. W.; Xu, L.; Jiang, X.; Liu, J.; Wei, N.; Kästner, M.; Zou, Y.; Ok, Y. S.; Shen, J.; Peng, D.; Zhang, W.; Barceló, D.; Zhou, Y.; Bai, Z.; Li, B.; Zhang, B.; Wei, K.; Cao, H.; Tan, Z.; Zhao, L. bin; He, X.; Zheng, J.; Bolan, N.; Liu, X.; Huang, C.; Dietmann, S.; Luo, M.; Sun, N.; Gong, J.; Gong, Y.; Brahushi, F.; Zhang, T.; Xiao, C.; Li, X.; Chen, W.; Jiao, N.; Lehmann, J.; Zhu, Y. G.; Jin, H.; Schäffer, A.; Tiedje, J. M.; Chen, J. M. Technologies and Perspectives for Achieving Carbon Neutrality. *Innov.* **2021**, *2* (4), 48.
- (34) Liu, W. J.; Jiang, H.; Yu, H. Q. Development of Biochar-Based Functional Materials: Toward a Sustainable Platform Carbon Material. *Chem. Rev.* **2015**, *115* (22), 12251–12285.

- (35) Zhang, Z.; Yang, S.; Li, H.; Zan, Y.; Li, X.; Zhu, Y.; Dou, M.; Wang, F. Sustainable Carbonaceous Materials Derived from Biomass as Metal-Free Electrocatalysts. *Adv. Mater.* **2019**, *31* (13), 1805718.
- (36) Niu, J.; Shao, R.; Liu, M.; Zan, Y.; Dou, M.; Liu, J.; Zhang, Z.; Huang, Y.; Wang, F. Porous Carbons Derived from Collagen-Enriched Biomass: Tailored Design, Synthesis, and Application in Electrochemical Energy Storage and Conversion. *Adv. Funct. Mater.* **2019**, *1905095*.
- (37) Yao, P.; Qiu, Y.; Zhang, T.; Su, P.; Li, X.; Zhang, H. N-Doped Nanoporous Carbon from Biomass as a Highly Efficient Electrocatalyst for the CO₂ Reduction Reaction. *ACS Sustain. Chem. Eng.* **2019**, *7* (5), 5249–5255.
- (38) Fu, S.; Li, M.; Asperti, S.; Jong, W. de; Kortlever, R. Unravelling the Effect of Activators Used in The Synthesis of Biomass-Derived Carbon Electrocatalysts on the Electrocatalytic Performance for CO₂ Reduction. *ChemSusChem* **2023**, *16*, e202202188.
- (39) Hao, X.; An, X.; Patil, A. M.; Wang, P.; Ma, X.; Du, X.; Hao, X.; Abudula, A.; Guan, G. Biomass-Derived N-Doped Carbon for Efficient Electrocatalytic CO₂ Reduction to CO and Zn-CO₂Batteries. *ACS Appl. Mater. Interfaces* **2021**, *13* (3), 3738–3747.
- (40) Chen, M.; Wang, S.; Zhang, H.; Zhang, P.; Tian, Z.; Lu, M.; Xie, X.; Huang, L.; Huang, W. Intrinsic Defects in Biomass-Derived Carbons Facilitate Electroreduction of CO₂. *Nano Res.* **2020**, *13* (3), 729–735.
- (41) Li, F.; Xue, M.; Knowles, G. P.; Chen, L.; MacFarlane, D. R.; Zhang, J. Porous Nitrogen-Doped Carbon Derived from Biomass for Electrocatalytic Reduction of CO₂ to CO. *Electrochim. Acta* **2017**, *245*, 561–568.
- (42) Kuang, M.; Guan, A.; Gu, Z.; Han, P.; Qian, L.; Zheng, G. Enhanced N-Doping in Mesoporous Carbon for Efficient Electrocatalytic CO₂ Conversion. *Nano Res.* **2019**, *12* (9), 2324–2329.
- (43) Li, H.; Xiao, N.; Hao, M.; Song, X.; Wang, Y.; Ji, Y.; Liu, C.; Li, C.; Guo, Z.; Zhang, F.; Qiu, J. Efficient CO₂ Electroreduction over Pyridinic-N Active Sites Highly Exposed on Wrinkled Porous Carbon Nanosheets. *Chem. Eng. J.* **2018**, *351*, 613–621.
- (44) Zhang, Z.; Yu, L.; Tu, Y.; Chen, R.; Wu, L.; Zhu, J.; Deng, D. Unveiling the Active Site of Metal-Free Nitrogen-Doped Carbon for Electrocatalytic Carbon Dioxide Reduction. *Cell Reports Phys. Sci.* **2020**, *1* (8), 100145.

- (45) Daiyan, R.; Tan, X.; Chen, R.; Saputera, W. H.; Tahini, H. A.; Lovell, E.; Ng, Y. H.; Smith, S. C.; Dai, L.; Lu, X.; Amal, R. Electroreduction of CO₂ to CO on a Mesoporous Carbon Catalyst with Progressively Removed Nitrogen Moieties. *ACS Energy Lett.* **2018**, *3* (9), 2292–2298.
- (46) Hursán, D.; Samu, A. A.; Janovák, L.; Artyushkova, K.; Asset, T.; Atanassov, P.; Janáky, C. Morphological Attributes Govern Carbon Dioxide Reduction on N-Doped Carbon Electrodes. *Joule* **2019**, *3* (7), 1719–1733.

2

Recent Progress of Biomass-derived Nitrogen-doped Carbon Materials as Electrocatalysts



Abstract: Coupling renewable energy with electrochemical energy conversion and storage techniques represents a promising solution to solve energy and environmental problems. Owing to their sustainability, earth abundance, low price and structural tunability, biomass-derived nitrogen-doped (N-doped) carbon materials have been widely used as efficient electrocatalysts for various electrochemical applications and achieved significant advancements. In this chapter, recent advances towards the preparation of N-doped biochar catalysts and their utilization for the hydrogen evolution reaction, oxygen reduction reaction and CO₂ reduction reaction are summarized. We highlight the correlations between synthesis – structure – performance of N-doped biochar catalysts. First, the most commonly used carbonization approaches, functionalization strategies and characterization methods for N-doped biochar materials are discussed. Then, the emerging N-doped biochar catalysts for different electrochemical reactions are scrutinized, with special attention on the similarities and differences of the properties of N-doped biochar for various reactions. Additionally, challenges and future perspectives on the development of N-doped biochar for further investigation are provided.

2.1 Introduction

With the immense growth of world population and overwhelming development of industrialization and urbanization, the pressing issues of the energy transition, global warming and environmental pollution have become increasingly apparent.^{1–3} To address these challenges, the coupling of clean and renewable energy sources and carbon-neutralization technologies, including fuel cells, metal-air batteries, water electrolysis and carbon capture, utilization, and storage (CCUS) have gained tremendous attentions.^{4–12} Nevertheless, the large-scale implementation of these technologies is still challenging, as their performances are highly dependent on the applied catalysts for critical electrochemical processes such as the hydrogen evolution reaction (HER), oxygen reduction reaction (ORR) and CO₂ reduction reaction (CO₂RR).¹³ Traditionally, precious metal-based catalysts, such as platinum, ruthenium and iridium, are well known as the best catalysts for the HER and ORR.^{14–16} However, the scarcity and high costs of these metals can have consequences for large-scale commercial applications. Although the catalysts for CO₂RR, such as silver, gold and copper, are relatively cheaper than these precious metals, the poor durability, susceptibility to impurities and the negative effects of mining and refinery to environment may limit their future applications.^{17–19} Therefore, seeking alternative catalysts that exhibit competitive catalytic performance similar to metal-based catalysts while being readily accessible, cost-effective, and environmentally friendly, is highly desirable.

Benefitting from their electronic properties, structure, surface chemistry and affordable price, carbon-based materials have been widely investigated as catalyst or catalyst support for various electrochemical energy conversion technologies.^{20,21} In 2009, Dai and co-workers found that metal-free nitrogen-doped (N-doped) aligned carbon nanotubes are alternative catalysts for the ORR and can potentially replace Pt, showing high catalytic activity, long stability and strong tolerance to impurities.²² Since then, N-doped carbon-based materials have been reported as efficient catalysts for the HER, ORR, OER, CO₂RR, and many other reactions.²³ As a consequence, developing novel N-doped carbon materials, improving their performances and revealing the reaction mechanisms of carbon-based catalysts for different electrochemical reactions have gained significant attention.

In recent years, many advanced N-doped carbon-based materials, including graphene, carbon nanotubes and carbon nanofibers, have been functionalized and applied to different electrochemical reactions, showing comparable performances as metal-based catalysts.^{24–29} Apart from these fossil-based carbon materials, a series of novel N-doped carbon catalysts derived from metal-organic frameworks (MOFs), MXene materials, and polymer precursors also exhibited eminent intrinsic properties and impressive catalytic performances.^{30–34} Recent research advancements have provided both experimental and theoretical evidence to support the promising future of well-designed N-doped carbon catalysts for various

applications such as the HER, ORR, OER, and CO₂RR.³⁵ However, the extensive application of these N-doped carbon catalysts is hindered by several challenges, including the presence of harsh synthetic conditions, energy-intensive preparation processes, and limited yields.³⁶ Therefore, developing scalable ways to manufacture N-doped carbon materials from renewable and abundant resources with good performances and a limited environmental impact is of significant interest.

Biomass, as the sole renewable energy source capable of naturally closing the carbon cycle, exhibits promising potential as a viable alternative to fossil feedstocks for generating carbon-based materials, fuels, and chemicals. In a broad sense, biomass encompasses all organic substances derived from plants, animals, microorganisms and by-products of processing these substances in industry.³⁷ These biomass sources can be transformed into solid, gas, and liquid products through diverse technologies, including chemical, thermochemical, and biochemical processes.^{38,39} Biomass-derived carbon, also called biochar, has emerged as a promising sustainable option for various electrochemical applications owing to its conductivity and catalytical activity.^{40–42} Biochar is a carbon-rich solid material from biomass by thermochemical conversion with limited oxygen, which exhibits a high specific surface area, abundant porosity, and high variability of surface functional groups. Through further activation and heteroatom (nitrogen) doping, biochar has emerged as a highly promising substitute for advanced carbon materials. Further, using N-doped biochar for electrochemical energy conversion brings multiple benefits. It offers sustainable and cost-effective materials for electrochemical devices while also enhancing the value of biomass residues. Figure 2.1 shows the concept of using functionalized biochar for electrochemical catalytic energy conversion processes.

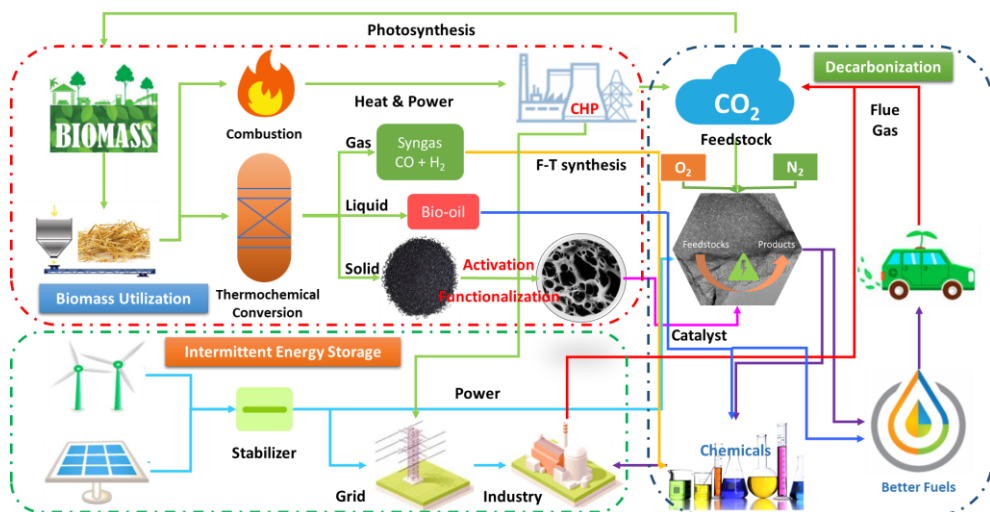


Figure 2.1 Schematic illustration of renewable biomass-derived carbon for sustainable electrochemical catalytic energy conversion.

Over the past few decades, an increased amount of applications of N-doped biochar have come up. This has led to a rising interest in utilizing functionalized biochar for purposes such as environmental remediation,⁴³ soil amendment,⁴⁴ wastewater treatment,⁴⁵ CO₂ absorption,⁴⁶ supercapacitors,⁴⁷ metal-air batteries,⁴⁸ lithium/sodium batteries⁴⁹ and catalysts⁵⁰. The utilization of N-doped biochar as electrocatalysts for the ORR, HER and CO₂RR has been extensively reported. However, there is no comprehensive review covering the preparation, functionalization, and applications of N-doped biochar-based materials as electrocatalysts for these reactions. Hence, this chapter aims to provide such a comprehensive overview on the strategies of carbonization, activation and heteroatom doping of biochar, highlighting the recent development of nitrogen-doped biomass-derived carbon catalysts for the HER, ORR and CO₂RR. Furthermore, the challenges and perspectives of N-doped biochar catalysts for electrochemical energy conversion applications will also be discussed.

2.2 Carbonization, functionalization and characterization of biomass-derived carbon materials

2.2.1 Carbonization

Biomass-derived carbon is a black, solid, carbon-rich material derived through the thermochemical conversion of biomass at elevated temperatures under oxygen-limited conditions.⁵¹ Depending on the type of biomass (forestry, agricultural residues, industrial and food residues, municipal waste), composition of the biomass (percentage of cellulose, hemicellulose, and lignin), conversion techniques (pyrolysis, gasification, hydrothermal), and reaction conditions (temperature, heating rate, residence time, gas atmosphere, pressure), the biomass-derived carbon material exhibits different properties. Recently, the influences of feedstocks have been reviewed by Qin et al.⁵³ and Li et al.⁵⁴, who have discussed lignocellulosic biomass and non-lignocellulosic biomass for biochar production, respectively. In this section, several different carbonization techniques for biochar preparation along with their characteristics are introduced. Table 2.1 shows the operating conditions and product yields of different commonly used techniques.

Table 2.1 Different biomass carbonization techniques, operation conditions and biochar yields.

Technique	Temperature (°C)	Residence time	Heating rate (°C/s)	Biochar yield (%)	Ref.
Slow pyrolysis	300-700	mins-days	0.02-1	20-40	⁵²
Fast pyrolysis	500-1000	<2 s	>2	10-20	⁵³
Gasification	800-1000	5-20 s	-	~ 10	⁵⁴
Hydrothermal conversion	180-260	1 -12 h	-	40-70	⁵⁵

2.2.1.1 Pyrolysis

Pyrolysis is one of the most investigated techniques for biochar production and is usually operated at a temperature range from 300 to 700 °C in an inert atmosphere.⁵⁶ It converts biomass into solid (biochar), gas (syngas, including H₂, H₂O, CH₄ and CO), and liquid (bio-oil) products by cross-linking, depolymerization, fragmentation and other secondary gas-solid interaction reactions.⁵⁷ Depending on the heating rate and residence time, pyrolysis can be divided into slow pyrolysis and fast pyrolysis. Slow pyrolysis is characterized by pyrolyzing with a low heating rate (0.02 - 1 °C/s) and long residence time (from minutes to days).⁵³ In addition, the low heating rate of slow pyrolysis favors biochar formation with larger particle sizes.⁵⁸ The biochar yield depends on the synergistic effect of the composition of feedstock, temperature, and residence time. Fast pyrolysis uses a high heating rate (generally > 2 °C/s) and short residence time (< 10 s) that benefits bio-oil production (up to 75%).^{54,59} The ratios of gas, solid and liquid products are also co-dependent on the temperature, residence time and the particle size and chemical compositions of the feedstock. In general, fast pyrolysis requires properly dried feedstocks with a particle size less than 2 mm⁶⁰, whereas slow pyrolysis can withstand larger particle sizes of the feedstock.⁶¹ Slow pyrolysis reaches higher yields of biochar at relatively milder reaction conditions than fast pyrolysis, although the reaction times are longer. Various reactors have been developed and used for biochar production. For instance, agitated drum sand rotating kilns, wagon reactors and paddle pyrolysis kilns are commonly used for slow pyrolysis,⁶² while circulating fluidized bed, rotating cone, and auger reactors are commonly used for fast pyrolysis.⁶³

2.2.1.2 Gasification

Gasification is a thermochemical process to convert carbonaceous feedstocks into small molecular gaseous mixtures (H_2 , CO , CO_2 , CH_4 and small quantities of higher hydrocarbons) by controlling the amount of oxidizing agent under high temperatures.⁶⁴ Typical oxidizing agents for biomass gasification are oxygen, air, carbon dioxide, steam or mixtures of these gases.⁶⁵ The gasification process contains four sequential steps, including drying, pyrolysis, partial oxidation, and gasification.⁶⁶ Fixed bed and fluidized bed gasifiers are the most commonly used setups for biomass gasification.⁶⁷ In general, biomass gasification is used for producing bio-syngas by cracking, partial oxidization, water-gas shift and Sabatier reactions. Therefore, the yields of biochar via gasification process are lower than that of the pyrolysis process. It is important to note that the biochar generated from gasification contains a relatively high level of alkali and alkaline earth metals (AAEMs) and polyaromatic hydrocarbons (PAHs), which are generally harmful for applications. The biomass gasification process is mainly affected by the type of feedstock, reaction temperature, gasification agent, particle size, pressure and equivalent ratio. Correspondingly, the yield, structure and chemical composition of biochar will also change in response to the variations of reaction conditions. In comparison to biochar production by pyrolysis, gasification is more economically viable and profitable, as it generates heat and electricity simultaneously. Seeking a balance between the output of biochar and the overall energy efficiency is an opportunity and challenge for biochar production from gasification.⁶⁸

2.2.1.3 Hydrothermal carbonization

Hydrothermal carbonization uses saturated water to convert biomass into a carbon-rich solid product at a mild temperature (180 – 260 °C) over the course of a few hours.⁶⁹ It usually is performed in an autoclave and the collected solid product is also called hydrochar. As the process is carried out with water, the drying of feedstock is not necessary. Moreover, the operating temperature is lower than with pyrolysis and gasification and therefore the hydrothermal carbonization process consumes less energy. Although the chemical composition of feedstock can differ, the reactions occurring during hydrothermal carbonization are similar, and include hydrolysis, dehydration, decarboxylation, polymerization, aromatization and re-condensation.^{70–72} The main parameters that affects the properties of the product obtained from hydrothermal carbonization are reaction temperature, pressure, residence time and the ratio between biomass and water.⁷³ The yield of hydrochar (40 - 70 %) is relatively higher than yield of biochar generated from pyrolysis (20 - 40%). However, the carbon content of hydrochar is lower than that of biochar.⁷⁴ In addition, the surface of hydrochar presents abundant O-containing functional groups, including hydroxyl/phenolic, carbonyl, and carboxylic, which are benefit for its affinity to

water.⁷⁵ Besides, due to the lower carbonization temperature, the specific surface area and porosity of hydrochar are lower than biochar generated from pyrolysis.⁷⁶

2.2.2 Functionalization

Due to the diversity of the feedstocks, carbonization techniques and operating conditions, the physicochemical characteristics of biochar are versatile. In general, the biochar generated directly from carbonization shows a low nitrogen content, poor functionality, and low specific surface area and porosity.⁷⁷ These intrinsic drawbacks hinder the direct application of biochar materials. Therefore, the biochar should be functionalized to better suit different applications, for instance by modifying its specific surface area, pore structure and surface functional groups. Fortunately, biochar materials exhibit good tunability of structure and porosity.⁷⁸ Activation and heteroatom doping are the most commonly used methods for biochar functionalization, and can be conducted before, during or after biochar production. The activation process, including physical activation and chemical activation, can effectively improve the specific surface area and porosity of biochar materials. Heteroatom doping, here represented as N-doping, can effectively increase the abundance of defects on the surface of biochar and redistribute the charge between carbon atoms and heteroatoms, thereby inducing activity for different electrochemical applications.^{79,80} Figure 2.2 depicts the common activation and N-doping methods for upgrading biochar properties.

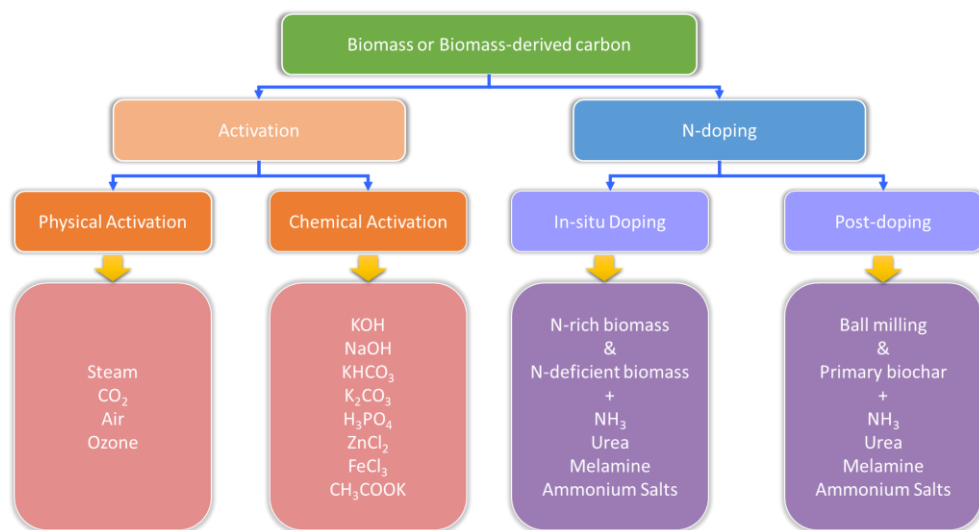


Figure 2.2 Classification of biochar activation and N-doping strategies.

2.2.2.1 Activation

The activation process enlarges the specific surface area and develops porosity in biomass-derived carbon materials. Depending on the activation mechanism, the activation method can be classified as physical activation and chemical activation.⁸¹ The porosity of biochar can be significantly improved by pore formation, expansion, combination and collapse.⁸² Meanwhile, the activated biochar can provide active sites, and an increased adsorption capacity. The activation process can either be carried out together with the carbonization process or after carbonization. The type of activator, mixing method of carbon precursor and activator, temperature, pressure, atmosphere, and activation time jointly determine the characteristics of activated biochar. The characteristics of physical and chemical activation methods are listed in Table 2.2.

Table 2.2 Characteristics of physical and chemical activation methods.

Feedstock	Activating agent	Mass ratio ^a	Temperature (°C)	Time (h)	S_{BET}^b (m ² /g)	V_t^c (cm ³ /g)	V_{mic}^d (cm ³ /g)	D_{avg}^e (nm)	Ref
Almond shell	Steam	-	950	1	1261	-	-	-	83
Coffee residue	Steam	-	700	2	641	0.33	0.23	2.06	84
Canola meal	Steam	-	800	1.5	403	-	-	2.70	85
Tea waste	Steam	-	850	0.5	725	0.51	0.21	2.81	86
Sewage sludge	CO ₂	-	700	1	240	0.39	0.04	6.46	87
Wood chips	CO ₂	-	800	3	590	0.34	0.18	3.44	88
Walnut shell	CO ₂	-	900	1.5	1011	0.65	0.53	2.17	89
Coconut shell	CO ₂	-	900	3.5	2288	1.30	1.01	-	90
Bamboo	CO ₂	-	900	1	684	0.47	0.37	2.19	91
Olive drupe	CO ₂	-	800	7	1355	0.65	0.59	-	92
Corn cob	KOH	4:1	850	1	3227	1.89	1.32	1.17	93

Tremella	KOH	5:1	800	3	3760	2.15	0.60	-	94
Formaldehyde resins	KOH	5:1	900	-	3537	1.96	0.97	-	95
Rice husk	KOH	5:1	850	1	2696	1.50	0.27	2.63	96
Wheat bran	NaOH	4:1	800	2	2543	1.68	0.80	2.65	97
Cellulose	KHCO ₃	4:1	900	1	1893	1.37	0.25	-	98
Coconut shell	K ₂ CO ₃	3:1	600	1	329	0.15	0.12	-	99
Coconut shell	H ₃ PO ₄	1:1	800	2	2648	1.50	0.88	-	100
Orange peel	H ₃ PO ₄	2:1	700	1	2210	1.24	1.19	-	101
Pinewood	H ₃ PO ₄	2:1	600	2	1547	1.17	0.51	-	102
Euphorbia rigida	H ₃ PO ₄	1:1	700	1	790	0.70	0.17	3.54	103
Tomato waste	ZnCl ₂	6:1	600	1	1093	1.57	0.13	5.92	104
Coffee husk	ZnCl ₂	1:1	550	3	1522	0.75	0.15	0.90	105
Textile waste	MgCl ₂	1:1	900	1.5	1307	3.56	0.06	-	106
Cotton woven	FeCl ₃	3:2	700	2	942	0.64	0.33	-	107
Bean curd	CH ₃ COOK	15:1	750	2	2180	1.18	0.83	2.17	108
Soft wood	KMnO ₄	5:4	800	2	1199	0.98	0.39	-	109

a. Mass ratio indicates the ratio between activator and carbon precursor;

b. BET surface area; c. Total pore volume; d. Micropore volume; e. Average pore diameter.

Physical activation of biochar is achieved by applying thermal treatment (> 700 °C) in gaseous activating agent, including steam, carbon dioxide, air or ozone. These gases penetrate into the internal structure of biochar and react with carbon atoms, thereby creating or expanding pores in the carbon framework.¹¹⁰ As a consequence, the specific surface area of activated biochar can be substantially increased. Physical activation is a clean and green production process without secondary waste disposals. However, it also shows

several disadvantages, including high activation temperature, long activation time, poor specific surface area and porosity and relatively low yield of activated biochar.

Steam and CO₂ are the most commonly used activating agent for physical activation of biomass. For example, Koltowski and co-workers activated biochar produced from willow (700 °C, slow pyrolysis) using CO₂ and steam. The specific surface area of the steam-activated biochar (840.6 m²/g) and the CO₂-activated biochar (512.0 m²/g) were higher than the biochar generated by slow pyrolysis (11.4 m²/g).¹¹¹ The larger specific surface area of steam-activated biochar is attributed to the smaller molecular size of water than CO₂, which facilitates the activation process by using steam and further generate more pores than using CO₂.¹¹² In addition, steam activation generates a wide distribution of micropores and mesopores, however, CO₂ activation mainly generates micropores.¹¹³ Moreover, under the same reaction condition, steam activation induces more O-containing functional groups on biochar surfaces than CO₂ activation, which further improves the hydrophilicity of biochar.^{114,115} Toles et al. simulated the steam- or CO₂ activation of almond shell derived biochar for large-scale production (2180 kg biochar per day) and showed that steam activation is more economically feasible than CO₂ activation.¹¹⁶ It is worth noting that the higher activation temperature (using steam or CO₂) is helpful to develop more pores, where longer activation time (> 4 h, depends on the source of biochar) consumes more carbon atoms and leads to the collapse of carbon framework and further decrease the specific surface area.^{117,118}

Besides the above methods that require gaseous agents activation and high temperature, some unconventional physical activation methods, including microwave assisted activation,¹¹⁹ ultrasound irradiation,¹²⁰ plasma treatment,¹²¹ and electrochemical modification methods,¹²² have recently emerged to upgrade the characteristics of biochar. Due to their less widespread use, we will not discuss these techniques in detail.

Chemical activation is one of the most efficient methods for carbon activation and applies activators at a temperature range from 400 - 1000 °C,¹²³ which helps to increase the porosity and specific surface area (up to ~4000 m²/g) of biochar.⁹⁴ Depending on the activation mechanisms, these chemical activators can be classified as alkaline, acidic, neutral, and self-activating agents.⁸² Furthermore, chemical activation can be divided into one-step activation (where carbonization and activation occur simultaneously) and two-step activation (where activation occurs after carbonization) processes. The two-step activation process generates activated biochar with a high specific surface area,¹²⁴ nevertheless, the energy consumption is higher and the manufacturing process is more complex than one-step activation. Chemical activation shows several advantages, such as a low activation temperature and short activation time to generate high specific surface area biochar with

abundant pores. However, the negative effects derived from the strong corrosiveness of the activators and the inevitable washing process need to be taken into account.¹²⁵

The most frequently used alkaline activators include but are not limited to KOH, NaOH, KHCO_3 and K_2CO_3 . Among these activators, KOH is the most effective activator for generating biochar with a high specific surface area. The KOH acts as an oxidant, generating pores by oxidizing carbon atoms on the carbon framework.¹²⁶ In addition, the generated potassium compounds penetrate into the internal structure of the carbon lattice and create pores by etching the carbon layer.¹²⁷ The acidic activators, such as H_3PO_4 , H_2SO_4 and HNO_3 , act as dehydrating agents,¹²⁸ promoting dehydration at lower carbonization temperatures and creating pores by oxidation reactions and aromatic condensations.^{100,129} The main activation mechanisms of the neutral activators (ZnCl_2 , FeCl_3 , MgCl_2 , KMnO_4 , etc.) are dehydration, oxidation, templating and gasification. The metal salts improve the dehydration, dicarboxylic and cross-linking reactions.¹⁰⁷ Further, metal oxides, e.g. MgO in the case of MgCl_2 , embed into the carbon matrix as a template, generating mesoporosity.¹⁰⁶ In general, the porosity of the biochar gets improved with an increased amount of activators, and the pore size distribution becomes wider.¹³⁰ On the other hand, the porosity of activated biochar increases to the maximum value as the activation temperature rises, and then begins to decrease with further increase of activation temperature, which is due to the collapse of pores and shrinkage of the carbon framework.¹³¹ In addition, depending on the type of activator, the activated biochar shows different characteristics. For instance, the carbon yield of biochar activated with alkaline activators is lower than that of biochar activated by acidic activators.¹³² Alkaline activators generate biochar in a powder form, whereas acidic activators generate biochar in a granular form.¹³³ The specific surface area of KOH-activated carbon ranges up to $4000 \text{ m}^2/\text{g}$, however, the maximum specific surface area of H_3PO_4 -activated carbon is around $2700 \text{ m}^2/\text{g}$.^{94,100} Furthermore, the KOH activation process mainly generates micropores, while the H_3PO_4 activation process develops mesopores and macropores and the ZnCl_2 activation process creates mainly micropores and a small percentage of mesopores.¹³⁴

Besides the difference of activators mentioned above, the activation temperature, the mixing method of biomass and activators (mixing in aqueous solution or mixing directly), the ratio of biomass to activator, the reaction atmosphere, etc., all have crucial effects on the physicochemical properties of biochar. Therefore, in practice, the pore structure and chemical composition of biochar can be adjusted in a targeted manner by selecting the appropriate activator and reaction conditions for different applications.

2.2.2.2 Nitrogen doping

Activated biochar typically exhibits a large specific surface area and abundant porous structure and can find applications in soil remediation, wastewater treatment, and supercapacitors. However, pristine carbon materials are inert for electrocatalytic conversion reactions due to the stability of neutral carbon atoms.¹³⁵ Therefore, heteroatom doping is key for imparting electrocatalytic activity to porous carbon materials. Introducing heteroatoms (e.g., B, N, or S) with a different electronegativity into the carbon framework can modulate the electrocatalytic performance of the pristine π -electron networks, redistribute the spin and charge densities and thereby form catalytically active sites.¹³⁶ Here, we focus on N-doping as this is most widely investigated for electrocatalytic applications.

In principle, the incorporated nitrogen can be designated as structural N and chemical N (Figure 2.3). Structural N is directly embedded into the carbon skeleton by replacing a carbon atom, including pyridinic N, pyrrolic N, graphitic N, and oxidized N. Chemical N exists on the surface of biochar in the form of N-containing functional groups, such as amine ($-NH_2$) and nitro ($-NO_2$) groups. Surface chemical N-containing functional groups are covalently bonded to the carbon frame. Structural N atoms are formed via dehydration, condensation and aromatization reactions. This is the reason that the structural N displays higher stability than chemical N, and the electronic properties of structural N shows the capability for catalyzing electrochemical reactions. In particular, the pyridinic N binds with two adjacent carbon atoms at the edge and donates one p-electron to the carbon conjugated framework. The pyrrolic N is hybridized with two carbons in a pentagonal ring and contributes two p-electrons to the framework. Graphitic N is sp^2 hybridized with three carbon atoms and the oxidized N is incorporated with two carbon atoms and one oxygen atom.^{137,138} Among these, graphitic N and oxidized N are the most stable, followed by pyridinic N and pyrrolic N.¹³⁹

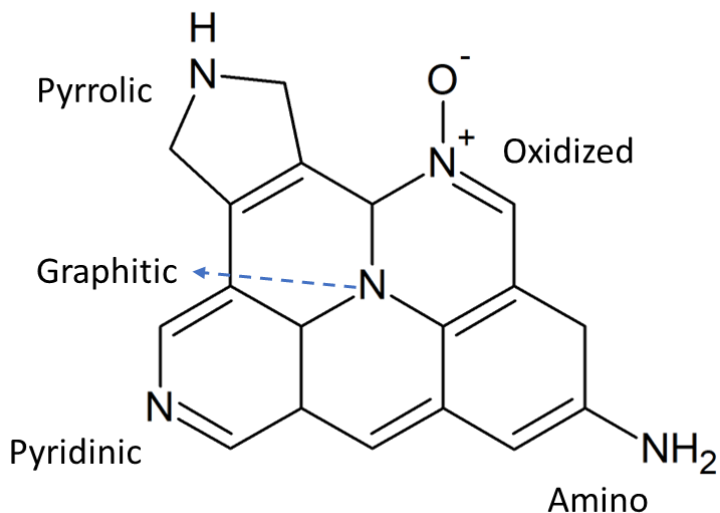


Figure 2.3 N-containing functional group in N-doped biochar.

According to the chemical composition of feedstocks, biomass can be categorized into N-rich biomass and N-deficient biomass. N-rich biomass, including algae, bean dregs, animal waste, and sewage sludge, can be directly used to prepare N-doped biochar by carbonization and activation. However, N-deficient biomass, such as wood, bamboo, straw and bagasse, needs external N dopants to prepare N-doped biochar. The doping method can be categorized into in-situ doping (N-rich biomass or dopants mix with N-deficient biomass) and post-doping (dopants mix with biochar). In addition, compared to the N-doped biochar produced from N-rich feedstock, the N content and configuration of the biochar generated with external nitrogen sources can be controlled by modulating the amount of additive and the operation conditions. Table 2.3 outline different methods for N-doping and characteristics of N-doped biochar.

Table 2.3 Different N-doping methods and characteristics of N-doped biochar.

Feedstock	N dopant	Activator	Method	Temperature (°C)	N content	Specific surface area (m ² /g)	Ref
Bean dreg	-	Steam	Pyrolysis	1000	2.42 wt%	1004	140
Camellia sinensis	-	KOH	Hydrothermal	280	6.18 wt%	6.5	141
Water hyacinth	-	ZnCl ₂	Molten salt	800	5.47 at%	829	142
Chitosan	-	-	Pyrolysis	800	7.9 at%	1052	143
Human hair	-	-	Pyrolysis	700	9.61 wt%	23.8	144
Fish scale	-	NaOH	Pyrolysis	800	19.5 at%	1867	145
Crab shell	-	KOH	Pyrolysis	700	5.1 wt%	1663	146
Bamboo waste	NH ₃	-	Pyrolysis	600	3.42 wt%	254.5	147
Corn straw	NH ₃	-	Pyrolysis	800	5.69 at%	418.7	148
Sugarcane bagasse	Urea	-	Pyrolysis	650	4.65 wt%	53.5	149
Sewage sludge	Melamine	-	Pyrolysis	800	9.5 at%	261.7	150
Cellulose	Ammonium oxalate	KHCO ₃	Pyrolysis	900	2.03 at%	2816	151
Coconut shell	Urea	KOH	Pyrolysis	700	0.61 wt%	1937	152

Industrial lignin	Urea	H ₃ PO ₄	Pyrolysis	500	1.52 wt%	1411	¹⁵³
Cotton stalk	NH ₃	CO ₂	Pyrolysis	800	1.52 wt%	627	¹⁵⁴
Arundo donax	Urea	ZnCl ₂	Pyrolysis	600	15.9 at%	582	¹⁵⁵
Cellulose	Melamine	KOH	Pyrolysis	800	1.68 at%	1703	¹⁵⁶

The selection of feedstock is important for preparing N-doped biochar from N-rich feedstocks. In general, the N content in the biochar is positively correlated with the original N content in the feedstock. Some feedstocks contain a high N content that can be used as precursors for the preparation of N-doped biochar by carbonization. For instance, Chu et al. prepared N-doped biochar derived from bean dregs with a N content as high as 6.3 wt%.¹⁴⁰ Liang et al. chose water hyacinth to prepare N-doped carbon without external nitrogen source and achieve a maximum N content of 7.71 at% with a large specific area (845 m²/g).¹⁴² Chang et al. used microalgal residue to prepare a series of N-doped biochar by slow pyrolysis with a N content distribution between 10.2 – 14.1 wt%.¹⁵⁷ Although N-rich feedstocks help to achieve high N-doping contents, the mechanisms of nitrogen transformation and evolution are complex. Chen et al. revealed the reaction pathways of nitrogen containing species during pyrolysis of algae (Figure 2.4), where protein-N species are the main sources for N-doping.¹⁵⁸

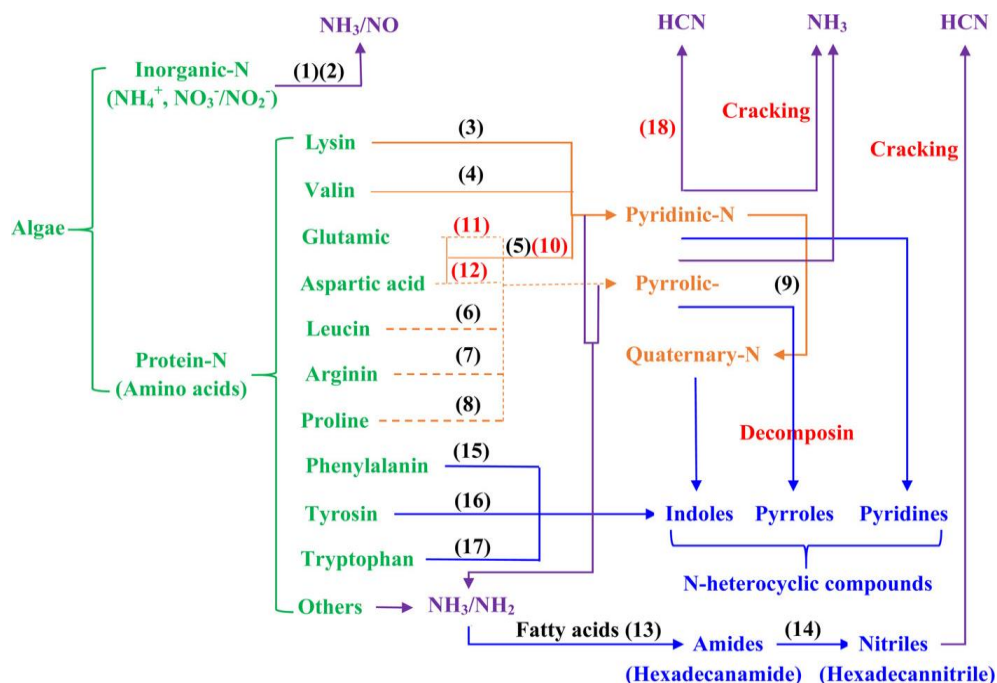


Figure 2.4 Mechanisms of nitrogen transformation and possible reaction pathways during algae pyrolysis. Black: possible reaction pathways at lower temperatures; red: possible reaction pathways at higher temperatures. Reproduced from ref. 158 with permission from the American Chemical Society.

N-containing chemicals are commonly added to N-deficient feedstocks to produce N-doped biochar. The most used N-dopants are ammonia, urea, melamine and ammonium salts. Ammonia is usually used as a gas dopant and inert atmosphere for pyrolysis, while ammonium salts or organics can be mixed directly with the feedstock or dissolved and mixed with the feedstock before carbonization and activation. N-doping with ammonia gas purging is an efficient way to incorporate nitrogen into the carbon matrix. The O-containing functional groups on biomass react with ammonia during the carbonization process and induce N-containing groups (amine, amide, etc.) on the biochar that are subsequently converted to structural N and embed into the carbon skeleton.^{154,159} Therefore, the abundance of O-containing functional groups in the feedstock is positively correlated with the N-doping level of the end-product.¹⁶⁰ Solid organic nitrogen additives, such as urea and melamine, and inorganic ammonium salts are generally easier to use and more efficient for N-doped biochar production than purging NH_3 as N-dopant. Oh et al. prepared N-doped biochar by pyrolyzing coffee residue and urea at various temperatures and residence times.

The N content increased from 2.1 wt% to higher levels (2.8 - 19.3 wt%) depending on the temperature. Moreover, the percentage of pyrrolic N and pyridinic N decreases with increasing temperatures, whereas the percentage of graphitic N show an opposite trend.¹⁶¹ The released NH_3 from the decomposition of urea is helpful to enlarge the specific surface area and porosity of N-doped biochar.¹⁶² Similarly, ammonium salts also release gaseous decomposition products (for instance NH_3 and N_2) during thermal decomposition, which expand the porous structure of N-doped biochar along with N-doping.¹⁶³

Post-doping is a two-step strategy, where the feedstocks are first converted to primary biochar and the N-dopant is directly reacted with primary biochar instead of the raw feedstock. Besides heat treatment of primary biochar with ammonia or nitrogen containing chemicals, ball milling of biochar with nitrogen containing chemicals can also be used for N-doping. It is reported that the treatment of biochar with N-dopants at lower temperatures leads to chemical N on biochar surfaces, while structural N atoms are incorporated into biochar at higher temperatures.¹⁶⁴ The doping mechanisms for biochar and ammonia, organic nitrogen additives and inorganic salts, are similar to the mechanisms for reactions of biomass with these different dopants. It is worthy to note that the oxygen content of biochar is lower than that of raw biomass, indicating that the efficiency of doping on biochar is lower than doping on biomass. Therefore, introducing oxygen functional group on biochar is helpful for the N-doping. Guo et al. used H_2O_2 to pre-oxidize coconut shell derived biochar before N-doping, and the N content of H_2O_2 pre-oxidized biochar increased from 14.4 wt% to 15.5 wt%, higher than the sample without H_2O_2 pre-oxidization.¹⁶⁵ Ball milling is another efficient way to produce N-doped biochar by mechanochemical effect to break chemical bonds to incorporate N with carbon atoms. For instance, Xu et al. mixed ammonium hydroxide and bagasse derived biochar using ball milling, with the nitrogen content increasing from 0.3 to 1.79 wt%.¹⁶⁶

One-step synthesis of activated N-doped biochar by calcinating the feedstock, N dopants, and activators simultaneously, is more attractive with respect to energy consumption. It is important to note that one-step doping methods are often influenced by various factors, including the type of biomass, the reaction temperature and residence time, the type and amount of N dopants and the type and amount of activators. For instance, a higher reaction temperature leads to a lower N-doping content, while the percentage of graphitic N increases.¹⁶⁷ The N content of N-doped biochar decreases with increasing reaction residence times at a high temperature ($> 500\text{ }^\circ\text{C}$), while an opposite trend is observed at a relatively low temperature ($< 500\text{ }^\circ\text{C}$).¹⁶⁸ Furthermore, the application of strong activators (e.g. KOH) and higher amount of activators could hinder the N-doping, which is attributed to the strong corrosive and oxidizing properties of these activators. However, the correlation between N-doping features and characteristics of activators is currently lacking systematic investigation.

2.2.3 Characterization

Due to the diversity of raw feedstocks, synthesis methods, process conditions, and other factors, the physicochemical properties of N-doped biochar have changed accordingly. Proper characterization helps to understand the relationship between raw material properties, carbonization conditions and the physicochemical properties of the obtained N-doped biochar, and can also reveal the correlation between the physicochemical properties and electrochemical performances of N-doped biochar.

The most commonly used characterizations methods include scanning electron microscopy (SEM), transmission electron microscopy (TEM), energy-dispersive X-ray spectroscopy (EDX or EDS), N₂ adsorption-desorption, X-Ray diffraction (XRD), Raman spectroscopy, Fourier transform infrared spectroscopy (FTIR), X-Ray photoelectron spectrometry (XPS), thermo gravimetric analysis (TGA), differential scanning calorimetry (DSC) and inductively coupled plasma optical emission spectroscopy (ICP-OES). Figure 2.5 shows the classification of different characterization techniques for biochar analysis, as summarized by Zeghioud et al.¹⁶⁹

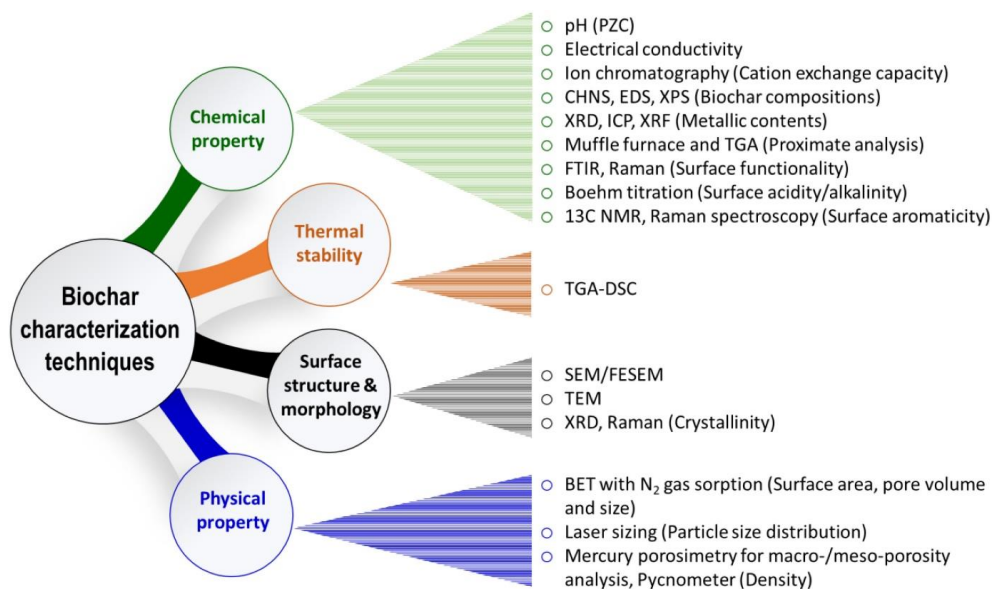


Figure 2.5 Classification of characterization techniques versus biochar properties reported in biochar literature. Reproduced from ref. 169 with permission from Elsevier.

SEM and TEM are widely used to visualize the morphology and microstructure of N-doped biochar. Besides, high-resolution TEM is a powerful tool to show the number of graphene layers and the distance of each layer of the highly graphitic structure in the N-doped biochar. The combination of SEM and EDX is often applied to identify the various components present on the surface of biochar. The specific surface area, pore volume, pore size distribution of carbon samples can be evaluated by the N_2 adsorption-desorption analysis. XRD is applied to determine the crystal structures and phase composition of biochar. For N-doped biochar, XRD can also be used to detect impurity crystals in the biochar, such as silica or metal oxides. Raman spectroscopy can delineate the abundance of defects and graphitic structure of biochar. For instance, the intensity ratio between the D band and G band (I_D/I_G) is an estimate for the abundance of defects and disordered carbon structures. Functional groups on N-doped biochar can be identified by FTIR, while XPS is helpful to identify the elemental composition and chemical configuration on the N-doped biochar surface. The deconvolution of high-resolution N 1s XPS spectrum helps to calculate the percentage of pyridinic N, pyrrolic N, graphitic N and oxidized N. TGA and DSC characterizations are used to evaluate the properties of N-doped biochar as a function of temperature. The trace amount of metal impurities in the N-doped biochar can be measured by ICP-OES.

2.3 Biomass-derived carbon as electrocatalysts

2.3.1 Hydrogen evolution reaction (HER)

Water electrolysis is a sustainable approach to generate green hydrogen. The hydrogen evolution reaction that generates this green hydrogen occurs at the cathode electrode. Platinum (Pt) is known as the most effective electrocatalyst for the acidic HER owing to its optimum bonding energy for hydrogen adsorption. However, the high cost and scarcity of Pt can potentially hinder the large-scale application of green hydrogen production via electrolysis. Therefore, reducing the loading of Pt or seeking alternative low cost and earth abundant HER catalysts with a good performance, and long stability is desired.

Metal-free N-doped carbon materials have been studied as alternative HER catalysts, as these materials are stable in both acidic and alkaline solutions.¹⁷⁰ Several activated N-doped biochars derived from N-rich biomass sources without additional N-doping, such as pine needle,¹⁷¹ peanut shell,¹⁷² palm waste,¹⁷³ and waste silk fabrics,¹⁷⁴ have been tested for the HER. For instance, Saravanan et al. synthesized a peanut shell-derived N-doped biochar by a two-step strategy, where the feedstock was carbonized at 400 °C for 4h under N_2 atmosphere and the obtained biochar was further mixed with KOH at 1: 3 weight ratio and activated at 700 °C for 2h. The as-prepared N-doped biochar displayed a 6.7 wt% N-doping

with a large specific surface area of 2338 m²/g and an I₀/I_G ratio of 0.99. HER tests in 0.5 M H₂SO₄ showed that this catalyst exhibited an overpotential of 390 mV at 10 mA/cm², with a Tafel slope of 75.7 mV/dec.¹⁷² Zhang et al. synthesized a N-doped carbon derived from waste silk fabrics (Figure 2.6a). After activation with KCl, the resulting product showed a 3D interwoven porous structure, with a specific surface area of 49 m²/g and a N-doping content of 5.2 at.%. Their best catalyst (KCl-900) exhibited an overpotential of 336 mV at a current density of 10 mA/cm² in a 0.5 M H₂SO₄ electrolyte, with a Tafel slope of 311 mV/dec. (Figure 2.6b and c).¹⁷⁴

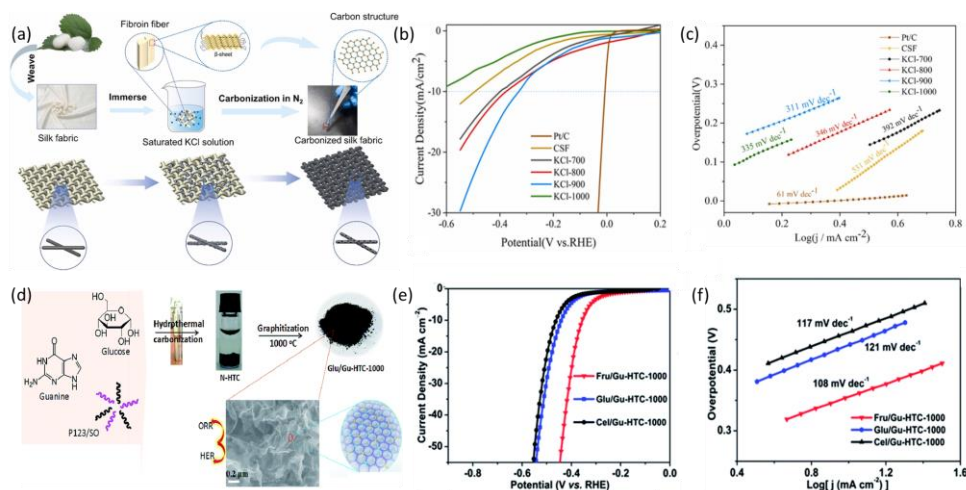


Figure 2.6 (a) The preparation process of waste silk fabric derived N-doped biochar; (b) Polarization curves for HER of KCl-T, CSF, and Pt/C catalysts in 0.5 M H₂SO₄; (c) Tafel slopes of KCl-T, CSF, and Pt/C catalysts. Adapted from ref.174 with permission from Elsevier. (d) The synthetic route of nitrogen-doped 2D carbon nanosheets; (e) LSV curves for the HER with 10 mV/s at 1600 rpm; (f) Tafel plots from the corresponding LSV curves. Adapted from ref.176 with permission from Royal Society of Chemistry.

In addition, N-doped biochar derived from N-deficient biomass with additional N-doping has been tested for the HER. Zhang et al. reported a N-doped cotton cloth, using polyacrylonitrile (PAN) as an N-dopant, pyrolyzed at 800 °C for 2h under N₂ atmosphere, as an electrocatalyst for HER in 1 M NaOH. It required a overpotential of 233 mV to achieve a current density of 10 mA/cm² with a Tafel slope of 135 mV/dec.¹⁷⁵ Huang et al. synthesized a N-doped carbon through a hydrothermal carbonization method combined with pyrolysis, using carbohydrates (glucose, fructose and cellulose) as carbon source and guanine as nitrogen source (Figure 2.6d). The fructose-derived N-doped biochar displayed a defect rich structure (I₀/I_G = 1.15) with a N-doping content of 1.53 at% and a specific surface area of

974 m²/g. HER test in 1 M KOH showed the overpotential at 10 mA/cm² is 350 mV and the Tafel slope is 108 mV/dec (Figure 2.6e and f).¹⁷⁶

In general, the content of pyridinic N and pyrrolic N in N-doped biochar is positively correlated with the HER performance of N-doped biochar.^{173,174} This correlation is explained due to the promoting effect that pyridinic N and pyrrolic N have on the adsorption of H atoms.¹⁷⁷ The carbon atoms adjacent to the N heteroatoms are demonstrated as the active sites for all-pH HER, which optimizes Gibbs free energy for hydrogen adsorption near zero via combined intermolecular electron transfer.^{178,179} However, a recent study by Lu and co-workers revealed that the N atoms are removed by hydrogenation during the HER. Subsequently, the carbon skeleton was reconstructed from hexagonal to 5,7-topological rings, and the 5,7-topological rings were identified as HER active sites.¹⁸⁰ In addition, Oates et al. demonstrated a power-law relationship between HER activity and amounts of metal impurities in carbon materials by statistical modeling, indicating that the trace amounts of metal impurities (within 100 ppm) are the predominantly responsible for HER activity.¹⁸¹

Although many studies are optimistic that N-doped biochar can be used as potential HER electrocatalysts, the performance of N-doped biochar for HER are far inferior to commercial Pt/C due to their high overpotentials. Several strategies could further improve the HER performance of N-doped biochar, such as N, S co-doping, N,P co-doping, and N, P, Ca co-doping.¹⁸² In addition, making use of the stability and abundant pore structure of carbon materials, using N-doped biochar as a catalyst support to load tungsten carbide, cobalt oxide/sulfide/phosphide, molybdenum carbide/sulfide/oxide or alloys of transition metals, could also provide a good strategy to use materials for the HER.¹⁸³

2.3.2 Oxygen reduction reaction (ORR)

The oxygen reduction reaction is an important reaction for several electrochemical energy conversion processes, including fuel cells and metal-air batteries. The sluggish kinetics of the ORR create a need for a robust and active catalyst to overcome high overpotentials. Platinum has been regarded as the best ORR catalyst.¹⁸⁴ Nevertheless, its high cost and weak tolerance to CO and methanol are still facing challenges for future applications. Gong et al. were the first to report an N-doped carbon nanotube catalyst for the ORR, which exhibited a better electrocatalytic activity, longer stability and higher tolerance to CO poisoning than the benchmark Pt/C catalyst.²² Since then, using N-doped carbon materials as catalysts for ORR has become a hot topic. Thereby, cheap and sustainable biomass-derived N-doped carbon materials have also been extensively studied.¹⁸⁵ For instance, Chen et al. prepared an N-doped carbon from Typha by combining hydrothermal carbonization and pyrolysis under NH₃ atmosphere. The as-prepared catalyst

exhibited a similar onset potential and half-wave potential as a 20 wt% Pt/C commercial catalyst in a 0.1 M KOH solution, and showed better durability than the Pt/C catalyst (Figure 2.7a, b, c).¹⁸⁶ Liu et al. reported water hyacinth derived N-doped biochar, which showed an onset potential of 0.98 V vs. RHE. This catalyst also exhibited satisfactory tolerance against methanol and a higher stability than a Pt/C catalyst (Figure 2.7d, e, f).¹⁸⁷

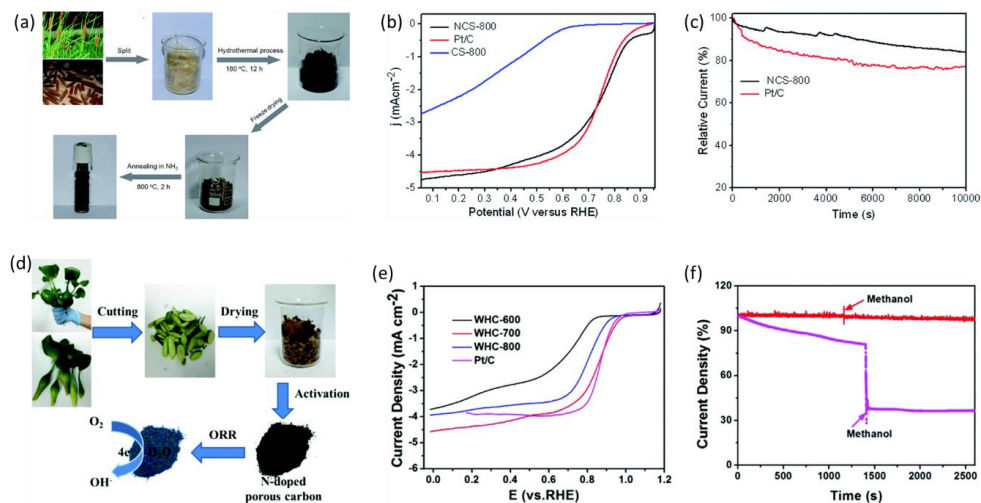


Figure 2.7 (a) Preparation of the nitrogen-doped nanoporous carbon nanosheets from Typha; (b) RDE voltammograms in O_2 -saturated 0.1 M KOH solution at room temperature (rotation speed 1600 rpm, sweep rate 20 mV/s) for NCS-800, CS-800 and Pt/C; (c) Current–time ($i-t$) chronoamperometric response of NCS-800 and Pt/C electrodes at 0.10 V (vs. RHE) in O_2 -saturated 0.1 M KOH solution at a rotation rate of 800 rpm. Adapted from ref.186 with permission from Royal Society of Chemistry. (d) Schematic of the synthesis of N self-doped porous carbon from water hyacinth; (e) Linear sweep voltammograms of WHC-600, WHC-700, WHC-800, and Pt/C RDE electrodes at 1600 rpm and 10 mV/s; (f) Current–time ($i-t$) responses for ORR at +0.4 V vs. RHE in an O_2 -saturated 0.1 M KOH solution at WHC-700 and Pt/C modified electrode with the addition of 3 M methanol at 1200 s and 1400 s, which is marked with an arrow. Adapted from ref.187 with permission from Royal Society of Chemistry.

Specific surface area and porosity are two important factors for ORR performance of N-doped biochar catalysts. In general, a larger specific surface area exposes more active sites and leads to better ORR performance. However, a high specific surface area itself does not ensure high ORR activity, instead, optimizing the porous structure and improving the accessibility of active sites is crucial for ORR performance. In particular, mesopores and

macropores serve as channels to accelerate mass transport of reactants and ions to active sites.¹⁸⁸ For instance, Li et al. synthesized an N-doped biochar by a two-step pyrolysis method. The resulting catalyst showed a large specific surface area of 1599 m²/g with abundant mesopores favoring the transport of reactants to active sites, and exhibited an onset potential of 0.995 V vs. RHE and a half-wave potential of 0.825 V vs. RHE in 0.1 M KOH.¹⁸⁹ In addition, Gabe et al. showed the positive correlation between ORR performances and microporosity by a mathematical model.¹⁹⁰ The trade-off between microporosity and mesoporosity of N-doped carbon materials for ORR performance is unclear. Therefore, seeking the optimal distribution of pores of hierarchical N-doped biochar is one of the key stone to achieve better ORR performances.

Although experimental results demonstrate that N-doping confers the activity of N-doped biochar for the ORR, this does not imply that a higher N-doping level leads to a better ORR performance. Instead, the type and characteristics of N species present are more important for the ORR. Density functional theory (DFT) modelling has been widely used to reveal the nature of the active sites and reaction mechanism for the ORR on N-doped carbon. Nonetheless, there is no consensus on the active sites for ORR in N-doped carbon materials. For instance, graphitic N, pyridinic N, and pyrrolic N have all been claimed as the active site for ORR.^{189,191–194} Guo et al. reported that the ORR activity is derived from pyridinic N by comparing the results from well-controlled model catalysts. In particular, the active sites are carbon atoms with Lewis basicity next to pyridinic N.¹⁹⁵ Lai et al. found that the ORR activity was dependent on the graphitic N content, while the pyridinic N content improved the onset potential for ORR.¹⁹⁶ Liu et al. categorized the ORR activity of different N-containing sites from experimental and theoretical points of view: pyridinic N > pyrrolic N > graphitic N > oxidized N.¹⁹⁷ On the contrary, Luo et al. pointed out that the pyridinic N is not favored for the ORR, due to the repulsive interaction between lone pair electrons of pyridinic N and O₂.¹⁹⁸ In addition, topological defects in carbon (carbon pentagon) and plasma generated defects in carbon (without N-doping) are also reported as highly active sites for ORR.^{199–201} This leads to question whether an impressive ORR performance of a N-doped carbon catalyst can simply be linked to the amount of one or two specific N-containing species. Overall, a more comprehensive analysis which considers the synergistic effect of different physicochemical characteristics of N-doped carbon materials for the ORR would be beneficial to properly understand the correlation between “synthesis-structure - performance”.

Aside from N, co-doping or multi-doping of additional heteroatoms, including boron (B), sulfur (S), phosphor (P), etc., into biochar could further improve the ORR performance. Improvements of the ORR performance is always attributed to the synergistic effect of different heteroatoms on the carbon materials, but the exact reaction mechanisms are unclear. Blind doping may improve the ORR performance but not helpful for the

development of carbon-based catalysts. Furthermore, introducing low amounts of transition metals (Co, Fe, etc.) into N-doped biochar is also an efficient strategy to improve the ORR performance. The transition metal coordinate with N and form a metal-nitrogen-carbon (M-N-C) structure, which has been demonstrated as a highly active site for ORR. Moreover, N-doped biochar can also be used as a carbon support to load noble metal or transition metal-based catalysts, and exhibits good ORR performance due to its abundant porous structure. Although considerable progress has been made in N-doped biochar-based ORR catalysts, more investigations are still needed for the identification of active sites, the revelation of reaction mechanisms, and the scale-up of catalyst preparation and ORR operation.

2.3.3 Carbon dioxide reduction reaction (CO₂RR)

The electrochemical CO₂ reduction reaction is a promising method to mitigate CO₂-related environmental problems. Electrochemical CO₂ reduction converts waste CO₂ into chemicals and fuels, thereby producing base chemicals and storing intermittent energy into chemical bonds. Depending on the employed catalysts and reaction conditions, CO₂ can be reduced to CO, CH₄, C₂H₄, formate and oxygenated hydrocarbons. However, due to the thermodynamic stability of CO₂, sluggish kinetics of the CO₂ reduction reaction, and competition with the HER, efficient, cost-effective, and stable electrocatalysts are highly desired to overcome the high overpotentials and improve the product selectivity. N-doped carbon materials are emerging catalysts for the CO₂RR and have attracted more attention in recent years. In 2013, Kumar et al. first reported an N-doped carbon nanofiber for the CO₂RR, which exhibited around 13 times higher current density than a bulk Ag electrode for the conversion of CO₂ to CO.²⁰² Since then, the interest of using N-doped carbon catalysts for CO₂RR has increased substantially. In most cases, N-doped carbon materials are considered efficient catalysts to convert CO₂ to CO or formate, and only rarely have N-doped carbon catalysts been reported to convert CO₂ to ethanol,²⁰³ multicarbon hydrocarbons and oxygenates.²⁰⁴

Biomass-derived carbon materials are demonstrated as viable catalysts for CO₂RR. Additional N-doping and activation are commonly used to improve the CO₂RR performances of N-doped biochar catalysts. Li et al. reported a porous carbon with a high specific surface area (1269 m²/g) via a one-step carbonization of wheat flour and KOH, showing a maximum 84% faradaic efficiency and a 6.6 mA/cm² partial current density toward CO at -0.82 V vs. RHE.²⁰⁵ Yao et al. obtained an N-doped carbon sheet from Typha via combining hydrothermal carbonization and pyrolysis in an NH₃ atmosphere. The best catalyst showed 90% faradaic efficiency toward CO at a low overpotential of -0.31 V vs. RHE.²⁰⁶ Zhang et al. developed a wood-derived N-doped carbon membrane using urea as the N-dopant. The

catalyst showed a larger specific surface area, hierarchical porous structure, and abundant pyridinic N species in the carbon framework, which exhibited a maximum CO faradaic efficiency of 78% at -0.68 V vs. RHE.²⁰⁷ Hao et al. synthesized a wood-derived N-doped carbon using melamine as N dopant and FeCl_3 as activator. The catalyst displayed a three-dimensional structure with an N-doping of 5.38 at.% and a specific surface area of 1673.6 m^2/g , which exhibited a 91% faradaic efficiency of CO at -0.56 V vs. RHE and a long-term stability for at least 20 hours (Figure 2.8).²⁰⁸

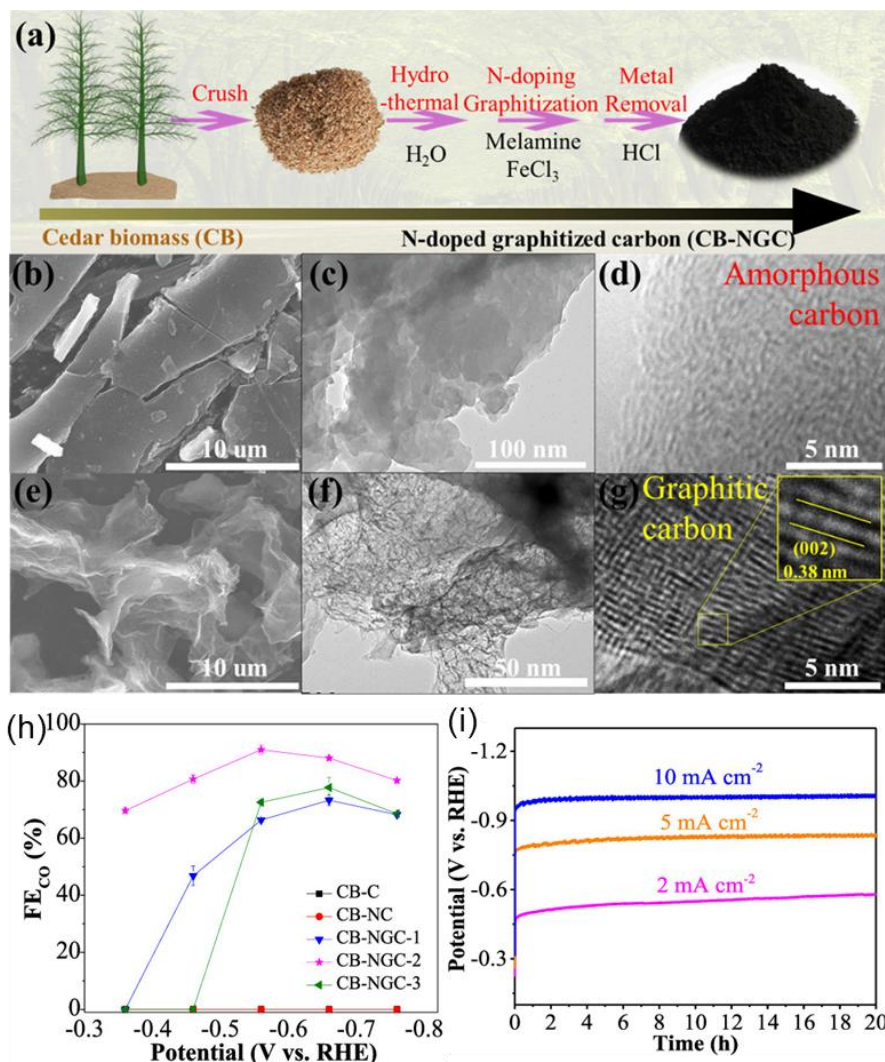


Figure 2.8 (a) Illustration of the CB-NGC preparation procedure; (b) SEM images of CB-C; (c,d) TEM and HRTEM images of CB-C; (e) SEM images of CB-NGC-2; (f,g) TEM and HRTEM images of CB-NGC-2; (h) Faradaic efficiency of CO; (i) Stability tests for the CB-NGC-2

electrocatalyst at different current densities. Adapted from ref.208 with permission from American Chemical Society.

The type and content of N-doping significantly influence the adsorption and activation of CO₂, and product selectivity. In general, N-doping is considered essential to obtain CO₂RR activity, but the debate about the exact active sites is still ongoing. Pyridinic N, graphitic N, and pyrrolic N are all demonstrated as the active sites for the CO₂RR on N-doped carbon catalysts. Many studies have claimed that the pyridinic N sites are the most active sites for the CO₂RR, owing to the lone pairs of electrons that improve CO₂ binding.^{209–211} Contradictorily, Zhang et al. demonstrated that graphitic N species enable the CO₂RR on adjacent carbon atoms, while pyridinic N favors HER at edge carbon sites.²¹² However, Cui et al. and Liu et al. reported the pyrrolic N species are also highly active for the CO₂RR.^{213,214} Vasileff et al. pointed out that the overall CO₂RR activity is synergistically influenced by the combination of CO₂ binding and electron transfer, which produced by graphitic N and pyridinic N, respectively.²¹⁵ On the contrary, some studies suggested that intrinsic defects in N-doped carbon materials are the active sites for the CO₂RR. This is supported by findings that the CO₂RR performance is improved after removing most of the N-containing species.²¹⁶ The discussion above illustrates the complexity of revealing the exact mechanism of the CO₂RR on N-doped carbon materials and indicates that the CO₂RR performance of N-doped carbon materials is not solely dependent on the type and amount of N-doping, other properties such as specific surface area, porosity, and degree of graphitization are also important for the CO₂RR performance.

The porosity of carbon materials is important for the adsorption/desorption and mass transfer of reactants, intermediates, and products. Therefore, optimizing the specific surface area, pore size and volume, and the composition of micro-meso-macro pores is crucial to improve the CO₂RR performance of N-doped carbon catalysts. Gadipelli et al. observed that the CO₂ adsorption capability of porous carbon reaches a maximum value for a specific surface area of approximately 2000 m²/g, while further increases in the specific surface area do not improve the CO₂ capacity proportionally.²¹⁷ Zhang et al. predicted the CO₂ adsorption behavior of porous carbon by a deep learning algorithm. The results demonstrate that the CO₂ adsorption at ambient pressure is governed by the micropores whereas mesopores play an important role in high pressure CO₂ adsorption.²¹⁸ In addition, Hursán et al. showed that solely modulating the pore size of N-doped carbon significantly influences the faradaic efficiencies, current densities and stability.²¹⁹ Furthermore, an interconnected hierarchical porous structure of biomass derived carbon catalyst shows unique advantages. While micropores provide abundant active sites, mesopores and macropores facilitate the mass

transport. As a result, the hierarchical structure improves the accessibility of reactants to active sites and further enhances the CO₂RR activity of N-doped carbon materials.

The degree of graphitization is directly related to the electrical conductivity and hydrophobicity of the N-doped carbon materials, which in turn strongly affects the CO₂RR performance of N-doped carbon. The electrical conductivity of porous graphitic carbon is more than 3 times higher than that of amorphous activated carbon, which facilitates electron transfer and exhibits good performances for various electrochemical applications.²²⁰ On the other hand, improving the hydrophobicity of carbon is helpful to suppress the HER and further improve the CO₂RR performance.

It is worth noting that there is a delicate trade-off between the amount of N-doping, the pore structure and the degree of graphitization for N-doped biochar catalysts used for the CO₂RR.²²¹ For instance, a higher carbonization temperature improves the degree of graphitization and hydrophobicity but decreases the N-doping content. Using an efficient activator could improve the porosity of N-doped carbon but decreases the N-doping content. Adding N-dopants increases the N-doping content but decreases the degree of graphitization. Optimizing the chemical composition and structural properties of N-doped biochar helps to exhibit better CO₂RR performance. However, the relationship between structural properties and electrochemical performance of N-doped biochar for CO₂RR is unclear yet.

In addition, a co-doping strategy could further improve the CO₂RR performance of biomass-derived carbon materials, including N, S doping, N, P doping, B, N doping, and transition metal, N doping, etc. In particular, M-N-C metals are currently one of the most promising catalysts to reduce CO₂ to CO at low overpotentials with high partial current densities.²²² Furthermore, optimization of electrodes (gas diffusion electrode, etc.), electrolyzer (flow cell, zero-gap, etc.), and reaction conditions (potential, pH, temperature, concentration, etc.) can also effectively improve the performance of CO₂RR with N-doped carbon materials. Although some progresses have been achieved of using N-doped biochar catalysts for CO₂RR, the investigation is still in its infancy. Consequently, a more comprehensive understanding of electrocatalytic processes to reveal the correlation between synthesis, properties and electrochemical performances is of great importance to developing, designing and manufacturing N-doped carbon catalysts with excellent CO₂RR performance.

2.3.4 Similarities and differences

N-doped biochar is versatile and shows a great application potential in electrochemical energy storage and conversion. In general, the catalytic activity is induced by N-doping. The

electrical features of heteroatoms, defects and topological carbon rings modulate the charge distribution of the carbon skeleton, further improve the adsorption and activation of reactants. From the viewpoint of kinetics, a large specific surface area exposes more active sites and hierarchical porous structures facilitate mass transfer and improves the accessibility of active sites, which further enhances the catalytic activity. By reviewing different applications of N-doped carbon catalysts, transferable knowledge can be found via analyzing the similarities of N-doped carbon catalysts for different electrochemical reactions. Meanwhile, carefully discerning the differences of N-doped carbon materials for different applications can help to target the design of functional catalysts.

Various reports emphasise the importance of the type of N-containing species for the HER, ORR, and CO₂RR. Therefore, precise control over the N-containing species generated during the synthesis of N-doped carbon catalysts is of importance for all of these electrochemical reactions. The adsorption and diffusion processes of reactants are determined by the porous structure of N-doped biochar. Many studies focus on understanding the synergistic effect of micropores, mesopores, and macropores for different reactions. A well-designed hierarchical pore structure can significantly improve mass transfer for the HER, ORR, and CO₂RR. Moreover, a higher degree of graphitization indicates a better electrical conductivity, which improves the electron transfer rate and enhances the electrochemical activity of N-doped biochar for different applications.

It must be noted that understanding the differences of various reactions is even more important for the design and evaluation of N-doped carbon electrocatalysts. The HER, ORR, and CO₂RR occur at the triple-phase boundary of the solid electrocatalyst, liquid electrolyte, and gaseous reactants/products. However, these reactions have different demands on the surface wettability of N-doped carbon catalysts. Since the HER consumes water and generates gas, the surfaces should be more hydrophilic to prevent the accumulation of gas bubbles that cover the active sites and thereby decrease the HER performance. Conversely, the ORR is an oxygen consuming reaction and generates water, therefore, hydrophobic surfaces are preferred. A hydrophobic surface improves the local concentration of oxygen and further enhances the ORR performance. Interestingly, the CO₂RR on N-doped carbon consumes CO₂ and mainly generates gas products (CO). Therefore, the surfaces need to achieve a delicate balance both favoring the adsorption of CO₂ reactants and preventing the aggregation of gaseous products. Increasing the hydrophobicity of the surfaces of N-doped biochar is also favorable for inhibiting the competitive HER, whereas superhydrophobic surfaces may not allow for enough contact between the electrolyte and the catalyst.²²³ Hence, the coexistence of hydrophobicity and hydrophilicity of N-doped biochar is necessary for the CO₂RR, while the further optimization of the surfaces wettability needs more investigation.

In addition, depending on the application conditions of different reactions, N-doped biochar catalysts have different demands for the tolerance and stability measurements. For HER, the water impurities conceivably influence the long-term operation of water electrolysis by adsorption, fouling, or corrosion.²²⁴ It is therefore necessary to scrutinise the effect of impurities (cations, anions, organics, etc.) in the water on the N-doped biochar catalysts for HER during prolonged testing. Since using methanol as hydrogen carries for fuel cells is getting more attractive, the tolerance and stability tests of ORR need to take into account the effect of impurities in the electrolyte, and also the poisoning effect from the migration of the anode reactants. As for CO₂RR, in addition to considering the impacts of impurities in the electrolyte, the effect of gaseous impurities (such as, SO_x, NO_x, VOCs, etc.) in industrial flue gases on N-doped carbon catalysts for CO₂RR needs to be further studied.

2.4 Conclusions and future perspectives

In summary, this chapter presents the recent progresses on biomass-derived N-doped carbon materials as efficient electrocatalysts for hydrogen evolution reaction, oxygen reduction reaction, and carbon dioxide reduction reactions, and summarized the commonly used strategies for biochar carbonization, functionalization and characterization. The synthesis conditions directly determine the properties of N-doped biochar, which in turn strongly affect the electrochemical performances for different applications. In general, its sustainability, earth abundance, versatile porous structure and tuneable surface chemistry make N-doped biochar a promising electrocatalysts for various energy conversion and storage technologies. Despite that the research in this field has achieved a considerable advancement, some vital issues still need to be further investigated.

First, more efforts should be made to elucidate the mechanisms of N-doped biochar formation. Currently, the fundamental understanding on the structural properties and doping features of N-doped biochar is mostly concluded from serendipitous discovery or trial and error approaches. Owing to the diversity of biomass feedstocks, dopants, activators and operation conditions, countless N-doped biochar materials have been prepared and used for different applications. This approach does not help to reveal the correlation between synthesis conditions and physicochemical properties of N-doped biochar, and has been severely criticized.²²⁵ Therefore, elucidating the regularity of N-doping and the mechanisms of N-doped biochar formation are more useful than blind doping processes. Understanding the interactions between feedstock compositions, dopants, and activators are helpful to reveal the migration principles of N-containing species. Moreover, precisely modulating the type and content of N-containing species in N-doped biochar is highly desired. Furthermore, investigating the correlation between the physicochemical properties

and preparation conditions of N-doped biochar catalysts is expected to guide the production of N-doped biochar with controllable porosity and surface chemistry.

Second, the assessment of active sites of N-doped biochar for different reactions should be further investigated. As discussed above, pyridinic N, graphitic N, pyrrolic N, and defects were proved as the most active sites for the HER, ORR, and CO₂RR. Different studies have even yielded completely opposite conclusions. Density functional theory is a powerful tool to help to reveal the reaction mechanisms, but it is important to note that DFT calculation results strongly depend on the ideal and simplified active site model. Synergistic effects emerging from surface curvature, multiple active sites, and ion effects are often overlooked. Therefore, taking into account the curvature effect of carbon materials,^{226,227} the kinetic barriers between reaction intermediates (by applying nudged elastic band-based methods),²²⁸ and the effects of pH and ions (via explicit solvent dynamics),²²⁹ to the overall electrochemical performance of N-doped carbon materials are encouraged. On the other hand, the degradation mechanisms of N-containing active sites remain relatively unexplored to date. A series of in-situ techniques would be helpful to explore the reaction and degradation mechanisms.

Third, further efforts are needed to understand the correlations between structural properties and electrochemical performances of N-doped biochar for various applications. The effect of the degree of graphitization, the abundance of defects, the surface wettability, and the configuration of porosity (the percentage of micro-meso-macropores), should be equally considered instead of overemphasizing the contribution of the type and content of N-doping and the specific surface area. The physicochemical properties of N-doped biochar change even if one of the preparation conditions is changed, making it difficult to screen for elucidating the structure-activity relationships. It should be underlined that the data processing of several techniques, including N₂ adsorption and desorption and the deconvolution of XPS spectra have intrinsic degrees of uncertainty.^{230–232} The results are relatively subjective and strongly influenced by the software and the personal experience. Therefore, it should be very carefully considered when comparing the analyses results by different research groups. In addition, some advanced characterization methods developed in recent years, such as in-situ XPS, in-situ Raman spectroscopy, small-angle neutron scattering (SANS), small-angle X-ray scattering (SAXS), X-ray adsorption spectroscopy (XAS) and electrochemical quartz crystal microbalance (EQCM) are gradually being used to reveal “synthesis-properties-performance” relationships of N-doped carbon materials.

Last, optimizing the operating conditions to fits the requirements for large-scale application needs more systematic studies. In addition to the catalysts, the type and concentration of the electrolyte, the type and size of the cell, and the reaction temperature and pressure have a critical impact on the performance of N-doped carbon materials in

different applications. Therefore, it is vital to select the most suitable reaction conditions, rather than endlessly improving the electrochemical performances of the catalysts. Linking the performance of the catalyst to the electrolyzer configurations, electrode structure, electrolyte selection (cations, anions, and organic electrolyte), temperature, pH, can provide new insights to improve the overall performance of the reaction processes.

Although there will be significant challenges to use N-doped biochar as catalysts for electrochemical energy conversion and storage applications, the achievements to date are very encouraging. Overall, the upcoming direction of N-doped biochar is to figure out the correlations between “synthesis conditions – physicochemical properties – electrochemical performances”, and to identify the active sites and reaction mechanisms. Furthermore, more fundamental work on optimizing the reaction conditions and processes are encouraged for integrating the N-doped biochar catalysts into the sustainable energy conversion and storage system.

References

- (1) Armstrong McKay, D. I.; Staal, A.; Abrams, J. F.; Winkelmann, R.; Sakschewski, B.; Loriani, S.; Fetzer, I.; Cornell, S. E.; Rockström, J.; Lenton, T. M. Exceeding 1.5 C Global Warming Could Trigger Multiple Climate Tipping Points. *Science*. **2022**, 377 (6611), eabn7950.
- (2) Zandalinas, S. I.; Fritschi, F. B.; Mittler, R. Global Warming, Climate Change, and Environmental Pollution: Recipe for a Multifactorial Stress Combination Disaster. *Trends Plant Sci.* **2021**, 26 (6), 588–599.
- (3) Yoro, K. O.; Daramola, M. O. CO₂ Emission Sources, Greenhouse Gases, and the Global Warming Effect. In *Advances in carbon capture*; Elsevier, 2020; pp 3–28.
- (4) Wang, Y.; Diaz, D. F. R.; Chen, K. S.; Wang, Z.; Adroher, X. C. Materials, Technological Status, and Fundamentals of PEM Fuel Cells—a Review. *Mater. today* **2020**, 32, 178–203.
- (5) Fan, L.; Tu, Z.; Chan, S. H. Recent Development of Hydrogen and Fuel Cell Technologies: A Review. *Energy Reports* **2021**, 7, 8421–8446.
- (6) Wang, H.-F.; Xu, Q. Materials Design for Rechargeable Metal-Air Batteries. *Matter* **2019**, 1 (3), 565–595.
- (7) Kumar, Y.; Mooste, M.; Tammeveski, K. Recent Progress of Transition Metal-Based Bifunctional Electrocatalysts for Rechargeable Zinc-Air Battery Application. *Curr. Opin. Electrochem.* **2023**, 101229.
- (8) Li, Y.; Sun, Y.; Qin, Y.; Zhang, W.; Wang, L.; Luo, M.; Yang, H.; Guo, S. Recent Advances on Water-splitting Electrocatalysis Mediated by Noble-metal-based Nanostructured Materials. *Adv. Energy Mater.* **2020**, 10 (11), 1903120.
- (9) Yu, Z.; Duan, Y.; Feng, X.; Yu, X.; Gao, M.; Yu, S. Clean and Affordable Hydrogen Fuel from Alkaline Water Splitting: Past, Recent Progress, and Future Prospects. *Adv. Mater.* **2021**, 33 (31), 2007100.
- (10) Chen, S.; Liu, J.; Zhang, Q.; Teng, F.; McLellan, B. C. A Critical Review on Deployment Planning and Risk Analysis of Carbon Capture, Utilization, and Storage (CCUS) toward Carbon Neutrality. *Renew. Sustain. Energy Rev.* **2022**, 167, 112537.
- (11) Hepburn, C.; Adlen, E.; Beddington, J.; Carter, E. A.; Fuss, S.; Mac Dowell, N.; Minx, J. C.; Smith, P.; Williams, C. K. The Technological and Economic Prospects for CO₂ Utilization and Removal. *Nature* **2019**, 575 (7781), 87–97.

- (12) Saravanan, A.; Vo, D.-V. N.; Jeevanantham, S.; Bhuvaneswari, V.; Narayanan, V. A.; Yaashikaa, P. R.; Swetha, S.; Reshma, B. A Comprehensive Review on Different Approaches for CO₂ Utilization and Conversion Pathways. *Chem. Eng. Sci.* **2021**, *236*, 116515.
- (13) Hu, C.; Paul, R.; Dai, Q.; Dai, L. Carbon-Based Metal-Free Electrocatalysts: From Oxygen Reduction to Multifunctional Electrocatalysis. *Chem. Soc. Rev.* **2021**, *50* (21), 11785–11843.
- (14) Li, C.; Baek, J.-B. Recent Advances in Noble Metal (Pt, Ru, and Ir)-Based Electrocatalysts for Efficient Hydrogen Evolution Reaction. *ACS omega* **2019**, *5* (1), 31–40.
- (15) Hansen, J. N.; Prats, H.; Toudahl, K. K.; Mørch Secher, N.; Chan, K.; Kibsgaard, J.; Chorkendorff, I. Is There Anything Better than Pt for HER? *ACS energy Lett.* **2021**, *6* (4), 1175–1180.
- (16) Liu, M.; Zhao, Z.; Duan, X.; Huang, Y. Nanoscale Structure Design for High-performance Pt-based ORR Catalysts. *Adv. Mater.* **2019**, *31* (6), 1802234.
- (17) Zheng, T.; Jiang, K.; Wang, H. Recent Advances in Electrochemical CO₂-to-CO Conversion on Heterogeneous Catalysts. *Adv. Mater.* **2018**, *30* (48), 1802066.
- (18) Lawrence, K. R.; Kumar, A. S.; Asperti, S.; van den Berg, D.; Girichandran, N.; Kortlever, R. Advances in Electrochemical Carbon Dioxide Reduction Toward Multi-Carbon Products. In *Chemical Valorisation of Carbon Dioxide*; 2022; pp 388–412.
- (19) Woldu, A. R.; Huang, Z.; Zhao, P.; Hu, L.; Astruc, D. Electrochemical CO₂ Reduction (CO₂RR) to Multi-Carbon Products over Copper-Based Catalysts. *Coord. Chem. Rev.* **2022**, *454*, 214340.
- (20) Hu, C.; Xiao, Y.; Zou, Y.; Dai, L. Carbon-Based Metal-Free Electrocatalysis for Energy Conversion and Storage. *Electrochem. Energy Rev.* **2018**, *1* (1), 84–112.
- (21) Paul, R.; Zhu, L.; Chen, H.; Qu, J.; Dai, L. Recent Advances in Carbon-Based Metal-Free Electrocatalysts. *Adv. Mater.* **2019**, *1806403*, 1–24.
- (22) Gong, K.; Du, F.; Xia, Z.; Durstock, M.; Dai, L. Nitrogen-Doped Carbon Nanotube Arrays with High Electrocatalytic Activity for Oxygen Reduction. *Science*. **2009**, *323* (5915), 760–764.
- (23) Paul, R.; Dai, Q.; Hu, C.; Dai, L. Ten Years of Carbon-based Metal-free Electrocatalysts. *Carbon Energy* **2019**, *1* (1), 19–31.

- (24) Shao, Y.; Jiang, Z.; Zhang, Q.; Guan, J. Progress in Nonmetal-doped Graphene Electrocatalysts for the Oxygen Reduction Reaction. *ChemSusChem* **2019**, *12* (10), 2133–2146.
- (25) Kuang, P.; Sayed, M.; Fan, J.; Cheng, B.; Yu, J. 3D Graphene-based H₂-production Photocatalyst and Electrocatalyst. *Adv. Energy Mater.* **2020**, *10* (14), 1903802.
- (26) Li, Y.; Zhou, W.; Wang, H.; Xie, L.; Liang, Y.; Wei, F.; Idrobo, J.-C.; Pennycook, S. J.; Dai, H. An Oxygen Reduction Electrocatalyst Based on Carbon Nanotube–Graphene Complexes. *Nat. Nanotechnol.* **2012**, *7* (6), 394–400.
- (27) Zhou, X.; Liu, X.; Zhang, J.; Zhang, C.; Yoo, S. J.; Kim, J.-G.; Chu, X.; Song, C.; Wang, P.; Zhao, Z. Highly-Dispersed Cobalt Clusters Decorated onto Nitrogen-Doped Carbon Nanotubes as Multifunctional Electrocatalysts for OER, HER and ORR. *Carbon* **2020**, *166*, 284–290.
- (28) Hou, Y.; Liang, Y.-L.; Shi, P.-C.; Huang, Y.-B.; Cao, R. Atomically Dispersed Ni Species on N-Doped Carbon Nanotubes for Electroreduction of CO₂ with Nearly 100% CO Selectivity. *Appl. Catal. B Environ.* **2020**, *271*, 118929.
- (29) Qiang, F.; Feng, J.; Wang, H.; Yu, J.; Shi, J.; Huang, M.; Shi, Z.; Liu, S.; Li, P.; Dong, L. Oxygen Engineering Enables N-Doped Porous Carbon Nanofibers as Oxygen Reduction/Evolution Reaction Electrocatalysts for Flexible Zinc–Air Batteries. *ACS Catal.* **2022**, *12* (7), 4002–4015.
- (30) Wang, H.-F.; Chen, L.; Pang, H.; Kaskel, S.; Xu, Q. MOF-Derived Electrocatalysts for Oxygen Reduction, Oxygen Evolution and Hydrogen Evolution Reactions. *Chem. Soc. Rev.* **2020**, *49* (5), 1414–1448.
- (31) Adegoke, K. A.; Maxakato, N. W. Porous Metal-Organic Framework (MOF)-Based and MOF-Derived Electrocatalytic Materials for Energy Conversion. *Mater. Today Energy* **2021**, *21*, 100816.
- (32) Liu, A.; Liang, X.; Ren, X.; Guan, W.; Gao, M.; Yang, Y.; Yang, Q.; Gao, L.; Li, Y.; Ma, T. Recent Progress in MXene-based Materials: Potential High-performance Electrocatalysts. *Adv. Funct. Mater.* **2020**, *30* (38), 2003437.
- (33) Tsounis, C.; Kumar, P. V.; Masood, H.; Kulkarni, R. P.; Gautam, G. S.; Müller, C. R.; Amal, R.; Kuznetsov, D. A. Advancing MXene Electrocatalysts for Energy Conversion Reactions: Surface, Stoichiometry, and Stability. *Angew. Chemie Int. Ed.* **2023**, *62* (4), e202210828.

- (34) Wang, H.; Shao, Y.; Mei, S.; Lu, Y.; Zhang, M.; Sun, J.; Matyjaszewski, K.; Antonietti, M.; Yuan, J. Polymer-Derived Heteroatom-Doped Porous Carbon Materials. *Chem. Rev.* **2020**, *120* (17), 9363–9419.
- (35) Wang, Y.; Wang, D.; Li, Y. Rational Design of Single-atom Site Electrocatalysts: From Theoretical Understandings to Practical Applications. *Adv. Mater.* **2021**, *33* (34), 2008151.
- (36) Liu, W.-J.; Jiang, H.; Yu, H.-Q. Emerging Applications of Biochar-Based Materials for Energy Storage and Conversion. *Energy Environ. Sci.* **2019**, *12* (6), 1751–1779.
- (37) Chakraborty, R.; Vilya, K.; Pradhan, M.; Nayak, A. K. Recent Advancement of Biomass-Derived Porous Carbon Based Materials for Energy and Environmental Remediation Applications. *J. Mater. Chem. A* **2022**, *10* (13), 6965–7005.
- (38) Yamakawa, C. K.; Qin, F.; Mussatto, S. I. Advances and Opportunities in Biomass Conversion Technologies and Biorefineries for the Development of a Bio-Based Economy. *Biomass and Bioenergy* **2018**, *119*, 54–60.
- (39) Walker, T. W.; Motagamwala, A. H.; Dumesic, J. A.; Huber, G. W. Fundamental Catalytic Challenges to Design Improved Biomass Conversion Technologies. *J. Catal.* **2019**, *369*, 518–525.
- (40) Cheng, B. H.; Zeng, R. J.; Jiang, H. Recent Developments of Post-Modification of Biochar for Electrochemical Energy Storage. *Bioresour. Technol.* **2017**, *246*, 224–233.
- (41) Senthil, C.; Lee, C. W. Biomass-Derived Biochar Materials as Sustainable Energy Sources for Electrochemical Energy Storage Devices. *Renew. Sustain. Energy Rev.* **2021**, *137*, 110464.
- (42) Rahman, M. Z.; Edvinsson, T.; Kwong, P. Biochar for Electrochemical Applications. *Curr. Opin. Green Sustain. Chem.* **2020**, *23*, 25–30.
- (43) Kazemi Shariat Panahi, H.; Dehghani, M.; Ok, Y. S.; Nizami, A. S.; Khoshnevisan, B.; Mussatto, S. I.; Aghbashlo, M.; Tabatabaei, M.; Lam, S. S. A Comprehensive Review of Engineered Biochar: Production, Characteristics, and Environmental Applications. *J. Clean. Prod.* **2020**, *270*, 122462.
- (44) Yi, Y.; Huang, Z.; Lu, B.; Xian, J.; Tsang, E. P.; Cheng, W.; Fang, J.; Fang, Z. Magnetic Biochar for Environmental Remediation: A Review. *Bioresour. Technol.* **2020**, *298*, 122468.
- (45) Gupta, M.; Savla, N.; Pandit, C.; Pandit, S.; Gupta, P. K.; Pant, M.; Khilari, S.; Kumar, Y.; Agarwal, D.; Nair, R. R.; Thomas, D.; Thakur, V. K. Use of Biomass-Derived Biochar in Wastewater Treatment and Power Production: A Promising Solution for a Sustainable Environment. *Sci. Total Environ.* **2022**, *825*, 153892.

- (46) Li, Y.; Xing, B.; Wang, X.; Wang, K.; Zhu, L.; Wang, S. Nitrogen-Doped Hierarchical Porous Biochar Derived from Corn Stalks for Phenol-Enhanced Adsorption. *Energy and Fuels* **2019**, *33*(12), 12459–12468.
- (47) Li, X.; Zhang, J.; Liu, B.; Su, Z. A Critical Review on the Application and Recent Developments of Post-Modified Biochar in Supercapacitors. *J. Clean. Prod.* **2021**, *310*, 127428.
- (48) Qiao, Y.; Zhang, C.; Kong, F.; Zhao, Q.; Kong, A.; Shan, Y. Activated Biochar Derived from Peanut Shells as the Electrode Materials with Excellent Performance in Zinc-Air Battery and Supercapacitance. *Waste Manag.* **2021**, *125*, 257–267.
- (49) Long, W.; Fang, B.; Ignaszak, A.; Wu, Z.; Wang, Y.-J.; Wilkinson, D. Biomass-Derived Nanostructured Carbons and Their Composites as Anode Materials for Lithium Ion Batteries. *Chem. Soc. Rev.* **2017**, *46* (23), 7176–7190.
- (50) Xiong, X.; Iris, K. M.; Cao, L.; Tsang, D. C. W.; Zhang, S.; Ok, Y. S. A Review of Biochar-Based Catalysts for Chemical Synthesis, Biofuel Production, and Pollution Control. *Bioresour. Technol.* **2017**, *246*, 254–270.
- (51) Ahmed, M. B.; Zhou, J. L.; Ngo, H. H.; Guo, W. Adsorptive Removal of Antibiotics from Water and Wastewater: Progress and Challenges. *Sci. Total Environ.* **2015**, *532*, 112–126.
- (52) Bridgwater, A. V. Review of Fast Pyrolysis of Biomass and Product Upgrading. *Biomass and Bioenergy* **2012**, *38*, 68–94.
- (53) Qambrani, N. A.; Rahman, M. M.; Won, S.; Shim, S.; Ra, C. Biochar Properties and Eco-Friendly Applications for Climate Change Mitigation, Waste Management, and Wastewater Treatment: A Review. *Renew. Sustain. Energy Rev.* **2017**, *79*, 255–273.
- (54) Qian, K.; Kumar, A.; Zhang, H.; Bellmer, D.; Huhnke, R. Recent Advances in Utilization of Biochar. *Renew. Sustain. Energy Rev.* **2015**, *42*, 1055–1064.
- (55) Meyer, S.; Glaser, B.; Quicker, P. Technical, Economical, and Climate-Related Aspects of Biochar Production Technologies: A Literature Review. *Environ. Sci. Technol.* **2011**, *45* (22), 9473–9483.
- (56) Seow, Y. X.; Tan, Y. H.; Mubarak, N. M.; Kansedo, J.; Khalid, M.; Ibrahim, M. L.; Ghasemi, M. A Review on Biochar Production from Different Biomass Wastes by Recent Carbonization Technologies and Its Sustainable Applications. *J. Environ. Chem. Eng.* **2022**, *10* (1), 107017.

- (57) Panwar, N. L.; Pawar, A. Influence of Activation Conditions on the Physicochemical Properties of Activated Biochar: A Review. *Biomass Convers. Biorefinery* **2022**, *12* (3), 925–947.
- (58) Roy, P.; Dias, G. Prospects for Pyrolysis Technologies in the Bioenergy Sector: A Review. *Renew. Sustain. Energy Rev.* **2017**, *77*, 59–69.
- (59) Greenhalf, C. E.; Nowakowski, D. J.; Harms, A. B.; Titiloye, J. O.; Bridgwater, A. V. A Comparative Study of Straw, Perennial Grasses and Hardwoods in Terms of Fast Pyrolysis Products. *Fuel* **2013**, *108*, 216–230.
- (60) Sri Shalini S; Palanivelu K; Ramachandran A; Raghavan, V. Biochar from Biomass Waste as a Renewable Carbon Material for Climate Change Mitigation in Reducing Greenhouse Gas Emissions—a Review. *Biomass Convers. Biorefinery* **2020**, *11* (5), 2247–2267.
- (61) Das, S. K.; Ghosh, G. K.; Avasthe, R. Applications of Biomass Derived Biochar in Modern Science and Technology. *Environ. Technol. Innov.* **2021**, *21*, 101306.
- (62) Garcia-Nunez, J. A.; Pelaez-Samaniego, M. R.; Garcia-Perez, M. E.; Fonts, I.; Abrego, J.; Westerhof, R. J. M.; Garcia-Perez, M. Historical Developments of Pyrolysis Reactors: A Review. *Energy and Fuels* **2017**, *31* (6), 5751–5775.
- (63) Brassard, P.; Godbout, S.; Raghavan, V. Pyrolysis in Auger Reactors for Biochar and Bio-Oil Production: A Review. *Biosyst. Eng.* **2017**, *161*, 80–92.
- (64) Hanping, C.; Bin, L.; Haiping, Y.; Guolai, Y.; Shihong, Z. Experimental Investigation of Biomass Gasification in a Fluidized Bed Reactor. *Energy & Fuels* **2008**, *22* (5), 3493–3498.
- (65) Song, H.; Yang, G.; Xue, P.; Li, Y.; Zou, J.; Wang, S.; Yang, H.; Chen, H. Recent Development of Biomass Gasification for H₂ Rich Gas Production. *Appl. Energy Combust. Sci.* **2022**, *10*, 100059.
- (66) Umenweke, G. C.; Afolabi, I. C.; Epelle, E. I.; Okolie, J. A. Machine Learning Methods for Modeling Conventional and Hydrothermal Gasification of Waste Biomass: A Review. *Bioresour. Technol. Reports* **2022**, *17*, 100976.
- (67) Singh Siwal, S.; Zhang, Q.; Sun, C.; Thakur, S.; Kumar Gupta, V.; Kumar Thakur, V. Energy Production from Steam Gasification Processes and Parameters That Contemplate in Biomass Gasifier – A Review. *Bioresour. Technol.* **2020**, *297*, 122481.
- (68) You, S.; Ok, Y. S.; Chen, S. S.; Tsang, D. C. W.; Kwon, E. E.; Lee, J.; Wang, C. H. A Critical Review on Sustainable Biochar System through Gasification: Energy and Environmental Applications. *Bioresour. Technol.* **2017**, *246*, 242–253.

- (69) Mumme, J.; Eckervogt, L.; Pielert, J.; Diakit , M.; Rupp, F.; Kern, J. Hydrothermal Carbonization of Anaerobically Digested Maize Silage. *Bioresour. Technol.* **2011**, *102* (19), 9255–9260.
- (70) Fakkaew, K.; Koottatep, T.; Polprasert, C. Effects of Hydrolysis and Carbonization Reactions on Hydrochar Production. *Bioresour. Technol.* **2015**, *192*, 328–334.
- (71) Reza, M. T.; Lynam, J. G.; Uddin, M. H.; Coronella, C. J. Hydrothermal Carbonization: Fate of Inorganics. *Biomass and Bioenergy* **2013**, *49*, 86–94.
- (72) Libra, J. A.; Ro, K. S.; Kammann, C.; Funke, A.; Berge, N. D.; Neubauer, Y.; Titirici, M.-M.; F hner, C.; Bens, O.; Kern, J.; others. Hydrothermal Carbonization of Biomass Residuals: A Comparative Review of the Chemistry, Processes and Applications of Wet and Dry Pyrolysis. *Biofuels* **2011**, *2* (1), 71–106.
- (73) Kambo, H. S.; Dutta, A. A Comparative Review of Biochar and Hydrochar in Terms of Production, Physico-Chemical Properties and Applications. *Renew. Sustain. Energy Rev.* **2015**, *45*, 359–378.
- (74) Yan, W.; Hastings, J. T.; Acharjee, T. C.; Coronella, C. J.; V squez, V. R. Mass and Energy Balances of Wet Torrefaction of Lignocellulosic Biomass. *Energy and Fuels* **2010**, *24* (9), 4738–4742.
- (75) Sevilla, M.; Fuertes, A. B. Sustainable Porous Carbons with a Superior Performance for CO₂ Capture. *Energy Environ. Sci.* **2011**, *4* (5), 1765–1771.
- (76) Fang, J.; Zhan, L.; Ok, Y. S.; Gao, B. Minireview of Potential Applications of Hydrochar Derived from Hydrothermal Carbonization of Biomass. *J. Ind. Eng. Chem.* **2018**, *57*, 15–21.
- (77) Liu, N.; Charrua, A. B.; Weng, C. H.; Yuan, X.; Ding, F. Characterization of Biochars Derived from Agriculture Wastes and Their Adsorptive Removal of Atrazine from Aqueous Solution: A Comparative Study. *Bioresour. Technol.* **2015**, *198*, 55–62.
- (78) Liu, W. J.; Jiang, H.; Yu, H. Q. Development of Biochar-Based Functional Materials: Toward a Sustainable Platform Carbon Material. *Chem. Rev.* **2015**, *115* (22), 12251–12285.
- (79) Wang, H.; Maiyalagan, T.; Wang, X. Review on Recent Progress in Nitrogen-Doped Graphene: Synthesis, Characterization, and Its Potential Applications. *Acs Catal.* **2012**, *2* (5), 781–794.
- (80) Zhang, J.; Dai, L. Heteroatom-Doped Graphitic Carbon Catalysts for Efficient Electrocatalysis of Oxygen Reduction Reaction. *Acs Catal.* **2015**, *5* (12), 7244–7253.

- (81) Sevilla, M.; Mokaya, R. Energy Storage Applications of Activated Carbons: Supercapacitors and Hydrogen Storage. *Energy Environ. Sci.* **2014**, 7 (4), 1250–1280.
- (82) Gao, Y.; Yue, Q.; Gao, B.; Li, A. Insight into Activated Carbon from Different Kinds of Chemical Activating Agents: A Review. *Sci. Total Environ.* **2020**, 746, 141094.
- (83) Nazem, M. A.; Zare, M. H.; Shirazian, S. Preparation and Optimization of Activated Nano-Carbon Production Using Physical Activation by Water Steam from Agricultural Wastes. *RSC Adv.* **2020**, 10 (3), 1463–1475.
- (84) Tehrani, N. F.; Aznar, J. S.; Kiros, Y. Coffee Extract Residue for Production of Ethanol and Activated Carbons. *J. Clean. Prod.* **2015**, 91, 64–70.
- (85) Rambabu, N.; Rao, B. V. S. K.; Surisetty, V. R.; Das, U.; Dalai, A. K. Production, Characterization, and Evaluation of Activated Carbons from de-Oiled Canola Meal for Environmental Applications. *Ind. Crops Prod.* **2015**, 65, 572–581.
- (86) Zhou, J.; Luo, A.; Zhao, Y. Preparation and Characterisation of Activated Carbon from Waste Tea by Physical Activation Using Steam. *J. of the Air & Waster Manag. Asso.* **2018**, 68 (12), 1269–1277.
- (87) Zhang, J.; Shao, J.; Jin, Q.; Li, Z.; Zhang, X.; Chen, Y.; Zhang, S.; Chen, H. Sludge-Based Biochar Activation to Enhance Pb(II) Adsorption. *Fuel* **2019**, 252, 101–108.
- (88) Kilpimaa, S.; Runtti, H.; Kangas, T.; Lassi, U.; Kuokkanen, T. Physical Activation of Carbon Residue from Biomass Gasification: Novel Sorbent for the Removal of Phosphates and Nitrates from Aqueous Solution. *J. Ind. Eng. Chem.* **2015**, 21, 1354–1364.
- (89) Wu, L.; Shang, Z.; Wang, H.; Wan, W.; Gao, X.; Li, Z.; Kobayashi, N. Production of Activated Carbon from Walnut Shell by CO₂ Activation in a Fluidized Bed Reactor and Its Adsorption Performance of Copper Ion. *J. Mater. Cycles Waste Manag.* **2018**, 20 (3), 1676–1688.
- (90) Yang, K.; Peng, J.; Srinivasakannan, C.; Zhang, L.; Xia, H.; Duan, X. Preparation of High Surface Area Activated Carbon from Coconut Shells Using Microwave Heating. *Bioresour. Technol.* **2010**, 101 (15), 6163–6169.
- (91) Taer, E.; Deraman, M.; Talib, I. A.; Umar, A. A.; Oyama, M.; Yunus, R. M. Physical, Electrochemical and Supercapacitive Properties of Activated Carbon Pellets from Pre-Carbonized Rubber Wood Sawdust by CO₂ Activation. *Curr. Appl. Phys.* **2010**, 10 (4), 1071–1075.
- (92) Guerrero-Pérez, M. O.; Valero-Romero, M. J.; Hernández, S.; Nieto, J. M. L.; Rodríguez-Mirasol, J.; Cordero, T. Lignocellulosic-Derived Mesoporous Materials: An Answer

to Manufacturing Non-Expensive Catalysts Useful for the Biorefinery Processes. *Catal. Today* **2012**, *195* (1), 155–161.

(93) Liu, B.; Wang, W.; Wanga, N.; Au, C. T. Preparation of Activated Carbon with High Surface Area for High-Capacity Methane Storage. *J. Energy Chem.* **2014**, *23* (5), 662–668.

(94) Guo, N.; Li, M.; Sun, X.; Wang, F.; Yang, R. Tremella Derived Ultrahigh Specific Surface Area Activated Carbon for High Performance Supercapacitor. *Mater. Chem. Phys.* **2017**, *201*, 399–407.

(95) Heimböckel, R.; Kraas, S.; Hoffmann, F.; Fröba, M. Increase of Porosity by Combining Semi-Carbonization and KOH Activation of Formaldehyde Resins to Prepare High Surface Area Carbons for Supercapacitor Applications. *Appl. Surf. Sci.* **2018**, *427*, 1055–1064.

(96) Muniandy, L.; Adam, F.; Mohamed, A. R.; Ng, E. P. The Synthesis and Characterization of High Purity Mixed Microporous/Mesoporous Activated Carbon from Rice Husk Using Chemical Activation with NaOH and KOH. *Microporous Mesoporous Mater.* **2014**, *197*, 316–323.

(97) Zhang, Y.; Song, X.; Xu, Y.; Shen, H.; Kong, X.; Xu, H. Utilization of Wheat Bran for Producing Activated Carbon with High Specific Surface Area via NaOH Activation Using Industrial Furnace. *J. Clean. Prod.* **2019**, *210*, 366–375.

(98) Deng, J.; Xiong, T.; Xu, F.; Li, M.; Han, C.; Gong, Y.; Wang, H.; Wang, Y. Inspired by Bread Leavening: One-Pot Synthesis of Hierarchically Porous Carbon for Supercapacitors-SI. *Green Chem.* **2015**, *17* (7), 4053–4060.

(99) Yue, L.; Xia, Q.; Wang, L.; Wang, L.; DaCosta, H.; Yang, J.; Hu, X. CO₂ Adsorption at Nitrogen-Doped Carbons Prepared by K₂CO₃ Activation of Urea-Modified Coconut Shell. *J. Colloid Interface Sci.* **2018**, *511*, 259–267.

(100) Zhang, Z.; Lei, Y.; Li, D.; Zhao, J.; Wang, Y.; Zhou, G.; Yan, C.; He, Q. Sudden Heating of H₃PO₄-Loaded Coconut Shell in CO₂ Flow to Produce Super Activated Carbon and Its Application for Benzene Adsorption. *Renew. Energy* **2020**, *153*, 1091–1099.

(101) Wei, Q.; Chen, Z.; Cheng, Y.; Wang, X.; Yang, X.; Wang, Z. Preparation and Electrochemical Performance of Orange Peel Based-Activated Carbons Activated by Different Activators. *Colloids Surfaces A Physicochem. Eng. Asp.* **2019**, *574*, 221–227.

(102) Cao, L.; Yu, I. K. M.; Tsang, D. C. W.; Zhang, S.; Ok, Y. S.; Kwon, E. E.; Song, H.; Poon, C. S. Phosphoric Acid-Activated Wood Biochar for Catalytic Conversion of Starch-Rich Food Waste into Glucose and 5-Hydroxymethylfurfural. *Bioresour. Technol.* **2018**, *267*, 242–248.

- (103) Kiliç, M.; Apaydin-Varol, E.; Pütün, A. E. Preparation and Surface Characterization of Activated Carbons from *Euphorbia Rigida* by Chemical Activation with ZnCl_2 , K_2CO_3 , NaOH and H_3PO_4 . *Appl. Surf. Sci.* **2012**, *261*, 247–254.
- (104) Saygili, H.; Güzel, F. High Surface Area Mesoporous Activated Carbon from Tomato Processing Solid Waste by Zinc Chloride Activation: Process Optimization, Characterization and Dyes Adsorption. *J. Clean. Prod.* **2016**, *113*, 995–1004.
- (105) Oliveira, L. C. A.; Pereira, E.; Guimaraes, I. R.; Vallone, A.; Pereira, M.; Mesquita, J. P.; Sapag, K. Preparation of Activated Carbons from Coffee Husks Utilizing FeCl_3 and ZnCl_2 as Activating Agents. *J. Hazard. Mater.* **2009**, *165* (1–3), 87–94.
- (106) Xu, Z.; Yuan, Z.; Zhang, D.; Chen, W.; Huang, Y.; Zhang, T.; Tian, D.; Deng, H.; Zhou, Y.; Sun, Z. Highly Mesoporous Activated Carbon Synthesized by Pyrolysis of Waste Polyester Textiles and MgCl_2 : Physiochemical Characteristics and Pore-Forming Mechanism. *J. Clean. Prod.* **2018**, *192*, 453–461.
- (107) Xu, Z.; Zhou, Y.; Sun, Z.; Zhang, D.; Huang, Y.; Gu, S.; Chen, W. Understanding Reactions and Pore-Forming Mechanisms between Waste Cotton Woven and FeCl_3 during the Synthesis of Magnetic Activated Carbon. *Chemosphere* **2020**, *241*, 125120.
- (108) Li, Q.; Wu, X.; Zhao, Y.; Miao, Z.; Xing, L.; Zhou, J.; Zhao, J.; Zhuo, S. Nitrogen-Doped Hierarchical Porous Carbon through One-Step Activation of Bean Curd for High-Performance Supercapacitor Electrode. *ChemElectroChem* **2018**, *5* (12), 1606–1614.
- (109) Qiu, D.; Guo, N.; Gao, A.; Zheng, L.; Xu, W.; Li, M.; Wang, F.; Yang, R. Preparation of Oxygen-Enriched Hierarchically Porous Carbon by KMnO_4 One-Pot Oxidation and Activation: Mechanism and Capacitive Energy Storage. *Electrochim. Acta* **2019**, *294*, 398–405.
- (110) Dalai, A. K.; Azargohar, R. Production of Activated Carbon from Biochar Using Chemical and Physical Activation: Mechanism and Modeling; ACS Publications, **2007**, pp 463–476.
- (111) Kołtowski, M.; Charmas, B.; Skubiszewska-Zięba, J.; Oleszczuk, P. Effect of Biochar Activation by Different Methods on Toxicity of Soil Contaminated by Industrial Activity. *Ecotoxicol. Environ. Saf.* **2017**, *136*, 119–125.
- (112) Feng, D.; Zhao, Y.; Zhang, Y.; Sun, S.; Meng, S.; Guo, Y.; Huang, Y. Effects of K and Ca on Reforming of Model Tar Compounds with Pyrolysis Biochars under H_2O or CO_2 . *Chem. Eng. J.* **2016**, *306*, 422–432.

- (113) Feng, D.; Zhang, Y.; Zhao, Y.; Sun, S.; Gao, J. Improvement and Maintenance of Biochar Catalytic Activity for In-Situ Biomass Tar Reforming during Pyrolysis and H₂O/CO₂ Gasification. *Fuel Process. Technol.* **2018**, *172*, 106–114.
- (114) Herath, I.; Kumarathilaka, P.; Al-Wabel, M. I.; Abduljabbar, A.; Ahmad, M.; Usman, A. R. A.; Vithanage, M. Mechanistic Modeling of Glyphosate Interaction with Rice Husk Derived Engineered Biochar. *Microporous mesoporous Mater.* **2016**, *225*, 280–288.
- (115) Feng, D.; Zhao, Y.; Zhang, Y.; Zhang, Z.; Zhang, L.; Gao, J.; Sun, S. Synergetic Effects of Biochar Structure and AAEM Species on Reactivity of H₂O-Activated Biochar from Cyclone Air Gasification. *Int. J. Hydrogen Energy* **2017**, *42* (25), 16045–16053.
- (116) Toles, C. A.; Marshall, W. E.; Wartelle, L. H.; McAloon, A. Steam-or Carbon Dioxide-Activated Carbons from Almond Shells: Physical, Chemical and Adsorptive Properties and Estimated Cost of Production. *Bioresour. Technol.* **2000**, *75* (3), 197–203.
- (117) Fan, M.; Marshall, W.; Daugaard, D.; Brown, R. C. Steam Activation of Chars Produced from Oat Hulls and Corn Stover. *Bioresour. Technol.* **2004**, *93* (1), 103–107.
- (118) Guo, S.; Peng, J.; Li, W.; Yang, K.; Zhang, L.; Zhang, S.; Xia, H. Effects of CO₂ Activation on Porous Structures of Coconut Shell-Based Activated Carbons. *Appl. Surf. Sci.* **2009**, *255* (20), 8443–8449.
- (119) Chu, G.; Zhao, J.; Chen, F.; Dong, X.; Zhou, D.; Liang, N.; Wu, M.; Pan, B.; Steinberg, C. E. W. Physi-Chemical and Sorption Properties of Biochars Prepared from Peanut Shell Using Thermal Pyrolysis and Microwave Irradiation. *Environ. Pollut.* **2017**, *227*, 372–379.
- (120) Chen, W.; Mattern, D. L.; Okinedo, E.; Senter, J. C.; Mattei, A. A.; Redwine, C. W. Photochemical and Acoustic Interactions of Biochar with CO₂ and H₂O: Applications in Power Generation and CO₂ Capture. *AIChE J.* **2014**, *60* (3), 1054–1065.
- (121) Gupta, R. K.; Dubey, M.; Kharel, P.; Gu, Z.; Fan, Q. H. Biochar Activated by Oxygen Plasma for Supercapacitors. *J. Power Sources* **2015**, *274*, 1300–1305.
- (122) Jung, K.-W.; Hwang, M.-J.; Jeong, T.-U.; Ahn, K.-H. A Novel Approach for Preparation of Modified-Biochar Derived from Marine Macroalgae: Dual Purpose Electro-Modification for Improvement of Surface Area and Metal Impregnation. *Bioresour. Technol.* **2015**, *191*, 342–345.
- (123) González-García, P. Activated Carbon from Lignocellulosics Precursors: A Review of the Synthesis Methods, Characterization Techniques and Applications. *Renew. Sustain. Energy Rev.* **2018**, *82*, 1393–1414.

- (124) Phiri, J.; Dou, J.; Vuorinen, T.; Gane, P. A. C.; Maloney, T. C. Highly Porous Willow Wood-Derived Activated Carbon for High-Performance Supercapacitor Electrodes. *ACS Omega* **2019**, 4 (19), 18108–18117.
- (125) Dai, J.; Tian, S.; Jiang, Y.; Chang, Z.; Xie, A.; Zhang, R.; Yan, Y. Facile Synthesis of Porous Carbon Sheets from Potassium Acetate via In-Situ Template and Self-Activation for Highly Efficient Chloramphenicol Removal. *J. Alloys Compd.* **2018**, 732, 222–232.
- (126) Lozano-Castelló, D.; Calo, J. M.; Cazorla-Amorós, D.; Linares-Solano, A. Carbon Activation with KOH as Explored by Temperature Programmed Techniques, and the Effects of Hydrogen. *Carbon N. Y.* **2007**, 45 (13), 2529–2536.
- (127) Fu, Y.; Shen, Y.; Zhang, Z.; Ge, X.; Chen, M. Activated Bio-Chars Derived from Rice Husk via One- and Two-Step KOH-Catalyzed Pyrolysis for Phenol Adsorption. *Sci. Total Environ.* **2019**, 646, 1567–1577.
- (128) Jagtoyen, M.; Derbyshire, F. Activated Carbons from Yellow Poplar and White Oak by H_3PO_4 Activation. *Carbon* **1998**, 36 (7–8), 1085–1097.
- (129) Elmouwahidi, A.; Bailón-García, E.; Pérez-Cadenas, A. F.; Maldonado-Hódar, F. J.; Carrasco-Marín, F. Activated Carbons from KOH and H_3PO_4 -Activation of Olive Residues and Its Application as Supercapacitor Electrodes. *Electrochim. Acta* **2017**, 229, 219–228.
- (130) Sevilla, M.; Valle-Vigón, P.; Fuertes, A. B. N-Doped Polypyrrole-Based Porous Carbons for CO_2 Capture. *Adv. Funct. Mater.* **2011**, 21 (14), 2781–2787.
- (131) Suárez-García, F.; Martínez-Alonso, A.; Tascón, J. M. D. Pyrolysis of Apple Pulp: Chemical Activation with Phosphoric Acid. *J. Anal. Appl. Pyrolysis* **2002**, 63 (2), 283–301.
- (132) Andas, J.; Wazil, N. From Waste Mango Kernel into High Surface Area Activated Carbon. *Mater. Today Proc.* **2019**, 19, 1541–1546.
- (133) Chiu, Y. H.; Lin, L. Y. Effect of Activating Agents for Producing Activated Carbon Using a Facile One-Step Synthesis with Waste Coffee Grounds for Symmetric Supercapacitors. *J. Taiwan Inst. Chem. Eng.* **2019**, 101, 177–185.
- (134) Heidari, A.; Younesi, H.; Rashidi, A.; Ghoreyshi, A. A. Adsorptive Removal of CO_2 on Highly Microporous Activated Carbons Prepared from Eucalyptus Camaldulensis Wood: Effect of Chemical Activation. *J. Taiwan Inst. Chem. Eng.* **2014**, 45 (2), 579–588.
- (135) Mazánek, V.; Luxa, J.; Matějková, S.; Kučera, J.; Sedmidubský, D.; Pumera, M.; Sofer, Z. Ultrapure Graphene Is a Poor Electrocatalyst: Definitive Proof of the Key Role of Metallic Impurities in Graphene-Based Electrocatalysis. *ACS Nano* **2019**, 13 (2), 1574–1582.

- (136) Asefa, T. Metal-Free and Noble Metal-Free Heteroatom-Doped Nanostructured Carbons as Prospective Sustainable Electrocatalysts. *Acc. Chem. Res.* **2016**, *49* (9), 1873–1883.
- (137) Wei, D.; Liu, Y.; Wang, Y.; Zhang, H.; Huang, L.; Yu, G. Synthesis of N-Doped Graphene by Chemical Vapor Deposition and Its Electrical Properties. *Nano Lett.* **2009**, *9* (5), 1752–1758.
- (138) Gao, K.; Wang, B.; Tao, L.; Cunnning, B. V.; Zhang, Z.; Wang, S.; Ruoff, R. S.; Qu, L. Efficient Metal-free Electrocatalysts from N-doped Carbon Nanomaterials: Mono-doping and Co-doping. *Adv. Mater.* **2019**, *31* (13), 1805121.
- (139) Leng, L.; Xu, S.; Liu, R.; Yu, T.; Zhuo, X.; Leng, S.; Xiong, Q.; Huang, H. Nitrogen Containing Functional Groups of Biochar: An Overview. *Bioresour. Technol.* **2020**, *298*, 122286.
- (140) Chu, B.; Amano, Y.; Machida, M. Preparation of Bean Dreg Derived N-Doped Activated Carbon with High Adsorption for Cr(VI). *Colloids Surfaces A Physicochem. Eng. Asp.* **2020**, *586*, 124262.
- (141) Guo, S.; Wang, Y.; Wei, X.; Gao, Y.; Xiao, B.; Yang, Y. Structural Analysis and Heavy Metal Adsorption of N-Doped Biochar from Hydrothermal Carbonization of Camellia Sinensis Waste. *Environ. Sci. Pollut. Res.* **2020**, *27* (15), 18866–18874.
- (142) Liang, J.; Tang, D.; Huang, L.; Chen, Y.; Ren, W.; Sun, J. High Oxygen Reduction Reaction Performance Nitrogen-Doped Biochar Cathode: A Strategy for Comprehensive Utilizing Nitrogen and Carbon in Water Hyacinth. *Bioresour. Technol.* **2018**, *267*, 524–531.
- (143) Yuan, X.; An, N.; Zhu, Z.; Sun, H.; Zheng, J.; Jia, M.; Lu, C.; Zhang, W.; Liu, N. Hierarchically Porous Nitrogen-Doped Carbon Materials as Efficient Adsorbents for Removal of Heavy Metal Ions. *Process Saf. Environ. Prot.* **2018**, *119*, 320–329.
- (144) Gao, Y.; Xu, S.; Yue, Q.; Ortaboy, S.; Gao, B.; Sun, Y. Synthesis and Characterization of Heteroatom-Enriched Biochar from Keratin-Based and Algous-Based Wastes. *Adv. Powder Technol.* **2016**, *27* (4), 1280–1286.
- (145) Marrakchi, F.; Auta, M.; Khanday, W. A.; Hameed, B. H. High-Surface-Area and Nitrogen-Rich Mesoporous Carbon Material from Fishery Waste for Effective Adsorption of Methylene Blue. *Powder Technol.* **2017**, *321*, 428–434.
- (146) Chen, T.; Deng, S.; Wang, B.; Huang, J.; Wang, Y.; Yu, G. CO₂ Adsorption on Crab Shell Derived Activated Carbons: Contribution of Micropores and Nitrogen-Containing Groups. *RSC Adv.* **2015**, *5* (60), 48323–48330.

- (147) Chen, W.; Fang, Y.; Li, K.; Chen, Z.; Xia, M.; Gong, M.; Chen, Y.; Yang, H.; Tu, X.; Chen, H. Bamboo Wastes Catalytic Pyrolysis with N-Doped Biochar Catalyst for Phenols Products. *Appl. Energy* **2020**, *260*, 114242.
- (148) Yu, W.; Lian, F.; Cui, G.; Liu, Z. N-Doping Effectively Enhances the Adsorption Capacity of Biochar for Heavy Metal Ions from Aqueous Solution. *Chemosphere* **2018**, *193*, 8–16.
- (149) Zheng, X.; Zhou, Y.; Liu, X.; Fu, X.; Peng, H.; Lv, S. Enhanced Adsorption Capacity of MgO/N-Doped Active Carbon Derived from Sugarcane Bagasse. *Bioresour. Technol.* **2020**, *297*, 122413.
- (150) Mian, M. M.; Liu, G.; Zhou, H. Preparation of N-Doped Biochar from Sewage Sludge and Melamine for Peroxymonosulfate Activation: N-Functionality and Catalytic Mechanisms. *Sci. Total Environ.* **2020**, *744*, 140862.
- (151) Lu, S.; Huang, X.; Tang, M.; Peng, Y.; Wang, S.; Makwarimba, C. P. Synthesis of N-Doped Hierarchical Porous Carbon with Excellent Toluene Adsorption Properties and Its Activation Mechanism. *Environ. Pollut.* **2021**, *284*, 117113.
- (152) Chen, J.; Yang, J.; Hu, G.; Hu, X.; Li, Z.; Shen, S.; Radosz, M.; Fan, M. Enhanced CO₂ Capture Capacity of Nitrogen-Doped Biomass-Derived Porous Carbons. *ACS Sustain. Chem. Eng.* **2016**, *4* (3), 1439–1445.
- (153) Zhou, H.; Li, X.; Jin, H.; She, D. Mechanism of a Double-Channel Nitrogen-Doped Lignin-Based Carbon on the Highly Selective Removal of Tetracycline from Water. *Bioresour. Technol.* **2022**, *346*, 126652.
- (154) Zhang, X.; Zhang, S.; Yang, H.; Feng, Y.; Chen, Y.; Wang, X.; Chen, H. Nitrogen Enriched Biochar Modified by High Temperature CO₂–Ammonia Treatment: Characterization and Adsorption of CO₂. *Chem. Eng. J.* **2014**, *257*, 20–27.
- (155) Singh, M. G.; Lakhi, K. S.; Park, D. H.; Srivastava, P.; Naidu, R.; Vinu, A. Facile One-Pot Synthesis of Activated Porous Biocarbons with a High Nitrogen Content for CO₂ Capture. *ChemNanoMat* **2018**, *4* (3), 281–290.
- (156) Tan, Y.; Wang, X.; Song, S.; Sun, M.; Xue, Y.; Yang, G. Preparation of Nitrogen-Doped Cellulose-Based Porous Carbon and Its Carbon Dioxide Adsorption Properties. *ACS Omega* **2021**, *6* (38), 24814–24825.
- (157) Chang, Y. M.; Tsai, W. T.; Li, M. H. Chemical Characterization of Char Derived from Slow Pyrolysis of Microalgal Residue. *J. Anal. Appl. Pyrolysis* **2015**, *111*, 88–93.

- (158) Chen, W.; Yang, H.; Chen, Y.; Xia, M.; Chen, X.; Chen, H. Transformation of Nitrogen and Evolution of N-Containing Species during Algae Pyrolysis. *Environ. Sci. Technol.* **2017**, *51* (11), 6570–6579.
- (159) Chen, W.; Yang, H.; Chen, Y.; Chen, X.; Fang, Y.; Chen, H. Biomass Pyrolysis for Nitrogen-Containing Liquid Chemicals and Nitrogen-Doped Carbon Materials. *J. Anal. Appl. Pyrolysis* **2016**, *120*, 186–193.
- (160) Duan, X.; Sun, H.; Wang, S. Metal-Free Carbocatalysis in Advanced Oxidation Reactions. *Acc. Chem. Res.* **2018**, *51* (3), 678–687.
- (161) Oh, W. Da; Lisak, G.; Webster, R. D.; Liang, Y. N.; Veksha, A.; Giannis, A.; Moo, J. G. S.; Lim, J. W.; Lim, T. T. Insights into the Thermolytic Transformation of Lignocellulosic Biomass Waste to Redox-Active Carbocatalyst: Durability of Surface Active Sites. *Appl. Catal. B Environ.* **2018**, *233*, 120–129.
- (162) Wang, X.; Liu, Y.; Zhu, L.; Li, Y.; Wang, K.; Qiu, K.; Tippayawong, N.; Aggarangsi, P.; Reubroycharoen, P.; Wang, S. Biomass Derived N-Doped Biochar as Efficient Catalyst Supports for CO₂ Methanation. *J. CO₂ Util.* **2019**, *34*, 733–741.
- (163) Zhou, Q.; Jiang, X.; Li, X.; Jia, C. Q.; Jiang, W. Preparation of High-Yield N-Doped Biochar from Nitrogen-Containing Phosphate and Its Effective Adsorption for Toluene. *RSC Adv.* **2018**, *8* (53), 30171–30179.
- (164) Li, D.; Chen, W.; Wu, J.; Jia, C. Q.; Jiang, X. The Preparation of Waste Biomass-Derived N-Doped Carbons and Their Application in Acid Gas Removal: Focus on N Functional Groups. *J. Mater. Chem. A* **2020**, *8* (47), 24977–24995.
- (165) Guo, L.; Yang, J.; Hu, G.; Hu, X.; Wang, L.; Dong, Y.; Dacosta, H.; Fan, M. Role of Hydrogen Peroxide Preoxidizing on CO₂ Adsorption of Nitrogen-Doped Carbons Produced from Coconut Shell. *ACS Sustain. Chem. Eng.* **2016**, *4* (5), 2806–2813.
- (166) Xu, X.; Zheng, Y.; Gao, B.; Cao, X. N-Doped Biochar Synthesized by a Facile Ball-Milling Method for Enhanced Sorption of CO₂ and Reactive Red. *Chem. Eng. J.* **2019**, *368*, 564–572.
- (167) Zhu, S.; Huang, X.; Ma, F.; Wang, L.; Duan, X.; Wang, S. Catalytic Removal of Aqueous Contaminants on N-Doped Graphitic Biochars: Inherent Roles of Adsorption and Nonradical Mechanisms. *Environ. Sci. Technol.* **2018**, *52* (15), 8649–8658.
- (168) Gao, W.; Lin, Z.; Chen, H.; Yan, S.; Huang, Y.; Hu, X.; Zhang, S. A Review on N-Doped Biochar for Enhanced Water Treatment and Emerging Applications. *Fuel Process. Technol.* **2022**, *237*, 107468.

- (169) Zeghioud, H.; Fryda, L.; Djelal, H.; Assadi, A.; Kane, A. A Comprehensive Review of Biochar in Removal of Organic Pollutants from Wastewater: Characterization, Toxicity, Activation/Functionalization and Influencing Treatment Factors. *J. Water Process Eng.* **2022**, *47*, 102801.
- (170) Zheng, Y.; Jiao, Y.; Zhu, Y.; Li, L. H.; Han, Y.; Chen, Y.; Du, A.; Jaroniec, M.; Qiao, S. Z. Hydrogen Evolution by a Metal-Free Electrocatalyst. *Nat. Commun.* **2014**, *5* (1), 1–8.
- (171) Zhu, G.; Ma, L.; Lv, H.; Hu, Y.; Chen, T.; Chen, R.; Liang, J.; Wang, X.; Wang, Y.; Yan, C.; Tie, Z.; Jin, Z.; Liu, J. Pine Needle-Derived Microporous Nitrogen-Doped Carbon Frameworks Exhibit High Performances in Electrocatalytic Hydrogen Evolution Reaction and Supercapacitors. *Nanoscale* **2017**, *9* (3), 1237–1243.
- (172) Saravanan, K. R. A.; Prabu, N.; Sasidharan, M.; Maduraiveeran, G. Nitrogen-Self Doped Activated Carbon Nanosheets Derived from Peanut Shells for Enhanced Hydrogen Evolution Reaction. *Appl. Surf. Sci.* **2019**, *489*, 725–733.
- (173) Prabu, N.; Saravanan, R. S. A.; Kesavan, T.; Maduraiveeran, G.; Sasidharan, M. An Efficient Palm Waste Derived Hierarchical Porous Carbon for Electrocatalytic Hydrogen Evolution Reaction. *Carbon* **2019**, *152*, 188–197.
- (174) Zhang, W.; Xi, R.; Li, Y.; Zhang, Y.; Wang, P.; Hu, D. Waste Silk Fabric Derived N-Doped Carbon as a Self-Supported Electrocatalyst for Hydrogen Evolution Reaction. *Colloids Surfaces A Physicochem. Eng. Asp.* **2023**, *658*, 130704.
- (175) Zhang, C.; Bhojate, S.; Hyatt, M.; Neria, B. L.; Siam, K.; Kahol, P. K.; Ghimire, M.; Mishra, S. R.; Perez, F.; Gupta, R. K. Nitrogen-Doped Flexible Carbon Cloth for Durable Metal Free Electrocatalyst for Overall Water Splitting. *Surf. Coatings Technol.* **2018**, *347*, 407–413.
- (176) Huang, B.; Liu, Y.; Xie, Z. Biomass Derived 2D Carbons via a Hydrothermal Carbonization Method as Efficient Bifunctional ORR/HER Electrocatalysts. *J. Mater. Chem. A* **2017**, *5* (45), 23481–23488.
- (177) Jiang, H.; Gu, J.; Zheng, X.; Liu, M.; Qiu, X.; Wang, L.; Li, W.; Chen, Z.; Ji, X.; Li, J. Defect-Rich and Ultrathin N Doped Carbon Nanosheets as Advanced Trifunctional Metal-Free Electrocatalysts for the ORR, OER and HER. *Energy Environ. Sci.* **2019**, *12* (1), 322–333.
- (178) Yang, M.; Zhang, Y.; Jian, J.; Fang, L.; Li, J.; Fang, Z.; Yuan, Z.; Dai, L.; Chen, X.; Yu, D. Donor–Acceptor Nanocarbon Ensembles to Boost Metal-Free All-PH Hydrogen Evolution Catalysis by Combined Surface and Dual Electronic Modulation. *Angew. Chemie Int. Ed.* **2019**, *58* (45), 16217–16222.

- (179) Hu, C.; Dai, L.; Hu, C.; Dai, L. Multifunctional Carbon-Based Metal-Free Electrocatalysts for Simultaneous Oxygen Reduction, Oxygen Evolution, and Hydrogen Evolution. *Adv. Mater.* **2017**, *29* (9), 1604942.
- (180) Lu, S.; Cheng, C.; Shi, Y.; Wu, Y.; Zhang, Z.; Zhang, B. Unveiling the Structural Transformation and Activity Origin of Heteroatom-Doped Carbons for Hydrogen Evolution. *Proc. Natl. Acad. Sci. U. S. A.* **2023**, *120* (20), e2300549120.
- (181) Oates, R. P.; Murawski, J.; Hor, C.; Shen, X.; Weber, D. J.; Oezaslan, M.; Shaffer, M. S. P.; Stephens, I. E. L. How to Minimise Hydrogen Evolution on Carbon Based Materials? *J. Electrochem. Soc.* **2022**, *169* (5), 54516.
- (182) Deng, L.; Zhang, Y.; Wang, Y.; Yuan, H.; Chen, Y.; Wu, Y. In Situ N-, P- and Ca-Codoped Biochar Derived from Animal Bones to Boost the Electrocatalytic Hydrogen Evolution Reaction. *Resour. Conserv. Recycl.* **2021**, *170*, 105568.
- (183) Wang, Q.; Guo, R.; Wang, Z.; Shen, D.; Yu, R.; Luo, K.; Wu, C.; Gu, S. Progress in Carbon-Based Electrocatalyst Derived from Biomass for the Hydrogen Evolution Reaction. *Fuel* **2021**, *293*, 120440.
- (184) Kulkarni, A.; Siahrostami, S.; Patel, A.; Nørskov, J. K. Understanding Catalytic Activity Trends in the Oxygen Reduction Reaction. *Chem. Rev.* **2018**, *118* (5), 2302–2312.
- (185) Borghei, M.; Lehtonen, J.; Liu, L.; Rojas, O. J. Advanced Biomass-Derived Electrocatalysts for the Oxygen Reduction Reaction. *Adv. Mater.* **2018**, *30* (24), 1–27.
- (186) Chen, P.; Wang, L.-K.; Wang, G.; Gao, M.-R.; Ge, J.; Yuan, W.-J.; Shen, Y.-H.; Xie, A.-J.; Yu, S.-H. Nitrogen-Doped Nanoporous Carbon Nanosheets Derived from Plant Biomass: An Efficient Catalyst for Oxygen Reduction Reaction. *Energy Environ. Sci.* **2014**, *7* (12), 4095–4103.
- (187) Liu, X.; Zhou, Y.; Zhou, W.; Li, L.; Huang, S.; Chen, S. Biomass-Derived Nitrogen Self-Doped Porous Carbon as Effective Metal-Free Catalysts for Oxygen Reduction Reaction. *Nanoscale* **2015**, *7* (14), 6136–6142.
- (188) Ouyang, C.; Wang, X. Recent Progress in Pyrolyzed Carbon Materials as Electrocatalysts for the Oxygen Reduction Reaction. *Inorg. Chem. Front.* **2019**, *7* (1), 28–36.
- (189) Li, D.; Fan, Y.; Yuan, H.; Deng, L.; Yang, J.; Chen, Y.; Luo, B. Renewable and Metal-Free Carbon Derived from Aquatic Scindapsus Affording Meso-Microporosity, Large Interface, and Enriched Pyridinic-N for Efficient Oxygen Reduction Reaction Catalysis. *Energy and Fuels* **2020**, *34* (10), 13089–13095.

- (190) Gabe, A.; Ruiz-Rosas, R.; González-Gaitán, C.; Morallón, E.; Cazorla-Amorós, D. Modeling of Oxygen Reduction Reaction in Porous Carbon Materials in Alkaline Medium. Effect of Microporosity. *J. Power Sources* **2019**, *412*, 451–464.
- (191) Quílez-Bermejo, J.; Morallón, E.; Cazorla-Amorós, D. On the Deactivation of N-Doped Carbon Materials Active Sites during Oxygen Reduction Reaction. *Carbon* **2022**, *189*, 548–560.
- (192) Quílez-Bermejo, J.; Pérez-Rodríguez, S.; Canevesi, R.; Torres, D.; Morallón, E.; Cazorla-Amorós, D.; Celzard, A.; Fierro, V. Easy Enrichment of Graphitic Nitrogen to Prepare Highly Catalytic Carbons for Oxygen Reduction Reaction. *Carbon* **2022**, *196*, 708–717.
- (193) Miao, H.; Li, S.; Wang, Z.; Sun, S.; Kuang, M.; Liu, Z.; Yuan, J. Enhancing the Pyridinic N Content of Nitrogen-Doped Graphene and Improving Its Catalytic Activity for Oxygen Reduction Reaction. *Int. J. Hydrogen Energy* **2017**, *42* (47), 28298–28308.
- (194) Wu, J.; Ma, L.; Yadav, R. M.; Yang, Y.; Zhang, X.; Vajtai, R.; Lou, J.; Ajayan, P. M. Nitrogen-Doped Graphene with Pyridinic Dominance as a Highly Active and Stable Electrocatalyst for Oxygen Reduction. *ACS Appl. Mater. Interfaces* **2015**, *7* (27), 14763–14769.
- (195) Guo, D.; Shibuya, R.; Akiba, C.; Saji, S.; Kondo, T.; Nakamura, J. Active Sites of Nitrogen-Doped Carbon Materials for Oxygen Reduction Reaction Clarified Using Model Catalysts. *Science* **2016**, *351* (6271), 361–365.
- (196) Lai, L.; Potts, J. R.; Zhan, D.; Wang, L.; Poh, C. K.; Tang, C.; Gong, H.; Shen, Z.; Lin, J.; Ruoff, R. S. Exploration of the Active Center Structure of Nitrogen-Doped Graphene-Based Catalysts for Oxygen Reduction Reaction. *Energy Environ. Sci.* **2012**, *5* (7), 7936–7942.
- (197) Liu, J.; Song, P.; Xu, W. Structure-Activity Relationship of Doped-Nitrogen (N)-Based Metal-Free Active Sites on Carbon for Oxygen Reduction Reaction. *Carbon* **2017**, *115*, 763–772.
- (198) Luo, Z.; Lim, S.; Tian, Z.; Shang, J.; Lai, L.; MacDonald, B.; Fu, C.; Shen, Z.; Yu, T.; Lin, J. Pyridinic N Doped Graphene: Synthesis, Electronic Structure, and Electrocatalytic Property. *J. Mater. Chem.* **2011**, *21* (22), 8038–8044.
- (199) Tao, L.; Wang, Q.; Dou, S.; Ma, Z.; Huo, J.; Wang, S.; Dai, L. Edge-Rich and Dopant-Free Graphene as a Highly Efficient Metal-Free Electrocatalyst for the Oxygen Reduction Reaction. *Chem. Commun.* **2016**, *52* (13), 2764–2767.
- (200) Wang, X.; Jia, Y.; Mao, X.; Zhang, L.; Liu, D.; Song, L.; Yan, X.; Chen, J.; Yang, D.; Zhou, J.; Wang, K.; Du, A.; Yao, X. A Directional Synthesis for Topological Defect in Carbon. *Chem* **2020**, *6* (8), 2009–2023.

- (201) Gao, H.; Wang, S.; Cheong, W. C. (Max); Wang, K.; Xu, H.; Huang, A.; Ma, J.; Li, J.; Ip, W. F. (Andy); San Hui, K.; Dinh, D. A.; Fan, X.; Bin, F.; Chen, F.; Hui, K. N. Topological Defect and Sp^3/Sp^2 Carbon Interface Derived from ZIF-8 with Linker Vacancies for Oxygen Reduction Reaction. *Carbon* **2023**, 203, 76–87.
- (202) Kumar, B.; Asadi, M.; Pisasale, D.; Sinha-Ray, S.; Rosen, B. A.; Haasch, R.; Abiade, J.; Yarin, A. L.; Salehi-Khojin, A. Renewable and Metal-Free Carbon Nanofibre Catalysts for Carbon Dioxide Reduction. *Nat. Commun.* **2013**, 4, 1–8.
- (203) Song, Y.; Chen, W.; Zhao, C.; Li, S.; Wei, W.; Sun, Y. Metal-Free Nitrogen-Doped Mesoporous Carbon for Electroreduction of CO_2 to Ethanol. *Angew. Chemie - Int. Ed.* **2017**, 56 (36), 10840–10844.
- (204) Wu, J.; Ma, S.; Sun, J.; Gold, J. I.; Tiwary, C.; Kim, B.; Zhu, L.; Chopra, N.; Odeh, I. N.; Vajtai, R. A Metal-Free Electrocatalyst for Carbon Dioxide Reduction to Multi-Carbon Hydrocarbons and Oxygenates. *Nat. Commun.* **2016**, 7 (1), 1–6.
- (205) Li, F.; Xue, M.; Knowles, G. P.; Chen, L.; MacFarlane, D. R.; Zhang, J. Porous Nitrogen-Doped Carbon Derived from Biomass for Electrocatalytic Reduction of CO_2 to CO. *Electrochim. Acta* **2017**, 245, 561–568.
- (206) Yao, P.; Qiu, Y.; Zhang, T.; Su, P.; Li, X.; Zhang, H. N-Doped Nanoporous Carbon from Biomass as a Highly Efficient Electrocatalyst for the CO_2 Reduction Reaction. *ACS Sustain. Chem. Eng.* **2019**, 7(5), 5249–5255.
- (207) Zhang, H.; Min, S.; Wang, F.; Zhang, Z.; Kong, C. Efficient Electrocatalytic CO_2 Reduction to CO with High Selectivity Using a N-Doped Carbonized Wood Membrane. *New J. Chem.* **2020**, 44 (16), 6125–6129.
- (208) Hao, X.; An, X.; Patil, A. M.; Wang, P.; Ma, X.; Du, X.; Hao, X.; Abudula, A.; Guan, G. Biomass-Derived N-Doped Carbon for Efficient Electrocatalytic CO_2 Reduction to CO and Zn- CO_2 Batteries. *ACS Appl. Mater. Interfaces* **2021**, 13(3), 3738–3747.
- (209) Li, W.; Herkt, B.; Seredych, M.; Bandoz, T. J. Pyridinic-N Groups and Ultramicropore Nanoreactors Enhance CO_2 Electrochemical Reduction on Porous Carbon Catalysts. *Appl. Catal. B Environ.* **2017**, 207, 195–206.
- (210) Li, H.; Xiao, N.; Hao, M.; Song, X.; Wang, Y.; Ji, Y.; Liu, C.; Li, C.; Guo, Z.; Zhang, F.; Qiu, J. Efficient CO_2 Electroreduction over Pyridinic-N Active Sites Highly Exposed on Wrinkled Porous Carbon Nanosheets. *Chem. Eng. J.* **2018**, 351, 613–621.

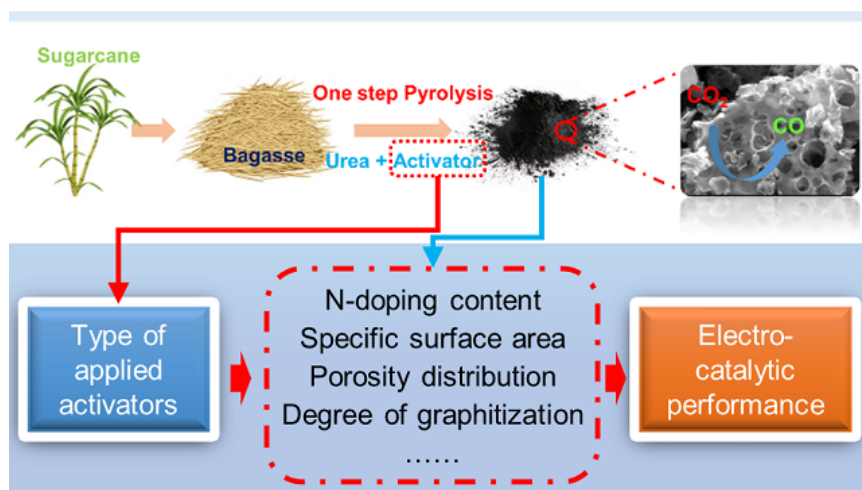
- (211) Ma, C.; Hou, P.; Wang, X.; Wang, Z.; Li, W.; Kang, P. Carbon Nanotubes with Rich Pyridinic Nitrogen for Gas Phase CO₂ Electroreduction. *Appl. Catal. B Environ.* **2019**, *250*, 347–354.
- (212) Zhang, Z.; Yu, L.; Tu, Y.; Chen, R.; Wu, L.; Zhu, J.; Deng, D. Unveiling the Active Site of Metal-Free Nitrogen-Doped Carbon for Electrocatalytic Carbon Dioxide Reduction. *Cell Reports Phys. Sci.* **2020**, *1* (8), 100145.
- (213) Cui, X.; Pan, Z.; Zhang, L.; Peng, H.; Zheng, G. Selective Etching of Nitrogen-Doped Carbon by Steam for Enhanced Electrochemical CO₂ Reduction. *Adv. Energy Mater.* **2017**, *7* (22), 1701456.
- (214) Liu, Y.; Zhao, J.; Cai, Q. Pyrrolic-Nitrogen Doped Graphene: A Metal-Free Electrocatalyst with High Efficiency and Selectivity for the Reduction of Carbon Dioxide to Formic Acid: A Computational Study. *Phys. Chem. Chem. Phys.* **2016**, *18* (7), 5491–5498.
- (215) Vasileff, A.; Zheng, Y.; Qiao, S. Z. Carbon Solving Carbon's Problems: Recent Progress of Nanostructured Carbon-Based Catalysts for the Electrochemical Reduction of CO₂. *Adv. Energy Mater.* **2017**, *7* (21), 1–21.
- (216) Daiyan, R.; Tan, X.; Chen, R.; Saputera, W. H.; Tahini, H. A.; Lovell, E.; Ng, Y. H.; Smith, S. C.; Dai, L.; Lu, X.; Amal, R. Electroreduction of CO₂ to CO on a Mesoporous Carbon Catalyst with Progressively Removed Nitrogen Moieties. *ACS Energy Lett.* **2018**, *3* (9), 2292–2298.
- (217) Gadipelli, S.; Howard, C. A.; Guo, J.; Skipper, N. T.; Zhang, H.; Shearing, P. R.; Brett, D. J. L.; Gadipelli, S.; Zhang, H.; Shearing, R.; Brett, D. J. L.; Howard, C. A.; Skipper, N. T. Superior Multifunctional Activity of Nanoporous Carbons with Widely Tunable Porosity: Enhanced Storage Capacities for Carbon-Dioxide, Hydrogen, Water, and Electric Charge. *Adv. Energy Mater.* **2020**, *10* (9), 1903649.
- (218) Zhang, Z.; Schott, J. A.; Liu, M.; Chen, H.; Lu, X.; Sumpter, B. G.; Fu, J.; Dai, S. Prediction of Carbon Dioxide Adsorption via Deep Learning. *Angew. Chemie Int. Ed.* **2019**, *58* (1), 259–263.
- (219) Hursán, D.; Samu, A. A.; Janovák, L.; Artyushkova, K.; Asset, T.; Atanassov, P.; Janáky, C. Morphological Attributes Govern Carbon Dioxide Reduction on N-Doped Carbon Electrodes. *Joule* **2019**, *3* (7), 1719–1733.
- (220) To, J. W. F.; Chen, Z.; Yao, H.; He, J.; Kim, K.; Chou, H. H.; Pan, L.; Wilcox, J.; Cui, Y.; Bao, Z. Ultrahigh Surface Area Three-Dimensional Porous Graphitic Carbon from Conjugated Polymeric Molecular Framework. *ACS Cent. Sci.* **2015**, *1* (2), 68–76.

- (221) Fu, S.; Li, M.; Asperti, S.; Jong, W. de; Kortlever, R. Unravelling the Effect of Activators Used in The Synthesis of Biomass-Derived Carbon Electrocatalysts on the Electrocatalytic Performance for CO₂ Reduction. *ChemSusChem* **2023**, e202202188.
- (222) Varela, A. S.; Ju, W.; Bagger, A.; Franco, P.; Rossmeisl, J.; Strasser, P. Electrochemical Reduction of CO₂ on Metal-Nitrogen-Doped Carbon Catalysts. *ACS Catal.* **2019**, *9* (8), 7270–7284.
- (223) Yang, K.; Kas, R.; Smith, W. A.; Burdyny, T. Role of the Carbon-Based Gas Diffusion Layer on Flooding in a Gas Diffusion Electrode Cell for Electrochemical CO₂ Reduction. *ACS Energy Lett.* **2021**, *6* (1), 33–40.
- (224) Becker, H.; Murawski, J.; Shinde, D. V.; Stephens, I. E. L.; Hinds, G.; Smith, G. Impact of Impurities on Water Electrolysis: A Review. *Sustain. Energy Fuels* **2023**, *7* (7), 1565–1603.
- (225) Wang, L.; Sofer, Z.; Pumera, M. Will Any Crap We Put into Graphene Increase Its Electrocatalytic Effect? *ACS Nano* **2020**, *14* (1), 21–25.
- (226) Xu, Q.; Li, H.; Shi, Y.; Bi, Z.; Wu, Y. Density Functional Theory Studies of Doping and Curvature Effects on the Electrocatalytic Hydrogen Evolution Activity of Carbon Nanotubes. *ACS Appl. Nano Mater.* **2021**, *4* (1), 600–611.
- (227) Cepitis, R.; Kongi, N.; Rossmeisl, J.; Ivaništšev, V. Surface Curvature Effect on Dual-Atom Site Oxygen Electrocatalysis. *ACS Energy Lett.* **2023**, *8* (3), 1330–1335.
- (228) Kronberg, R.; Lappalainen, H.; Laasonen, K. Revisiting the Volmer–Heyrovský Mechanism of Hydrogen Evolution on a Nitrogen Doped Carbon Nanotube: Constrained Molecular Dynamics versus the Nudged Elastic Band Method. *Phys. Chem. Chem. Phys.* **2020**, *22* (19), 10536–10549.
- (229) Orndorff, P. B.; Le Phan, S. T.; Li, K. H.; Van Der Vaart, A. Conformational Free-Energy Differences of Large Solvated Systems with the Focused Confinement Method. *J. Chem. Theory Comput.* **2020**, *16* (8), 5163–5173.
- (230) Daems, N.; Sheng, X.; Vankelecom, I. F. J.; Pescarmona, P. P. Metal-Free Doped Carbon Materials as Electrocatalysts for the Oxygen Reduction Reaction. *J. Mater. Chem. A* **2014**, *2* (12), 4085–4110.
- (231) Ayiania, M.; Smith, M.; Hensley, A. J. R.; Scudiero, L.; McEwen, J. S.; Garcia-Perez, M. Deconvoluting the XPS Spectra for Nitrogen-Doped Chars: An Analysis from First Principles. *Carbon* **2020**, *162*, 528–544.
- (232) Osterrieth, J. W. M.; Rampersad, J.; Madden, D.; Rampal, N.; Skoric, L.; Connolly, B.; Allendorf, M. D.; Stavila, V.; Snider, J. L.; Ameloot, R.; Marreiros, J.; Ania, C.; Azevedo, D.;

Vilarrasa-Garcia, E.; Santos, B. F.; Bu, X. H.; Chang, Z.; Bunzen, H.; Champness, N. R.; Griffin, S. L.; Chen, B.; Lin, R. B.; Coasne, B.; Cohen, S.; Moreton, J. C.; Colón, Y. J.; Chen, L.; Clowes, R.; Coudert, F. X.; Cui, Y.; Hou, B.; D'Alessandro, D. M.; Doheny, P. W.; Dincă, M.; Sun, C.; Doonan, C.; Huxley, M. T.; Evans, J. D.; Falcaro, P.; Ricco, R.; Farha, O.; Idrees, K. B.; Islamoglu, T.; Feng, P.; Yang, H.; Forgan, R. S.; Bara, D.; Furukawa, S.; Sanchez, E.; Gascon, J.; Telalović, S.; Ghosh, S. K.; Mukherjee, S.; Hill, M. R.; Sadiq, M. M.; Horcajada, P.; Salcedo-Abraira, P.; Kaneko, K.; Kukobat, R.; Kevin, J.; Keskin, S.; Kitagawa, S.; Otake, K. ichi; Lively, R. P.; DeWitt, S. J. A.; Llewellyn, P.; Lotsch, B. V.; Emmerling, S. T.; Pütz, A. M.; Martí-Gastaldo, C.; Padial, N. M.; García-Martínez, J.; Linares, N.; MasPOCH, D.; Suárez del Pino, J. A.; Moghadam, P.; Oktavian, R.; Morris, R. E.; Wheatley, P. S.; Navarro, J.; Petit, C.; Danaci, D.; Rosseinsky, M. J.; Katsoulidis, A. P.; Schröder, M.; Han, X.; Yang, S.; Serre, C.; Mouchaham, G.; Sholl, D. S.; Thyagarajan, R.; Siderius, D.; Snurr, R. Q.; Goncalves, R. B.; Telfer, S.; Lee, S. J.; Ting, V. P.; Rowlandson, J. L.; Uemura, T.; Iiyuka, T.; van der Veen, M. A.; Rega, D.; Van Speybroeck, V.; Rogge, S. M. J.; Lamaire, A.; Walton, K. S.; Bingel, L. W.; Wuttke, S.; Andreo, J.; Yaghi, O.; Zhang, B.; Yavuz, C. T.; Nguyen, T. S.; Zamora, F.; Montoro, C.; Zhou, H.; Kirchon, A.; Fairen-Jimenez, D. How Reproducible Are Surface Areas Calculated from the BET Equation? *Adv. Mater.* **2022**, *34* (27), 2201502.

3

Unravelling the effect of activators used in the synthesis of biomass-derived carbon electrocatalysts on the electrocatalytic performance for CO₂ reduction



Abstract: N-doped carbon materials can be efficient and cost-effective catalysts for the electrochemical CO₂ reduction reaction (CO₂RR). Activators are often used in the synthesis process to increase the specific surface area and porosity of these carbon materials. However, due to the diversity of activators and the differences in physicochemical properties that these activators induce, the influence of activators used for the synthesis of N-doped carbon catalysts on their electrochemical performance is unclear. Here, we prepare a series of bagasse-derived N-doped carbon catalysts with the assistance of different activators to understand the correlation between the activators, physicochemical properties, and the electrocatalytic performance for the CO₂RR. We show that the properties of N-doped carbon catalysts, for instance, the N-doping content, microstructures, and the degree of graphitization, are highly dependent on the type of activator applied in the synthesis procedure. Moreover, we demonstrate that the overall performance of the CO₂RR on the synthesized electrocatalysts is not only determined by the N-doping level and the configuration of N-dopant, but rather by the overall surface chemistry, where the porosity and the degree of graphitization are jointly responsible for significant differences in CO₂RR performance.

3.1 Introduction

The electrochemical CO₂ reduction reaction (CO₂RR) is a promising approach to close the carbon cycle and convert CO₂ into value-added chemicals and fuels.^{1–3} This process can be driven by renewable electricity sources such as solar and wind and conducted at ambient conditions, making it an attractive option for energy storage and the electrification of the chemical industry.⁴ However, the thermodynamic stability of CO₂ and the competition with the hydrogen evolution reaction (HER), taking place in the same potential window as the CO₂RR in aqueous electrolytes, hinders the development of the CO₂RR.⁵ Challenges that need to be overcome include slow kinetics, high overpotentials for the formation of products and low product selectivities.^{6–8} Thus, developing more efficient and selective electrocatalysts for the CO₂RR is highly desired. Various metal-based CO₂RR electrocatalysts, containing for instance Ag,⁹ Au,¹⁰ Pd,¹¹ Pt,¹² Zn,¹³ Sn,¹⁴ and Cu,^{15,16} have been extensively studied in the past few decades. Although some advanced metal-based catalysts exhibit very high product selectivity and impressive overall catalytic performances, their relatively high cost, limited availability, and poor stability hinder large-scale applications.^{17,18} Therefore, the development of sustainable low-cost catalysts is crucial.

Metal-free carbon-based electrocatalysts, especially nitrogen-doped carbon materials, have attracted increasing attention recently owing to their interesting properties. These materials have a relatively low price, high conductivity, high stability, strong tolerance to impurities and a good structure tenability.^{18–21} N-doped carbon materials have been used as catalysts for the CO₂RR to produce CO,^{22–24} CH₄,²⁵ HCOOH,^{26,27} and even multi-carbon products such as ethanol.²⁸ However, most of these carbon materials are derived from fossil feedstocks and their production processes are energy-intensive with generally low yields. Moreover, the harsh synthesis conditions to prepare these materials hamper the scale-up needed for industrial utilization.²⁹

Biochar, carbon derived from biomass carbonization, can be a sustainable source to prepare cost-effective carbonaceous catalysts.^{30,31} Additionally, the unique natural microstructures and specific chemical compositions of biomass precursors endow the derived carbon materials with ingenious porous structures, high surface areas, abundant defect sites, and heteroatom doping that can improve the electrocatalytic performance.^{32–34} Additional heteroatom doping and the use of activators, to respectively provide more active sites and enlarge the specific surface area and porosity are often part of the preparation procedure to produce biomass-derived carbon electrocatalysts.³⁵ Biomass-derived N-doped carbon materials have already been demonstrated as effective electrocatalysts for the oxygen reduction reaction (ORR),^{36,37} whereas a limited amount of studies report on their performance for the CO₂RR. Li et al.³⁸ prepared a porous N-doped carbon electrocatalyst from wheat flour carbonization, using KOH as activator, showing CO₂

reduction to CO with a maximum faradaic efficiency (FE) of 83.7% at -0.82 V vs. RHE. Hao et al.³⁹ synthesized a cedar wood biomass-derived three-dimensional (3D) N-doped graphitized carbon electrocatalyst, using an FeCl₃ activator, that achieved a 91% FE toward CO at -0.56 V vs. RHE.

The activation process has been shown to significantly affect the textural properties of carbon catalysts, such as the specific surface area, porosity, N-doping content and the degree of graphitization. Most of the studies investigating activated N-doped carbon electrocatalysts attribute the electrocatalytic performances to the larger specific area and higher N-doping content.⁴⁰ However, the effect of other structural properties, such as the porosity and the degree of graphitization, have been largely overlooked. A comprehensive analysis that couples the physicochemical properties of N-doped carbon electrocatalysts after the activation process with the resultant electrochemical performances is therefore highly desired. However, currently there is no systematic study linking the effects of activators used in the preparation of biomass-derived carbon electrocatalysts for the CO₂RR to the electrocatalytic performance.

Here, we report a series of systematic experiments to unravel the effect different activators have on the CO₂RR performance of biomass-derived N-doped carbon materials. In this study, we are not aiming to develop a robust catalyst with impressive performance but aim to understand how the applied activator influences the properties of the N-doped carbon and subsequently influences the electrochemical performance. Sugarcane bagasse was selected as the carbon precursor, as it is an abundantly available and easily collected biomass residue from sugar production. Various N-doped porous carbon catalysts were synthesized with the assistance of urea as nitrogen source and different activators, KOH, KHCO₃, K₂CO₃, NaOH, NaHCO₃, and Mg₅(OH)₂(CO₃)₄, using a one-step pyrolysis method. We show that the activators play a critical role during the carbonization process, and the choice of activator significantly affects the resulting electrocatalytic performance of the material for the CO₂RR. The best biomass-derived catalyst exhibited a maximum FE_{CO} of 80% and a partial current density j_{CO} of -2.31 mA/cm² at -0.93 V vs. RHE, whereas the worst catalyst has a very limited activity for the CO₂RR, only displaying a FE_{CO} of 6.9% with a j_{CO} of less than -0.01 mA/cm². Combining the results of the physicochemical characterization with the electrochemical performance, we find that the overall CO₂RR performance is not only dominated by the N-doping level, but is also dependent on the interplay of the microstructure and the degree of graphitization of the material.

3.2 Experimental Section

3.2.1 Materials and chemicals

Sugarcane bagasse, which mainly consists of lignocellulose, was collected from a sugarcane processing factory (India, Maharashtra). The abundant natural vascular fiber bundles in bagasse make it a good precursor to prepare the porous carbon materials. The material was milled and sieved to obtain a particle size class smaller than 425 μm and dried overnight at 105 $^{\circ}\text{C}$ in an oven (BINDER, Model E28). In this work, urea was used as an additive N source to provide additional nitrogen doping.

The activators, such as potassium carbonate (K_2CO_3 , 99%), potassium bicarbonate (KHCO_3 , 99.7%), potassium hydroxide (KOH, 98%), sodium bicarbonate (NaHCO_3 , 99.7%), sodium hydroxide (NaOH, 98%), magnesium carbonate hydroxide pentahydrate ($\text{Mg}_5(\text{OH})_2(\text{CO}_3)_4 \cdot 5\text{H}_2\text{O}$, Bioextra), and the auxiliary chemicals, such as hydrochloric acid (HCl, 37%), urea ($\text{CN}_2\text{H}_4\text{O}$, 99%), isopropanol ($\text{C}_3\text{H}_8\text{O}$, 99.9%) and Nafion perfluorinated resin solution (5 wt.% in lower aliphatic alcohols and 15-20 % water) were all purchased from Sigma-Aldrich. Glassy carbon plates polished to a mirror-like finish were purchased from HTW Hochtemperatur-Werkstoffe GmbH (Germany) and used as working electrodes. All chemicals were used as received without further purification. Electrolyte solutions and 1 M HCl solutions were prepared from ultrapure water (Milli-Q IQ 7000, 18.2 M Ω).

3.2.2 Catalyst preparation

The activated N-doped porous carbon catalysts were prepared using a one-step pyrolysis method. Bagasse (5 g), urea (10 g), and one of the earlier mentioned activators (15 g) were fully mixed with a weight ratio of 1:2:3 and subsequently loaded into a crucible for pyrolysis. The mixtures were carbonized in a muffle furnace (Nabertherm, Model: L9/12/B180, Germany) under a nitrogen atmosphere (N_2 , Linde, 99.99%) with a flow rate of 100 mL/min and a heating rate of 10 $^{\circ}\text{C}/\text{min}$ from ambient temperature to 800 $^{\circ}\text{C}$, holding the temperature at 800 $^{\circ}\text{C}$ for 1h. Subsequently, the pyrolyzed carbon materials were washed with a 1 M HCl solution to remove any impurities and washed with ultrapure water until the solution reached a neutral pH. Finally, the activated N-doped carbon catalysts were dried at 105 $^{\circ}\text{C}$ for 12h in an oven. The obtained biomass-derived carbon catalysts were marked as ANBC1 (NaHCO_3), ANBC2 (K_2CO_3), ANBC3 ($\text{Mg}_5(\text{OH})_2(\text{CO}_3)_4$), ANBC4 (NaOH), ANBC5 (KOH) and ANBC6 (KHCO_3), respectively.

For comparison, the original biomass-derived carbon (without urea and activator) and pure N-doped carbon (mixed with urea but without any activator) were prepared using the same procedure, and named BC and NBC, respectively.

3.2.3 Catalyst characterization

The morphology and microstructures of all carbon catalysts were visualized with a JEOL JSM-6500F scanning electron microscope (SEM), operating at an acceleration voltage of 15 kV and equipped with an Energy-Dispersive X-ray Spectroscopy (EDX) detector (UltraDry, ThermoScientific, USA), and a JEOL JEM1400 transmission electron microscope (TEM), operating at a voltage of 120 kV. The pore characteristics of all samples were measured by isothermal N₂ adsorption-desorption at 77 K using a Micromeritics TriStar II 3020 instrument. The samples were outgassed at 300 °C for 15 h before each adsorption test. The specific surface area (S_{BET}) was calculated according to the Brunauer-Emmett-Teller (BET) method and the estimation of pore size distribution plots were generated by applying Density Functional Theory (DFT) modelling. The surface area (S_{micro}) and volume (V_{micro}) of micropores were determined by the t-plot method. The total pore volume (V_{total}) was calculated by single-point adsorption total pore volume analysis. The average pore diameter (D_{avg}) was obtained as $4V/S_{\text{BET}}$.

X-ray powder diffraction (XRD) measurements were carried out using a Bruker AXS D2 Phaser. The diffractometer was operated in Bragg-Brentano diffraction mode, with Cu K α radiation at 30 kV and 10 mA. The scanning 2θ angle range was between 10.0° and 90.0° using a step length of 0.020°. Raman spectra were recorded from 1000 to 2000 cm⁻¹ on a Horiba Scientific LabRAM HR Evolution Raman Spectroscopy system with an excitation wavelength of 514 nm.

The surface chemical compositions of all carbon catalysts were investigated by X-ray photoelectron spectroscopy (XPS) using a Thermo Scientific K α system with Al K α radiation (1486.7 eV). Survey scans were performed with a spot size of 200 μm , pass energy of 55 eV, and energy step of 0.1 eV. All binding energies for XPS spectra were calibrated according to the C1s peak at 284.8 eV in CasaXPS.

3.2.4 Electrochemical measurements

The electrochemical performance of different catalysts were evaluated in a gas-tight two-compartment flow cell, where the anode and cathode compartment were separated by a Selemion AMV membrane (AGC group, Japan).⁸⁵ Each compartment contained 1.8 mL of 0.1 M KHCO₃ electrolyte. A platinum foil (MaTeck GmbH, 99.9%) was used as a counter electrode, while a leak-free Ag/AgCl electrode (Innovative Instruments, Inc.) was used as a reference electrode. The cathode chamber of the cell was purged using CO₂ or Ar, depending on the experiment, with a flow rate of 8 mL/min for at least 15 min before the electrochemical test.

The working electrode was prepared by drop casting a catalyst ink on a glassy carbon substrate. The catalyst ink was prepared by dispersing 4 mg of catalyst powder in a solvent

mixture containing 800 μL deionized water, 150 μL isopropanol, and 50 μL of 5% Nafion solution with sonication for 1h to obtain a homogeneous ink. Afterwards, 200 μL of the ink was drop-casted on the center of the 25mm \times 25mm glassy carbon plate and dried at room temperature. The geometric surface area of the working electrode exposed to the electrolyte was equal to 1 cm^2 .

The electrochemical measurements were carried out using a Biologic SP-200 potentiostat (Biologic, France), equipped with the software EC-lab (Biologic, France). All applied potentials were converted to the reversible hydrogen electrode (RHE) scale according to the formula: $E \text{ (V vs. RHE)} = E \text{ (V vs. Ag/AgCl)} + 0.197 + 0.059 \cdot \text{pH}$. The cell resistance (R_u) was measured by potentiostatic electrochemical impedance spectroscopy (PEIS). 85% of R_u was used to conduct the Ohmic Drop Correction automatically with EC-Lab during CO_2RR , while the remaining 15% was corrected manually afterwards. Linear sweep voltammograms (LSV) were recorded in Ar-saturated ($\text{pH} = 8.3$) and CO_2 -saturated ($\text{pH} = 6.8$) 0.1 M KHCO_3 electrolytes at a scan rate of 5 mV/s. The electrochemically active surface area (ECSA) of the electrode was determined by measuring the double layer capacitance (C_{dl}), which is derived from cyclic voltammetry measurements with a scan rate at 5, 10, 25 and 50 mV/s in the potential window of 0.45 to 0.55 V vs. RHE. The C_{dl} was estimated by plotting the $\Delta j \text{ (} j_a - j_c \text{)}/2$ at 0.50 V vs. RHE against the scan rates, where the slope of the plot gives the C_{dl} .

Chronoamperometry was applied to measure the electrocatalytic performance of different samples over the course of one hour. CO_2 was purged into the catholyte with a flow rate of 8 mL/min through a mass flow controller. A mass flow meter downstream of the electrochemical cell was inserted to ensure the absence of leakages during the test. The gas-phase products were sampled automatically every 2 min by an online gas chromatograph (Compact GC 4.0, equipped with Rt-QBond columns). A flame ionization detector (FID) was used to measure the hydrocarbon compounds and two thermal conductivity detectors (TCD) were used to measure CO and H_2 , respectively. A standard calibration curve, made from gas mixture cylinders with known concentrations (Linde gas Benelux B.V.), was used to calculate the concentration of product gasses in the gas stream. The liquid-phase products were measured by injecting an aliquot of the electrolyte, taken at the end of the measurement, on a high-performance liquid chromatograph (HPLC, Agilent 1260 Infinity). Sample vials were placed in an autosampler and 10 μL was injected onto two Aminex HPX 87-H columns (Biorad) placed in series. During analysis the column oven temperature was maintained constant at 60 $^\circ\text{C}$, with a steady flow of rate of 0.600 mL/min of an aqueous 1 mM H_2SO_4 eluent.

3.3 Results and Discussions

3.3.1 Characterization of the biomass-derived materials

The porous carbon catalysts were prepared by a one-step pyrolysis method. The morphology of the sugarcane bagasse before carbonization, the prepared biochar (BC), N-doped biochar (NBC), and all activated N-doped biochar (ANBC) samples were visualized by SEM, as shown in Figure S3.1 and Figure 3.1.

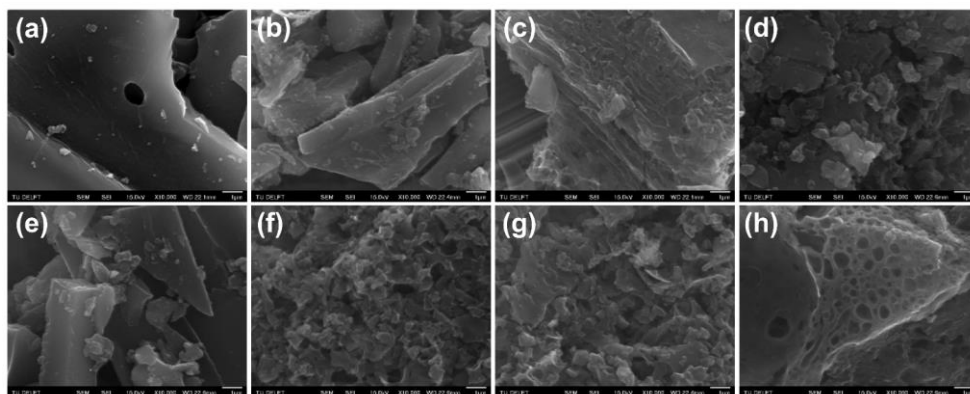


Figure 3.1 SEM images of different biomass-derived carbon catalysts (a) BC, (b) NBC, (c) ANBC1(NaHCO_3), (d) ANBC2(K_2CO_3), (e) ANBC3($\text{Mg}_5(\text{OH})_2(\text{CO}_3)_4$), (f) ANBC4(NaOH), (g) ANBC5(KOH), (h) ANBC6(KHCO_3). (Scale bar is $1\mu\text{m}$)

The sugarcane bagasse shows a long vascular fiber structure. The original BC sample derived from pure bagasse pyrolysis is composed of larger particles with a smooth surface. When urea was added as a nitrogen source, the surface became rougher in comparison to BC. This can be associated to the etching effect of NH_3 , which is released by urea decomposition during the pyrolysis procedure. For ANBC3 ($\text{Mg}_5(\text{OH})_2(\text{CO}_3)_4$), the morphology did not show a significant difference with BC, as only bulk particles with no visible pores on the surface are observed. The addition of other activators created higher porosity in the carbon samples. ANBC1 (NaHCO_3), ANBC2 (K_2CO_3), and ANBC6 (KHCO_3) maintain a similar bulk shape as the NBC, while developing a highly porous structure due to the etching effect of the activators. For ANBC4 (NaOH) and ANBC5 (KOH), the bulk carbon was etched into smaller particles, with a large number of porous structures formed by stacking between the particles, exhibiting a hierarchically porous structure with an interconnected carbon matrix. The energy-dispersive X-ray spectroscopy (EDX) results shown in Figure S3.2 reveal only the presence of carbon, nitrogen, oxygen and silicon. This

indicates that residues of the activators have been successfully washed out. The observed silicon originates from the biomass cultivation process and cannot be removed by acid washing. Although carbon and nitrogen show consistent dispersion in the elemental mapping, the carbon (0.282 eV) and nitrogen (0.392 eV) peaks in the EDX spectra overlap due to the influence of inter-elemental interference.⁴¹ Hence, the presence of nitrogen will be double-checked by XPS. To further visualize the microstructure of the samples, TEM measurements were carried out and the resulting images are displayed in Figure S3.3. Samples BC, NBC, and ANBC3 ($\text{Mg}_5(\text{OH})_2(\text{CO}_3)_4$) exhibit a carbon structure with stacked carbon layers that mainly consists of micropores. Mesopores formed during the activation process can be easily observed for the other samples. Thereby, the activation process both increases the specific surface area of the catalysts and promotes the mass transfer of reactants and products into the carbon catalysts by the formation of mesopores. This can improve the accessibility of active sites, which can potentially contribute to improving the CO_2RR performance of the materials.

N_2 adsorption-desorption isothermal analyses were performed to quantify the specific surface areas and pore size distributions of the samples. As shown in Figure 3.2a, the increase of all isotherms at very low relative pressure indicates the presence of micropores in all samples. A higher adsorption value at very low relative pressures indicates a larger micropores-derived pore volume. For BC and NBC, the total adsorption quantity remains almost constant with the increase of relative pressure, showing a type I isotherm behavior according to the IUPAC classification, indicating that these catalysts only possess microporosity.⁴² For ANBC3 ($\text{Mg}_5(\text{OH})_2(\text{CO}_3)_4$), the isotherm shows a small amount of microporous adsorption. In addition, a negligible type IV hysteresis loop was observed (Figure S3.4a), indicating that mesoporous structures were successfully created in the carbon matrix despite the very small specific surface area (Table S3.1). The isotherms of other samples display a combination of a type I and type IV isotherms, with an obvious hysteresis loop of type H4 at P/P_0 from 0.45 to 0.95, suggesting the presence of mesopores.⁴³ The increasing trends at the higher relative pressure regime ($P/P_0 > 0.95$) indicate the existence of macropores in these samples.⁴⁴ As can be seen from the pore size distribution plots in Figure 3.2b, samples BC and NBC mainly have narrow micropores of pore sizes lower than 1 nm. ANBC3 ($\text{Mg}_5(\text{OH})_2(\text{CO}_3)_4$) shows a pore size distribution with narrow micropores, with the additional formation of some mesopores (~4 nm) (Figure S3.4b). The other samples exhibit a broad pore size distribution including wider micropores (1-2 nm), narrow mesopores (2-6 nm), and a small amount of large mesopores (35-45 nm). Such a hierarchically porous structure with a strong adsorption behavior can potentially enhance the adsorption of CO_2 and facilitate the diffusion of both the reactants and products, thereby improving the electrocatalytic performance of the material.^{45,46}

The specific surface areas and pore volumes measured are summarized in Table S3.1. Sample BC exhibits a specific surface area of 724.8 m²/g with a total pore volume of 0.3 cm³/g. After introducing urea as a nitrogen source, the specific surface area and pore volume of NBC decreases to 431.6 m²/g and 0.18 cm³/g, respectively. Moreover, the sample ANBC3 (Mg₅(OH)₂(CO₃)₄) displays an even worse porosity with a lower specific surface area and pore volume. This is due to the thermal decomposition of urea and Mg₅(OH)₂(CO₃)₄ in the carbonization process, which absorbs a large amount of heat. This inhibits the carbonization of bagasse, resulting in worse textural properties (Table S3.1). By contrast, the other activators created abundant pores, resulting in specific surface areas from 960.5 to 1786.9 m²/g, and pore volumes from 0.50 to 0.87 cm³/g. The enlarged surface area is conducive to exposing more active sites and thereby can improve the catalytic performance.⁴⁷ It is noteworthy that the mesopore ratios and average pore sizes of the different carbon samples are highly related to the properties of the activators (Table S3.1). ANBC3 (Mg₅(OH)₂(CO₃)₄) and ANBC4 (NaOH) had a higher ratio of mesopores than other samples, ANBC1 (NaHCO₃) and ANBC4 (NaOH) exhibited a relatively larger average pore size. Both of these properties are considered to be key factors affecting mass transfer processes during the CO₂RR. In general, the larger specific surface area can expose more active sites, while the porosity (pore size distribution and average pore size) affects the accessibility of the reactant to active sites. A good balance between specific surface area and porosity can therefore help to improve the performance of the carbon catalyst.

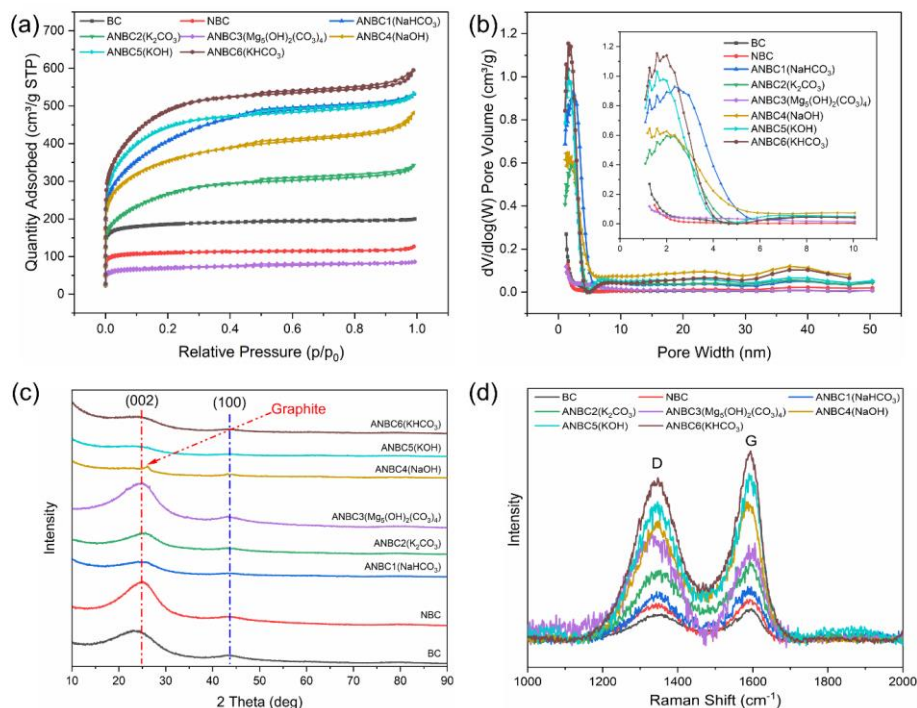


Figure 3.2 (a) N₂ adsorption-desorption isotherms; (b) pore size distributions; (c) XRD patterns; and (d) Raman spectra of different biomass-derived carbon catalysts.

XRD was used to determine the crystallographic structure of the as-prepared carbon samples and the diffractograms are displayed in Figure 3.2c. All samples exhibited an analogous diffraction feature with two broad peaks located at about $2\theta = 25^\circ$ and 44° , which can be assigned to the diffraction of the (002) plane and (100) plane of graphitic-like carbon, respectively.⁴⁸ The peak located at around $2\theta = 25^\circ$ suggests a disordered amorphous carbon structure.⁴⁸ For the non-activated biochar sample (BC), the peak shifted to a smaller angle, indicating a relatively low degree of crystallinity.⁴⁹ A tiny sharp peak appeared at the right side of the (002) peak for ANBC4 (NaOH) and was identified as a signal of graphite,⁵⁰ indicating that this sample is more graphitized than the other samples. The low intensity peak located at 44° was attributed to graphitic carbon with a limited degree of graphitization.⁵¹ The local disorder and graphitization of the carbon samples was determined by Raman spectroscopy measurements. As shown in Figure 3.2d, all carbon samples presented two peaks at around 1350 and 1580 cm⁻¹, corresponding to the D band and G band, respectively.⁵² The D band derives from crystal defects and the disordered structure of carbon, while the G band relates to the lattice vibration of sp²-hybridized

graphitic carbon.⁵³ Generally, the intensity ratio between the D and G band (I_D/I_G) is adopted as an index to evaluate the degree of graphitization of carbon materials. A high I_D/I_G value signifies a lower degree of graphitization.⁵⁴ Here, we observe that the value of I_D/I_G increases after activation, indicating that more defects and disordered carbon lattice structures were generated during the activation processes (Table S3.1). The more disordered structure is associated with a larger surface area and provides more defects that can act as active sites.⁵⁵ However, a higher degree of graphitization enhances the electrical conductivity of carbon materials, hence facilitating electron/charge transfer and potentially improving the catalytic performance.⁵⁶ Therefore, the optimal graphitization degree of carbon catalysts is a trade-off between a more activated surface and a material with higher conductivity.

To elucidate the surface chemical compositions of all carbon samples, XPS measurements were performed. The full survey spectra of the samples are presented in Figure S3.5 and the elemental compositions are summarized in Table S3.2. Three strong signals were detected for all carbon samples, which were attributed to C 1s, N 1s, and O 1s peaks. Trace amounts of silicon were detected on the as-prepared catalysts after the acid treatment. The observed silicon originates from the biomass cultivation process and cannot be removed by acid washing. It is noted that the BC had a 1.05% N content, stemming from the pyrolysis of the original proteins or N-functional groups on lignin. Compared with the biochar without modification, the NBC exhibited a 10.81% N content due to the addition of urea in the pyrolysis process. With the use of activators, the N content decreased to 3.85 ~ 8.7%, indicating that the activators regulate the chemical composition of the carbon samples. Some powerful activators such as KOH and NaOH, remove nitrogen and oxygen functional groups on the carbon surface during the activation process, resulting in a lower N-doping content. However, for sample ANBC3, the use of $Mg_5(OH)_2(CO_3)_4$ hindered carbonization and lowered the C content to 77.3% while creating disordered structures, which is in good agreement with the Raman spectroscopy results. In conclusion, nitrogen was successfully doped into the matrix of biomass-derived carbon samples via the one-step pyrolysis method, whereas the doping content strongly depends on the type of activator used.

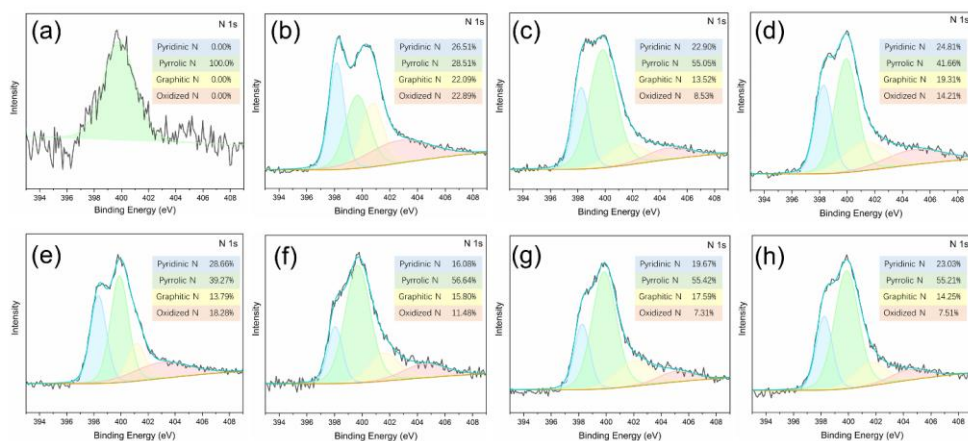


Figure 3.3 High-resolution N 1s spectrum of different biomass-derived carbon catalysts (a) BC, (b) NBC, (c) ANBC1(NaHCO_3), (d) ANBC2(K_2CO_3), (e) ANBC3($\text{Mg}_5(\text{OH})_2(\text{CO}_3)_4$), (f) ANBC4(NaOH), (g) ANBC5(KOH), (h) ANBC6(KHCO_3). Intensity is given in arbitrary units.

To further investigate the type of N-containing species present in the carbon catalysts, the high-resolution N 1s spectra shown in Figure 3.3 were deconvoluted into four individual peaks at around 398.2, 399.9, 401.6, and 404.4 eV, referring to pyridinic N, pyrrolic N, graphitic N, and oxidized N, respectively.^{51,57,58} The blank BC only contained pyrrolic N species while other N species were detected when urea was used as nitrogen source. As shown in Figure 3.3 and Table S3.2, the used activators play a crucial role in controlling the distribution of N-bonding configurations on the carbon surface. In general, pyrrolic N is the main nitrogen-containing species observed, followed by pyridinic N, graphitic N, and oxidized N. The existence of oxidized N is attributed to the strong reaction between urea and the oxygen functional groups of the biomass-derived carbon surface.⁵⁹ The N-doping changes the charge and spin distribution in the N dopant and adjacent C atoms, which enhances the interaction with reactants for dissociative adsorption and facilitates the electron donor-acceptor charge transfer to improve the electrocatalytic performance.^{30,60,61} Interestingly, both pyridinic N and graphitic N were demonstrated as the active site for the CO_2RR by experimental results and theoretical calculations.^{62,63} However, owing to the complexity of the reaction mechanism and N dopant properties, the role of these N containing active sites during the CO_2RR is still under debate. In addition, the fitted C 1s and O 1s spectrum are shown in Figure S3.6 and Figure S3.7. The high-resolution C 1s spectrum can be split into three peaks at ~ 284.8 , ~ 285.5 , ~ 288.5 eV, which can be assigned to C-C, C-N, and C-O, respectively.³⁶ The high-resolution O 1s spectrum can be fitted by three peaks at ~ 530.6 , ~ 532.5 , and ~ 535.0 eV, representing O-N, O=C, and O-C, respectively.⁶⁴

3.3.2 Understanding the effect of activators

$\text{Mg}_5(\text{OH})_2(\text{CO}_3)_4$ has previously been used as an activator to produce porous carbon materials.^{36,65} During the carbonization process, $\text{Mg}_5(\text{OH})_2(\text{CO}_3)_4$ gradually decomposes into MgO , CO_2 , and H_2O , where the nanocrystals of MgO are embedded in the carbon structure as a template, endowing the carbon material with a rich mesoporous structure after acid washing, while CO_2 and H_2O are involved in the activation of the carbon material as physical activators and give it a rich microporous structure.⁶⁵ As shown in Table S3.1, ANBC3 ($\text{Mg}_5(\text{OH})_2(\text{CO}_3)_4$) exhibited a higher ratio of mesopores than other catalysts, which should be beneficial for mass transfer during the CO_2RR . However, the one-step pyrolysis method resulted in only limited interaction between the bagasse and the activator, leading to a similar morphology as BC and keeping a relatively high N-doping content. In addition, the excess amount of $\text{Mg}_5(\text{OH})_2(\text{CO}_3)_4$ absorbed a large amount of heat during decomposition, which resulted in poor carbonization of the sample, showing a higher I_D/I_G value and a smaller specific surface area.

NaOH and NaHCO_3 are two commonly used chemical activators and are both capable of producing carbon samples with a well-developed pore structure.⁶⁶ NaOH works as an oxidant, oxidizing the carbon framework and thereby improving the porosity.⁶⁷ NaHCO_3 is considered a chemical foaming agent,⁶⁸ as it decomposes during carbonization, releasing large amounts of CO_2 and H_2O , which leads to the formation of a hierarchical porosity. Interestingly, both NaOH and NaHCO_3 decompose to form Na_2CO_3 . The Na_2CO_3 is embedded in the carbon matrix and acts as a template to provide a large number of mesopores for the carbon material.⁶⁹ Sample ANBC4 (NaOH) and ANBC1 (NaHCO_3) show a larger ratio of mesoporous structure and larger average pore diameter than other catalysts (Table S3.1). In particular, due to the strong oxidizing properties of NaOH , the carbon framework is strongly etched resulting in ANBC4 (NaOH) showing smaller particles and a relatively low N-doping content. As for ANBC1 (NaHCO_3), the porosity is well developed while keeping a higher N-doping content. In short, NaOH and NaHCO_3 endow the catalysts with a large specific area, rich meso-porosity and effective N-doping.

Potassium salts, such as KOH , KHCO_3 , and K_2CO_3 are also widely used as activators to endow high porosity to lignocellulose-derived carbon materials. However, their activation characteristics lead to variations in structures and properties of the biochar. KOH reacts with carbon at high temperatures, generating various potassium species (K_2CO_3 , K_2O , K) and releasing a large amount of gas (CO_2 , H_2O). This leads to etching of the carbon matrix by redox reactions, and samples with a large specific surface area and high microporosity are obtained (Table S3.1).⁷⁰ In addition, KOH has a low fusion point ($\sim 380^\circ\text{C}$) and the molten salt results in the disintegration of the carbon material, which roughens the surface and forms

small particles (see Figure 3.1g).⁷¹ The activation mechanism of KHCO_3 is similar to that of NaHCO_3 .⁷² KHCO_3 decomposes at $\sim 200^\circ\text{C}$ to K_2CO_3 and released gases, which develops macropores in the carbon matrix. The released CO_2 and H_2O are further involved in the activation process, producing additional micropores or further enlarging the existing pore structure.⁵³ By contrast, K_2CO_3 is more stable than KOH and KHCO_3 (the fusion point of K_2CO_3 is $\sim 890^\circ\text{C}$), and its activation performance is strongly dependent on the pyrolysis temperature. Some studies point out that K_2CO_3 has a time-dependent reduction and decomposition starting from 700°C to produce K_2O , K , and CO_2 , which further improves the porosity.⁷¹ The longer the residence time, the larger the specific surface area and the higher the porosity.⁷³ When the temperature reaches 900°C , K_2CO_3 melts and this results in the shrinkage and collapse of porous structures.⁵³ In this study, ANBC5 (KOH) and ANBC6 (KHCO_3) exhibited a similar degree of graphitization, whereas these activators developed a larger specific surface and a higher pore volume than other samples (Table S3.1). However, the dominance of micropores can induce a higher mass transfer resistance during the CO_2RR , which potentially hinders the catalytic performance. Although ANBC2 (K_2CO_3) showed a higher N-doping content, it did not generate a well-developed porous structure due to the short pyrolysis residence time (1 hour), with its specific surface area only reaching $\sim 960\text{ m}^2/\text{g}$ and the porosity being mostly composed of micropores.

3.3.3 Electrochemical performance

To evaluate the electrochemical performance of the prepared catalysts, linear sweep voltammetry (LSV) were performed in an Ar-saturated and CO_2 -saturated aqueous 0.1 M KHCO_3 electrolyte. As shown in Figure S3.8, the current densities of BC, NBC, and ANBC3 ($\text{Mg}_5(\text{OH})_2(\text{CO}_3)_4$) were lower in a CO_2 -saturated electrolyte than in an Ar-saturated electrolyte over the entire potential range, indicating that these catalysts have little activity for the CO_2RR . By contrast, ANBC1 (NaHCO_3), ANBC2 (K_2CO_3), ANBC4 (NaOH), ANBC5 (KOH), and ANBC6 (KHCO_3) exhibited higher current densities in the CO_2 -saturated electrolyte at more negative potentials, beyond -0.7 V vs. RHE, indicating that they are active electrocatalysts for the CO_2 reduction reaction. A comparison of the LSVs with different samples in a CO_2 -saturated electrolyte is shown in Figure 3.4a. Due to the different physicochemical properties of the catalysts, significant differences in the LSV results can be observed. ANBC3 ($\text{Mg}_5(\text{OH})_2(\text{CO}_3)_4$) showed an almost negligible current density due to its low specific surface area and low degree of graphitization. In contrast, ANBC4 (NaOH) exhibited better CO_2 electrocatalytic activity than other samples, displaying a lower onset potential and higher current density. This can be attributed to the larger surface area and hierarchically porous structure of the ANBC4 (NaOH) sample. However, as the trends in

current density observed in the voltammograms is not decisive evidence for CO₂ reduction activity, direct evidence for the formation of CO₂ reduction products is needed.

To thoroughly evaluate the electrocatalytic performance of the various carbon materials for the CO₂RR, chronoamperometry measurements were conducted at various potentials from -0.50 to -1.15 V vs. RHE. For all the samples, CO and H₂ were the main gaseous products observed, while trace amounts of CH₄ with a FE for CH₄ lower than 1% could be detected when the applied potential was more negative than -0.8 V vs. RHE. Besides these gaseous products, no liquid products were detected by HPLC. The FEs of CO and H₂ obtained at the tested potentials for all the samples are plotted in Figure 3.4b and Figure S3.9a, respectively. The BC, NBC, and ANBC3 (Mg₅(OH)₂(CO₃)₄) electrocatalysts exhibited a poor selectivity toward CO and produce H₂ as the dominant product. These performances are consistent with the LSV results, indicating that these materials are poor CO₂ reduction catalysts. For ANBC1 (NaHCO₃), ANBC2 (K₂CO₃), ANBC4 (NaOH), ANBC5 (KOH), and ANBC6 (KHCO₃), the product selectivity was strongly dependent on the applied potential (see Figure 3.4b). With a decrease in applied potential, the trend of CO selectivity displays a volcano-like curve. Among these materials, ANBC4 (NaOH) exhibited the highest FE_{CO} of 80% at -0.93 V vs. RHE, while ANBC5 (KOH) reached 74.4% at the same potential, whereas the maximum FE_{CO} for ANBC1(NaHCO₃), ANBC2 (K₂CO₃), and ANBC6 (KHCO₃) was 42.4%, 45.8%, and 46.0% at -0.91 V vs. RHE, -1.00 V vs. RHE and -0.80 V vs. RHE, respectively. With a further decrease of applied potential, the CO selectivity reduced gradually, and H₂ production regained dominance at the more negative potentials. Meanwhile, the FE_{H₂} presented an opposite trend (Figure S3.9a), with ANBC4 (NaOH) and ANBC5 (KOH) exhibiting the lowest selectivity toward H₂. It should be noted that the total FE was below 100% at the more positive potentials due to low current densities resulting in product concentrations below or near the detection limit of the gas chromatograph, such that the FE cannot accurately be calculated.⁷⁴

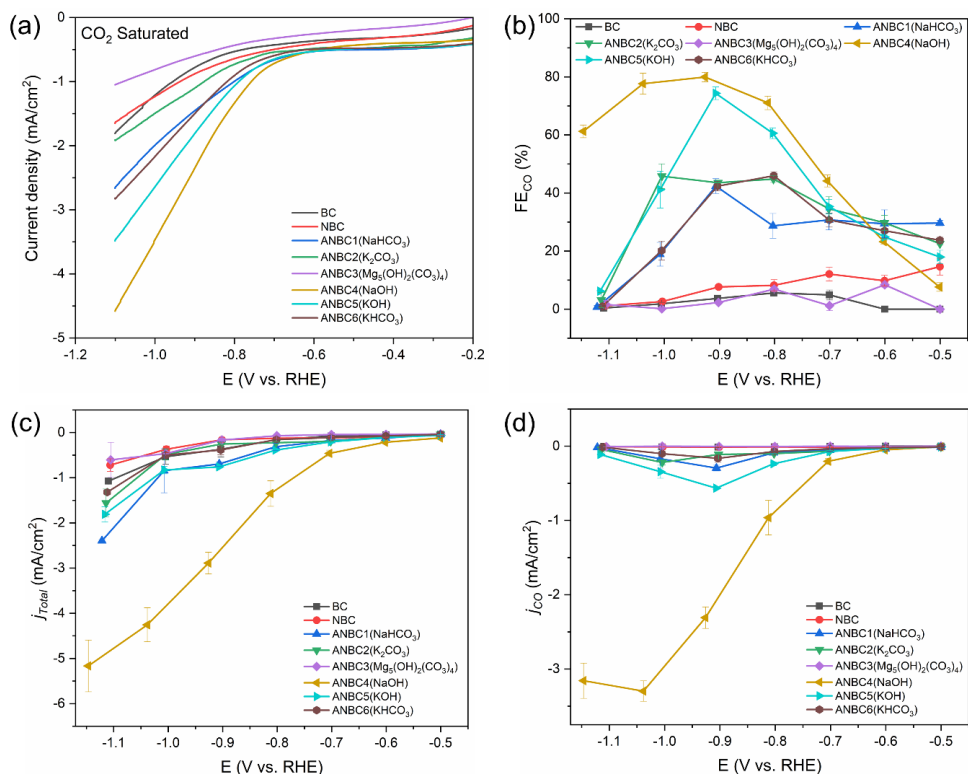


Figure 3.4 (a) LSV curves recorded at a scan rate of 5 mV/s of all catalysts in a CO_2 -saturated 0.1 M KHCO_3 electrolyte; (b) FE of CO production at applied potentials from -0.50 to -1.15 V vs. RHE; (c) Total current density of all catalysts at different applied potentials.

The total current density and partial current densities j_{CO} and j_{H_2} are plotted in Figure 3.4c, 4d, and Figure S3.9b, respectively. The total current density of all prepared catalysts increased with more negative potentials. Notably, carbon catalysts activated with the sodium salts (NaOH , NaHCO_3) exhibited greater current densities than those activated by potassium salts (KOH , KHCO_3 , K_2CO_3). As for the j_{CO} , except for BC, NBC, and ANBC3 ($\text{Mg}_5(\text{OH})_2(\text{CO}_3)_4$), which are not catalytically active, the other catalysts showed a similar trend, where the j_{CO} increases first and then decreases when the potential becomes more negative. Especially ANBC4 (NaOH) presented a significantly higher total current density and j_{CO} in comparison to the other samples. In the potential range between -0.8 V to -1.0 V vs. RHE, j_{CO} is higher than j_{H_2} , indicating that the CO_2 reduction is the dominant reaction.

The electrochemically active surface area (ECSA) of each catalyst was determined by the double layer capacitance (C_{dl}), which was determined with cyclic voltammetry measurements in the non-faradaic region. As shown in Figure S3.10, the C_{dl} values of these ANBCs are positively correlated with their specific area, corresponding to earlier results by Taer et al.⁷⁵ Although ANBC6 (KHCO_3) and ANBC1 (NaHCO_3) showed a higher ECSA than other samples, their catalytic performances were not as good as ANBC4 (NaOH) and ANBC5 (KOH). This means that not all electrochemically active sites show catalytic activity for the CO_2RR . This is in line with results of Voiry et al.,⁷⁶ who report that non-active carbon can lead to an overestimation of the ECSA and an underestimation of the catalytic performance.

In addition, the charge transfer resistance also has a crucial effect on the current density, as smaller charge transfer resistances lead to a larger current density. The Nyquist plots of each sample are depicted in Figure S3.11. ANBC4 (NaOH) and ANBC5 (KOH) showed lower interfacial charge transfer resistance than other samples, demonstrating more rapid electron transfer than the other samples in CO_2RR process.⁶⁰ In general, the high FE_{CO} and small charge transfer resistance of ANBC4 (NaOH) gives it a superior electrocatalytic performance over other samples.

To investigate the kinetics of the CO_2RR on various catalysts, a Tafel slope analysis of ANBC1 (NaHCO_3), ANBC2 (K_2CO_3), ANBC4 (NaOH), ANBC5 (KOH), ANBC6 (KHCO_3) was conducted and the results are shown in Figure S3.12. ANBC4 (NaOH) exhibited a lower Tafel slope (155 mV/dec) than that of the other 4 samples, indicating that ANBC4 (NaOH) has faster kinetics for CO_2 reduction to CO . The other samples showed a Tafel slope between 226 and 382 mV/dec. Since a Tafel slope close to 118 mV/dec indicates that the rate-determining step of the CO_2RR is a single-electron transfer process, where CO_2 absorbs the first electron to generate the $^*\text{CO}_2^-$ intermediates,⁶⁰ these higher Tafel slope values indicate that other processes determine the kinetics of the CO_2RR on these materials. Consequently, we hypothesize that the rate-determining step for ANBC1 (NaHCO_3), ANBC2 (K_2CO_3), ANBC5 (KOH), and ANBC6 (KHCO_3) is the diffusion of CO_2 from the electrolyte to the active sites.⁴⁰

Control experiments to verify whether the observed CO was produced from CO_2 were carried out using ANBC4 (NaOH) and ANBC5 (KOH) at an applied potential of -0.9 V vs. RHE in Ar -saturated 0.1 M KHCO_3 electrolyte. As shown in Figure S3.13, only H_2 was detected with Ar -saturated electrolytes, indicating that the observed CO only originates from electrochemical CO_2 reduction and not from the disintegration of functional groups on the carbon surface.

3.3.4 Understanding the structure-activity relationship

To get an understanding of how the structure and composition of the carbon catalysts affects the electrocatalytic performance, we will here combine the results of the physicochemical characterization with the results of electrochemical testing. Generally, the higher N-doping content and larger specific surface area are considered as the most important parameters to enhance the CO₂RR performance of N-doped carbon materials. However, several studies have shown impressive performances with lower specific surface areas and lower N-doping contents.^{77–79} Therefore, we think that overemphasizing the impact of one or two factors on the overall catalytic performance can lead to lopsided conclusions. To avoid this, a comprehensive analysis of the effect of the physicochemical properties of the carbon catalyst on the catalytic performance is essential.

Introducing N as a heteroatom into a carbon matrix can modulate the charge distribution on the carbon surface and provide active sites for the CO₂RR. In addition, previous studies have demonstrated that the adsorption behavior of CO₂ can be improved by introducing N into the carbon matrix.^{22,80} Many studies have demonstrated through experimental analyses and theoretical calculations that the product selectivity and the activity of N-doped carbon materials for the CO₂RR strongly depends on the N doping content.^{24,81} Both pyridinic N and graphitic N have been reported as the active sites for the CO₂RR.⁶³ Some studies have set out to improve the catalytic performance of N-doped carbon catalysts by enhancing the N-doping content or by controlling the preparation conditions to increase the ratio of pyridinic/graphitic N.^{62,63} However, unlike the aforementioned studies, we find that the catalytic selectivity and activity of bagasse-derived N-doped carbon catalysts are not linearly correlated with the total N, pyridinic N, and graphitic N content. The five best electrocatalysts prepared in this study were selected and compared at the highest j_{CO} (-0.90V vs. RHE for ANBC6 (KHCO₃), -0.91V vs. RHE for ANBC1 (NaHCO₃) and ANBC5 (KOH), -1.00V vs. RHE for ANBC2 (K₂CO₃), and -1.04V vs. RHE for ANBC4(NaOH), respectively). The relationship between the total pyridinic and graphitic N content and the FE_{CO} and j_{CO} for these materials is shown in Figure 3.5. This shows that neither the total N content nor the pyridinic/graphitic N content is positively correlated to the selectivity and activity of the N-doped carbon catalyst. Therefore, overemphasizing the contribution of N-doping is not helpful to understand the structure-activity relationship. Similarly, several studies have reported that lower N-doping levels can lead to a better catalytic performance for the CO₂RR.^{77,82} The improvement of CO₂RR performances were attributed to the increased concentration of defects, which were generated by removing N atoms from the N-doped carbon. However, these N atoms generally could not be entirely removed. Therefore, it is difficult to identify whether the N-containing sites or the defect sites are the dominant active sites for the CO₂RR. Although the relationship analysis with limited samples is not perfect, this observation provides direct evidence that the catalytic performance of

N-doped carbon materials for CO₂RR is determined by a synergistic effect of different factors and is not solely determined by N-doping content or the configuration of N-dopant. This conclusion is similar to the results of Yao et al.,⁶⁰ who reported an N-doped carbon derived from Typha that maintains a large surface area and pore volume but lower N-doping content that outperformed a sample with a higher N-doping level. Although this dataset does not help to understand which nitrogen configuration acts as the real active sites, it highlights the trade-off between N loading content and the microstructures of the carbon catalysts.

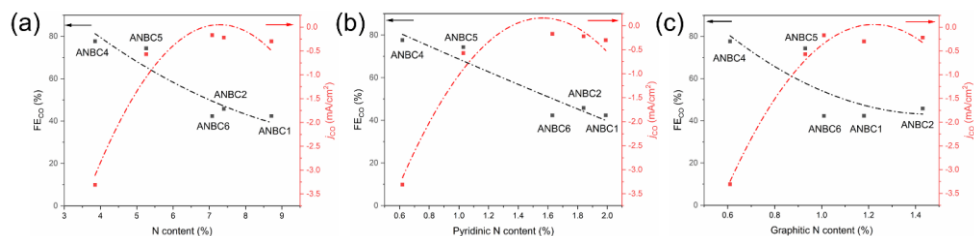


Figure 3.5 The relationship between electrochemical performance and (a) total N content; (b) pyridinic N content; (c) graphitic N content.

A larger specific surface area of the catalysts exposes more active sites and thus enhances the catalytic performance for CO₂RR. When the specific surface area of the catalyst is small, other advantageous factors are suppressed, resulting in poor catalytic performance, such as is the case for NBC, ANBC2 (K₂CO₃) and ANBC3 (Mg₅(OH)₂(CO₃)₄). However, this does not mean that the larger specific surface always leads to better catalytic performances.⁴⁰ As shown in Figure S3.14a, there is no direct correlation between the performance of the catalysts and the specific surface area. Similarly, the electrochemical performance does not show a positive correlation with the electrochemically active surface area (Figure S3.14b). Not all electrochemically active sites are catalytically active toward the CO₂RR and not all of the CO₂ can be effectively transported to the active sites of the N-doped carbon catalyst. Many studies have indicated that the porous structure plays an important role in the mass transfer of reactants and products, and electrolyte diffusion processes.^{33,60} Several studies have pointed out that a hierarchically porous structure helps to improve the performance of N-doped carbon catalysts for CO₂RR in the aqueous phase. Macropores and mesopores act as a reservoir to minimize the diffusion distance of reactants and electrolytes, which facilitates the mass transfer process, while micropores provide a large specific surface area and expose more active sites, further enhancing the CO₂RR performance of N-doped carbon materials.⁴⁴ Among the porous structures, the availability of mesopores is considered a key factor determining the overall performance. Ma et al. verified that catalysts with higher mesoporous content exhibit better performance for CO₂RR by electrochemical

impedance spectroscopy (EIS) tests and suggested that the mesoporous structure allows more active sites to be exposed to the electrolyte and accelerates the diffusion of the electrolyte to those active sites.⁸³ Hursan et al.⁸⁴ indicated that the selectivity, activity, and stability of the CO₂RR on N-doped carbon catalysts are highly dependent on the porosity. The results obtained in this study are consistent with these literature reports. ANBC4 (NaOH) shows the best electrocatalytic performance with a 3.85% N-doping, 1277.94 m²/g specific surface area and 17.3% mesopores. Although ANBC5 (KOH) and ANBC6 (KHCO₃) show a larger specific surface area and higher N-doping level than ANBC4 (NaOH), their electrocatalytic performances are worse. This can be attributed to the lower mesopore ratios (12.5% and 11.3%, respectively) in ANBC5 (KOH) and ANBC6 (KHCO₃) that hinder the mass transfer of reactants to the active sites.

The degree of graphitization is also considered to be one of the important factors affecting catalytic performance, as a higher degree of graphitization can be beneficial to improve electron transfer during CO₂RR.³⁹ N-doping, activation processes, and pyrolysis temperature all have significant effects on the degree of graphitization. Anthony et al.²⁰ point out that a delicate balance between the N-doping level and the degree of graphitization is essential, with sufficient N sites helping to improve catalytic activity, but an excessive number of N sites reduces the degree of graphitization, negatively affecting the conductivity and charge transfer. A strong activator induces lots of defects into the carbon material, which improves the specific surface area but reduces the degree of graphitization.³⁴ In addition, high pyrolysis temperatures promote the structural alignment of carbon materials but will remove the heteroatoms, generating a more disordered carbon lattice.³⁴ In this study, most of the catalysts showed similar degrees of graphitization due to the application of the same pyrolysis temperature and N-doping strategy. Notably, ANBC3 (Mg₅(OH)₂(CO₃)₄) exhibited the lowest degree of graphitization and specific surface area and therefore, despite its high mesopores ratio, displayed the worst catalytic performance.

3.4 Conclusions

In conclusion, we have prepared a series of N-doped carbon catalysts derived from sugarcane bagasse, carbonized and activated with different activators, to investigate the specific effect that these activators have on the overall CO₂RR performance of the resulting carbon catalysts. The textural properties of the carbon catalysts are highly dependent on the type of activator used, which further affects the electrochemical performance. The obtained results show that the CO₂RR performance of the carbon-based catalysts did not solely depend on the N-doping level or the configuration of N-dopants, but the synergistic effect of the N-doping, the specific surface area, the porosity and the degree of graphitization jointly determines the catalytic performance. The ratio of mesoporosity is demonstrated as

an important parameter, which can enhance the mass transfer and improve the accessibility of the reactant to the active sites. The degree of graphitization affects the conductivity of carbon catalysts, with a higher degree of graphitization leading to higher current densities for CO₂RR. In this study, different activators endow the carbon catalysts with various physicochemical properties, thus exhibiting significant differences in electrochemical performance for CO₂RR. Among them, sodium hydroxide has been demonstrated as the most effective activator, endowing the carbon catalyst with a proper N-doping content, large surface area, abundant pores with high mesoporosity, and relatively higher degree of graphitization, enabling it to reach a high performance for CO₂RR with 80% faradaic efficiency towards CO at -0.93 V vs. RHE. This work presents a comprehensive analysis of the function of different activators on N-doped carbon catalysts for CO₂RR, which can provide guidance for the design and synthesis of high-performance N-doped carbon catalysts.

3.5 Supporting Information

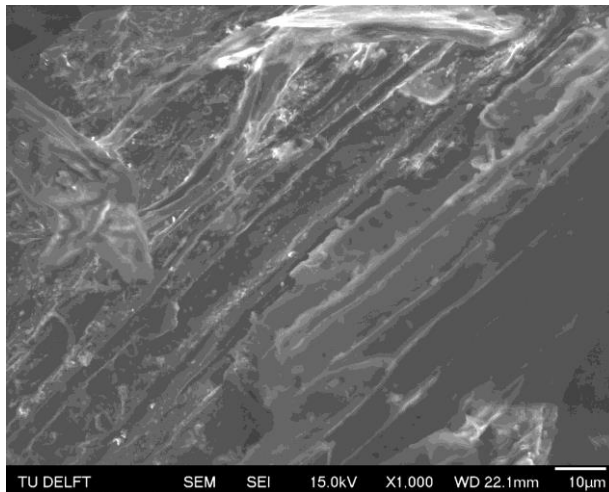


Figure S3.1 SEM image of sugarcane bagasse before carbonization.

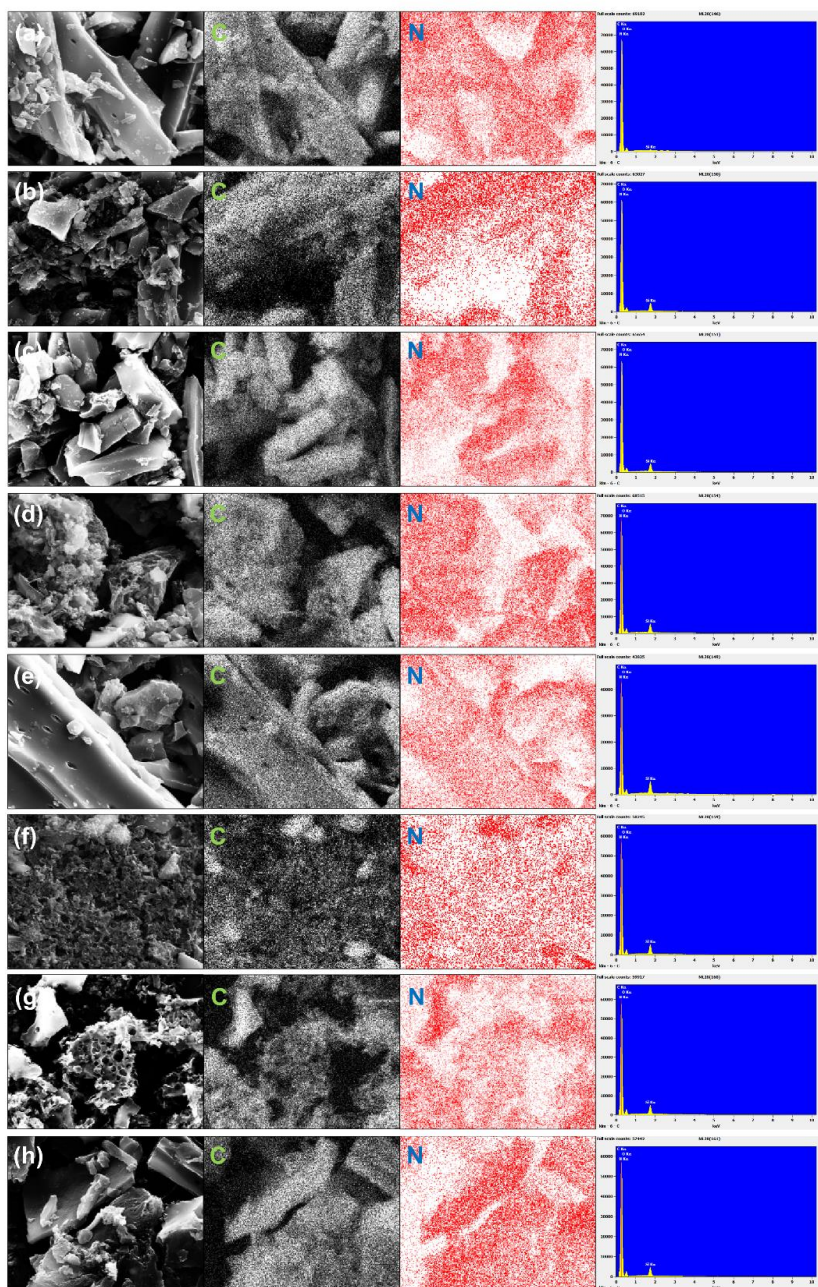


Figure S3.2 SEM-EDX elemental mapping of C, N and spectra results of (a) BC, (b) NBC, (c) ANBC1(NaHCO_3), (d) ANBC2(K_2CO_3), (e) ANBC3($\text{Mg}_5(\text{OH})_2(\text{CO}_3)_4$), (f) ANBC4(NaOH), (g) ANBC5(KOH), (h) ANBC6(KHCO_3). (Scale bar is $5\mu\text{m}$)

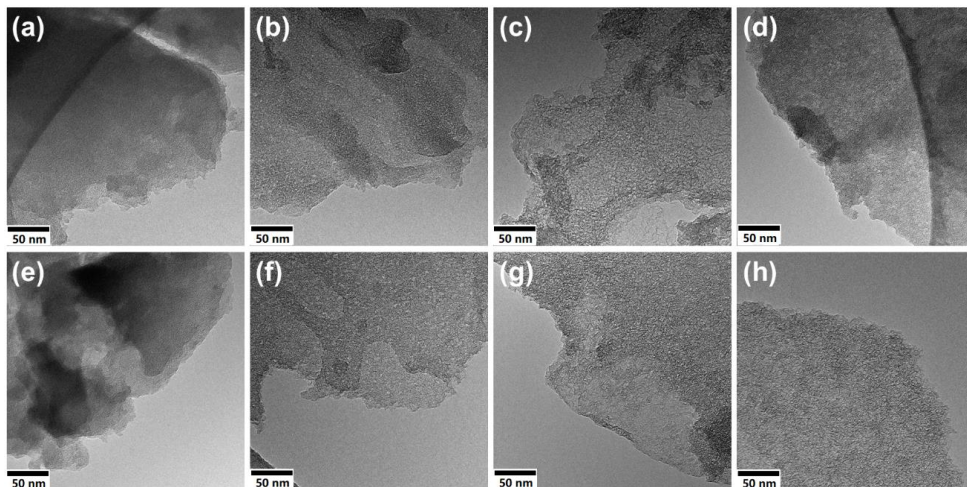


Figure S3.3 TEM images of different biomass-derived carbon catalysts (a) BC, (b) NBC, (c) ANBC1(NaHCO_3), (d) ANBC2(K_2CO_3), (e) ANBC3($\text{Mg}_5(\text{OH})_2(\text{CO}_3)_4$), (f) ANBC4(NaOH), (g) ANBC5(KOH), (h) ANBC6(KHCO_3).

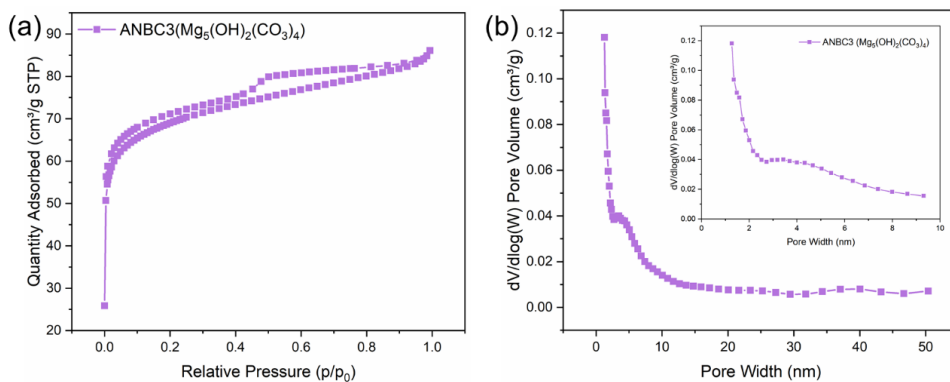


Figure S3.4 (a) N_2 adsorption-desorption isotherm and (b) pore size distribution of ANBC3($\text{Mg}_5(\text{OH})_2(\text{CO}_3)_4$).

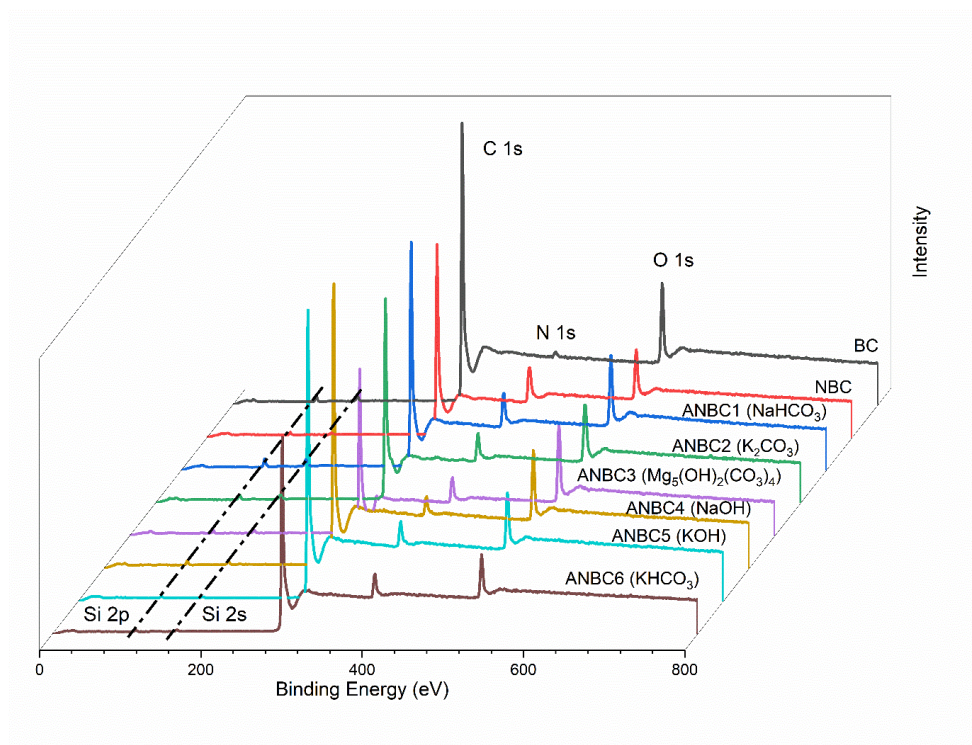


Figure S3.5 XPS survey spectra of different biomass-derived carbon catalysts. (Intensity is in arbitrary units)

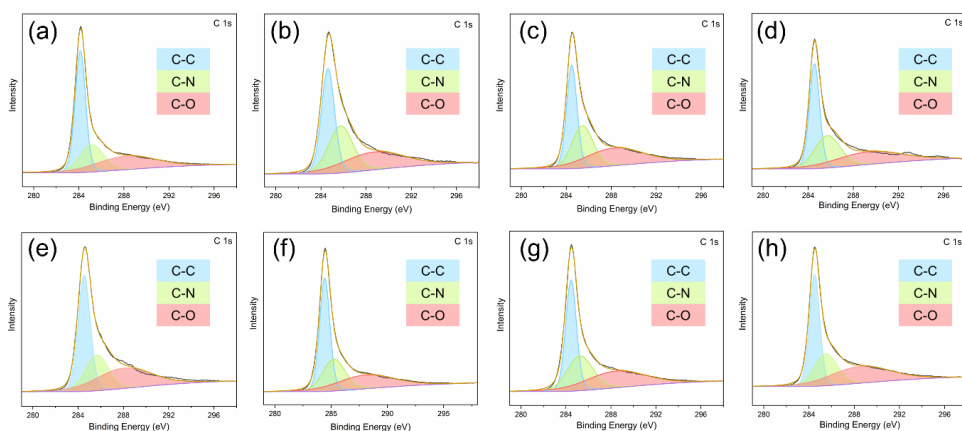


Figure S3.6 High-resolution C 1s spectrum of different biomass-derived carbon catalysts (a) BC, (b) NBC, (c) ANBC1(NaHCO_3), (d) ANBC2(K_2CO_3), (e) ANBC3($\text{Mg}_5(\text{OH})_2(\text{CO}_3)_4$), (f) ANBC4(NaOH), (g) ANBC5(KOH), (h)ANBC6(KHCO_3). (Intensity is in arbitrary units)

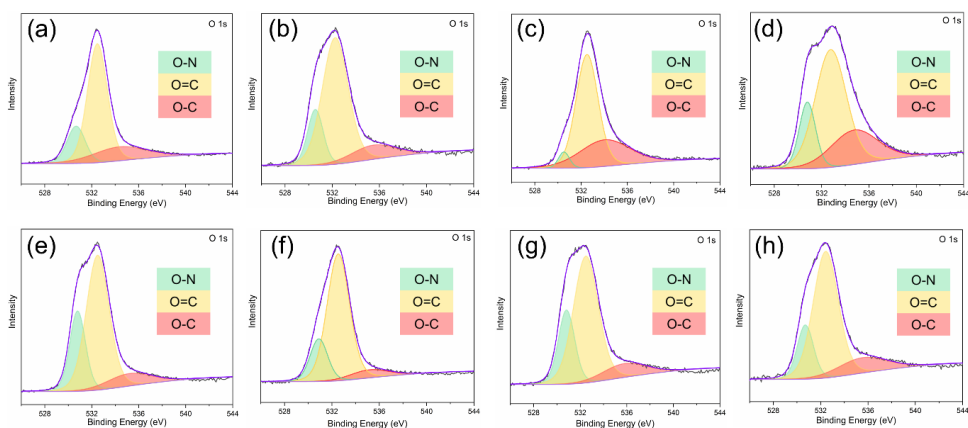


Figure S3.7 High-resolution O 1s spectrum of different biomass-derived carbon catalysts (a) BC, (b) NBC, (c) ANBC1(NaHCO_3), (d) ANBC2(K_2CO_3), (e) ANBC3($\text{Mg}_5(\text{OH})_2(\text{CO}_3)_4$), (f) ANBC4(NaOH), (g) ANBC5(KOH), (h)ANBC6(KHCO_3). (Intensity is in arbitrary units)

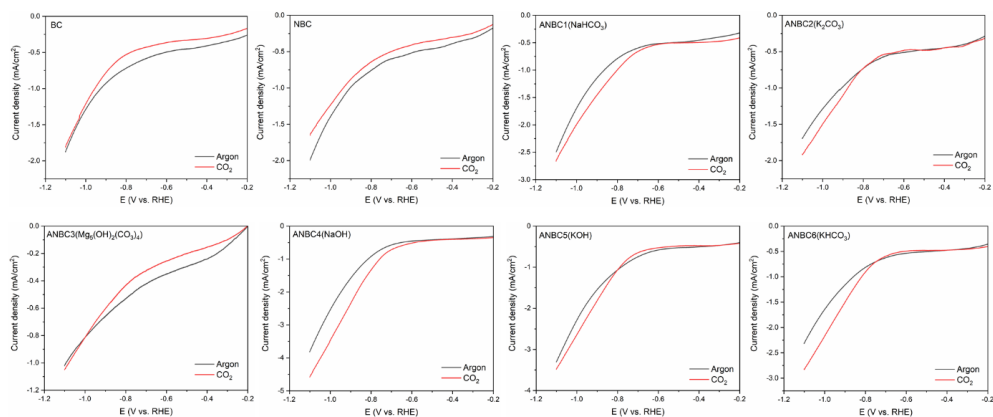


Figure S3.8 LSV curves of all catalysts in Argon- and CO_2 -saturated 0.1M KHCO_3 .

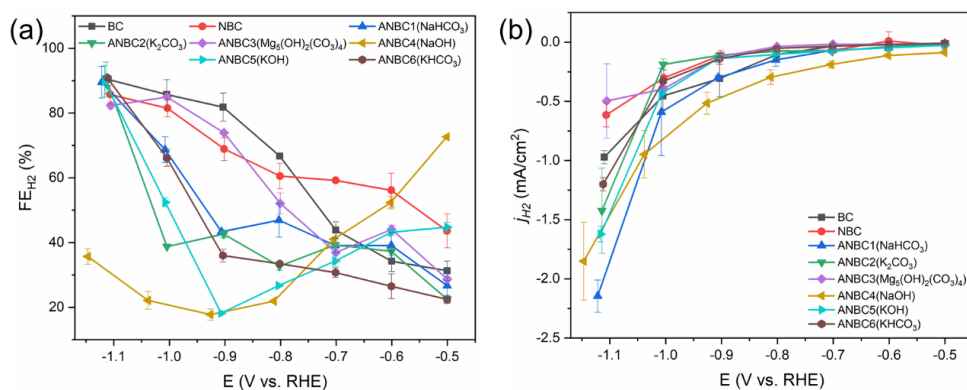


Figure S3.9 (a) FE of H_2 at different applied potentials; (b) Partial current density of H_2 at different applied potentials.

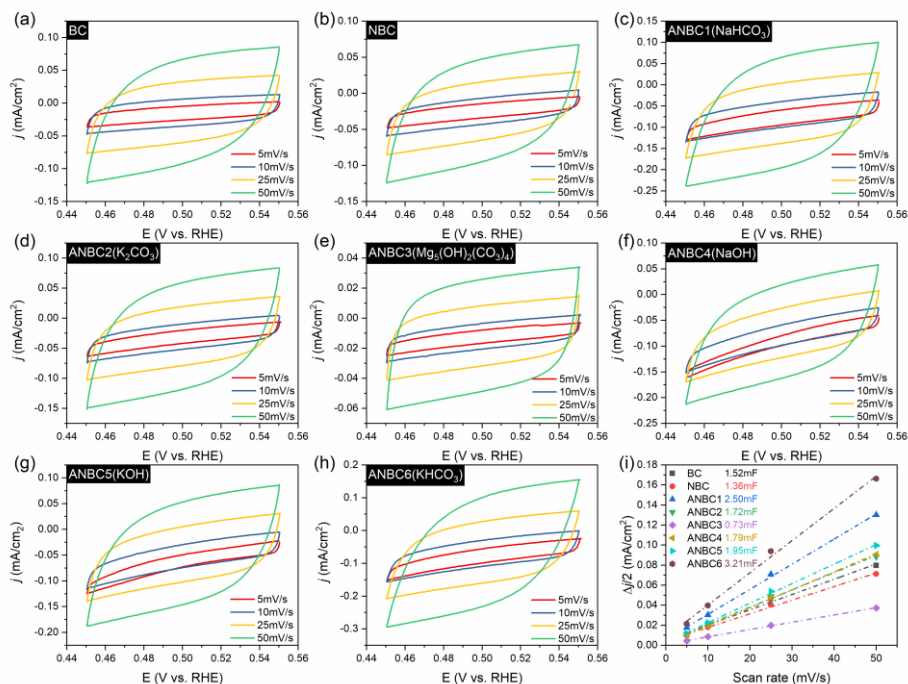


Figure S3.10 CVs of (a) BC, (b) NBC, (c) ANBC1 (NaHCO₃), (d) ANBC2 (K₂CO₃), (e) ANBC3 (Mg₅(OH)₂(CO₃)₄), (f) ANBC4 (NaOH), (g) ANBC5 (KOH), (h) ANBC6 (KHCO₃) from 0.45 to 0.55 V vs. RHE at various scan rates and (i) The double layer capacitance of all samples.

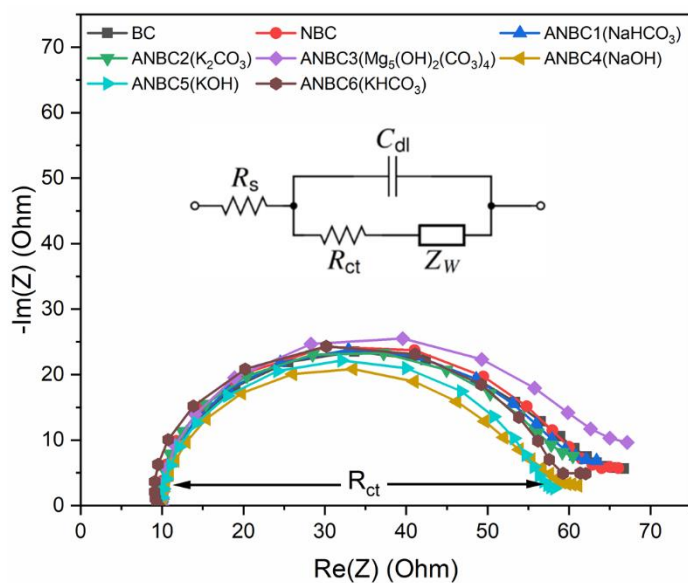


Figure S3.11 The Nyquist plots and equivalent circuit for the catalysts.

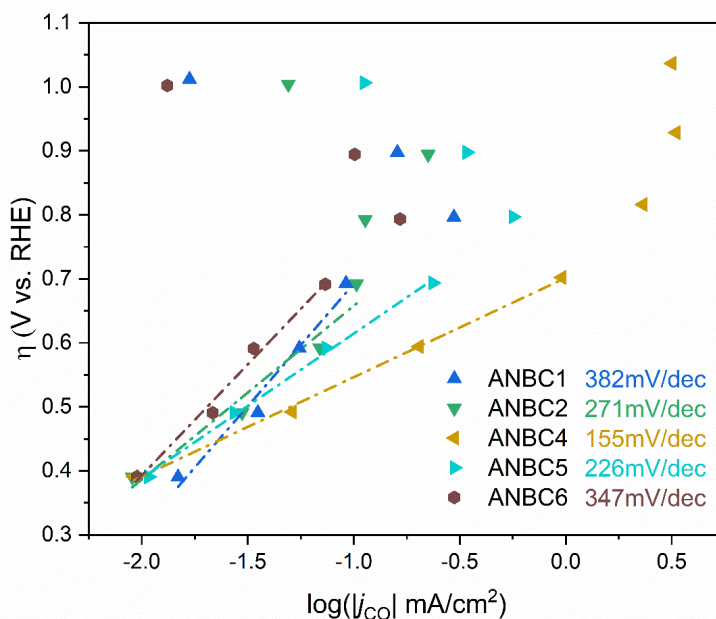


Figure S3.12 Tafel plots of ANBC1 (NaHCO_3), ANBC2 (K_2CO_3), ANBC3 ($\text{Mg}_5(\text{OH})_2(\text{CO}_3)_4$), ANBC4 (NaOH), ANBC5 (KOH), ANBC6 (KHCO_3).

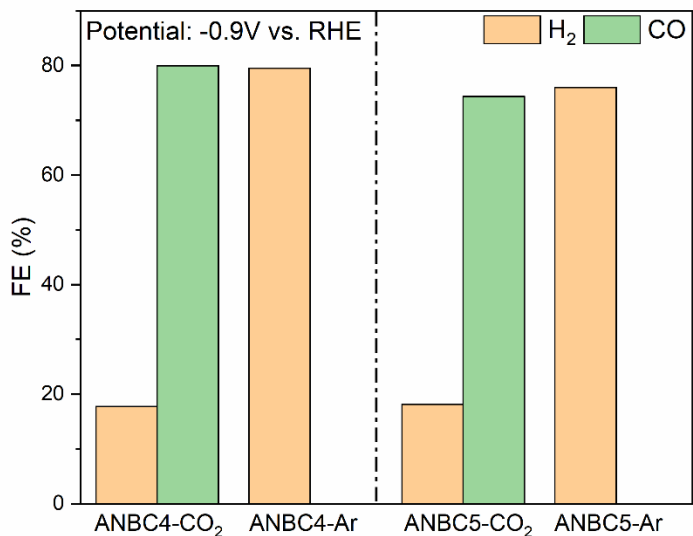


Figure S3.13 Gas products selectivity of chronoamperometry test with a CO₂- and Ar-saturated 0.1 M KHCO₃ electrolyte at -0.9 V vs. RHE using ANBC4(NaOH) and ANBC5(KOH).

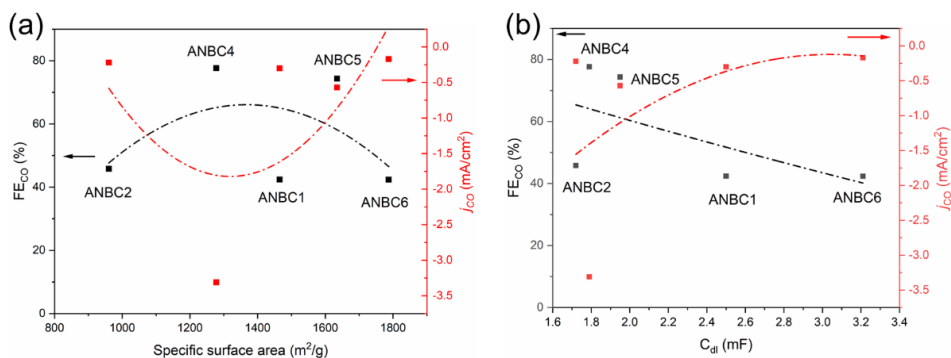


Figure S3.14 The relationship between (a) electrochemical performance and specific surface area, (b) electrochemical performance and ECSA of ANBC1 (NaHCO₃), ANBC2 (K₂CO₃), ANBC3 (Mg₅(OH)₂(CO₃)₄), ANBC4 (NaOH), ANBC5 (KOH), ANBC6 (KHCO₃).

Table S3.1 Textural properties of different carbon catalysts.

Samples	Activator	N ₂ adsorption/desorption				Raman	
		S _{BET}	V _{total} (P/P ₀ =0.95)	V _{meso}	V _{meso} /V _t	D _{avg}	I _D /I _G
		m ² /g	cm ³ /g	cm ³ /g	%	nm	-
BC	-	724.80	0.30	0.012	3.87	1.66	0.84
NBC	-	431.63	0.18	0.011	6.00	1.67	0.89
ANBC1	NaHCO ₃	1465.21	0.80	0.101	12.68	2.18	0.91
ANBC2	K ₂ CO ₃	960.46	0.50	0.075	14.98	2.08	0.88
ANBC3	Mg ₅ (OH) ₂ (CO ₃) ₄	261.98	0.13	0.029	22.46	1.98	1.14
ANBC4	NaOH	1277.94	0.69	0.120	17.33	2.16	0.88
ANBC5	KOH	1634.89	0.79	0.099	12.54	1.93	0.83
ANBC6	KHCO ₃	1786.88	0.87	0.098	11.28	1.95	0.84

Table S3.2 Surface elemental contents and N1s XPS data of different carbon catalysts.

Samples	Activator	C	O	N	Pyridinic N(at.%)	Pyrrolic N(at.%)	Graphitic N(at.%)	Oxidized N(at.%)
		(at.%)	(at.%)	(at.%)	~398.2eV	~399.9eV	~401.6eV	~404.4eV
BC	-	88.41	10.54	1.05	0.00	1.05	0.00	0.00
NBC	-	80.44	8.76	10.81	2.87	3.08	2.39	2.47
ANBC1	NaHCO ₃	80.97	10.32	8.71	1.99	4.79	1.18	0.74
ANBC2	K ₂ CO ₃	81.51	11.09	7.40	1.84	3.08	1.43	1.05
ANBC3	Mg ₅ (OH) ₂ (CO ₃) ₄	77.33	14.97	7.70	2.21	3.02	1.06	1.41
ANBC4	NaOH	87.42	8.73	3.85	0.62	2.18	0.61	0.44
ANBC5	KOH	87.44	7.30	5.26	1.03	2.92	0.93	0.38
ANBC6	KHCO ₃	84.94	7.98	7.08	1.63	3.91	1.01	0.53

References

- (1) Kortlever, R.; Shen, J.; Schouten, K. J. P.; Calle-Vallejo, F.; Koper, M. T. M. Catalysts and Reaction Pathways for the Electrochemical Reduction of Carbon Dioxide. *J. Phys. Chem. Lett.* **2015**, *6* (20), 4073–4082.
- (2) Dinh, C.-T.; Burdyny, T.; Kibria, M. G.; Seifitokaldani, A.; Gabardo, C. M.; De Arquer, F. P. G.; Kiani, A.; Edwards, J. P.; De Luna, P.; Bushuyev, O. S. CO₂ Electroreduction to Ethylene via Hydroxide-Mediated Copper Catalysis at an Abrupt Interface. *Science*. **2018**, *360* (6390), 783–787.
- (3) Birdja, Y. Y.; Pérez-Gallent, E.; Figueiredo, M. C.; Göttle, A. J.; Calle-Vallejo, F.; Koper, M. T. M. Advances and Challenges in Understanding the Electrocatalytic Conversion of Carbon Dioxide to Fuels. *Nat. Energy* **2019**, *4* (9), 732–745.
- (4) Kondratenko, E. V.; Mul, G.; Baltrusaitis, J.; Larrazábal, G. O.; Pérez-Ramírez, J. Status and Perspectives of CO₂ Conversion into Fuels and Chemicals by Catalytic, Photocatalytic and Electrocatalytic Processes. *Energy Environ. Sci.* **2013**, *6* (11), 3112–3135.
- (5) Moura de Salles Pupo, M.; Kortlever, R. Electrolyte Effects on the Electrochemical Reduction of CO₂. *ChemPhysChem* **2019**, *20* (22), 2926–2935.
- (6) Ma, T.; Fan, Q.; Tao, H.; Han, Z.; Jia, M.; Gao, Y.; Ma, W.; Sun, Z. Heterogeneous Electrochemical CO₂ Reduction Using Nonmetallic Carbon-Based Catalysts: Current Status and Future Challenges. *Nanotechnology* **2017**, *28* (47), 472001.
- (7) Lu, Q.; Jiao, F. Electrochemical CO₂ Reduction: Electrocatalyst, Reaction Mechanism, and Process Engineering. *Nano Energy* **2016**, *29*, 439–456.
- (8) Zhang, W.; Hu, Y.; Ma, L.; Zhu, G.; Wang, Y.; Xue, X.; Chen, R.; Yang, S.; Jin, Z. Progress and Perspective of Electrocatalytic CO₂ Reduction for Renewable Carbonaceous Fuels and Chemicals. *Adv. Sci.* **2018**, *5* (1).
- (9) Clark, E. L.; Ringe, S.; Tang, M.; Walton, A.; Hahn, C.; Jaramillo, T. F.; Chan, K.; Bell, A. T. Influence of Atomic Surface Structure on the Activity of Ag for the Electrochemical Reduction of CO₂ to CO. *Acs Catal.* **2019**, *9* (5), 4006–4014.
- (10) Fang, Y.; Flake, J. C. Electrochemical Reduction of CO₂ at Functionalized Au Electrodes. *J. Am. Chem. Soc.* **2017**, *139* (9), 3399–3405.
- (11) Zhu, W.; Kattel, S.; Jiao, F.; Chen, J. G. Shape-controlled CO₂ Electrochemical Reduction on Nanosized Pd Hydride Cubes and Octahedra. *Adv. Energy Mater.* **2019**, *9* (9), 1802840.

- (12) Ertem, M. Z.; Konezny, S. J.; Araujo, C. M.; Batista, V. S. Functional Role of Pyridinium during Aqueous Electrochemical Reduction of CO₂ on Pt (111). *J. Phys. Chem. Lett.* **2013**, *4* (5), 745–748.
- (13) Zhang, T.; Li, X.; Qiu, Y.; Su, P.; Xu, W.; Zhong, H.; Zhang, H. Multilayered Zn Nanosheets as an Electrocatalyst for Efficient Electrochemical Reduction of CO₂. *J. Catal.* **2018**, *357*, 154–162.
- (14) Cui, C.; Han, J.; Zhu, X.; Liu, X.; Wang, H.; Mei, D.; Ge, Q. Promotional Effect of Surface Hydroxyls on Electrochemical Reduction of CO₂ over SnO_x/Sn Electrode. *J. Catal.* **2016**, *343*, 257–265.
- (15) Jiang, K.; Huang, Y.; Zeng, G.; Toma, F. M.; Goddard III, W. A.; Bell, A. T. Effects of Surface Roughness on the Electrochemical Reduction of CO₂ over Cu. *ACS Energy Lett.* **2020**, *5* (4), 1206–1214.
- (16) Chou, T.-C.; Chang, C.-C.; Yu, H.-L.; Yu, W.-Y.; Dong, C.-L.; Velasco-Vélez, J.-J.; Chuang, C.-H.; Chen, L.-C.; Lee, J.-F.; Chen, J.-M. Controlling the Oxidation State of the Cu Electrode and Reaction Intermediates for Electrochemical CO₂ Reduction to Ethylene. *J. Am. Chem. Soc.* **2020**, *142* (6), 2857–2867.
- (17) Van Daele, K.; De Mot, B.; Pupo, M.; Daems, N.; Pant, D.; Kortlever, R.; Breugelmans, T. Sn-Based Electrocatalyst Stability: A Crucial Piece to the Puzzle for the Electrochemical CO₂ Reduction toward Formic Acid. *ACS Energy Lett.* **2021**, *6* (12), 4317–4327.
- (18) Hu, C.; Dai, L. Doping of Carbon Materials for Metal-Free Electrocatalysis. *Adv. Mater.* **2019**, *31* (7), 1–17.
- (19) Hu, C.; Qu, J.; Xiao, Y.; Zhao, S.; Chen, H.; Dai, L. Carbon Nanomaterials for Energy and Biorelated Catalysis: Recent Advances and Looking Forward. *ACS Cent. Sci.* **2019**, *5* (3), 389–408.
- (20) Vasileff, A.; Zheng, Y.; Qiao, S. Z. Carbon Solving Carbon's Problems: Recent Progress of Nanostructured Carbon-Based Catalysts for the Electrochemical Reduction of CO₂. *Adv. Energy Mater.* **2017**, *7* (21), 1–21.
- (21) Duan, X.; Xu, J.; Wei, Z.; Ma, J.; Guo, S.; Wang, S.; Liu, H.; Dou, S. Metal-Free Carbon Materials for CO₂ Electrochemical Reduction. *Adv. Mater.* **2017**, *29* (41), 1–20.
- (22) Ma, C.; Hou, P.; Wang, X.; Wang, Z.; Li, W.; Kang, P. Carbon Nanotubes with Rich Pyridinic Nitrogen for Gas Phase CO₂ Electroreduction. *Appl. Catal. B Environ.* **2019**, *250*, 347–354.

- (23) Jhong, H. R. M.; Tornow, C. E.; Smid, B.; Gewirth, A. A.; Lyth, S. M.; Kenis, P. J. A. A Nitrogen-Doped Carbon Catalyst for Electrochemical CO₂ Conversion to CO with High Selectivity and Current Density. *ChemSusChem* **2017**, *10* (6), 1094–1099.
- (24) Cui, X.; Pan, Z.; Zhang, L.; Peng, H.; Zheng, G. Selective Etching of Nitrogen-Doped Carbon by Steam for Enhanced Electrochemical CO₂ Reduction. *Adv. Energy Mater.* **2017**, *7* (22), 201701456.
- (25) Sun, X.; Kang, X.; Zhu, Q.; Ma, J.; Yang, G.; Liu, Z.; Han, B. Very Highly Efficient Reduction of CO₂ to CH₄ Using Metal-Free N-Doped Carbon Electrodes. *Chem. Sci.* **2016**, *7* (4), 2883–2887.
- (26) Wang, H.; Chen, Y.; Hou, X.; Ma, C.; Tan, T. Nitrogen-Doped Graphenes as Efficient Electrocatalysts for the Selective Reduction of Carbon Dioxide to Formate in Aqueous Solution. *Green Chem.* **2016**, *18* (11), 3250–3256.
- (27) Wang, H.; Jia, J.; Song, P.; Wang, Q.; Li, D.; Min, S.; Qian, C.; Wang, L.; Li, Y. F.; Ma, C.; Wu, T.; Yuan, J.; Antonietti, M.; Ozin, G. A. Efficient Electrocatalytic Reduction of CO₂ by Nitrogen-Doped Nanoporous Carbon/Carbon Nanotube Membranes: A Step Towards the Electrochemical CO₂ Refinery. *Angew. Chemie - Int. Ed.* **2017**, *56* (27), 7847–7852.
- (28) Song, Y.; Chen, W.; Zhao, C.; Li, S.; Wei, W.; Sun, Y. Metal-Free Nitrogen-Doped Mesoporous Carbon for Electroreduction of CO₂ to Ethanol. *Angew. Chemie - Int. Ed.* **2017**, *56* (36), 10840–10844.
- (29) Liu, W.-J.; Jiang, H.; Yu, H.-Q. Emerging Applications of Biochar-Based Materials for Energy Storage and Conversion. *Energy Environ. Sci.* **2019**, *12* (6), 1751–1779.
- (30) Zhang, Z.; Yang, S.; Li, H.; Zan, Y.; Li, X.; Zhu, Y.; Dou, M.; Wang, F. Sustainable Carbonaceous Materials Derived from Biomass as Metal-Free Electrocatalysts. *Adv. Mater.* **2019**, *31* (13), 1–16.
- (31) Yu, F.; Li, S.; Chen, W.; Wu, T.; Peng, C. Biomass-Derived Materials for Electrochemical Energy Storage and Conversion: Overview and Perspectives. *Energy Environ. Mater.* **2019**, *2* (1), 55–67.
- (32) Peng, X.; Zhang, L.; Chen, Z.; Zhong, L.; Zhao, D.; Chi, X.; Zhao, X.; Li, L.; Lu, X.; Leng, K.; Liu, C.; Liu, W.; Tang, W.; Loh, K. P. Hierarchically Porous Carbon Plates Derived from Wood as Bifunctional ORR/OER Electrodes. *Adv. Mater.* **2019**, *31* (16).
- (33) Niu, J.; Shao, R.; Liu, M.; Zan, Y.; Dou, M.; Liu, J.; Zhang, Z.; Huang, Y.; Wang, F. Porous Carbons Derived from Collagen-Enriched Biomass: Tailored Design, Synthesis, and

Application in Electrochemical Energy Storage and Conversion. *Adv. Funct. Mater.* **2019**, 1905095.

(34) Niu, Q.; Gao, K.; Tang, Q.; Wang, L.; Han, L.; Fang, H.; Zhang, Y.; Wang, S.; Wang, L. Large-Size Graphene-like Porous Carbon Nanosheets with Controllable N-Doped Surface Derived from Sugarcane Bagasse Pith/Chitosan for High Performance Supercapacitors. *Carbon*. **2017**, 123, 290–298.

(35) Liu, W. J.; Jiang, H.; Yu, H. Q. Emerging Applications of Biochar-Based Materials for Energy Storage and Conversion. *Energy Environ. Sci.* **2019**, 12 (6), 1751–1779.

(36) Li, X.; Guan, B. Y.; Gao, S.; Lou, X. W. A General Dual-Templating Approach to Biomass-Derived Hierarchically Porous Heteroatom-Doped Carbon Materials for Enhanced Electrocatalytic Oxygen Reduction. *Energy Environ. Sci.* **2019**, 12 (2), 648–655.

(37) Borghei, M.; Lehtonen, J.; Liu, L.; Rojas, O. J. Advanced Biomass-Derived Electrocatalysts for the Oxygen Reduction Reaction. *Adv. Mater.* **2018**, 30 (24), 1–27.

(38) Li, F.; Xue, M.; Knowles, G. P.; Chen, L.; MacFarlane, D. R.; Zhang, J. Porous Nitrogen-Doped Carbon Derived from Biomass for Electrocatalytic Reduction of CO₂ to CO. *Electrochim. Acta* **2017**, 245, 561–568.

(39) Hao, X.; An, X.; Patil, A. M.; Wang, P.; Ma, X.; Du, X.; Hao, X.; Abudula, A.; Guan, G. Biomass-Derived N-Doped Carbon for Efficient Electrocatalytic CO₂ Reduction to CO and Zn–CO₂ Batteries. *ACS Appl. Mater. Interfaces* **2021**, 13(3), 3738–3747.

(40) Liu, W.; Qi, J.; Bai, P.; Zhang, W.; Xu, L. Utilizing Spatial Confinement Effect of N Atoms in Micropores of Coal-Based Metal-Free Material for Efficiently Electrochemical Reduction of Carbon Dioxide. *Appl. Catal. B Environ.* **2020**, 272, 118974.

(41) Scimeca, M.; Bischetti, S.; Lamsira, H. K.; Bonfiglio, R.; Bonanno, E. Energy Dispersive X-Ray (EDX) Microanalysis: A Powerful Tool in Biomedical Research and Diagnosis. *Eur. J. Histochem. EJH* **2018**, 62 (1).

(42) Thommes, M.; Kaneko, K.; Neimark, A. V.; Olivier, J. P.; Rodriguez-Reinoso, F.; Rouquerol, J.; Sing, K. S. W. Physisorption of Gases, with Special Reference to the Evaluation of Surface Area and Pore Size Distribution (IUPAC Technical Report). *Pure Appl. Chem.* **2015**, 87 (9–10), 1051–1069.

(43) Liu, Y.; Dai, G.; Zhu, L.; Wang, S. Green Conversion of Microalgae into High-Performance Sponge-like Nitrogen-Enriched Carbon. *ChemElectroChem* **2019**, 6 (3), 602.

- (44) Hou, L.; Hu, Z.; Wang, X.; Qiang, L.; Zhou, Y.; Lv, L.; Li, S. Hierarchically Porous and Heteroatom Self-Doped Graphitic Biomass Carbon for Supercapacitors. *J. Colloid Interface Sci.* **2019**, *540* (c), 88–96.
- (45) Katsounaros, I.; Cherevko, S.; Zeradjanin, A. R.; Mayrhofer, K. J. J. Oxygen Electrochemistry as a Cornerstone for Sustainable Energy Conversion. *Angew. Chemie Int. Ed.* **2014**, *53* (1), 102–121.
- (46) Feng, H.; Hu, H.; Dong, H.; Xiao, Y.; Cai, Y.; Lei, B.; Liu, Y.; Zheng, M. Hierarchical Structured Carbon Derived from Bagasse Wastes: A Simple and Efficient Synthesis Route and Its Improved Electrochemical Properties for High-Performance Supercapacitors. *J. Power Sources* **2016**, *302*, 164–173.
- (47) Li, H.; Xiao, N.; Hao, M.; Song, X.; Wang, Y.; Ji, Y.; Liu, C.; Li, C.; Guo, Z.; Zhang, F.; Qiu, J. Efficient CO₂ Electroreduction over Pyridinic-N Active Sites Highly Exposed on Wrinkled Porous Carbon Nanosheets. *Chem. Eng. J.* **2018**, *351*, 613–621.
- (48) Sharma, P. P.; Wu, J.; Yadav, R. M.; Liu, M.; Wright, C. J.; Tiwary, C. S.; Yakobson, B. I.; Lou, J.; Ajayan, P. M.; Zhou, X. D. Nitrogen-Doped Carbon Nanotube Arrays for High-Efficiency Electrochemical Reduction of CO₂: On the Understanding of Defects, Defect Density, and Selectivity. *Angew. Chemie - Int. Ed.* **2015**, *54* (46), 13701–13705.
- (49) Zou, K.; Deng, Y.; Chen, J.; Qian, Y.; Yang, Y.; Li, Y.; Chen, G. Hierarchically Porous Nitrogen-Doped Carbon Derived from the Activation of Agriculture Waste by Potassium Hydroxide and Urea for High-Performance Supercapacitors. *J. Power Sources* **2018**, *378*, 579–588.
- (50) Zhao, C.; Wang, Q.; Lu, Y.; Li, B.; Chen, L.; Hu, Y.-S. High-Temperature Treatment Induced Carbon Anode with Ultrahigh Na Storage Capacity at Low-Voltage Plateau. *Sci. Bull.* **2018**, *63* (17), 1125–1129.
- (51) Li, Y.; Xing, B.; Wang, X.; Wang, K.; Zhu, L.; Wang, S. Nitrogen-Doped Hierarchical Porous Biochar Derived from Corn Stalks for Phenol-Enhanced Adsorption. *Energy and Fuels* **2019**, *33*(12), 12459–12468.
- (52) Brun, N.; Prabakaran, S. R. S.; Surcin, C.; Morcrette, M.; Deleuze, H.; Birot, M.; Babot, O.; Achard, M.-F.; Backov, R. Design of Hierarchical Porous Carbonaceous Foams from a Dual-Template Approach and Their Use as Electrochemical Capacitor and Li Ion Battery Negative Electrodes. *J. Phys. Chem. C* **2012**, *116* (1), 1408–1421.
- (53) Deng, J.; Xiong, T.; Xu, F.; Li, M.; Han, C.; Gong, Y.; Wang, H.; Wang, Y. Inspired by Bread Leavening: One-Pot Synthesis of Hierarchically Porous Carbon for Supercapacitors. *Green Chem.* **2015**, *17* (7), 4053–4060.

- (54) Li, K.; Chen, W.; Yang, H.; Chen, Y.; Xia, S.; Xia, M.; Tu, X.; Chen, H. Mechanism of Biomass Activation and Ammonia Modification for Nitrogen-Doped Porous Carbon Materials. *Bioresour. Technol.* **2019**, *280*, 260–268.
- (55) Wang, Q.; Yan, J.; Wang, Y.; Wei, T.; Zhang, M.; Jing, X.; Fan, Z. Three-Dimensional Flower-like and Hierarchical Porous Carbon Materials as High-Rate Performance Electrodes for Supercapacitors. *Carbon* **2014**, *67*, 119–127.
- (56) Kang, X.; Zhu, H.; Wang, C.; Sun, K.; Yin, J. Biomass Derived Hierarchically Porous and Heteroatom-Doped Carbons for Supercapacitors. *J. Colloid Interface Sci.* **2018**, *509*, 369–383.
- (57) Wang, L.; Yan, W.; He, C.; Wen, H.; Cai, Z.; Wang, Z.; Chen, Z.; Liu, W. Microwave-Assisted Preparation of Nitrogen-Doped Biochars by Ammonium Acetate Activation for Adsorption of Acid Red 18. *Appl. Surf. Sci.* **2018**, *433*, 222–231.
- (58) Liu, J.; Deng, Y.; Li, X.; Wang, L. Promising Nitrogen-Rich Porous Carbons Derived from One-Step Calcium Chloride Activation of Biomass-Based Waste for High Performance Supercapacitors. *ACS Sustain. Chem. Eng.* **2016**, *4* (1), 177–187.
- (59) Yu, W.; Lian, F.; Cui, G.; Liu, Z. N-Doping Effectively Enhances the Adsorption Capacity of Biochar for Heavy Metal Ions from Aqueous Solution. *Chemosphere* **2018**, *193*, 8–16.
- (60) Yao, P.; Qiu, Y.; Zhang, T.; Su, P.; Li, X.; Zhang, H. N-Doped Nanoporous Carbon from Biomass as a Highly Efficient Electrocatalyst for the CO₂ Reduction Reaction. *ACS Sustain. Chem. Eng.* **2019**, *7* (5), 5249–5255.
- (61) Paul, R.; Zhu, L.; Chen, H.; Qu, J.; Dai, L. Recent Advances in Carbon-Based Metal-Free Electrocatalysts. *Adv. Mater.* **2019**, *1806403*, 1–24.
- (62) Kuang, M.; Guan, A.; Gu, Z.; Han, P.; Qian, L.; Zheng, G. Enhanced N-Doping in Mesoporous Carbon for Efficient Electrocatalytic CO₂ Conversion. *Nano Res.* **2019**, *12* (9), 2324–2329.
- (63) Zhang, Z.; Yu, L.; Tu, Y.; Chen, R.; Wu, L.; Zhu, J.; Deng, D. Unveiling the Active Site of Metal-Free Nitrogen-Doped Carbon for Electrocatalytic Carbon Dioxide Reduction. *Cell Reports Phys. Sci.* **2020**, *1* (8), 100145.
- (64) Duan, B.; Gao, X.; Yao, X.; Fang, Y.; Huang, L.; Zhou, J.; Zhang, L. Unique Elastic N-Doped Carbon Nanofibrous Microspheres with Hierarchical Porosity Derived from Renewable Chitin for High Rate Supercapacitors. *Nano Energy* **2016**, *27*, 482–491.

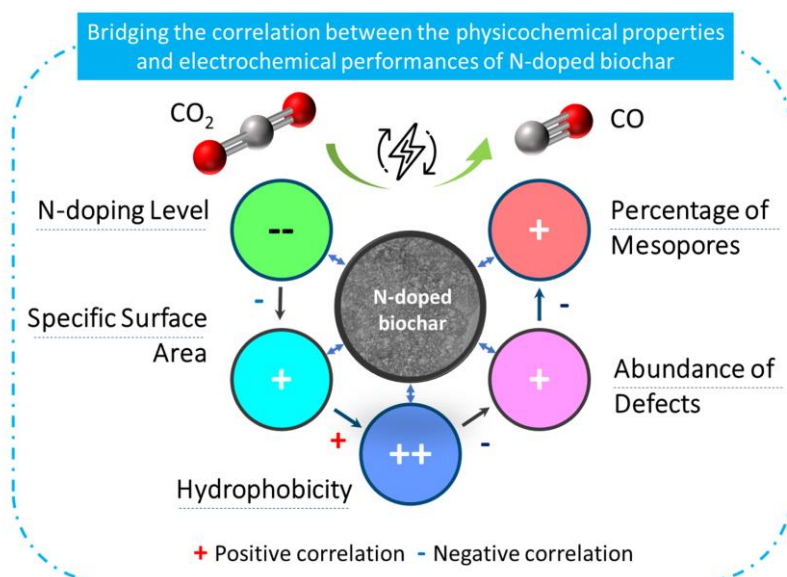
- (65) Przepiórski, J.; Karolczyk, J.; Takeda, K.; Tsumura, T.; Toyoda, M.; Morawski, A. W. Porous Carbon Obtained by Carbonization of PET Mixed with Basic Magnesium Carbonate: Pore Structure and Pore Creation Mechanism. *Ind. Eng. Chem. Res.* **2009**, *48* (15), 7110–7116.
- (66) Dobeles, G.; Dizhbite, T.; Gil, M. V; Volperts, A.; Centeno, T. A. Production of Nanoporous Carbons from Wood Processing Wastes and Their Use in Supercapacitors and CO₂ Capture. *Biomass and Bioenergy* **2012**, *46*, 145–154.
- (67) Pezoti, O.; Cazetta, A. L.; Bedin, K. C.; Souza, L. S.; Martins, A. C.; Silva, T. L.; Júnior, O. O. S.; Visentainer, J. V; Almeida, V. C. NaOH-Activated Carbon of High Surface Area Produced from Guava Seeds as a High-Efficiency Adsorbent for Amoxicillin Removal: Kinetic, Isotherm and Thermodynamic Studies. *Chem. Eng. J.* **2016**, *288*, 778–788.
- (68) Ouyang, T.; Zhang, T.; Wang, H.; Yang, F.; Yan, J.; Zhu, K.; Ye, K.; Wang, G.; Zhou, L.; Cheng, K. High-Throughput Fabrication of Porous Carbon by Chemical Foaming Strategy for High Performance Supercapacitor. *Chem. Eng. J.* **2018**, *352*, 459–468.
- (69) Yu, S.; Sun, N.; Hu, L.; Wang, L.; Zhu, Q.; Guan, Y.; Xu, B. Self-Template and Self-Activation Synthesis of Nitrogen-Doped Hierarchical Porous Carbon for Supercapacitors. *J. Power Sources* **2018**, *405*, 132–141.
- (70) Wu, T.; Wang, G.; Dong, Q.; Zhan, F.; Zhang, X.; Li, S.; Qiao, H.; Qiu, J. Starch Derived Porous Carbon Nanosheets for High-Performance Photovoltaic Capacitive Deionization. *Environ. Sci. Technol.* **2017**, *51* (16), 9244–9251.
- (71) Sevilla, M.; Fuertes, A. B. A Green Approach to High-Performance Supercapacitor Electrodes: The Chemical Activation of Hydrochar with Potassium Bicarbonate. *ChemSusChem* **2016**, *9* (14), 1880–1888.
- (72) Deng, J.; Xiong, T.; Wang, H.; Zheng, A.; Wang, Y. Effects of Cellulose, Hemicellulose, and Lignin on the Structure and Morphology of Porous Carbons. *ACS Sustain. Chem. Eng.* **2016**, *4* (7), 3750–3756.
- (73) Arslanoğlu, H. Direct and Facile Synthesis of Highly Porous Low Cost Carbon from Potassium-Rich Wine Stone and Their Application for High-Performance Removal. *J. Hazard. Mater.* **2019**, *374*, 238–247.
- (74) Li, W.; Herkt, B.; Seredych, M.; Bandoz, T. J. Pyridinic-N Groups and Ultramicropore Nanoreactors Enhance CO₂ Electrochemical Reduction on Porous Carbon Catalysts. *Appl. Catal. B Environ.* **2017**, *207*, 195–206.

- (75) Taer, E.; Agustino, A.; Farma, R.; Taslim, R.; Paiszal, M.; Ira, A.; Yardi, S. D.; Sari, Y. P.; Yusra, H.; Nurjanah, S. The Relationship of Surface Area to Cell Capacitance for Monolith Carbon Electrode from Biomass Materials for Supercapacitor Application. In *Journal of Physics: Conference Series*; IOP Publishing, 2018; Vol. 1116, p 32040.
- (76) Voiry, D.; Chhowalla, M.; Gogotsi, Y.; Kotov, N. A.; Li, Y.; Penner, R. M.; Schaak, R. E.; Weiss, P. S. Best Practices for Reporting Electrocatalytic Performance of Nanomaterials. *ACS nano*. **2018**, *12*(10), 9635–9638.
- (77) Daiyan, R.; Tan, X.; Chen, R.; Saputera, W. H.; Tahini, H. A.; Lovell, E.; Ng, Y. H.; Smith, S. C.; Dai, L.; Lu, X.; Amal, R. Electroreduction of CO₂ to CO on a Mesoporous Carbon Catalyst with Progressively Removed Nitrogen Moieties. *ACS Energy Lett.* **2018**, *3* (9), 2292–2298.
- (78) Dong, Y.; Zhang, Q.; Tian, Z.; Li, B.; Yan, W.; Wang, S.; Jiang, K.; Su, J.; Oloman, C. W.; Gyenge, E. L.; Ge, R.; Lu, Z.; Ji, X.; Chen, L. Ammonia Thermal Treatment toward Topological Defects in Porous Carbon for Enhanced Carbon Dioxide Electroreduction. *Adv. Mater.* **2020**, *32* (28), 2001300.
- (79) Adegoke, K. A.; Maxakato, N. W. Electrochemical CO₂ Conversion to Fuels on Metal-Free N-Doped Carbon-Based Materials: Functionalities, Mechanistic, and Technoeconomic Aspects. *Mater. Today Chem.* **2022**, *24*, 100838.
- (80) Wang, H.; Maiyalagan, T.; Wang, X. Review on Recent Progress in Nitrogen-Doped Graphene: Synthesis, Characterization, and Its Potential Applications. *Acs Catal.* **2012**, *2* (5), 781–794.
- (81) Wang, H.; Jia, J.; Song, P.; Wang, Q.; Li, D.; Min, S.; Qian, C.; Wang, L.; Li, Y. F.; Ma, C. Efficient Electrocatalytic Reduction of CO₂ by Nitrogen-doped Nanoporous Carbon/Carbon Nanotube Membranes: A Step towards the Electrochemical CO₂ Refinery. *Angew. Chemie* **2017**, *129* (27), 7955–7960.
- (82) Wang, W.; Shang, L.; Chang, G.; Yan, C.; Shi, R.; Zhao, Y.; Waterhouse, G. I. N.; Yang, D.; Zhang, T. Intrinsic Carbon-Defect-Driven Electrocatalytic Reduction of Carbon Dioxide. *Adv. Mater.* **2019**, *31* (19), 1–7.
- (83) Ma, X.; Du, J.; Sun, H.; Ye, F.; Wang, X.; Xu, P.; Hu, C.; Zhang, L.; Liu, D. Boron, Nitrogen Co-Doped Carbon with Abundant Mesopores for Efficient CO₂ Electroreduction. *Appl. Catal. B Environ.* **2021**, *298*, 120543.
- (84) Hursán, D.; Samu, A. A.; Janovák, L.; Artyushkova, K.; Asset, T.; Atanassov, P.; Janáky, C. Morphological Attributes Govern Carbon Dioxide Reduction on N-Doped Carbon Electrodes. *Joule* **2019**, *3* (7), 1719–1733.

(85) Lobaccaro, P.; Singh, M. R.; Clark, E. L.; Kwon, Y.; Bell, A. T.; Ager, J. W. Effects of Temperature and Gas–Liquid Mass Transfer on the Operation of Small Electrochemical Cells for the Quantitative Evaluation of CO₂ Reduction Electrocatalysts. *Phys. Chem. Chem. Phys.* **2016**, *18* (38), 26777–26785.

4

Tuning the properties of N-doped biochar for selective CO₂ electroreduction to CO



Abstract: Nitrogen-doped (N-doped) carbon catalysts have been widely studied for electrochemical CO₂ reduction to CO. However, the correlation between the physicochemical properties of N-doped carbon catalysts and their electrocatalytic performance for the CO₂RR is still unclear. Herein, a series of N-doped biochar catalysts with different physicochemical properties were synthesized by tuning the carbonization temperature and N-doping level and used for the CO₂RR to analyze the structure-performance relationship. The prepared catalysts exhibited massive differences in maximum faradaic efficiency to CO from 26.8% to 94.9% at around -0.8 to -0.9 V vs. RHE. In addition, we find that simply increasing the specific surface area and N-doping level of the catalysts does not effectively improve the catalytic performance for CO₂RR. A multivariate correlation analysis reveals a negative correlation between the N-doping content and the electrochemical performance. The porous structural properties exhibit a positive correlation to the FE_{CO} but almost no correlation to j_{CO} . Interestingly, improving the degree of graphitization, surface hydrophobicity, the abundance of defects and optimizing the porosity of N-doped biochar catalyst can efficiently enhance the catalytic performance for the CO₂RR. We conclude that comprehensively analyzing the synergistic effect of various properties of N-doped biochar is critical to reveal structure-activity relationships.

4.1 Introduction

Excessive CO₂ emissions have given rise to global warming and climate change.¹ In the past few decades, CO₂ conversion technologies have been developed to convert waste CO₂ into valuable products and close the anthropogenic carbon cycle.² Among them, the electrochemical CO₂ reduction reaction (CO₂RR) has attracted much attention,^{3,4} as it can convert CO₂ into fuels and chemicals, simultaneously storing intermittent renewable electricity into chemical bonds.⁵ Various reduction products such as CO, formic acid, methane, ethylene and ethanol can be produced from the CO₂RR via different reaction pathways.^{6,7} CO is an attractive product that can be widely used for downstream chemical transformations.⁸ Moreover, the conversion of CO₂ to CO is a 2-electron transfer process that can be performed at relatively low overpotentials with a high selectivity to CO.⁹ Although the market price (per ton) of CO is lower than that of hydrocarbons, considering the power consumption and the cost of separation of multi-carbon products, CO is still one of the most competitive products from the CO₂RR.¹⁰ Au and Ag have been identified as effective electrocatalysts to reduce CO₂ to CO,¹¹ however, scarcity and a relatively high price can hinder the large-scale utilization of precious metal-based catalysts for the CO₂RR.

Recently, metal-free N-doped carbon materials have been shown as efficient alternative catalysts for the CO₂RR to CO.^{12,13} Almost all advanced carbon materials, such as carbon nanotubes,¹⁴ graphene,¹⁵ and nanodiamonds,¹⁶ can be used as carbon precursors to synthesize N-doped carbon materials by in-situ doping or post-doping. Compared with Ag and Au-based electrodes, N-doped carbon materials exhibit a comparable catalytic performance but offer advantages, such as a relatively low cost, long stability, high tunability, and strong resistance to harsh reaction conditions.¹⁷ However, the exact correlation between the physicochemical properties of N-doped carbon materials and their electrochemical performance for CO₂RR is still unclear. Generally, specific surface area and N-doping content are considered as two important factors governing catalytic performance, with many studies attributing better catalytic performances to an increase in either the specific surface area or N-doping levels.^{18,19} The rationale behind this is that a larger specific area and rich pore structure enhances the mass transfer of reactants and electrolyte,²⁰ while the introduction of N into the carbon skeleton tunes the atomic charge and spin distribution of carbon materials and acts as an active site for the CO₂RR.²¹ Although the exact nature of the active site of N-doped carbon materials is still under debate, the catalytic performance for the CO₂RR has been enhanced by increasing either the total N-doping content or the content of specific N-containing species, as verified by theoretical calculations and experimental analyses.^{22–27}

Interestingly, there are some studies that do not fully support the relationship between the electrocatalytic performance and the specific surface area and N-doping content. For

instance, Daiyan et al.²⁸ gradually reduced the N content by an annealing treatment and found that a lower N content leads to better performances, ultimately linking the catalytic performance to the abundance of defects. Furthermore, Hursán et al.²⁹ prepared N-doped carbon catalysts with different pore sizes via a sacrificial support method and found that the catalysts showed different selectivity, activity and stability even with similar N-doping content and a similar distribution of N-containing species, and no correlation was found between the specific surface area and catalytic performance. In previous work, we also found that there is no significant correlation between the catalytic performance and specific surface area and N-doping content, and that the ratio of mesopores and the degree of graphitization play an essential role.³⁰ We believe that an over-emphasis on the effects of specific surface area and N-doping level can easily lead to lopsided conclusions, which do not fully reflect the actual structure-performance relationships of N-doped carbon catalysts. Therefore, to develop better N-doped carbon catalysts for the CO₂RR, it is necessary to further elucidate the structure-performance relationship of N-doped carbon materials through a comprehensive and integrated analysis.

Biomass can be used as a carbon precursor to synthesize N-doped carbon materials for the CO₂RR. Compared to fossil-derived carbon materials, biochar is a renewable source, and the raw materials are generally widely distributed, abundantly available, easily accessible, and more eco-friendly.³¹ In addition, using biochar to synthesize N-doped carbon materials can provide sustainable and “green” catalysts for the CO₂RR, simultaneously enhancing the added value of waste biomass and providing a possibility to realize a high-value application of waste biomass materials.³² More importantly, the lignocellulose-derived biochar catalysts have good textural tunability. By changing different preparation conditions, such as the carbonization temperature, N doping precursor and doping amount and the type and amount of activator, one can easily obtain carbon materials with significantly different physicochemical properties. Therefore, testing biomass-derived N-doped carbon materials with different properties for the CO₂RR can help to investigate the correlation between different physicochemical properties of catalysts and their catalytic performance.

In this study, a set of sugarcane bagasse-derived N-doped carbon catalysts were synthesized by a one-step pyrolysis method. The physicochemical properties of the N-doped biochar catalysts were tuned by changing the carbonization temperature and N-doping level, respectively. Combining the characterization results and the electrochemical measurements, we have conducted a comprehensive analysis of the influence of the physicochemical properties of N-doped biochar materials on their CO₂RR performance. A higher carbonization temperature (800 °C) yielded an optimal N-doped biochar, which showed an 89.3% faradaic efficiency to CO at -0.82 V vs. RHE. Interestingly, we find that simply increasing the amount of N-doping is not an efficient method to improve the CO₂RR performance of the catalysts. Moreover, we perform a multivariate correlation analysis by a

statistical approach to analyze the correlation between physicochemical properties and electrochemical performance. The N-doping content shows a negative correlation to the CO₂RR performance whereas the surface hydrophobicity shows a strong positive correlation. Additionally, the porous structural properties (specific surface area, pore volume, etc.) exhibit a positive correlation to the FE_{CO} but almost no correlation to the j_{CO} . Our results show that the CO₂RR performance can be enhanced by improving the hydrophobicity, abundance of defects and optimizing the porosity distribution of N-doped biochar catalysts. These insights can provide guidance for the design and analysis of efficient N-doped carbon catalysts for CO₂RR.

4.2 Experimental

All chemicals were used as received without further purification. The urea (CN₂H₄O, $\geq 99\%$), sodium hydroxide (NaOH, $\geq 98\%$), potassium bicarbonate (KHCO₃, $\geq 99.95\%$, trace metal basis) and Nafion resin solution (5 wt.% in lower aliphatic alcohol and 15-20% water) were purchased from Sigma-Aldrich. The hydrochloric acid (HCl, 37%) and isopropanol (C₃H₈O, $\geq 99.5\%$) were purchased from VWR International. 0.1 M KHCO₃ electrolyte solutions and 1 M HCl solutions were prepared from ultrapure water (Milli-Q IQ 7000, 18.2 M Ω). ICP-OES analyses of the freshly prepared and used 0.1 M KHCO₃ electrolytes indicated that the concentration of transition metal is below the limit of detection, preventing the spontaneous formation of M-N_x sites on the N-doped carbon catalysts.

4.2.1 Synthesis of catalysts

Activated N-doped biochar (ANBC) samples were synthesized by a one-step pyrolysis method. In brief, the received sugarcane bagasse (Maharashtra, India) was washed with ultrapure water three times to remove dust and gravel from the surface and dried in an oven (105 °C) overnight. The dried sugarcane bagasse was ground and sieved to obtain particle sizes of less than 425 μ m before use. Afterwards, 5 g of sugarcane bagasse powder, 10 g of urea, and 15 g of NaOH (mass ratio = 1: 2: 3) were added into a crucible and stirred for 30 minutes to make a homogeneous mixture. Then, the mixture was transferred into a muffle furnace which was purged N₂ with a flow rate of 100 mL/min for 1 hour. The carbonization was carried out at the desired final temperature (600, 700, 800, or 900 °C) for 1 hour with a ramping rate of 10 °C/min under a N₂ atmosphere (100 mL/min, 99.99%, Linde gas). After cooling down to ambient temperature, the obtained product was washed with 1M HCl for 4h at 60 °C to remove the residual sodium containing salts and other impurities. Afterwards the black powder was filtered and rinsed thoroughly with ultrapure water until it reached a neutral pH. Finally, the activated N-doped biochar catalyst was collected and dried at 105 °C

for 12 hours. The obtained catalysts are designated as ANBCT where T represents the carbonization temperature.

To investigate the effect of N-doping level on the performance of the ANBC for the CO₂RR, a series of catalysts with different N-doping levels (ANBC800-XN) were synthesized using the same pyrolysis method at 800 °C while changing the ratio of urea. ANBC800-SN (ANBC800 doped with a slight amount of nitrogen) was synthesized with the mass ratio of sugarcane bagasse, urea, and NaOH being 1: 0.5: 3, ANBC800-LN (ANBC800 doped with a low amount of nitrogen) was synthesized with the ratio of 1: 1: 3, and ANBC800-HN (ANBC800 doped with a high amount of nitrogen) was synthesized with the ratio of 1: 3: 3, respectively. The specific formulation and carbon yields of all prepared samples are listed in Table S4.1.

4.2.2 Catalyst characterization

The morphology and microstructures of all samples were visualized by using a JEOL JSM-6500F scanning electron microscope (SEM) and a JEOL JEM1400 transmission electron microscope (TEM). The porosity characteristics of all carbon catalysts were measured by isothermal N₂ adsorption-desorption at 77 K using a Micromeritics TriStar II 3020 instrument. Specific surface areas were determined by the Brunauer-Emmett-Teller (BET) method, and pore size distributions were calculated based on a density function theory (DFT) model. X-ray diffraction (XRD) patterns were obtained using a Bruker AXS D2 Phaser with Cu-K α radiation ($\lambda = 0.15406$ nm). Raman spectra were recorded from 500 to 3000 cm⁻¹ on a Horiba Scientific LabRAM HR Evolution Raman Spectroscopy system with an excitation wavelength of 514 nm. X-ray photoelectron spectroscopy (XPS) measurements were carried out on a Thermo Scientific K α system with Al K α radiation (1486.7 eV). All binding energies for XPS spectra were calibrated according to the C1s peak at 284.8 eV in CasaXPS. Contact angle measurements were performed via sessile drop using an OCA 25 goniometer (Dataphysics instruments GmbH, Filderstadt, Germany), 2 μ L droplets were dispensed onto substrates using an automatic pipetting unit. Measurements were taken in ambient air with a temperature in the range of 20–24 °C.

4.2.3 Electrode preparation

To prepare a working electrode, 4 mg of catalyst powder was dispersed in a solvent mixture containing 800 μ L ultrapure water, 150 μ L isopropanol, and 50 μ L of 5% Nafion perfluorinated resin solution (5 wt.% in lower aliphatic alcohols and 15-20% water) under sonication for 1h to obtain a homogeneous ink. Afterwards, 200 μ L of the catalyst ink was drop-casted on the center of a 25mm \times 25mm glassy carbon plate (HTW Hochtemperatur-Werkstoffe GmbH, Germany) and dried at room temperature. The geometric surface area of

the working electrode exposed to the electrolyte was equal to 1 cm^2 and the catalyst loading was equal to 0.8 mg/cm^2 .

A $25 \text{ mm} \times 25 \text{ mm} \times 0.1 \text{ mm}$ platinum foil (99.9 %, Mateck, Germany) was used as counter electrode. The counter electrode was cleaned by flame annealing 3 times to remove any possible impurities before use. A leak-free Ag/AgCl electrode (40 mm length, Innovative instrument, USA) was used as reference electrode. The reference electrode was checked every time before use by comparing with a master Ag/AgCl reference electrode (BASi, MF-2056, USA), which is never used experimentally and is kept in pristine working condition.

4.2.4 Electrochemical measurements

Electrochemical measurements of different catalysts were performed in a gas-tight two-compartment H-cell at ambient conditions. Each compartment contained 1.8 mL of 0.1 M KHCO_3 electrolyte, with the anode and cathode compartment separated by a SelemionTM AMV anion exchange membrane (AGC group, Japan).³³ Before electrolysis, the electrolyte was purged with CO_2 for at least 15 min to saturate the 0.1 M KHCO_3 electrolyte. A Biologic SP-200 potentiostat (Biologic, France) was used to control the potential and measure the resulting currents. All potentials in this study are converted to the reversible hydrogen electrode (RHE) scale according to the formula: $E \text{ (V vs. RHE)} = E \text{ (V vs. Ag/AgCl)} + 0.197 + 0.059 \cdot \text{pH}$. Linear sweep voltammograms (LSV) were recorded in Ar-saturated ($\text{pH} = 8.3$) and CO_2 -saturated ($\text{pH} = 6.8$) 0.1 M KHCO_3 electrolytes at a scan rate of 5 mV/s. The electrochemically active surface areas (ECSA) of the electrodes were determined by measuring the double layer capacitance (C_{dl}), which were derived from cyclic voltammetry measurements with a scan rate at 5, 10, 25, and 50 mV/s in a potential window from 0.45 to 0.55 V vs. RHE. The C_{dl} was estimated by plotting the $\Delta j (j_a - j_c)/2$ at 0.50 V vs. RHE against the scan rates, where the slope of the plot gives the C_{dl} . Chronoamperometric electrolysis measurements were conducted for 7 different potentials from -0.5 to -1.1 V vs. RHE (with iR-compensation), and each potential was applied for 1h. The cell resistance (R_u) was measured by potentiostatic electrochemical impedance spectroscopy (PEIS). Automatic ohmic drop correction corrected for 85% of R_u during CO_2RR measurements, while the remaining 15% was corrected manually afterwards. During the chronoamperometry tests, CO_2 was purged continuously into the catholyte with a flow rate of 8 mL/min through a mass flow controller (EL-FLOW Select, Bronkhorst). The gaseous products from the catholyte compartment were measured every 2 min by an in-line gas chromatograph (Compact GC 4.0, G.A.S). The GC was equipped with a flame ionization detector (FID) to measure the hydrocarbon compounds and two thermal conductivity detectors (TCD) to measure CO and H_2 , respectively. A standard calibration curve was made using custom gas mixture cylinders with known concentrations of product gasses in CO_2 (Linde gas Benelux B.V.). An aliquot of the catholyte was collected at the end of the measurements and liquid-phase products were

quantified using a high-performance liquid chromatograph (HPLC, Agilent 1260 Infinity). 5 μL of the liquid sample was injected on two Aminex HPX 87-H columns (Biorad) placed in series. The column oven temperature was maintained constant at 60 $^{\circ}\text{C}$, with a steady flow of rate of 0.6 mL/min of an aqueous 1 mM H_2SO_4 eluent and a refractive index detector (RID) was used for product detection. The total current density and the faradaic efficiency of gaseous products for each sample are average values that were collected from the reaction interval between 42 to 54 minutes, where a relatively stable CO_2RR performance is obtained.

4.3 Results and Discussions

4.3.1 Effect of carbonization temperature

SEM and TEM measurements were performed to visualize the morphology of the activated N-doped biochar (ANBCT) samples prepared at different temperatures (see Figure 4.1). As the carbonization temperature increased from 600 to 900 $^{\circ}\text{C}$, similar morphological structures are observed with SEM which displayed an intertwined particle-stacked structure with multilevel channels. SEM-EDS measurements confirmed that N heteroatoms were doped uniformly into the carbon framework (see Figure S4.1). To further study the microstructure of the prepared samples, TEM measurements were carried out. As shown in Figure 4.1b and d, numerous micropores can be observed in the catalysts prepared at 600 and 700 $^{\circ}\text{C}$. At higher carbonization temperatures, mesopores and wrinkled nano-textures were generated and can be observed clearly in the catalysts prepared at 800 and 900 $^{\circ}\text{C}$.

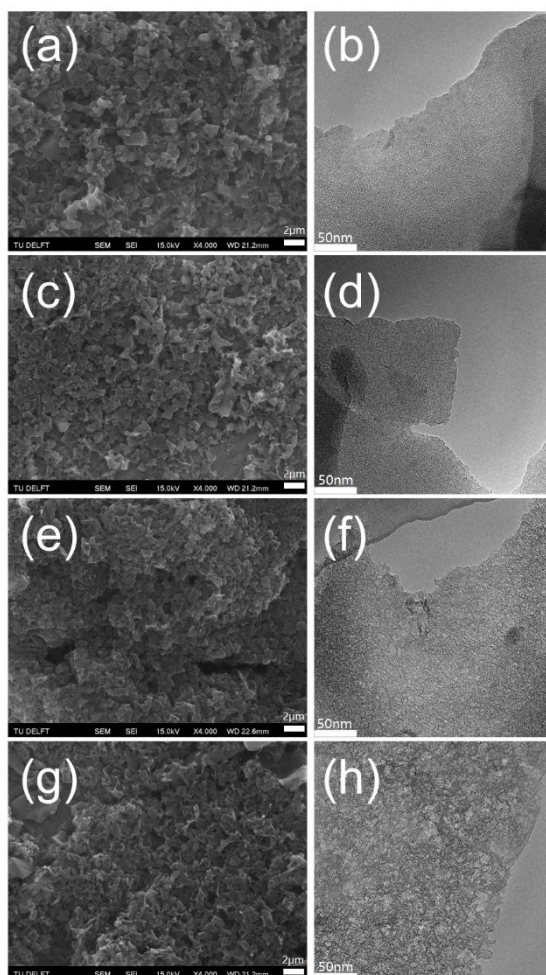


Figure 4.1 SEM (left) and TEM (right) images of ANBC600: (a), (b); ANBC700: (c), (d); ANBC800: (e), (f); and ANBC900: (g), (h).

To further evaluate the porosity of the ANBCT catalysts, N_2 adsorption-desorption isothermal analyses were executed. As shown in Figure 4.2a, the isotherms of ANBC600, ANBC700 and ANBC800 can be categorized into a combined type I and type IV isotherm according to the IUPAC classification. The isotherm increased rapidly at low relative pressure ($P/P_0 < 0.05$) and then remained almost constant. A small hysteresis loop can be observed in these isotherms, which indicates that a small amount of mesopores were developed in these samples. In addition, the small upturned tail observed at high relative pressure ($P/P_0 > 0.95$), indicates that macropores retain in these samples. The isotherm of ANBC900 can be

classified as type IV. An apparent H4 hysteresis loop in the relative pressure ranges from 0.45 to 0.95 suggests the existence of mesopores, which agrees well with the TEM images. The pore size distribution of ANBCT samples calculated by a Density Functional Theory (DFT) model is shown in Figure 4.2b. The pore structural properties are summarized in Table S4.2. Overall, with an increase of carbonization temperature, the ANBC samples exhibit a broader pore size distribution. Moreover, the specific surface area increases from 450.5 m²/g for ANBC600 to 1426.9 m²/g for ANBC800 with the increase of carbonization temperature from 600 °C to 800 °C. As the carbonization temperature increased further to 900 °C, the specific surface area of ANBC900 decreased slightly to 1228.7 m²/g. However, the total pore volume kept increasing with rising carbonization temperatures. The increase in specific surface area and total pore volume is explained by a more efficient reaction of the activator (NaOH) with the bagasse and urea with increasing carbonization temperatures.³⁴ When the carbonization temperature is increased to 900 °C, the extreme temperature damages the structure and part of the micropores collapse or merge into mesopores.³⁵ This leads to a decrease in specific surface area but an increase in total pore volume. Therefore, the ratio of mesopores (56.3%) and the average pore size (2.7 nm) of ANBC900 are larger than for other samples (Table S4.2), which is consistent with the TEM results. In summary, these results indicate that the carbonization temperature plays a vital role in the porosity development of the ANBC samples.

The XRD patterns of the ANBCT samples are plotted in Figure 4.2c. All of the ANBCT samples show two broad diffraction peaks located at around $2\theta = 25^\circ$ and 44° , which are ascribed to the (002) and (100) planes of graphite, showing as dominant feature of amorphous carbon.³⁶ Notably, the (002) peak reflection of ANBC900 shifts slightly to around 26° , indicating a higher degree of graphitization than other samples.³⁷ The Raman spectra in Figure 4.2d show two intensive peaks centered at around 1350 cm⁻¹ and 1590 cm⁻¹ that are attributed to the D band and G band of carbon materials. In particular, ANBC900 shows another distinct peak at 2700 cm⁻¹, which is considered as a typical signal of a graphite/graphene structure,³⁸ indicating that ANBC900 has a higher degree of graphitization. The relative intensity ratio of the D and G bands (I_D/I_G) is used as an index to evaluate the abundance of defects of carbon materials, with higher I_D/I_G value indicating a larger amount of defects.³⁹ The I_D/I_G values of ANBCT samples show a slowly increasing trend from 1.029 (ANBC600) to 1.101 (ANBC800) and then a slight decrease to 0.949 as the temperature rises to 900 °C. This suggests that the activator and nitrogen precursor create more defects in the carbon structure from 600 to 800 °C. However, the extremely high temperature (900 °C) also promotes the structural alignment by removing heteroatoms, thus increasing the degree of graphitization.⁴⁰ Therefore, the carbonization temperature leads to a trade-off between the abundance of defects and the degree of graphitization.

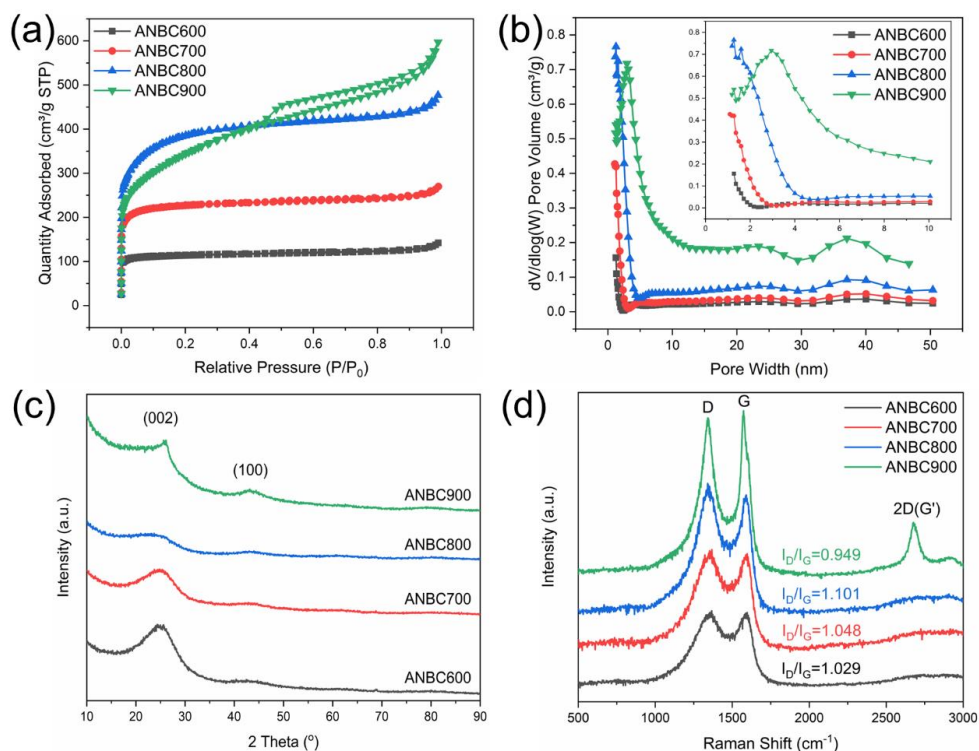


Figure 4.2 (a) N₂ adsorption-desorption isotherms; (b) Pore size distribution; (c) XRD patterns and (d) Raman spectra of the ANBCT samples with different carbonization temperatures.

X-ray photoelectron spectroscopy (XPS) was used to verify the surface chemical composition of the ANBCT samples.⁴¹ In the XPS survey scan spectra (Figure S4.2), three obvious peaks located at around 285.1, 400.1 and 533.3 eV are observed that are ascribed to C 1s, N 1s, and O 1s, respectively. The surface atomic element concentrations are summarized in Table S4.3. With the carbonization temperature increasing from 600 °C to 900 °C, the surface concentrations of N and O are gradually reduced, however, the atomic concentration of C gradually increases from 82.5 at.% (ANBC600) to 92.7 at.% (ANBC900). This indicates that the higher carbonization temperature can effectively increase the degree of graphitization and leads to the removal of more heteroatoms. The high-resolution N 1s spectra of the ANBCT samples (Figure 4.3) are deconvoluted into four peaks at around 398.7, 400.3, 401.8 and 404.9 eV, corresponding to pyridinic N, pyrrolic N, graphitic N, and oxidized N configurations, respectively. With the increase in carbonization temperature, only the percentage of oxidized N showed a decreasing trend, while the percentage of pyridinic N,

pyrrolic N and graphitic N did not exhibit a clear trend. At all different carbonization temperatures, pyrrolic N is the main component, followed by pyridinic N and graphitic N. The high-resolution C 1s spectra of the ANBCT samples are shown in Figure S4.3. The C 1s can be resolved into three individual peaks at around 284.8, 285.7 and 288.0 eV, referring to C-C, C-N and C-O, respectively.⁴² The percentage of C-C (sp^2 carbon) from the deconvolution of high-resolution C 1s spectra is used as a descriptor to estimate the degree of graphitization of carbon materials.⁴³ The percentage of C-C (sp^2 carbon) shows an increasing trend with the increase of carbonization temperature, from 37.6% (ANBC600) to 46.7% (ANBC900), suggesting that the higher carbonization temperature induces a higher degree of graphitization of ANBCT samples.

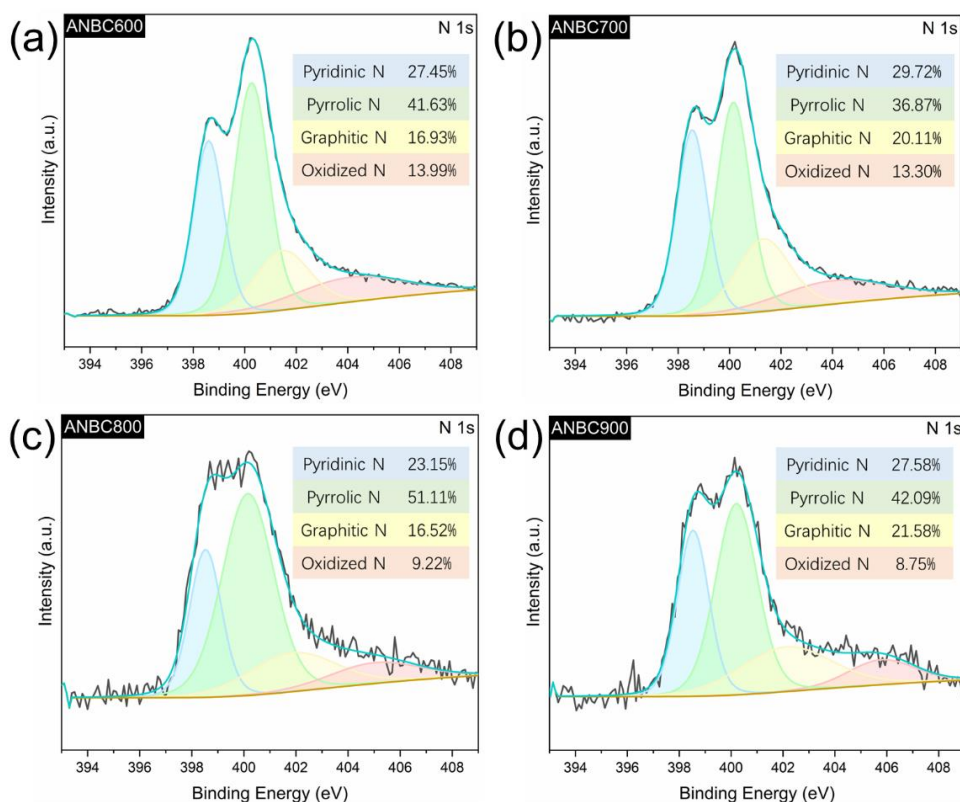


Figure 4.3 XPS high-resolution N 1s spectra of (a) ANBC600; (b) ANBC700; (c) ANBC800 and (d) ANBC900.

To understand the hydrophilicity/hydrophobicity of the ANBCT samples, static contact angle measurements were carried out by the sessile drop method on the as-prepared

electrode. The contact angle of fresh and used electrodes for each sample is depicted in Figure S4.4 and the data of each trial is summarized in Table S4.4. The contact angle increases with increasing carbonization temperature and gradually becomes stable. ANBC600 shows hydrophilicity, while the other samples show hydrophobicity, which can be explained by the removal of more hydrophilic O-containing and N-containing functional groups at higher carbonization temperature, thus making the carbon surface more hydrophobic.⁴⁴ The comparison between fresh and used samples (after CO₂ electrochemical reduction) shows that the hydrophilicity/hydrophobicity characteristics of the N-doped biochar remained stable after 1 h CO₂ electrolysis.

Linear sweep voltammograms (LSV) were recorded in an Ar-saturated and CO₂-saturated 0.1 M aqueous KHCO₃ electrolyte at a scan rate of 5 mV/s to examine the electrochemical response of the ANBCT samples. As shown in Figure S4.5, all of the ANBCT samples exhibit a larger current density in the CO₂-saturated electrolyte than in the Ar-saturated electrolyte, suggesting that the biochars are active for the CO₂ reduction reaction. The voltammograms in a CO₂-saturated electrolyte are plotted in Figure 4.4a, and show that all the samples have a similar onset potential but reach different current densities in a potential window from -0.2 to -1.1 V vs. RHE. Among them, ANBC600 shows a lower current density than other samples, which is attributed to its lower carbonization temperature. The lower degree of graphitization, smaller specific surface area, and less porosity jointly determine the poor electrochemical activity of ANBC600.

To further evaluate the catalytic performance of the ANBCT samples, chronoamperometry measurements were performed for all samples at cathode potentials from -0.5 to -1.15 V vs. RHE (with iR compensation, Figure S4.6). During these one-hour experiments, gaseous products were measured over two-minute intervals with an in-line gas chromatograph (GC) and aliquots of the electrolyte were injected into a high-performance liquid chromatograph (HPLC) to quantify liquid products. CO and H₂ were detected as the dominant gas products, while trace amount of CH₄ (<1%) were detected at applied potentials more negative than -1 V vs. RHE. No liquid products were detected by HPLC. The faradaic efficiencies (FE) of CO for the ANBCT samples are presented in Figure 4.4b, where the FE_{CO} of all samples increased from -0.5 to -0.8 V vs. RHE, reaching a maximum value at around -0.8 or -0.9 V vs. RHE and then declining with the potential becoming more negative. This decline at higher applied potentials can be mainly attributed to the competition with the hydrogen evolution reaction (HER).⁴⁵ Figure 4.4b clearly shows that the FE_{CO} increases with increasing carbonization temperature, with ANBC800 exhibiting the highest FE_{CO} (89.3%) of all samples at -0.82 V vs. RHE. Interestingly, the FE_{CO} shows a significant increase when the carbonization temperature is increased from 600 °C to 700 °C, while it only shows a slight increase when the carbonization temperature is increased from 700 °C to 900 °C. Similarly, the total current density (j_{Total}) increases with the increase of

carbonization temperature (see Figure 4.4c). Both ANBC800 and ANBC900 show a high FE_{CO} and the highest partial current density toward CO (j_{CO}) as shown in Figure 4.4d. Moreover, the j_{CO} curves show significant differences in catalytic activity with ANBC600 showing almost no activity toward CO_2 reduction. Additionally, the FE_{H_2} and j_{H_2} are presented in Figure S4.7, with the FE_{H_2} showing an opposite trend to that of FE_{CO} and ANBC900 showing the lowest FE_{H_2} values, indicating that it is least active towards the HER.

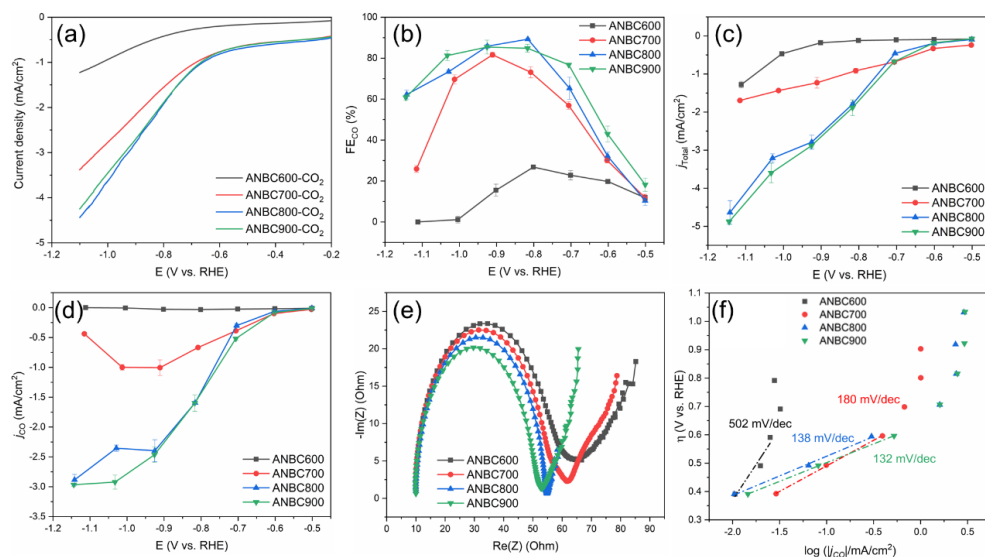


Figure 4.4 (a) LSV curves recorded in a CO_2 -saturated 0.1 M $KHCO_3$ electrolyte; (b) FE of CO production at applied potentials from -0.5 to -1.15 V vs. RHE; (c) Total current density at different applied potentials; (d) Partial current density of CO at different applied potentials; (e) Nyquist plots for the ANBC samples; (f) Tafel plots of CO partial current density for the ANBC samples in CO_2 -saturated 0.1 M $KHCO_3$ electrolyte.

Electrochemical impedance spectroscopy (EIS) was used to evaluate the charge transfer resistance of all ANBC samples (see Figure 4.4e). ANBC900 shows the lowest charge transfer resistance (R_{ct}) compared to other samples, suggesting faster charge transfer during the CO_2RR .⁴⁶ The CO_2RR kinetics for the ANBC samples were determined by plotting the Tafel slopes using the j_{CO} (Figure 4.4f). ANBC900 shows a lower Tafel slope (~ 132 mV/dec) than other samples, implying faster kinetics for CO formation.⁴⁷ The electrochemically active surface areas (ECSA) of ANBC samples were determined by the double layer capacitance (C_{dl}) from cyclic voltammetry measurements (see Figure S4.8). With the increase of carbonization temperature, the C_{dl} value increases from 1.07 mF to 2.06 mF and then decreases to 1.50 mF. The measured C_{dl} shows a clear correlation with the specific surface

area of ANBCT samples determined with N_2 adsorption-desorption isothermal analyses. However, there is no clear correlation between the C_{dl} values and the N-doping content of the samples. Even though the C_{dl} of ANBC800 is higher than ANBC900, they still show similar performance for CO_2RR . To further confirm that the detected CO originates from CO_2 reduction instead of from the decomposition of carbon catalysts, control tests were carried out with a Ar-saturated electrolyte at -0.8 V vs. RHE. As shown in Figure S4.9, only H_2 was detected during the Ar-saturated electrolysis, proving that the CO was produced from CO_2 .

The carbonization temperature has a crucial influence on the physicochemical properties of N-doped biochar catalysts, which further affects its electrochemical performance for the CO_2RR . In general, the N-doped biochar synthesized at higher carbonization temperatures shows a better performance. In particular, ANBC800 and ANBC900 exhibit similar electrochemical performances, although they show significant differences in physicochemical properties, including N-doping content, specific surface area, porosity, and the degree of graphitization, etc. We find that the CO_2RR performance of N-doped biochar is synergistically influenced by a multitude of the physicochemical properties. For instance, the local environment surrounding the active sites has a critical impact on the expression of the electrocatalytic performance.⁴⁸ Our results show that the hydrophilicity/hydrophobicity of the N-doped biochar is strongly correlated with the FE_{CO} . Increasing the carbonization temperature leads to a higher hydrophobicity of the carbon catalysts, which enhances the FE_{CO} by inhibiting the HER. Moreover, the higher carbonization temperature leads to the removal of more heteroatoms, which improves the conductivity of the carbon catalysts. The higher carbonization temperature thereby causes smaller charge transfer resistances and results in faster CO_2 conversion kinetics to CO, which can be considered as an important feature to improve the catalytic performance for the CO_2RR .

4.3.2 Effect of N-doping level

To further investigate the effect of N-doping on the electrochemical performance for the CO_2RR , we synthesized a series of N-doped biochar catalysts with different amounts of N-doping by modifying the amount of urea added during the preparation processes. Taking into account the product selectivity and catalytic activity of the catalysts, ANBC800 was selected as reference material as it exhibited a high catalytic performance and had a higher carbon yield than ANBC900 (Table S4.1). The specific preparation procedure for the ANBC800-XN samples with modified N-doping amounts can be found in Table S4.1. The designation of the samples depends of the amount of urea addition. ANBC800-SN, ANBC800-LN, and ANBC800-HN imply that the ratio of bagasse to added urea to NaOH is 1: 0.5: 3, 1: 1: 3, and 1: 3: 3, respectively. The carbon yield increased from 1.6 wt.% (ANBC800-SN) to 11.8 wt.% (ANBC800-HN) with increasing urea addition. As the thermal

decomposition of urea is an endothermic reaction, the lower amount of urea additions consume less heat, which improves the biomass-activator interaction, and results in a lower carbon yield. Conversely, a higher urea addition leads to more heat consumption during the pyrolysis, which weakens the interaction between the NaOH activator and the bagasse, resulting in a higher carbon yield.

The SEM and TEM images of the ANBC800-XN samples are depicted in Figure 4.5. SEM images show the morphology of the carbon samples and the EDS images (Figure S4.10) show the elemental distribution. With low amounts of urea used during synthesis, for example with ANBC800-SN and ANBC800-LN, a larger bulk particle-stacked structure (Figure 4.5a and c) is observed. This effect is attributed to the stronger interaction between bagasse and NaOH, causing the collapse and shrinkage of the carbon materials, thus resulting in denser particles.⁴⁹ When the urea addition was higher, with ANBC800 and ANBC800-HN, a fluffier particle-stacked 3D structure is observed. The mesoporous structure of all ANBC800-XN samples can be clearly observed in the TEM images shown in Figure 4.5. Although the TEM images cannot quantify the size and proportion of mesopores, they illustrate that the mesoporous structures are effectively generated by the etching effect of the activator (ANBC800-SN and ANBC800-LN) and by gas-solid interaction reactions (ANBC800 and ANBC800-HN).

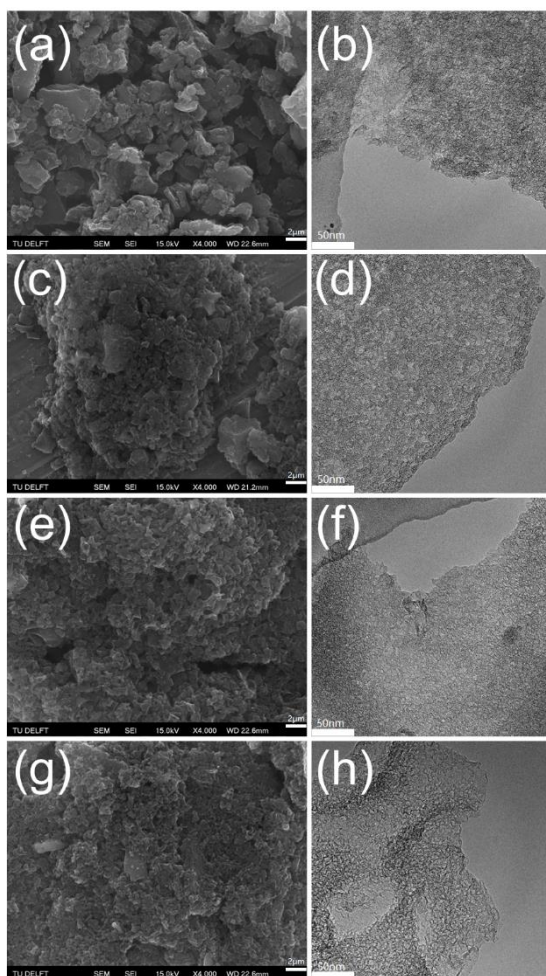


Figure 4.5 SEM (left) and TEM (right) images of ANBC800-SN: (a), (b); ANBC800-LN: (c), (d); ANBC800: (e), (f); and ANBC800-HN: (g), (h).

The mesoporosity of the samples is also reflected in the N_2 adsorption-desorption measurements. As shown in Figure 4.6a, ANBC800-SN and ANBC800-LN exhibit a clear hysteresis loop at relative pressures from 0.45 to 0.95, indicating that a large number of mesopores were created. For ANBC800 and ANBC800-HN this hysteresis loop is almost negligible, suggesting a lower percentage of mesopores. Figure 4.6b displays the pore size distribution of the ANBC800-XN samples which was calculated by a DFT model. ANBC800-SN and ANBC800-LN show a broad pore size distribution and the peak is mainly centered at around 3 nm. However, ANBC800 and ANBC800-LN show a relatively narrow pore size

distribution and the pore size is concentrated at around 2 nm. The textural properties of the ANBC800-XN samples are summarized in Table S4.2. Both ANBC800-SN and ANBC800-LN display a large specific surface area ($>2100 \text{ m}^2/\text{g}$) and larger ratio of mesopores (75.3% and 66.2%, respectively), which is mainly ascribed to the adequate reactions between bagasse and NaOH. By contrast, ANBC800 only has a specific surface area of $1426.9 \text{ m}^2/\text{g}$ and less than 20% mesopores. The specific surface area, total pore volume and ratio of mesopores for ANBC800-HN increased slightly compared to ANBC800. Despite the higher amount of urea added, leading to a higher heat consumption resulting in weaker biomass-activator interactions, the large amount of NH_3 released from urea decomposition etches the carbon skeleton, thereby increasing the specific surface area and total pore volume of the catalyst with respect to ANBC800.^{36,50} Thus, the effect of the added amount of urea and the effect of the added activator jointly influences the development of porosity of N-doped biochar. The XRD patterns of all the ANBC800-XN samples show coinciding characteristic peaks of the (002) and (100) planes of graphite (Figure 4.6c). The (002) peak reflection of ANBC800-SN and ANBC800-LN shifts to around 26° , indicating a higher degree of graphitization than for the other samples. Similar conclusions can also be drawn from the Raman spectra depicted in Figure 4.6d, where ANBC800-SN shows a lower I_D/I_G value (0.938) than other samples and also shows a 2D band at around 2700cm^{-1} , implying a higher degree of graphitization for ANBC800-SN. The I_D/I_G value increases from 0.938 to 1.109 with the increase in urea addition, since more urea will bring about more defects due to the etching of the carbon skeleton by NH_3 ⁴⁵. Therefore, although the carbonization temperature is the same, the different urea additions affect the structural properties of the carbon materials.

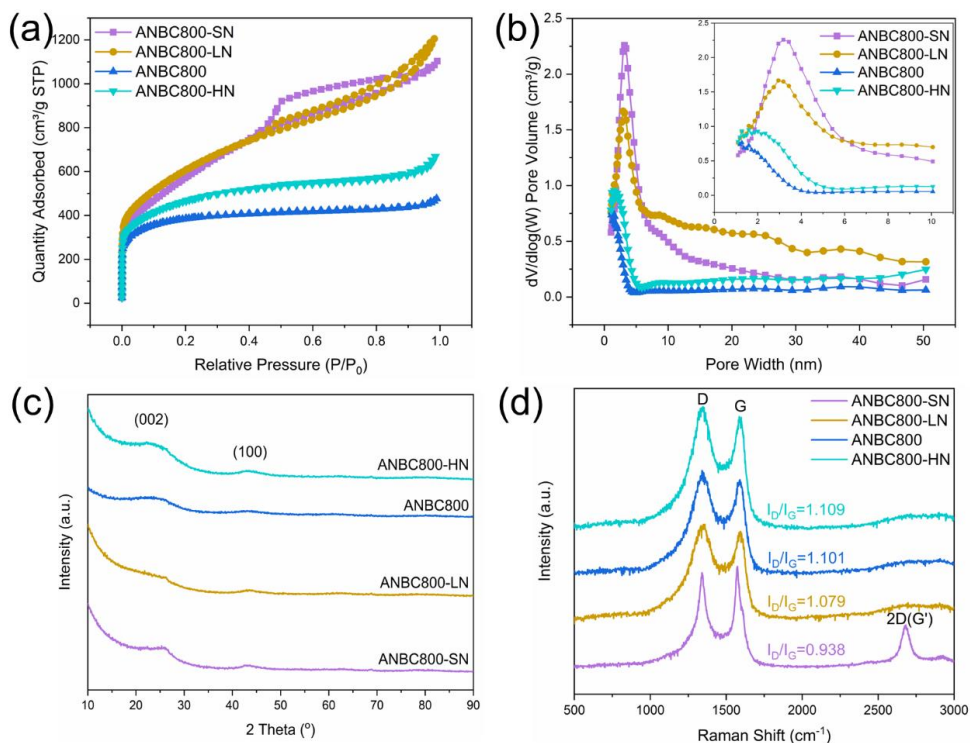


Figure 4.6 (a) N_2 adsorption-desorption isotherms; (b) Pore size distribution; (c) XRD patterns and (d) Raman spectra of the ANBC800-XN samples with different N-doping contents.

The full survey spectra of all the ANBC800-XN samples in Figure S4.11 reveal the presence of C, N, and O on the carbon surface and no other elements were detected. As shown in Table S4.3, the atomic concentration of N on the carbon surface increased gradually from 3.19 at.% (ANBC800-SN) to 3.49 at.% (ANBC800-LN) and further to 3.73 at.% (ANBC800) and 4.19 at.% (ANBC800-HN) with the increase of employed urea addition, but the concentration of C and O did not show an apparent trend with the changing of urea addition. In Figure 4.7, the high-resolution N 1s spectra of the ANBC800-XN samples are fitted into four individual peaks, corresponding to pyridinic N, pyrrolic N, graphitic N and oxidized N. At the same carbonization temperature, the increase of total N-doping level did not have a significant effect on the distribution of different N-containing species. Pyrrolic N is still the main component, followed by pyridinic N, graphitic N and oxidized N species. The high-resolution C 1s spectra of the ANBC800-XN samples are deconvoluted into three peaks, as shown in Figure S4.12, referring to C-C, C-N, and C-O.⁴² All of the ANBC800-XN samples

show a similar percentage of C-C (sp^2) carbon (40.5% - 46.5%), suggesting that modulating the N-doping level has a limited effect on the degree of graphitization of N-doped biochar at the same carbonization temperature.

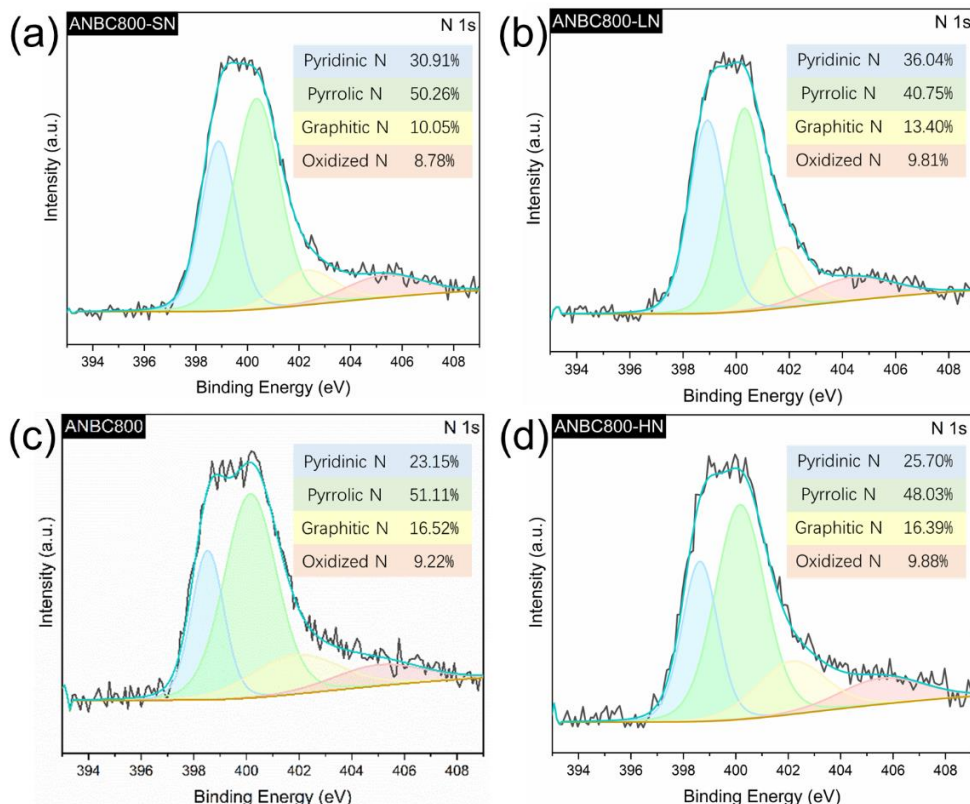


Figure 4.7 High-resolution N 1s spectrum of (a) ANBC800-SN; (b) ANBC800-LN; (c) ANBC800 and (d) ANBC800-HN.

The surface hydrophobicity measurements of the ANBC800-XN samples were carried out by static contact angle tests. As shown in Figure S4.13, due to the same carbonization temperature, all catalysts showed similar hydrophobicity on the surface. With the increase of N-doping, the increase of N-containing functional groups on the surface can improve the surface wettability of porous carbon materials, resulting in a slight decrease of surface hydrophobicity.⁵¹ The comparison of the contact angle of the fresh and used electrodes also shows that the hydrophobicity of the drop-cast catalysts is stable.

The LSV tests in Ar-saturated and CO₂-saturated 0.1 M KHCO₃ electrolytes are shown in Figure S4.14. ANBC800-SN shows almost the same catalytic activity in the Ar-saturated and CO₂-saturated electrolyte. ANBC800-LN and ANBC800-HN exhibit a slightly improved current density in a CO₂-saturated electrolyte with respect to the Ar-saturated electrolyte. However, this difference in current density diminishes as the potential becomes more negative, and even the ANBC800-HN displays a smaller current in a CO₂-saturated electrolyte than the Ar-saturated electrolyte at -1.0 to -1.1 V vs. RHE. Only ANBC800 maintains better CO₂RR activity at -0.2 to -1.1 V vs. RHE. According to the comparison from Figure 4.8a, ANBC800 shows higher current density in CO₂-saturated electrolysis than the other samples. The onset potential is similar for each sample. The chronoamperometry results are depicted in Figure S4.15 and the FE_{CO} of all samples are presented in Figure 4.8b, where ANBC800-SN, with the lowest N-doping level (3.19 at.%), shows a relatively poor FE towards CO (68.2%). When the N-doping content was raised to 3.49 at.%, the FE_{CO} of ANBC800-LN showed a better FE_{CO} at all potentials than the other samples, reaching a FE_{CO} of 94.9% at -0.82 V vs. RHE. When the N-doping is further increased to 3.73 at.% for ANBC800 and 4.19 at.% for ANBC800-HN, the FE_{CO} is slightly reduced. ANBC800 shows a higher total current density than other samples, as shown in Figure 4.8c. Although ANBC800 shows a slightly lower FE_{CO} than ANBC800-LN, it maintains a larger partial current density toward CO than the other samples due to its higher activity (see Figure 4.8d). The FE_{H₂} and *j*_{H₂} are presented in Figure S4.16 and show that ANBC800-SN exhibits higher activity toward HER at more negative potentials. The obtained results illustrate that the product selectivity to CO and catalytic activity of the catalysts are not consistently enhanced by increasing the amount of N-doping. Taking into account the charge transfer resistance of the catalysts, as shown in Figure 4.8e, ANBC800 exhibits smaller resistance than other samples, indicating the charge transfer is more rapid than other samples. The Tafel plots are depicted in Figure 4.8f, with ANBC800-SN, ANBC800-LN, ANBC800 and ANBC800-HN displaying Tafel slopes of 187, 151, 138, and 127 mV/dec, respectively. All Tafel slopes are close to the theoretical value of 118 mV/dec (except for ANBC800-SN), suggesting that the rate determining step of CO₂RR for these samples is the single electron transfer to the adsorbed CO₂ to generate *CO₂⁻ intermediates.^{26,52} The ECSA measurement results of the ANBC800-XN samples are shown in Figure S4.17. Although ANBC800 and ANBC800-HN exhibit smaller specific surface area than ANBC800-SN and ANBC800-LN, their *C_{dl}* is higher than ANBC800-SN and ANBC800-LN, which is attributed to the higher percentage of micropores in these samples.⁵³ On the contrary, the larger pore sizes of ANBC800-SN and ANBC800-LN lead to a lower capacitance.⁵⁴ The *C_{dl}* of all samples does not show a clear correlation with the catalytic performances, indicating that not all of the electrochemically active sites show catalytic activity to CO₂RR. The results of control tests in Figure S4.18 confirm that CO₂ is the only carbon source for CO production.

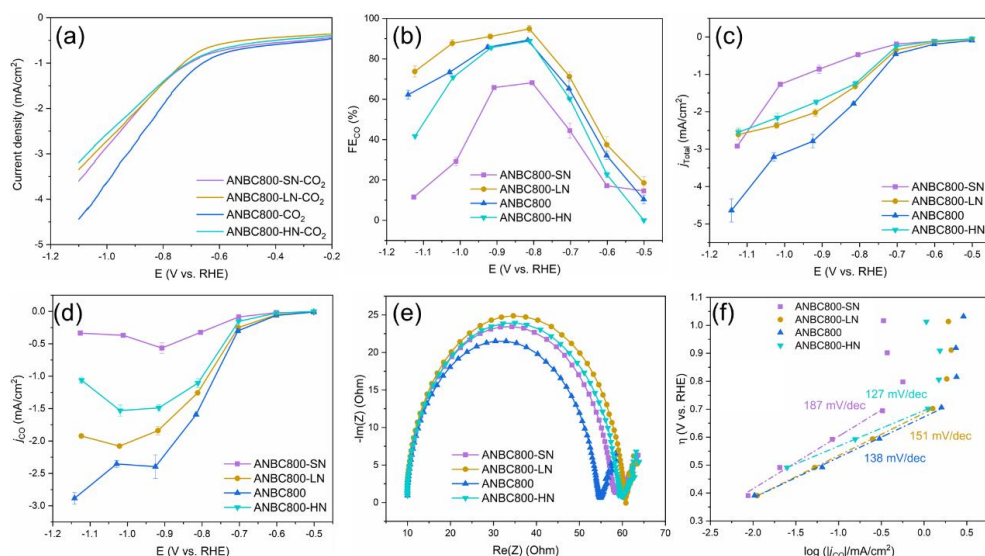


Figure 4.8 (a) LSV curves recorded in a CO₂-saturated 0.1 M KHCO₃ electrolyte; (b) FE of CO production at applied potentials from -0.5 to -1.15 V vs. RHE; (c) Total current density at different applied potentials; (d) Partial current density of CO at different applied potentials; (e) Nyquist plots for the ANBC800-XN samples; (f) Tafel plots of CO partial current density for the ANBC800-XN samples in CO₂-saturated 0.1 M KHCO₃ electrolyte.

In summary, we synthesized ANBC800-XN samples with different N-doping levels by adjusting the amount of urea addition during the preparation process and analyzed their physicochemical properties and electrochemical performance. Although all samples were prepared at the same carbonization temperature, the interaction between bagasse, urea and NaOH was affected by the different amounts of urea addition, which changed the N-doping level, and also showed a significant effect on the pore structures of the catalysts. Among the synthesized samples, ANBC800-SN and ANBC800-LN exhibit an impressively large specific surface area (>2100 m²/g) and a high ratio of mesopores (>60%), but a relatively low N-doping level of 3.19 at.% and 3.49 at.%, respectively. ANBC800 and ANBC800-HN show relatively lower specific surface area and the ratio of mesopores, but a higher N-doping level of 3.73 at.% and 4.19 at.%, respectively. We demonstrate that neither the N-doping level nor the specific surface area are positively correlated to the observed CO₂RR performance of N-doped biochar catalysts, which is consistent with other literature findings.⁵⁵ Although ANBC800-SN and ANBC800-LN show a similar specific surface area and N-doping content, ANBC800-SN does not show a similar CO₂RR performance as ANBC800-LN. This is probably due to the excessive percentage of mesopores of ANBC800-SN (75.3%)

that is not favorable for the adsorption of reactants and intermediates on the carbon surface, resulting in a lower FE and current density towards CO. Therefore, the contribution of micropores should not be underestimated. For example, Estevez et al. found that a higher microporous content can enhance the CO₂ capture performance.⁵⁶ Additionally, Liu et al. reported a coal-based N-doped carbon catalyst for CO₂RR and emphasized that the spatial confinement effect of the micropores can help to CO₂ convert to CO efficiently.²⁰ Therefore, we hypothesize that a rational adjustment of the porosity of the catalyst, namely, the trade-off between mesopores and micropores structures, is crucial for the synthesis of superior CO₂RR electrocatalysts.

4.3.3 Understanding the correlation between physicochemical properties and electrochemical performance

As discussed above, the surface chemistry, the porous structure, the abundance of defects, the degree of graphitization and surface hydrophobicity of N-doped carbon catalysts all have a critical impact on their catalytic performance. Therefore, the overall performance of the catalysts for the CO₂RR cannot simply be reflected by one or two indicators. Therefore, a multivariate correlation analysis which combines the electrochemical performance and physicochemical properties of the N-doped biochar catalysts was carried out. The electrochemical performances of all samples were represented by the FE_{CO} and j_{CO} at around -0.81 V vs. RHE, where most of the catalysts show their maximum FE to CO. The physicochemical properties were represented by the performed characterization of the surface chemical composition (the total N content, amount of pyridinic N, graphitic N, the percentage of sp² carbon and the ratio of O 1s/C 1s from XPS), the pore structure (the specific surface area, total pore volume, micropore volume, mesopore volume, mesopore ratio, and average pore size from N₂ adsorption-desorption), the abundance of defects and the degree of graphitization (I_D/I_G ratio from Raman spectroscopy), and the surface hydrophobicity (contact angle measurements). JMP software was employed to perform the multivariate correlation analysis.⁵⁷ The resulting heat maps in Figure 4.9, which use Pearson correlation coefficients, were generated to visualize the correlation between pairs of variables. The red color indicates that the correlation coefficient is close to 1, suggesting a positive correlation, the blue color indicates that the correlation coefficient is close to -1, referring to a negative correlation and the light grey color indicates the coefficient is close to 0, implying that there is no correlation. More detailed multivariate scatterplots can be found in Figure S4.19 and Figure S4.20.

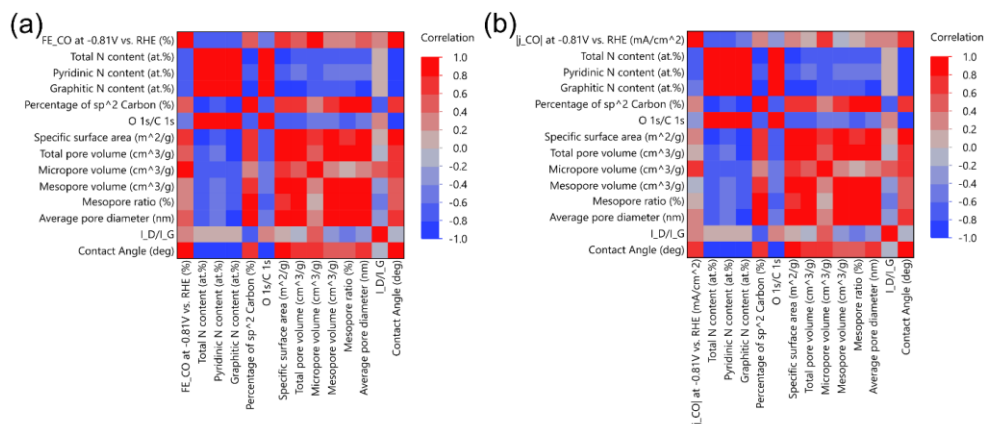


Figure 4.9 Heat maps indicating Pearson correlation between (a) FE_{CO} at -0.81 V vs. RHE and different physicochemical properties; (b) |j_{CO}| at -0.81 V vs. RHE and different physicochemical properties.

As shown in Figure 4.9a and b, the heat maps reveal a negative correlation between the surface N-doping content and the FE_{CO} and j_{CO}. Furthermore, both pyridinic-N and graphitic-N show a negative correlation with the electrochemical performance for CO₂RR. This negative correlation does not mean that less N-doping will result in better catalytic performance, it however does show that increasing the N-doping content is not an effective way to improve the catalytic performance for the CO₂RR. The percentage of sp² carbon positively correlate with the FE_{CO} and j_{CO}, indicating that improving the degree of graphitization is helpful for the CO₂RR performance on N-doped carbon catalysts. The ratio of O 1s/C 1s shows a negative correlation with the FE_{CO} and j_{CO}, suggesting the O-containing functional groups on the carbon surface hinder the catalytic performance. Interestingly, the porous structural properties of the catalysts show a positive correlation with the FE_{CO} (Figure 4.9a), indicating that increasing the specific surface area, micropore volume and average pore size of the catalyst is an effective way to improve the product selectivity of the catalyst. However, the properties of these porous structures (except micropore volume) have almost no correlation with the partial current density of CO (Figure 4.9b). The abundance of defects (the I_D/I_G value) on the carbon surface shows a weak positive correlation with both the FE_{CO} and j_{CO}. The surface hydrophobicity also exhibits a positive correlation with both the FE_{CO} and j_{CO}, which indicates that this is an important parameter that significantly affects the CO₂RR performance.

Although the multivariate correlation analysis does not reveal the active sites for CO₂RR on N-doped biochar, it highlights the importance of other physicochemical properties of N-

doped biochar, which are usually overlooked. For instance, enhancing the degree of graphitization of N-doped carbon is helpful to improve the electrical conductivity, leading to improvement in the current densities on N-doped biochar catalysts. However, the graphitization process also promotes the structural alignment by removing heteroatoms and defects, leading to the removal of active sites on N-doped carbon and a subsequent decrease in the product selectivity for the CO₂RR. On the other hand, the hydrophobicity of the N-doped biochar catalysts is improved with the increase of the degree of graphitization, by removing the O-containing and N-containing functional groups. The higher hydrophobicity can improve the CO₂RR performance by suppressing the competitive HER reaction. Furthermore, modulating the porosity, especially the percentage of mesopores of N-doped biochar, is helpful to improve the CO₂ transport within the catalyst, which also promotes the CO₂RR performance.

In addition, some interesting correlations between different physicochemical properties are observed. For instance, the N-containing and O-containing species on the carbon surface show a negative correlation to the structural properties of the N-doped biochar catalysts. This is due to the enhancement of the porous structure during the carbonization process which is inevitably accompanied by the removal of heteroatoms. The surface hydrophobicity also shows a negative correlation to the surface heteroatom content, indicating that either N-containing species or O-containing species will reduce the hydrophobicity of the catalyst surface. However, the surface hydrophobicity shows a positive correlation with the porous structural properties.

Through the multivariate correlation analysis, we show a comprehensive analysis of the relationship between physicochemical properties and electrochemical performance. Although the limited number of samples cannot perfectly describe the correlation between the physicochemical properties and the electrochemical performance, our analysis is a useful guide for the design of N-doped carbon catalysts for the CO₂RR. Our results indicate that simply enlarging the specific surface area and increasing the N-doping level of N-doped biochar catalysts is not an effective way to improve the CO₂RR performance. However, improving the surface hydrophobicity, the abundance of defects and optimizing the porosity distribution of N-doped carbon can significantly improve the overall catalytic performance for CO₂ electrochemical reduction. It is important to note that the synergistic effect of various physicochemical properties, including N-doping content, specific surface area, porosity, degree of graphitization, the abundance of defects and hydrophobicity, jointly determine the CO₂RR performance of N-doped biochar catalysts. Therefore, successfully revealing the structural-activity relationship of N-doped carbon catalysts for CO₂RR needs a more systematic and comprehensive analyses.

4.4 Conclusions

In this study, we prepared N-doped carbon materials with different physicochemical properties and analyzed their electrochemical performances by controlling different carbonization temperatures and urea additions. Electrochemical measurements demonstrate that the higher carbonization temperature helps the N-doped carbon exhibit better electrochemical performance for the CO₂RR, even with lower N-doping levels. ANBC800 achieves 89.3% faradaic efficiency to CO with a CO partial current density of -1.59 mA/cm² at -0.82 V vs. RHE. However, increasing the amount of N-doping did not effectively improve the performance of the catalysts for CO₂RR. Adjusting the urea addition during the preparation process not only results in different amounts of N-doping, but also dramatically changes the structural properties of the carbon material. In spite of showing a specific surface area larger than 2100 m²/g, ANBC800-SN does not exhibit superb catalytic performance for CO₂RR. In contrast, ANBC800-LN shows a similar specific surface area as ANBC800-SN but with a higher N-doping, and it exhibits 94.9% FE to CO at -0.82 V vs. RHE. However, its lower catalytic activity leads to a lower partial current density for CO than ANBC800. These results further suggest that the CO₂RR performance of N-doped biochar is dependent on the synergistic effect of different physicochemical properties. The contribution of N-doping and specific surface area should therefore not be overemphasized. Further, a statistical-based multivariate correlation analysis visualizes the correlation between physicochemical properties and the electrocatalytic performances of the carbon materials prepared in this study. The N-doping content shows a negative correlation with the CO₂RR performance. The porous structural properties show a positive correlation to the FE_{CO} but almost no correlation to the j_{CO} . Therefore, tailoring the local environment of the N-doped carbon catalysts, such as the degree of graphitization, surface hydrophobicity and the abundance of defects is crucial for optimizing the electrocatalytic performance of N-doped carbon catalysts in CO₂RR. Our data highlights the importance of a comprehensive analysis of the physicochemical properties of N-doped carbon catalysts for CO₂RR performance, and enables the rational design of high-performance N-doped carbon catalysts for the CO₂RR in the future.

4.5 Supporting Information

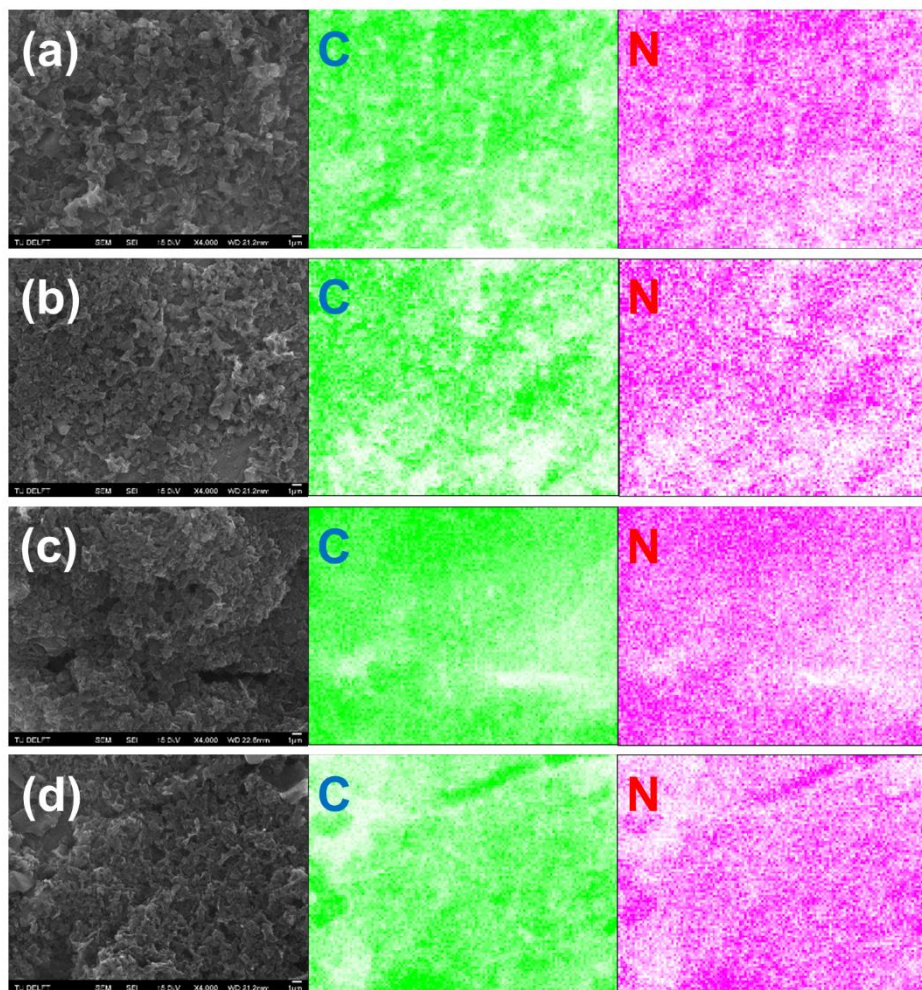


Figure S4.1 SEM-EDS elemental mapping results of C, and N for (a) ANBC600; (b) ANBC700; (c) ANBC800; (d) ANBC900.

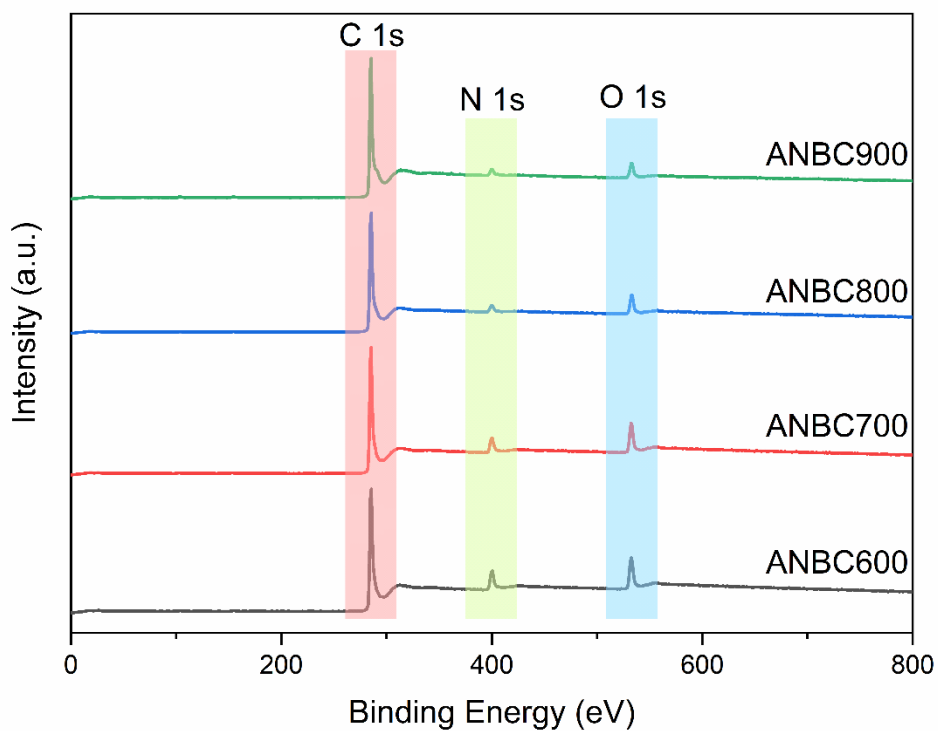


Figure S4.2 XPS survey spectra of the ANBCT samples.

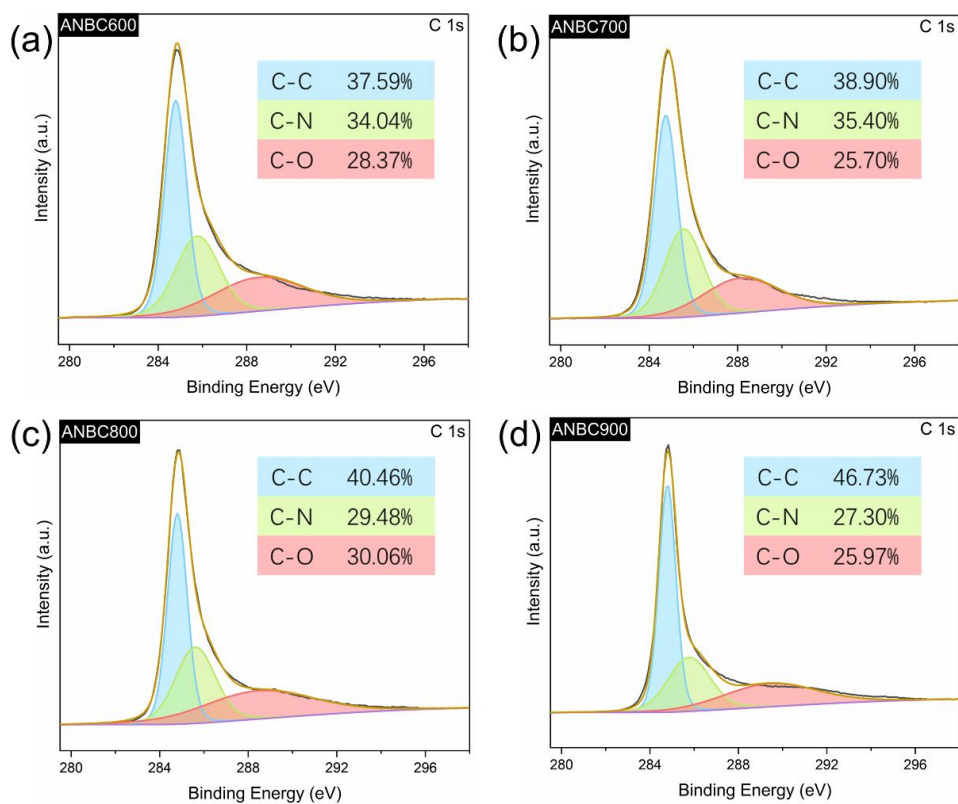


Figure S4.3 High-resolution C 1s spectra of (a) ANBC600; (b) ANBC700; (c) ANBC800 and (d) ANBC900.

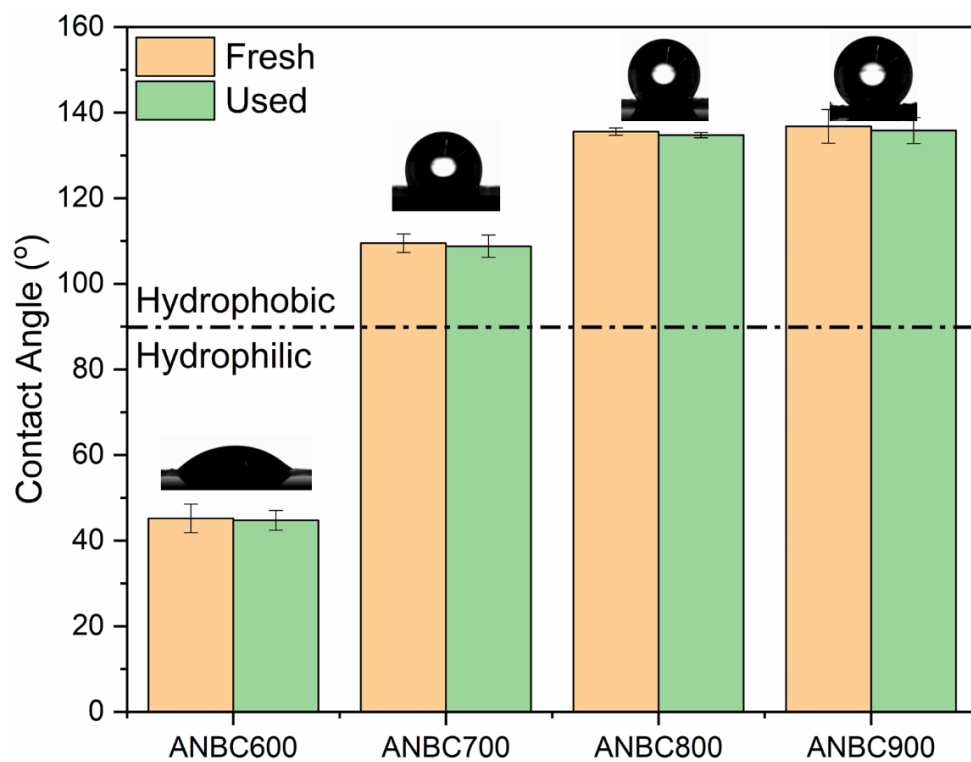


Figure S4.4 Contact angle measurements of the ANBCT samples.

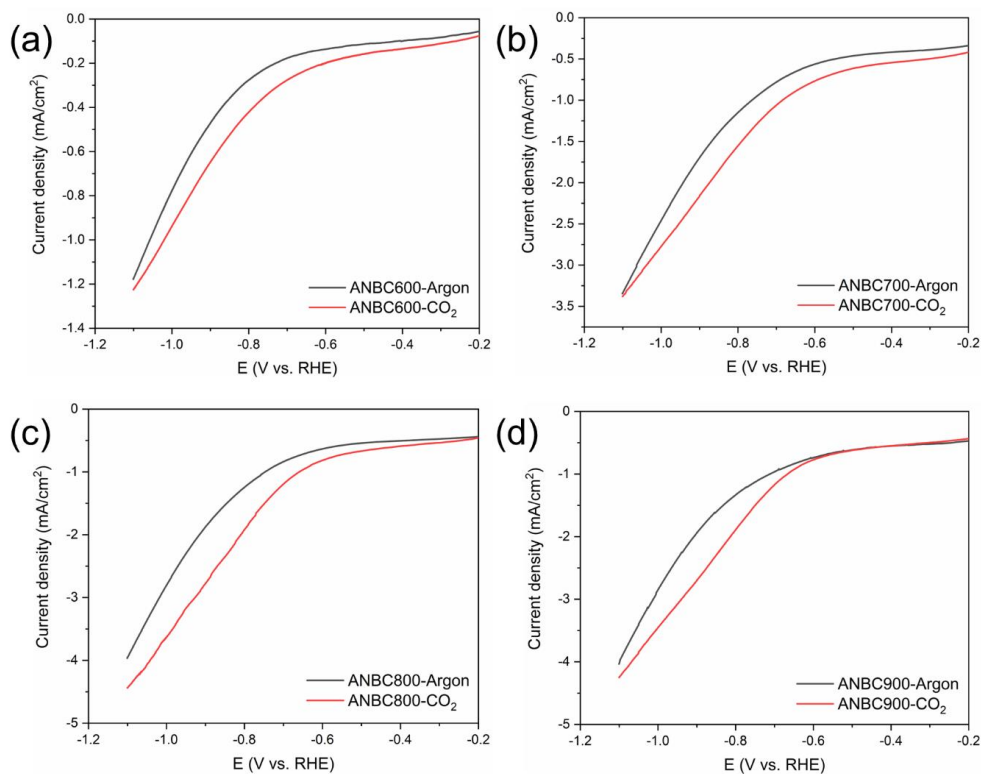


Figure S4.5 LSV curves of (a) ANBC600; (b) ANBC700; (c) ANBC800 and (d) ANBC900 in Argon-saturated and CO₂-saturated 0.1M KHCO₃ electrolyte.

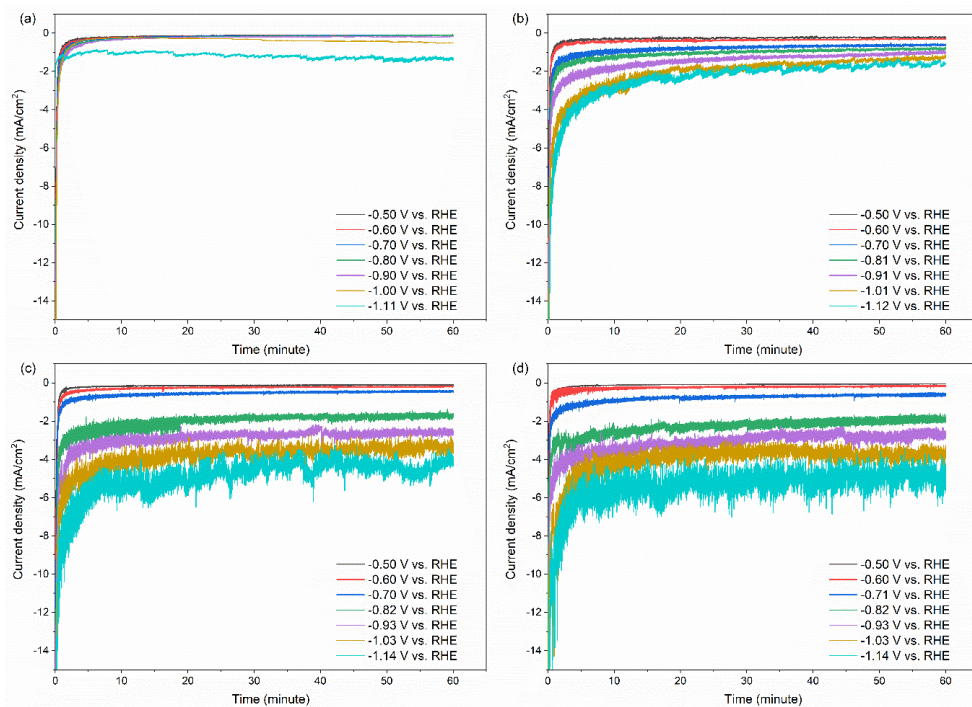


Figure S4.6 Chronoamperometry results of (a) ANBC600; (b) ANBC700; (c) ANBC800 and (d) ANBC900 at different potentials in CO_2 -saturated 0.1M KHCO_3 electrolyte.

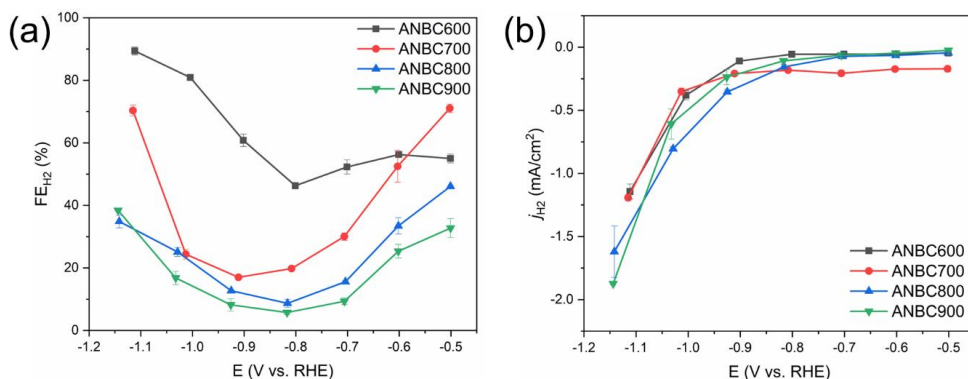


Figure S4.7 (a) FE of H_2 production at applied potentials from -0.5 to -1.15V vs. RHE; (b) Partial current density of H_2 at different applied potentials.

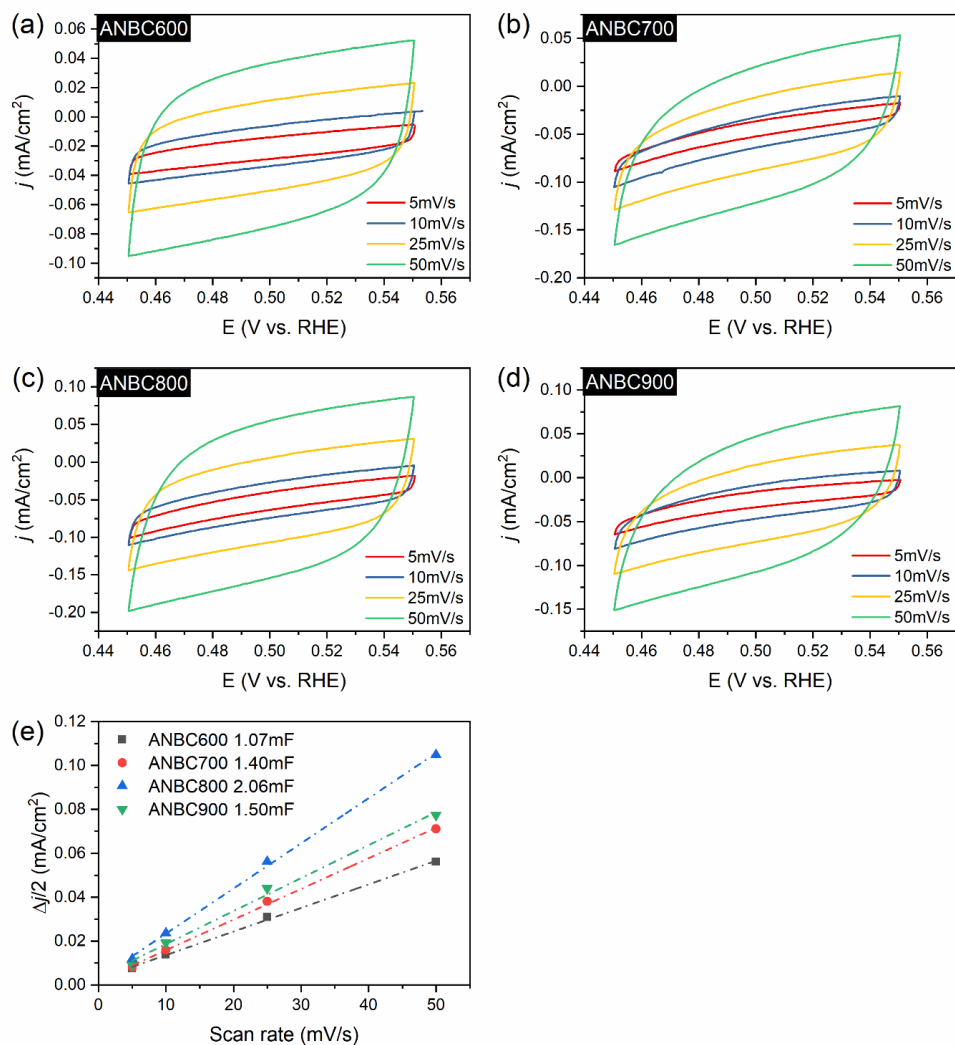


Figure S4.8 CVs of (a) ANBC600, (b) ANBC700, (c) ANBC800, (d) ANBC900 from 0.45 to 0.55 V vs. RHE at various scan rates and (e) The double layer capacitances of all samples.

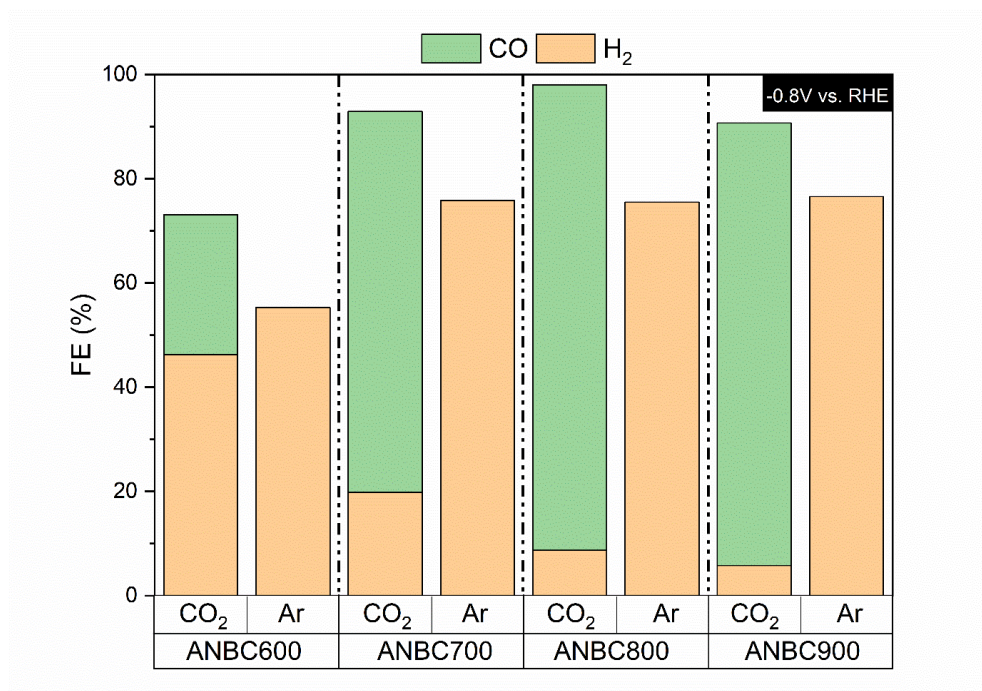


Figure S4.9 Gas products selectivity of chronoamperometry tests with a CO₂-saturated and Argon-saturated 0.1 M KHCO₃ electrolyte at -0.8V vs. RHE of the ANBCT samples.

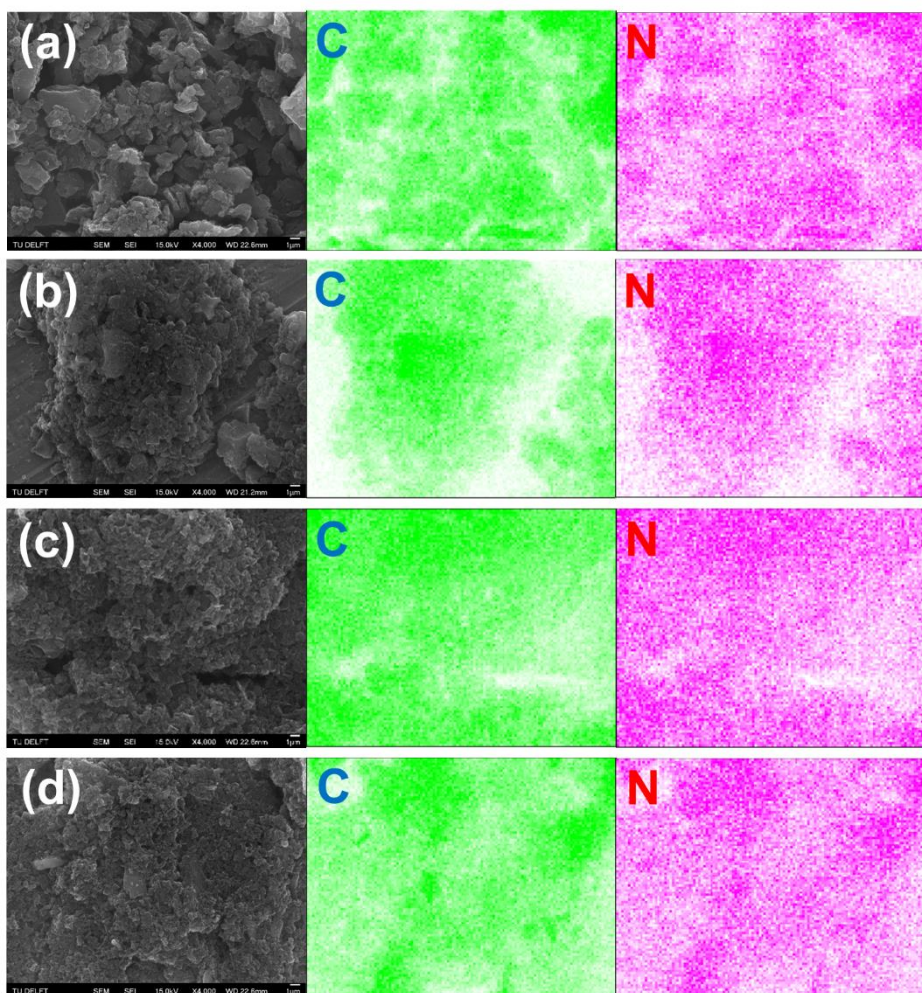


Figure S4.10 SEM-EDS elemental mapping results of C, and N for (a) ANBC800-SN; (b) ANBC800-LN; (c) ANBC800; (d) ANBC800-HN.

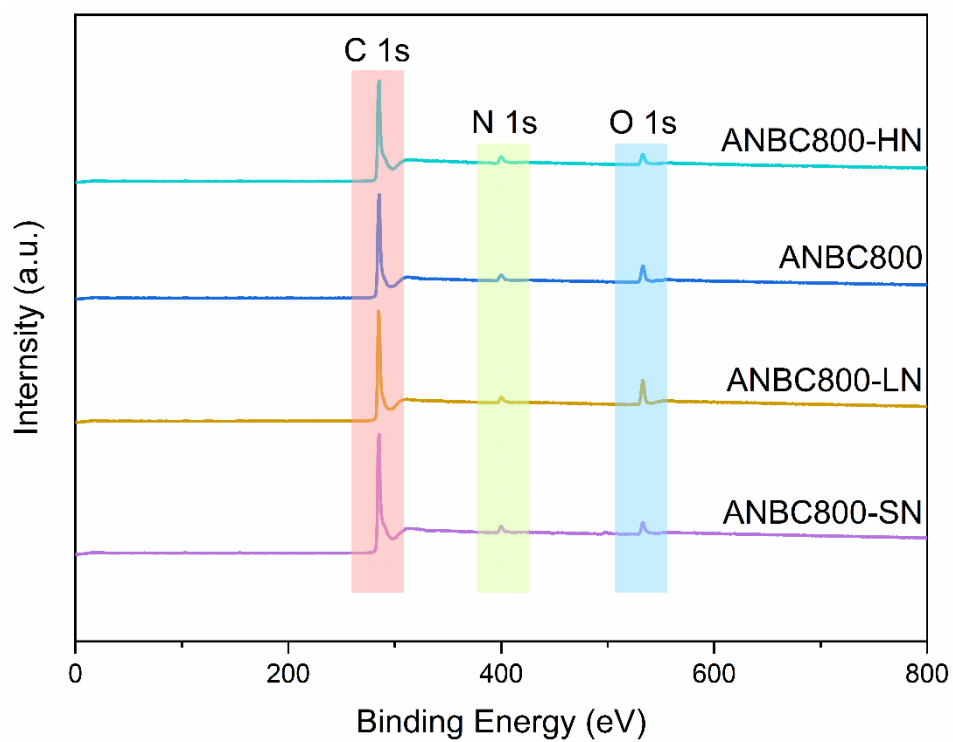


Figure S4.11 XPS full scan spectra of the ANBC800-XN samples.

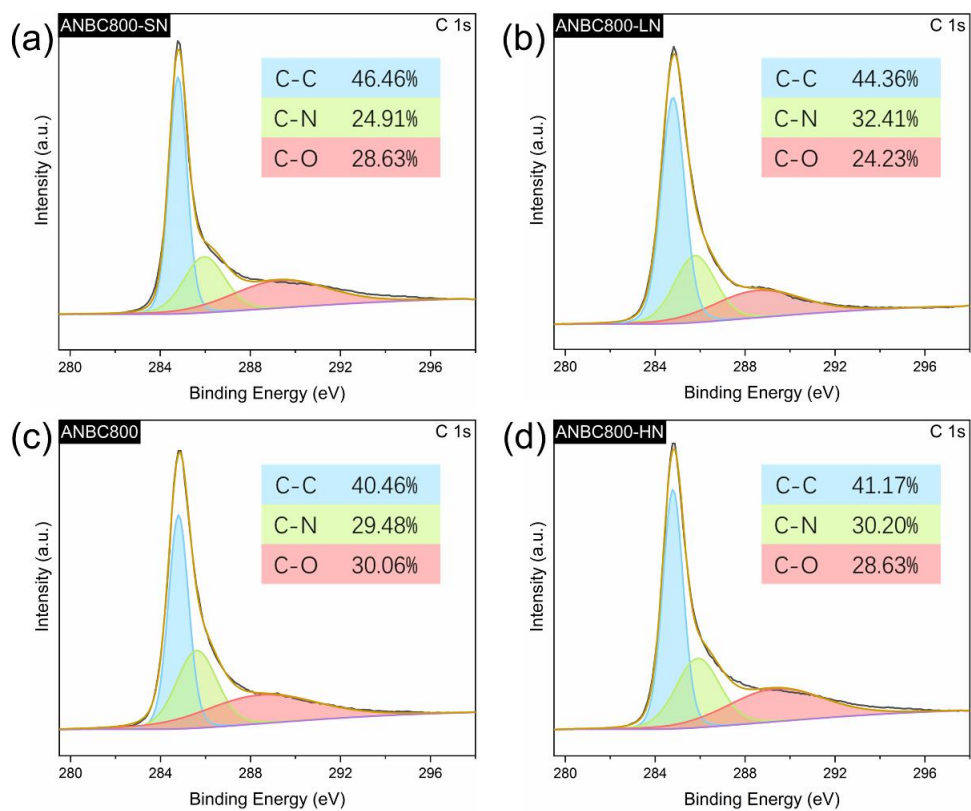


Figure S4.12 High-resolution C 1s spectra of (a) ANBC800-SN; (b) ANBC800-LN; (c) ANBC800 and (d) ANBC800-HN.

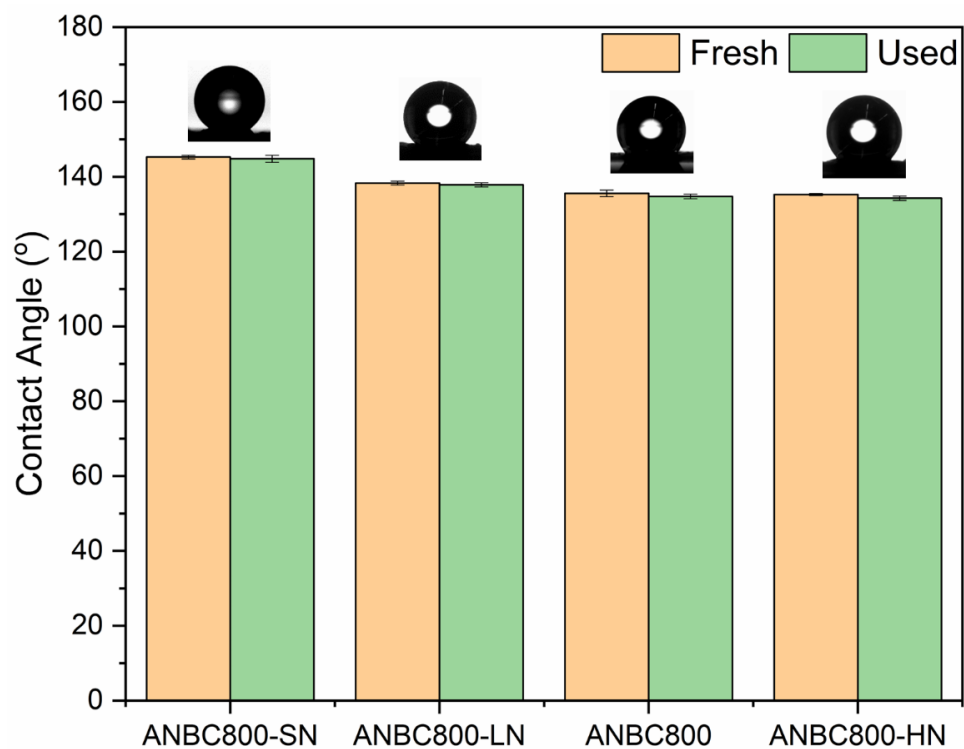


Figure S4.13 Contact angle measurements of the ANBC800-XN samples.

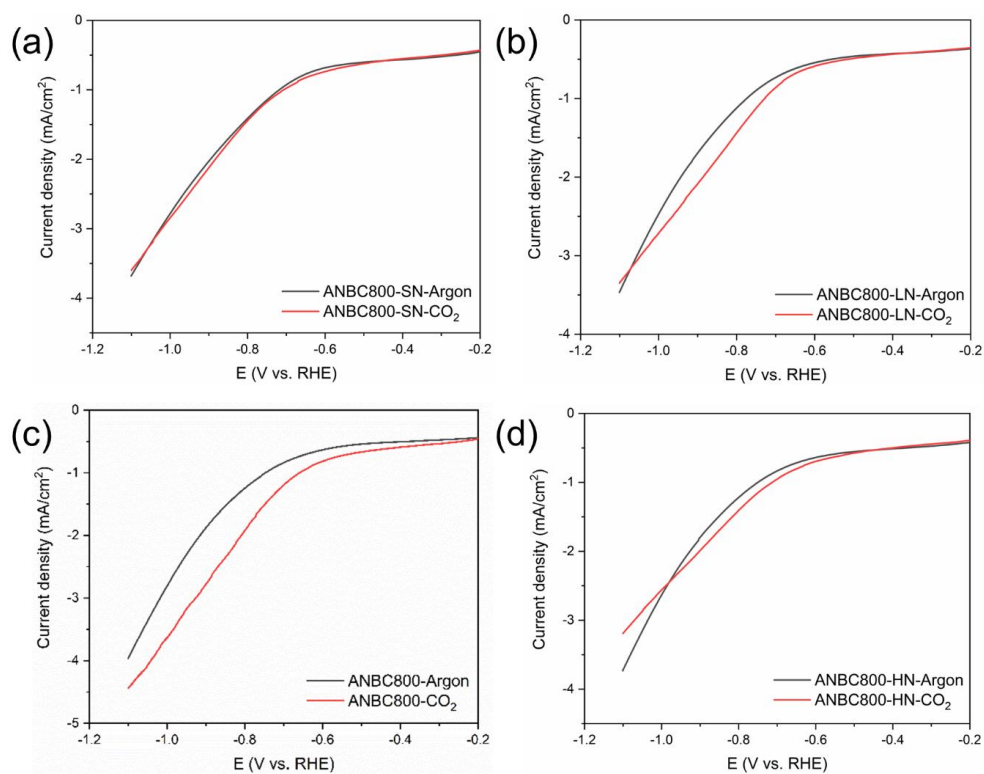


Figure S4.14 LSV curves of (a) ANBC800-SN; (b) ANBC800-LN; (c) ANBC800 and (d) ANBC800-HN in Argon-saturated and CO₂-saturated 0.1M KHCO₃ electrolyte.

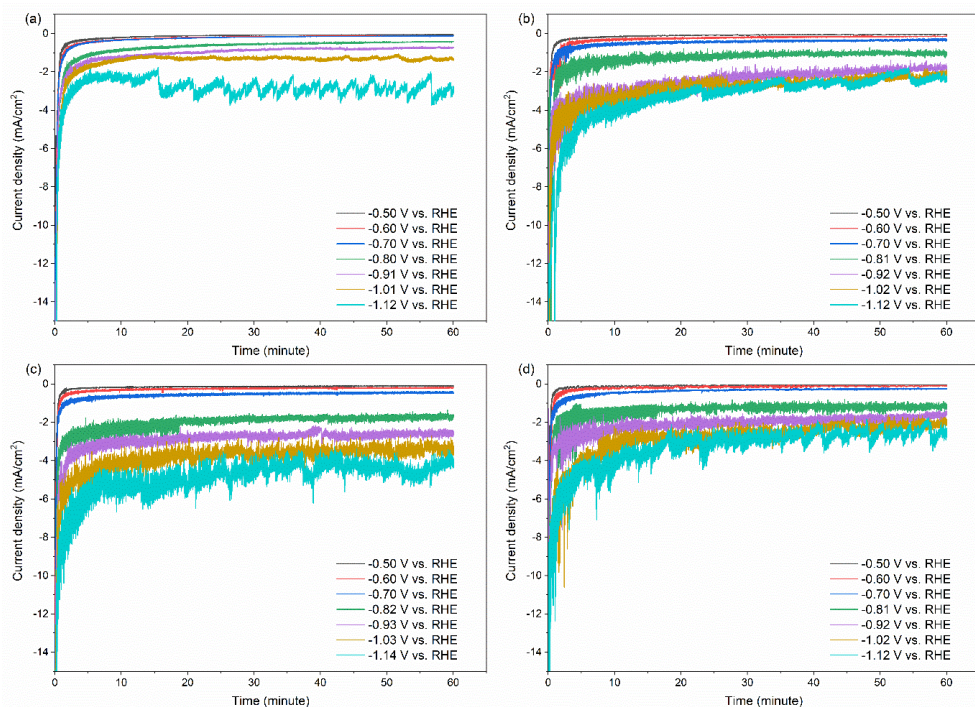


Figure S4.15 Chronoamperometry results of (a) ANBC800-SN; (b) ANBC800-LN; (c) ANBC800 and (d) ANBC800-HN at different potentials in CO₂-saturated 0.1M KHCO₃ electrolyte.

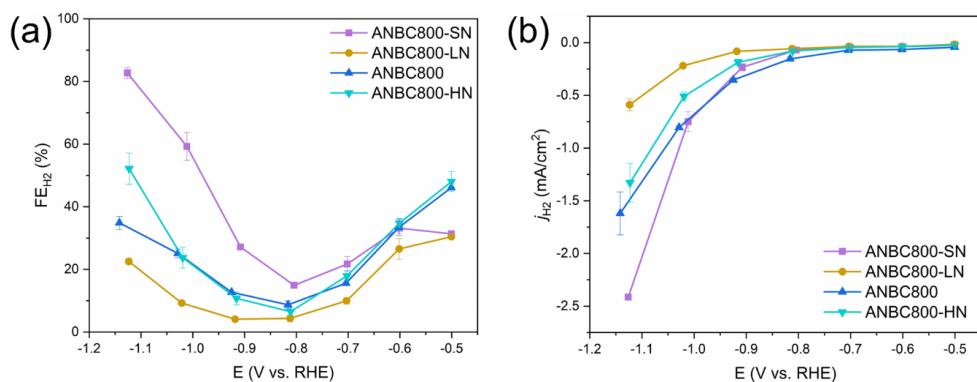


Figure S4.16 (a) FE of H₂ production at applied potentials from -0.5 to -1.15V vs. RHE; (b) Partial current density of H₂ at different applied potentials.

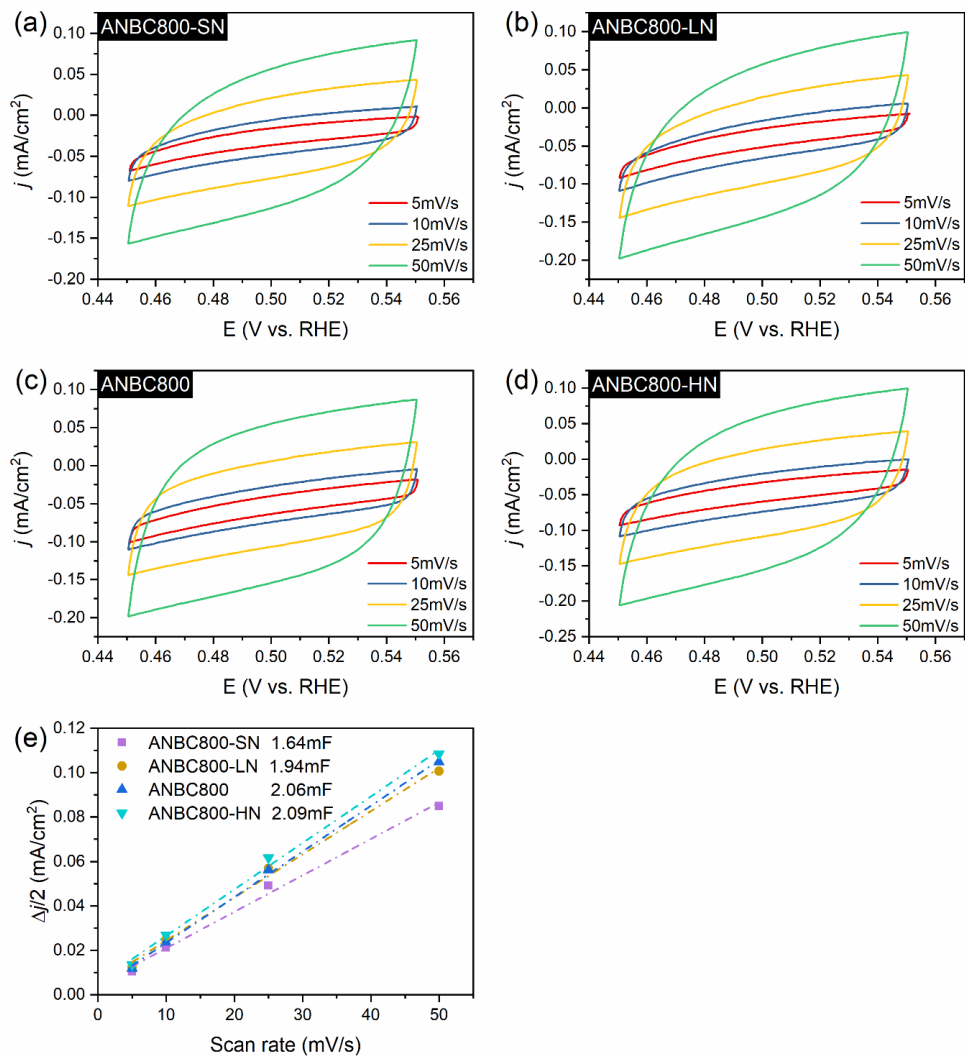


Figure S4.17 CVs of (a) ANBC800-SN, (b) ANBC800-LN, (c) ANBC800, (d) ANBC800-HN from 0.45 to 0.55 V vs. RHE at various scan rates and (e) The double layer capacitances of all samples.

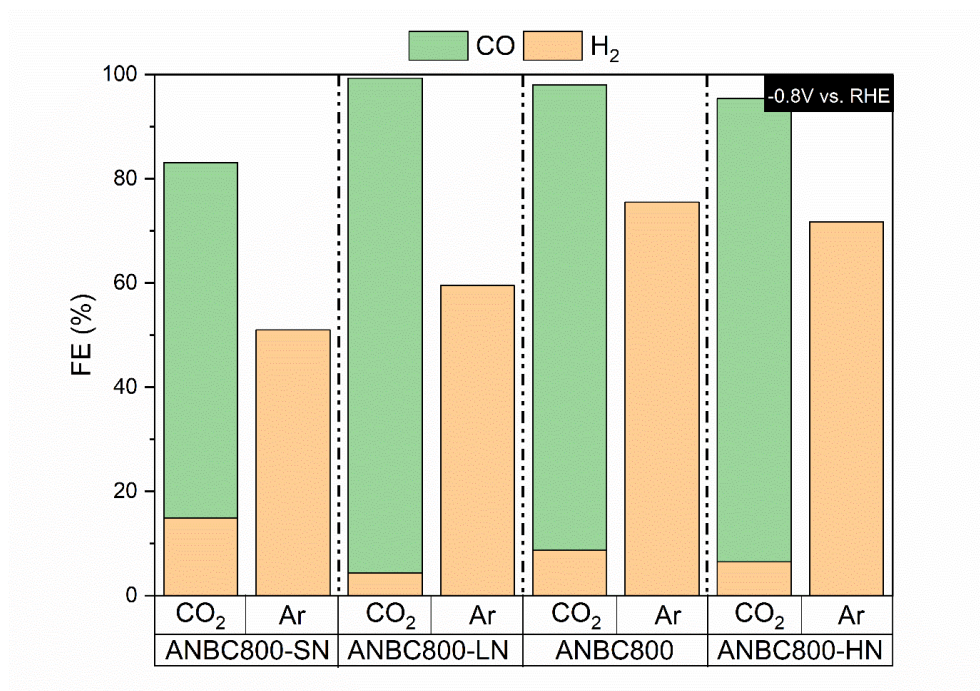


Figure S4.18 Gas products selectivity of chronoamperometry tests with a CO₂-saturated and Argon-saturated 0.1 M KHCO₃ electrolyte at -0.8V vs. RHE of the ANBC800-XN samples.

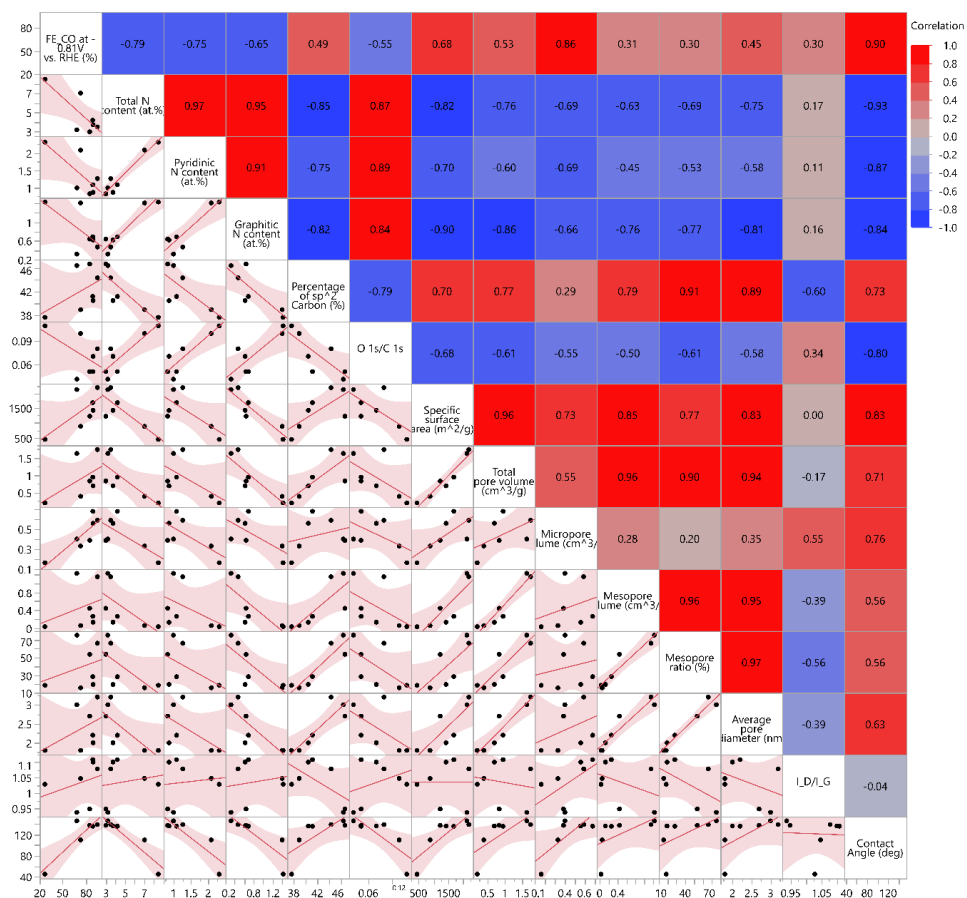


Figure S4.19 Scatter plot matrix for the multivariate correlation analysis between FE_{CO} at -0.81V vs. RHE and different physicochemical properties of all ANBC catalysts.

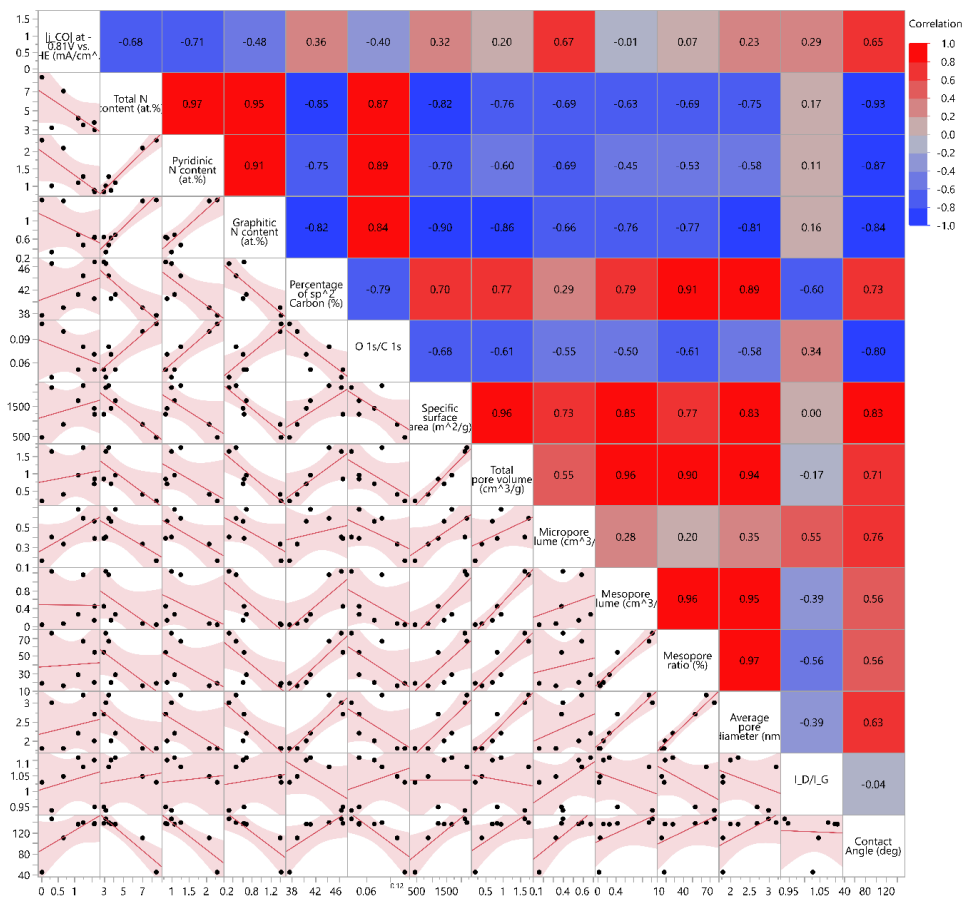


Figure S4.20 Scatter plot matrix for the multivariate correlation analysis between $|j_{CO}|$ at -0.81V vs. RHE and different physicochemical properties of all ANBC catalysts.

Table S4.1 Brief summary for the preparation of catalysts

Sample	Bagasse	Urea	NaOH	Total Amount	Carbonization Temperature	Obtained Carbon	Carbon Yield
ANBC600	5g	10g	15g	30.0g	600°C	1.07g	21.4%
ANBC700	5g	10g	15g	30.0g	700°C	0.86g	17.2%
ANBC800	5g	10g	15g	30.0g	800°C	0.51g	10.2%
ANBC900	5g	10g	15g	30.0g	900°C	0.23g	4.6%
ANBC800-SN	5g	2.5g	15g	22.5g	800°C	0.08g	1.6%
ANBC800-LN	5g	5g	15g	25.0g	800°C	0.31g	6.2%
ANBC800	5g	10g	15g	30.0g	800°C	0.51g	10.2%
ANBC800-HN	5g	15g	15g	35.0g	800°C	0.59g	11.8%

Table S4.2 Textural properties of different carbon catalysts

Samples	N ₂ adsorption/desorption						
	S _{BET}	S _{micro}	V _{total} (P/P0=0.95)	V _{micro}	V _{meso}	V _{meso} /V _t	D _{avg}
	m ² /g	m ² /g	cm ³ /g	cm ³ /g	cm ³ /g	%	nm
ANBC600	450.5	420.1	0.20	0.163	0.037	18.5	1.8
ANBC700	888.7	833.9	0.39	0.329	0.061	15.7	1.8
ANBC800	1426.9	1298.4	0.69	0.555	0.135	19.5	2.0
ANBC900	1228.7	812.1	0.83	0.385	0.445	53.6	2.7
ANBC800-SN	2126.2	968.7	1.62	0.399	1.220	75.3	3.0
ANBC800-LN	2191.9	1200.5	1.73	0.585	1.145	66.2	3.2
ANBC800	1426.9	1298.4	0.69	0.555	0.135	19.5	2.0
ANBC800-HN	1686.0	1453.7	0.94	0.674	0.266	28.3	2.2

Table S4.3 Surface elemental contents and N1s XPS data of different carbon catalysts

Samples	C	O	N	Pyridinic N(at.%)	Pyrrolic N(at.%)	Graphitic N(at.%)	Oxidized N(at.%)
	(at.%)	(at.%)	(at.%)	~398.7eV	~400.3eV	~401.8eV	~404.9eV
ANBC600	82.53	9.01	8.46	2.32	3.52	1.43	1.18
ANBC700	84.27	8.71	7.02	2.09	2.59	1.41	0.93
ANBC800	89.93	6.34	3.73	0.86	1.91	0.62	0.34
ANBC900	92.65	4.37	2.98	0.82	1.25	0.64	0.26
ANBC800-SN	93.20	3.61	3.19	0.99	1.60	0.32	0.28
ANBC800-LN	88.95	7.56	3.49	1.26	1.42	0.47	0.34
ANBC800	89.93	6.34	3.73	0.86	1.91	0.62	0.34
ANBC800-HN	91.68	4.13	4.19	1.08	2.01	0.69	0.41

Table S4.4 Contact Angle data for different carbon samples

Sample		Contact angle (°)				
		Drop 1	Drop 2	Drop 3	Mean	Standard Deviation
ANBC600	Fresh	45.8	48.2	41.6	45.2	3.34
	Used	47.0	42.4	44.9	44.8	2.30
ANBC700	Fresh	111.3	107.1	110.1	109.5	2.16
	Used	107.1	111.8	107.5	108.8	2.61
ANBC800	Fresh	136.3	135.8	134.6	135.6	0.87
	Used	135.4	134.6	134.2	134.7	0.61
ANBC900	Fresh	141.0	136.2	133.2	136.8	3.93
	Used	138.8	136	132.7	135.8	3.05
ANBC800-SN	Fresh	144.7	145.5	145.6	145.3	0.49
	Used	145.4	143.7	145.3	144.8	0.95
ANBC800-LN	Fresh	138.6	138.6	137.7	138.3	0.52
	Used	137.7	137.4	138.5	137.9	0.57
ANBC800	Fresh	136.3	135.8	134.6	135.6	0.87
	Used	135.4	134.6	134.2	134.7	0.61
ANBC800-HN	Fresh	135.2	135.0	135.5	135.2	0.25
	Used	134.1	134.9	133.8	134.3	0.57

References

- (1) Chu, S.; Majumdar, A. Opportunities and Challenges for a Sustainable Energy Future. *Nature* **2012**, *488* (7411), 294–303.
- (2) Saravanan, A.; Vo, D.-V. N.; Jeevanantham, S.; Bhuvaneswari, V.; Narayanan, V. A.; Yaashikaa, P. R.; Swetha, S.; Reshma, B. A Comprehensive Review on Different Approaches for CO₂ Utilization and Conversion Pathways. *Chem. Eng. Sci.* **2021**, *236*, 116515.
- (3) Seh, Z. W.; Kibsgaard, J.; Dickens, C. F.; Chorkendorff, I. B.; Nørskov, J. K.; Jaramillo, T. F. Combining Theory and Experiment in Electrocatalysis: Insights into Materials Design. *Science*. **2017**, *355*, 6321.
- (4) Peter, S. C. Reduction of CO₂ to Chemicals and Fuels: A Solution to Global Warming and Energy Crisis. *ACS Energy Lett.* **2018**, *3* (7), 1557–1561.
- (5) Kortlever, R.; Shen, J.; Schouten, K. J. P.; Calle-Vallejo, F.; Koper, M. T. M. Catalysts and Reaction Pathways for the Electrochemical Reduction of Carbon Dioxide. *J. Phys. Chem. Lett.* **2015**, *6* (20), 4073–4082.
- (6) Pan, F.; Yang, Y. Designing CO₂ Reduction Electrode Materials by Morphology and Interface Engineering. *Energy Environ. Sci.* **2020**, *13* (8), 2275–2309.
- (7) Lawrence, K. R.; Kumar, A. S.; Asperti, S.; van den Berg, D.; Girichandran, N.; Kortlever, R. Advances in Electrochemical Carbon Dioxide Reduction Toward Multi-Carbon Products. In *Chemical Valorisation of Carbon Dioxide*; 2022; pp 388–412.
- (8) Zheng, T.; Jiang, K.; Wang, H. Recent Advances in Electrochemical CO₂-to-CO Conversion on Heterogeneous Catalysts. *Adv. Mater.* **2018**, *30* (48), 1802066.
- (9) Chen, C.; Khosrowabadi Kotyk, J. F.; Sheehan, S. W. Progress toward Commercial Application of Electrochemical Carbon Dioxide Reduction. *Chem* **2018**, *4* (11), 2571–2586.
- (10) Han, N.; Ding, P.; He, L.; Li, Y.; Li, Y. Promises of Main Group Metal-Based Nanostructured Materials for Electrochemical CO₂ Reduction to Formate. *Adv. Energy Mater.* **2020**, *10* (11), 1902338.
- (11) Zhao, S.; Jin, R.; Jin, R. Opportunities and Challenges in CO₂ Reduction by Gold-and Silver-Based Electrocatalysts: From Bulk Metals to Nanoparticles and Atomically Precise Nanoclusters. *ACS energy Lett.* **2018**, *3* (2), 452–462.
- (12) Adegoke, K. A.; Maxakato, N. W. Electrochemical CO₂ Conversion to Fuels on Metal-Free N-Doped Carbon-Based Materials: Functionalities, Mechanistic, and Technoeconomic Aspects. *Mater. Today Chem.* **2022**, *24*, 100838.

- (13) Paul, R.; Zhu, L.; Chen, H.; Qu, J.; Dai, L. Recent Advances in Carbon-Based Metal-Free Electrocatalysts. *Adv. Mater.* **2019**, *1806403*, 1–24.
- (14) Wu, J.; Yadav, R. M.; Liu, M.; Sharma, P. P.; Tiwary, C. S.; Ma, L.; Zou, X.; Zhou, X. D.; Yakobson, B. I.; Lou, J.; Ajayan, P. M. Achieving Highly Efficient, Selective, and Stable CO₂ Reduction on Nitrogen-Doped Carbon Nanotubes. *ACS Nano* **2015**, *9* (5), 5364–5371.
- (15) Liu, S.; Yang, H.; Huang, X.; Liu, L.; Cai, W.; Gao, J.; Li, X.; Zhang, T.; Huang, Y.; Liu, B. Identifying Active Sites of Nitrogen-Doped Carbon Materials for the CO₂ Reduction Reaction. *Adv. Funct. Mater.* **2018**, *28* (21), 1800499.
- (16) Liu, Y.; Chen, S.; Quan, X.; Yu, H. Efficient Electrochemical Reduction of Carbon Dioxide to Acetate on Nitrogen-Doped Nanodiamond. *J. Am. Chem. Soc.* **2015**, *137* (36), 11631–11636.
- (17) Hu, C.; Dai, L. Doping of Carbon Materials for Metal-Free Electrocatalysis. *Adv. Mater.* **2019**, *31* (7), 1–17.
- (18) Li, F.; Xue, M.; Knowles, G. P.; Chen, L.; MacFarlane, D. R.; Zhang, J. Porous Nitrogen-Doped Carbon Derived from Biomass for Electrocatalytic Reduction of CO₂ to CO. *Electrochim. Acta* **2017**, *245*, 561–568.
- (19) Abdelkader-Fernandez, V. K.; Fernandes, D. M.; Freire, C. Carbon-Based Electrocatalysts for CO₂ Electroreduction Produced via MOF, Biomass, and Other Precursors Carbonization: A Review. *J. CO₂ Util.* **2020**, *42*, 101350.
- (20) Liu, W.; Qi, J.; Bai, P.; Zhang, W.; Xu, L. Utilizing Spatial Confinement Effect of N Atoms in Micropores of Coal-Based Metal-Free Material for Efficiently Electrochemical Reduction of Carbon Dioxide. *Appl. Catal. B Environ.* **2020**, *272*, 118974.
- (21) Zhu, D. D.; Liu, J. L.; Qiao, S. Z. Recent Advances in Inorganic Heterogeneous Electrocatalysts for Reduction of Carbon Dioxide. *Adv. Mater.* **2016**, *28* (18), 3423–3452.
- (22) Kuang, M.; Guan, A.; Gu, Z.; Han, P.; Qian, L.; Zheng, G. Enhanced N-Doping in Mesoporous Carbon for Efficient Electrocatalytic CO₂ Conversion. *Nano Res.* **2019**, *12* (9), 2324–2329.
- (23) Ma, C.; Hou, P.; Wang, X.; Wang, Z.; Li, W.; Kang, P. Carbon Nanotubes with Rich Pyridinic Nitrogen for Gas Phase CO₂ Electroreduction. *Appl. Catal. B Environ.* **2019**, *250*, 347–354.
- (24) Zhang, Z.; Yu, L.; Tu, Y.; Chen, R.; Wu, L.; Zhu, J.; Deng, D. Unveiling the Active Site of Metal-Free Nitrogen-Doped Carbon for Electrocatalytic Carbon Dioxide Reduction. *Cell Reports Phys. Sci.* **2020**, *1* (8), 100145.

- (25) Cui, X.; Pan, Z.; Zhang, L.; Peng, H.; Zheng, G. Selective Etching of Nitrogen-Doped Carbon by Steam for Enhanced Electrochemical CO₂ Reduction. *Adv. Energy Mater.* **2017**, *7* (22), 1–6.
- (26) Li, H.; Xiao, N.; Hao, M.; Song, X.; Wang, Y.; Ji, Y.; Liu, C.; Li, C.; Guo, Z.; Zhang, F.; Qiu, J. Efficient CO₂ Electroreduction over Pyridinic-N Active Sites Highly Exposed on Wrinkled Porous Carbon Nanosheets. *Chem. Eng. J.* **2018**, *351*, 613–621.
- (27) Li, J.; Zan, W. Y.; Kang, H.; Dong, Z.; Zhang, X.; Lin, Y.; Mu, Y. W.; Zhang, F.; Zhang, X. M.; Gu, J. Graphitic-N Highly Doped Graphene-like Carbon: A Superior Metal-Free Catalyst for Efficient Reduction of CO₂. *Appl. Catal. B Environ.* **2021**, *298*, 120510.
- (28) Daiyan, R.; Tan, X.; Chen, R.; Saputera, W. H.; Tahini, H. A.; Lovell, E.; Ng, Y. H.; Smith, S. C.; Dai, L.; Lu, X.; Amal, R. Electroreduction of CO₂ to CO on a Mesoporous Carbon Catalyst with Progressively Removed Nitrogen Moieties. *ACS Energy Lett.* **2018**, *3* (9), 2292–2298.
- (29) Hursán, D.; Samu, A. A.; Janovák, L.; Artyushkova, K.; Asset, T.; Atanassov, P.; Janáky, C. Morphological Attributes Govern Carbon Dioxide Reduction on N-Doped Carbon Electrodes. *Joule* **2019**, *3* (7), 1719–1733.
- (30) Fu, S.; Li, M.; Asperti, S.; De Jong, W.; Kortlever, R. Unravelling the Effect of Activators Used in the Synthesis of Biomass-Derived Carbon Electrocatalysts on the Electrocatalytic Performance for CO₂ Reduction. *ChemSusChem* **2023**, *16*, e202202188.
- (31) Liu, W. J.; Jiang, H.; Yu, H. Q. Development of Biochar-Based Functional Materials: Toward a Sustainable Platform Carbon Material. *Chem. Rev.* **2015**, *115* (22), 12251–12285.
- (32) Liu, W.-J.; Jiang, H.; Yu, H.-Q. Emerging Applications of Biochar-Based Materials for Energy Storage and Conversion. *Energy Environ. Sci.* **2019**, *12* (6), 1751–1779.
- (33) Lobaccaro, P.; Singh, M. R.; Clark, E. L.; Kwon, Y.; Bell, A. T.; Ager, J. W. Effects of Temperature and Gas–Liquid Mass Transfer on the Operation of Small Electrochemical Cells for the Quantitative Evaluation of CO₂ Reduction Electrocatalysts. *Phys. Chem. Chem. Phys.* **2016**, *18* (38), 26777–26785.
- (34) Zhang, Y.; Song, X.; Xu, Y.; Shen, H.; Kong, X.; Xu, H. Utilization of Wheat Bran for Producing Activated Carbon with High Specific Surface Area via NaOH Activation Using Industrial Furnace. *J. Clean. Prod.* **2019**, *210*, 366–375.
- (35) Lin, L.; Zhai, S.-R.; Xiao, Z.-Y.; Song, Y.; An, Q.-D.; Song, X.-W. Dye Adsorption of Mesoporous Activated Carbons Produced from NaOH-Pretreated Rice Husks. *Bioresour. Technol.* **2013**, *136*, 437–443.

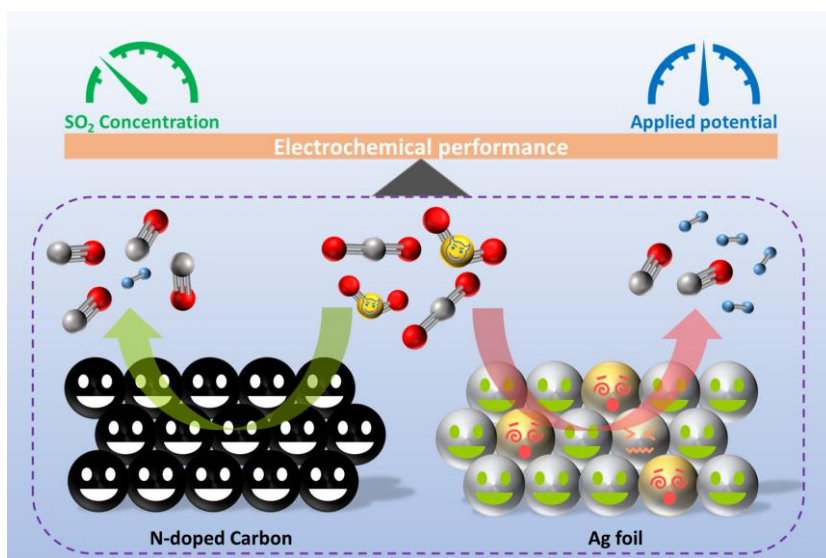
- (36) Zou, K.; Deng, Y.; Chen, J.; Qian, Y.; Yang, Y.; Li, Y.; Chen, G. Hierarchically Porous Nitrogen-Doped Carbon Derived from the Activation of Agriculture Waste by Potassium Hydroxide and Urea for High-Performance Supercapacitors. *J. Power Sources* **2018**, *378*, 579–588.
- (37) Qiu, T.; Yang, J.-G.; Bai, X.-J.; Wang, Y.-L. The Preparation of Synthetic Graphite Materials with Hierarchical Pores from Lignite by One-Step Impregnation and Their Characterization as Dye Absorbents. *RSC Adv.* **2019**, *9* (22), 12737–12746.
- (38) Vinayan, B. P.; Nagar, R.; Raman, V.; Rajalakshmi, N.; Dhathathreyan, K. S.; Ramaprabhu, S. Synthesis of Graphene-Multiwalled Carbon Nanotubes Hybrid Nanostructure by Strengthened Electrostatic Interaction and Its Lithium Ion Battery Application. *J. Mater. Chem.* **2012**, *22* (19), 9949–9956.
- (39) Li, K.; Chen, W.; Yang, H.; Chen, Y.; Xia, S.; Xia, M.; Tu, X.; Chen, H. Mechanism of Biomass Activation and Ammonia Modification for Nitrogen-Doped Porous Carbon Materials. *Bioresour. Technol.* **2019**, *280*, 260–268.
- (40) Niu, Q.; Gao, K.; Tang, Q.; Wang, L.; Han, L.; Fang, H.; Zhang, Y.; Wang, S.; Wang, L. Large-Size Graphene-like Porous Carbon Nanosheets with Controllable N-Doped Surface Derived from Sugarcane Bagasse Pith/Chitosan for High Performance Supercapacitors. *Carbon* **2017**, *123*, 290–298.
- (41) Ayiania, M.; Smith, M.; Hensley, A. J. R.; Scudiero, L.; McEwen, J. S.; Garcia-Perez, M. Deconvoluting the XPS Spectra for Nitrogen-Doped Chars: An Analysis from First Principles. *Carbon* **2020**, *162*, 528–544.
- (42) Li, X.; Guan, B. Y.; Gao, S.; Lou, X. W. A General Dual-Templating Approach to Biomass-Derived Hierarchically Porous Heteroatom-Doped Carbon Materials for Enhanced Electrocatalytic Oxygen Reduction. *Energy Environ. Sci.* **2019**, *12* (2), 648–655.
- (43) Lin, Y.; Feng, Z.; Yu, L.; Gu, Q.; Wu, S.; Su, D. S. Insights into the Surface Chemistry and Electronic Properties of sp^2 and sp^3 -Hybridized Nanocarbon Materials for Catalysis. *Chem. Commun.* **2017**, *53* (35), 4834–4837.
- (44) Masoumi, S.; Dalai, A. K. Optimized Production and Characterization of Highly Porous Activated Carbon from Algal-Derived Hydrochar. *J. Clean. Prod.* **2020**, *263*, 121427.
- (45) Li, C.; Wang, Y.; Xiao, N.; Li, H.; Ji, Y.; Guo, Z.; Liu, C.; Qiu, J. Nitrogen-Doped Porous Carbon from Coal for High Efficiency CO_2 Electrocatalytic Reduction. *Carbon* **2019**, *151*, 46–52.

- (46) Yao, P.; Qiu, Y.; Zhang, T.; Su, P.; Li, X.; Zhang, H. N-Doped Nanoporous Carbon from Biomass as a Highly Efficient Electrocatalyst for the CO₂ Reduction Reaction. *ACS Sustain. Chem. Eng.* **2019**, *7* (5), 5249–5255.
- (47) Ma, X.; Du, J.; Sun, H.; Ye, F.; Wang, X.; Xu, P.; Hu, C.; Zhang, L.; Liu, D. Boron, Nitrogen Co-Doped Carbon with Abundant Mesopores for Efficient CO₂ Electroreduction. *Appl. Catal. B Environ.* **2021**, *298*, 120543.
- (48) Wu, Q.; Gao, J.; Feng, J.; Liu, Q.; Zhou, Y.; Zhang, S.; Nie, M.; Liu, Y.; Zhao, J.; Liu, F.; Zhong, J.; Kang, Z. A CO₂ Adsorption Dominated Carbon Defect-Based Electrocatalyst for Efficient Carbon Dioxide Reduction. *J. Mater. Chem. A* **2020**, *8* (3), 1205–1211.
- (49) Liu, W.; Qi, J.; Bai, P.; Zhang, W.; Xu, L. Utilizing Spatial Confinement Effect of N Atoms in Micropores of Coal-Based Metal-Free Material for Efficiently Electrochemical Reduction of Carbon Dioxide. *Appl. Catal. B Environ.* **2020**, *272*, 118974.
- (50) Ning, H.; Guo, D.; Wang, X.; Tan, Z.; Wang, W.; Yang, Z.; Li, L.; Zhao, Q.; Hao, J.; Wu, M. Efficient CO₂ Electroreduction over N-Doped Hieratically Porous Carbon Derived from Petroleum Pitch. *J. Energy Chem.* **2021**, *56*, 113–120.
- (51) Gang, X.; Krishnamoorthy, M.; Jiang, W.; Pan, J.; Pan, Z.; Liu, X. A Novel In-Situ Preparation of N-Rich Spherical Porous Carbon as Greatly Enhanced Material for High-Performance Supercapacitors. *Carbon* **2021**, *171*, 62–71.
- (52) Deng, W.; Zhang, P.; Seger, B.; Gong, J. Unraveling the Rate-Limiting Step of Two-Electron Transfer Electrochemical Reduction of Carbon Dioxide. *Nat. Commun.* **2022**, *13* (1), 1–9.
- (53) Chmiola, J.; Yushin, G.; Gogotsi, Y.; Portet, C.; Simon, P.; Taberna, P.-L. Anomalous Increase in Carbon Capacitance at Pore Sizes Less than 1 Nanometer. *Science*. **2006**, *313* (5794), 1760–1763.
- (54) Largeot, C.; Portet, C.; Chmiola, J.; Taberna, P.-L.; Gogotsi, Y.; Simon, P. Relation between the Ion Size and Pore Size for an Electric Double-Layer Capacitor. *J. Am. Chem. Soc.* **2008**, *130* (9), 2730–2731.
- (55) Daiyan, R.; Tan, X.; Chen, R.; Saputera, W. H.; Tahini, H. A.; Lovell, E.; Ng, Y. H.; Smith, S. C.; Dai, L.; Lu, X.; Amal, R. Electroreduction of CO₂ to CO on a Mesoporous Carbon Catalyst with Progressively Removed Nitrogen Moieties. *ACS Energy Lett.* **2018**, *3* (9), 2292–2298.
- (56) Estevez, L.; Barpaga, D.; Zheng, J.; Sabale, S.; Patel, R. L.; Zhang, J. G.; McGrail, B. P.; Motkuri, R. K. Hierarchically Porous Carbon Materials for CO₂ Capture: The Role of Pore Structure. *Ind. Eng. Chem. Res.* **2018**, *57* (4), 1262–1268.

(57) Oates, R. P.; Murawski, J.; Hor, C.; Shen, X.; Weber, D. J.; Oezaslan, M.; Shaffer, M. S. P.; Stephens, I. E. L. How to Minimise Hydrogen Evolution on Carbon Based Materials? *J. Electrochem. Soc.* **2022**, *169* (5), 54516.

5

Electrochemical CO₂ Reduction in the Presence of SO₂ Impurities on a Nitrogen-doped Carbon Electrocatalyst



Abstract: Electrochemical CO₂ reduction to CO is a promising route for converting waste CO₂ into sustainable chemicals and fuels. While most advanced catalysts for CO production have been tested using pure CO₂, the presence of SO₂ as a main impurity in industrial CO₂ streams presents a challenge. Several pioneering studies have explored the effects of SO₂ impurities on metallic catalysts for CO₂ reduction, but little is known about the impact on nitrogen-doped carbon catalysts. In this study, a self-made nitrogen-doped carbon catalyst was tested for CO₂ reduction to CO with varying concentrations of SO₂ impurities. The catalyst outperformed an Ag foil electrode in the presence of SO₂, displaying a stronger tolerance to higher SO₂ concentrations. It maintained over 90% faradaic efficiency for CO during an 8-hour stability measurement at -1.0 V vs. RHE with 100 ppm SO₂. SEM and XPS analyses reveal the absence of sulfur-containing species resulting from SO₂ reduction on the catalyst surface after these tests. Overall, our study demonstrates the strong tolerance and robustness of N-doped carbon catalysts compared to the Ag foil for the electrochemical CO₂ reduction to CO in the presence of SO₂ impurities.

5.1 Introduction

Coupling clean and renewable energy sources with the electrochemical CO₂ reduction reaction (CO₂RR) is a promising approach to convert waste CO₂ to chemicals and fuels and to store intermittent energy in chemical bonds.^{1,2} Depending on the choice of electrocatalyst and reaction conditions, CO₂ can be reduced to CO, formate, CH₄, C₂H₄ and oxygenated hydrocarbons.^{3,4} Among these products, CO is an attractive and competitive product that can be generated with relatively high product selectivity, showing potential for large-scale applications.⁵ Notably, almost all of the electrocatalysts for CO production with excellent performances were tested under ideal reaction conditions, using high-purity CO₂ gas ($\geq 99.99\%$) for electrochemical measurements to prevent contamination.^{6–9} However, industrial CO₂-rich sources, such as exhaust streams from power plants and metallurgical industry, often contain various gaseous impurities such as sulfur oxides (SO_x) and nitrogen oxides (NO_x).^{10–12} Several recent studies have reported the effect of these gaseous impurities on the CO₂RR on metallic catalysts. These studies show additional reactions competing with the CO₂RR and the reconfiguration and deactivation of the catalyst surface.^{13–16} Although these impurities can be removed by scrubbing and absorption to obtain high-purity CO₂, several techno-economic analyses have shown that the purification processes significantly increase the cost for CO₂ utilization.^{17,18} In this sense, developing a stable catalyst that is not affected by feedstock impurities can become crucial for the future scale-up of electrochemical reduction of CO₂ to CO.

Nitrogen-doped (N-doped) carbon materials have been demonstrated as efficient electrocatalysts for the CO₂RR to CO and are a viable alternative to metal-based catalysts.^{19–21} In previous studies, we developed a series of biomass-derived N-doped carbon catalysts and revealed the correlation between the physicochemical properties of N-doped biochar catalysts and CO₂RR performances.²² By altering the type of activator, carbonization temperature and N-doping level, we obtained an N-doped biochar catalyst which showed a promising performance for the CO₂RR with over 90% faradaic efficiency toward CO. Interestingly, benefiting from the high resistance of carbon materials to acids and bases,²³ N-doped carbon catalysts can potentially be very stable electrocatalysts for CO₂RR even in the presence of gaseous impurities. However, to the best of our knowledge, there is no information about the effect of gaseous impurities on the CO₂RR performances of N-doped carbon catalysts.

5.2 Experimental Methods

Chemicals and Materials: All chemical were used as received without further purification. Electrolyte solutions and 1 M HCl solutions were prepared from ultrapure water

(Milli-Q IQ 7000, 18.2 M Ω). Urea (CN₂H₄O, 99%), sodium hydroxide (NaOH, 98%), potassium bicarbonate (KHCO₃, 99.95%) and Nafion perfluorinated resin solution (5 wt.% in lower aliphatic alcohols and 15–20% water) were purchased from Sigma-Aldrich. Hydrochloric acid (HCl, 37%), and isopropanol (C₃H₈O, 99%) were purchased from VWR International. Carbon paper (Toray, TGP-H-60) was purchased from Thermo Scientific Chemicals, while the silver foil (25 × 25 × 1 mm, 99.995%) and the platinum foil (25 × 25 × 0.1 mm, 99.99%) were purchased from MaTeck GmbH.

Catalyst preparation: The activated nitrogen-doped biochar (ANBC) catalyst was synthesized by a one-step pyrolysis method. In brief, the received sugarcane bagasse (Maharashtra, India) was washed with ultrapure water three times to remove dust and gravel from the raw materials and then dried in a 105 °C oven overnight. The dried sugarcane bagasse was ground and sieved to obtain particle sizes of less than 425 μ m before use. Subsequently, 5 g of sugarcane bagasse powder, 10 g of urea, and 15 g of NaOH (mass ratio = 1: 2: 3) were added into a crucible and stirred for 30 minutes to make a homogeneous mixture. Then, the mixture was transferred into a muffle furnace followed by heating at 800 °C for 1 h with a ramping rate of 10 °C/min under a N₂ atmosphere (100 sccm/min, 99.99%, Linde Gas). After naturally cooling down to the ambient temperature, the obtained product was washed with 1 M HCl for 4 h at 60 °C to remove the sodium containing salts and other impurities. Afterwards, the product was rinsed and filtered thoroughly with ultrapure water until the washing effluent reached a neutral pH. Finally, the black powder was collected and dried at 105 °C for 12 h and the obtained catalyst was designated as ANBC.

Characterization: The morphology of the ANBC was visualized by using a JEOL JSM-6500F scanning electron microscope (SEM), operating at an acceleration voltage of 15 kV, and equipped with an energy-dispersive X-ray spectroscopy (EDX) detector (Ultradry, Thermo Scientific). The microstructure of ANBC was further investigated by transmission electron microscopy (TEM) with a JEOL JEM1400 microscope operated at 120 kV. TEM specimens were prepared by mixing the sample with isopropanol and ultrasonicated for 15 minutes, before dispersing the suspension onto a copper TEM grid with lacey carbon film. The specific surface area and porosity of ANBC were characterized by isothermal N₂ adsorption-desorption at 77 K using a Micromeritics TriStar II 3020 instrument. The sample was degassed at 300 °C for 15 h before measurement. The specific surface area (S_{BET}) of ANBC was determined by the Brunauer-Emmett-Teller (BET) equation and the pore size distribution plot was obtained by applying the Density Functional Theory (DFT) method. The surface area (S_{micro}) and volume (V_{micro}) of micropores were determined by the t-plot method. The total pore volume (V_{Total}) was calculated by single-point adsorption total pore volume analysis. The crystal structure of ANBC was performed by using an X-ray diffractometer (Bruker AXS D2 Phaser) with Cu-K α radiation (λ = 0.15406 nm). The scanning 2 θ angle range was between 10.0° and 80.0° using a step length of 0.020°. Raman spectrum of ANBC was

recorded from 500 to 3000 cm^{-1} on a LabRAM HR Evolution microscope (Horiba Scientific) with an excitation wavelength of 514 nm. The surface chemical compositions of ANBC were investigated by X-ray photoelectron spectroscopy (XPS) using a Thermo Scientific K-Alpha system with Al $\text{K}\alpha$ X-ray source (1486.6 eV). The C 1s peak position at 284.8 eV was used as an internal standard. CasaXPS (Version 2.3.22PR1.0) was used for the further elemental identification and peak deconvolution.

In particular, we also carried out SEM and XPS measurements of the ANBC drop casted electrodes and silver foil electrodes, before and after the electrolysis measurements, to characterize the changes in morphology and chemical composition of these electrodes.

Electrodes preparations: The working electrode was prepared by a drop casting method. 4 mg of ANBC powder was dispersed in a solvent mixture containing 950 μL isopropanol and 50 μL of 5 wt.% Nafion perfluorinated resin solution. Then the mixture was ultrasonicated for 1 h to obtain a homogeneous ink. Afterwards, 10 μL of the ink was drop casted on a 1 cm^2 round-shaped carbon paper and thoroughly dried at room temperature. The drop casting procedure was repeated 4 times more and the final catalyst loading was around 0.2 mg/cm^2 . A platinum foil was used as a counter electrode, which was flame annealed at least three times to remove any possible impurities before use. A leak-free Ag/AgCl electrode (Innovative instrument, LF-1-45) was used as the reference electrode. The reference electrode was checked before every experiment by comparing with a master Ag/AgCl reference electrode (BASi, MF-2056), which is kept in a pristine working condition and never used for any experiment. The potential drift of the test reference electrode against the master reference electrode was measured by an open circuit potential (OCP) test and the drift value was always ensured to be lower than 5 mV.

As a contrast, a silver foil was also used as the working electrode. Before each measurement, the silver foil was mechanically polished with a 1 μm diamond-based suspension (MetaDi supreme, Poly, 1 μm , Buehler) two times to a mirror-like finish and then sonicated in isopropanol and ultrapure water.

Gas mixer: A gas mixer (EnviroNics® Series 4020) was used to generate the gas mixtures for the electrochemical measurements. The mass flow controllers and gas lines in the gas mixer were coated by SilcoNert® and sealed by Kalrez® to prevent the corrosion from SO_2 gas. Two standard gas cylinders with known concentrations of SO_2 (100 ppm and 10000 ppm, balanced by CO_2 , Linde Gas) were used to generate the desired concentrations (100 ppm, 1000 ppm, and 10000 ppm) of SO_2 by diluting with CO_2 (99.999%, Linde Gas). The detailed information about the gas mixtures for electrochemical measurements are listed in Table S5.2.

Electrochemical measurements: All working electrodes were tested in a two-compartment compact H-cell, which was designed by Lobaccaro and co-workers. Each compartment contained 1.8 mL of 0.1 M KHCO_3 as the electrolyte and the cathode and anode chambers were separated by an anion-conducting membrane (Selecion AMV, AGC Engineering). Before each measurement, the cathodic compartment of the H-cell was purged with pure CO_2 or CO_2 with different concentrations of SO_2 impurities for 15 minutes to obtain a saturated catholyte. The pH values of different gas mixtures-saturated electrolytes are listed in Table S5.3. Electrochemical measurements in this study were carried out using an SP-200 potentiostat (Biologic). All potentials measured in this study were converted to the reversible hydrogen electrode (RHE) scale according to the formula: $E \text{ (V vs. RHE)} = E \text{ (V vs. Ag/AgCl)} + 0.197 + 0.059 \times \text{pH}$. Linear sweep voltammetry (LSV) measurements were recorded in different gas mixtures-saturated 0.1 M KHCO_3 electrolytes at a scan rate of 5 mV/s from -0.1 to -1.3 V vs. RHE. Chronoamperometric electrolysis measurements (without iR compensation) were carried out at different applied potentials from -0.7 to -1.3 V vs. RHE and each potential was applied for 1 h. During the chronoamperometry tests, CO_2 or CO_2 mixed with different concentrations of SO_2 impurities were purged continuously into the catholyte with a flow rate of 10 sccm/min using a mass flow controller. The faradaic efficiencies (FEs) reported in this study for different gas products were determined by using the data collected from 42 to 54 minutes.

Product detection: An online gas chromatography (Compact GC 4.0, Global Analyzer Solutions), equipped with one flame ionization detector (FID) and two thermal conductivity detectors (TCD), was used to quantify the gaseous products every 2 minutes. The gas chromatography (GC) was calibrated by using five calibration gas cylinders with different concentrations of 50, 100, 1000, 3000, and 8000 ppm of each gas component (Linde Gas). The liquid-phase products were collected at the end of the CO_2RR measurements and quantified using a high-performance liquid chromatography (HPLC, Agilent 1260 Infinity), which was equipped with two Aminex HPX 87-H columns (Bio-Rad). The column oven was maintained at 60 °C constantly, using a 1 mM H_2SO_4 aqueous solution as eluent with a steady flow of 0.6 mL/min and using a refractive index detector (RID) for the product detection.

5.3 Results and Discussions

Here, we selected an activated N-doped biochar (ANBC) catalyst to perform a systematic study on the impact of SO_2 impurities on its performance for the CO_2RR to CO. The ANBC catalyst was synthesized by a one-step pyrolysis method (Figure 5.1a and Experimental Methods in Supporting Information). The morphology and microstructure of ANBC were visualized by a scanning electron microscope coupled with energy-dispersive X-ray spectroscopy (SEM-EDX) and transmission electron microscope (TEM). The ANBC

catalyst morphology displays an intertwined, three-dimensional structure with multilevel channels (Figure 5.1b). EDX mapping images show that the nitrogen heteroatoms were uniformly doped into the carbon matrix (Figure 5.1d - f). The TEM image shows a wrinkled nanosheet structure with abundant pores of ANBC (Figure 5.1c). X-ray diffraction (XRD) and Raman spectroscopy were performed to investigate the crystallographic structure. For XRD, two broad diffraction peaks located at around $2\theta = 25^\circ$ and 44° are observed, corresponding to the (002) and (100) planes of graphite, showing dominant features of amorphous carbon (Figure S5.1a).²⁴ The Raman spectrum of ANBC shows two peaks at around 1350 cm^{-1} and 1590 cm^{-1} that are attributed to the D band and G band of carbon materials, respectively (Figure S5.1b).²⁵ The I_D/I_G value is equal to 1.101, suggesting a disordered carbon structure of ANBC with abundant defects and a relatively low degree of graphitization, which is in good agreement with the XRD result. N_2 adsorption-desorption isothermal analysis was executed to further evaluate the specific surface area and porosity of ANBC. ANBC exhibits a combination of type I and type IV isotherm according to the IUPAC classification (Figure S5.2a). The sharp increase of the isotherm at low relative pressure indicates the presence of micropores. A weak hysteresis loop appears at a relative pressure from 0.45 to 0.95, suggesting the existence of mesopores. In addition, a steep increase of isotherm at a high relative pressure (0.95 to 1.0) shows the presence of macropores.²⁶ The pore width distribution of ANBC was calculated by a density functional theory (DFT) method, showing a strong peak located at around 2 nm and a weak peak located at around 40 nm (Figure S5.2b). The ANBC sample possesses a large specific surface area ($1426.9\text{ m}^2/\text{g}$) and pore volume ($0.69\text{ cm}^3/\text{g}$) with a hierarchical porous structure (ca. 19.5% mesopores). X-ray photoelectron spectroscopy (XPS) was used to verify the chemical composition. The XPS survey spectrum shows three peaks at around 285.1, 400.1 and 533.3 eV that are assigned to C 1s, N 1s, and O 1s peaks, respectively (Figure S5.3). The N content of ANBC is calculated as 3.7 at.% and the high-resolution N 1s spectrum is deconvoluted into four peaks at 398.7, 400.3, 401.8 and 404.9 eV, corresponding to pyridinic N, pyrrolic N, graphitic N, and oxidized N configurations, respectively (Figure 5.1g).²⁷ Overall, the aforementioned characterizations reveal that we have successfully synthesized an N-doped biochar catalyst with uniform N-doping, a large specific area and a hierarchical porous structure, which shows potential as an efficient catalyst for electrochemical CO_2 reduction to CO .^{28–30}

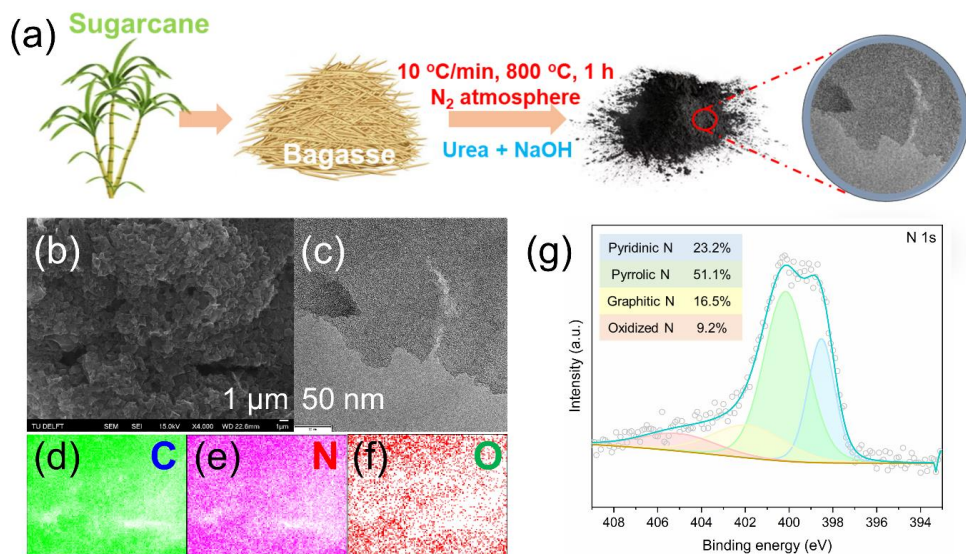


Figure 5.1 (a) A schematic illustration of the synthesis method of the ANBC catalyst; (b) SEM image; (c) TEM image; (d - f) EDX mapping images; and (g) High-resolution XPS N 1s spectrum of the synthesized ANBC.

The electrocatalytic performances of ANBC were evaluated at different potentials (-0.7 to -1.3 V vs. RHE) with and without the presence of different concentrations of SO₂ impurities (0, 100, 1000 and 10000 ppm), using a compact H-cell. The concentration of SO₂ in the CO₂ feed was adjusted using a gas mixer (Figure S5.4 and Supporting Information). The gaseous products were analyzed using an in-line gas chromatograph (GC), which was calibrated using custom gas mixture cylinders with known concentrations of product gases in CO₂ (Figure S5.5). Aliquots of the electrolyte were collected after each electrolysis experiment to quantify liquid products using a high-performance liquid chromatograph (HPLC). For comparison, a silver foil (Ag foil) electrode, the most widely used electrocatalyst for CO₂ reduction to CO, was used as a benchmark.

Linear sweep voltammograms (LSV) of ANBC electrodes were recorded in a 0.1 M KHCO₃ catholyte saturated with CO₂ and different concentrations of SO₂ from -0.1 to -1.3 V vs. RHE, with a scan rate of 5 mV/s. All of the voltammograms show a significant increase in current density between -0.6 to -0.7 V vs. RHE (Figure 5.2a). The voltammogram in the presence of 100 ppm SO₂ is very similar to the voltammograms obtained using pure CO₂. The presence of 1000 ppm SO₂ induces a slight increase in current density from -0.1 to -0.8 V vs. RHE, while the presence of 10000 ppm SO₂ shows more significant current changes

from -0.1 to -1.0 V vs. RHE, indicating that electrochemical SO₂ reduction occurs at more positive potentials than the CO₂RR (Table S5.1).³¹ As a comparison, voltammograms with Ag foil electrodes show similar trends as the ANBC electrodes; however, the Ag foil electrodes are more sensitive to the presence of SO₂ than ANBC electrodes, especially at higher concentrations (Figure S5.6a).

At first, we benchmarked the electrochemical performance of the ANBC electrode by performing chronoamperometry measurements without SO₂ impurities in the CO₂ feedstock. CO and H₂ are the main gaseous products detected by the in-line GC and no liquid products were detected with HPLC. The faradaic efficiency toward CO (FE_{CO}) for ANBC is consistently above 80% in a wide potential window from -0.7 V to -1.3 V vs. RHE and reaches a maximum of 94.5% FE_{CO} at -1.0 V vs. RHE. The partial current density of CO (j_{CO}) gradually increases from -0.63 mA/cm² at -0.7 V vs. RHE to -3.51 mA/cm² at -1.3 V vs. RHE (Figure 5.2b). By contrast, the FE_{CO} of the Ag foil electrode increases from 13.1% at -0.7 V vs. RHE to 91.4% at -1.3 V vs. RHE and the j_{CO} of the Ag foil electrode is only higher than that of the ANBC electrode at more negative potentials than -1.2 V vs. RHE (Figure S5.6b).

We further evaluated the CO₂RR performance of the ANBC electrode in the presence of different concentrations of SO₂ impurities. Depending on the chemical composition of fuels and post-treatment strategies, the concentration of SO₂ in flue gas typically varies from 100 to 10000 ppm.³² As an upper limit, we first selected the harshest reaction conditions (CO₂ + 10000 ppm SO₂ gas mixture). Using these conditions, the faradaic efficiency toward CO₂RR products of ANBC electrodes shows significant decreases in the whole potential window (Figure 5.2c), which is attributed to the preferential reduction of SO₂ over CO₂ (Table S5.1). Notwithstanding, the FE_{CO} of ANBC increases from only 0.5% at -0.7 V vs. RHE to 57% at -1.3 V vs. RHE. Moreover, the j_{CO} increases to -3.04 mA/cm² at -1.3 V vs. RHE, which is just slightly lower than that in the case of pure CO₂. In contrast, the Ag foil electrodes loses all of its CO₂RR activities under the same testing conditions, with the FE_{CO} and j_{CO} at different potentials being close to 0 (Figure S5.6c).

Subsequently, we also tested the ANBC electrode in the presence of 1000 ppm and 100 ppm SO₂ at -0.7, -1.0 and -1.3 V vs. RHE, and compared the changes of FE_{CO} and j_{CO} at different conditions. SO₂ impurities show a significant negative impact on the CO₂RR performance of ANBC electrodes only when the SO₂ concentration is extremely high (10000 ppm) or the potential is relatively positive (-0.7 V vs. RHE). Compared with the CO₂RR performance without SO₂ impurities, the changes of FE_{CO} and j_{CO} in the presence of 1000 ppm and 100 ppm SO₂ at -1.0 and -1.3 V vs. RHE are almost negligible (Figure 5.2d). It is noteworthy that the FE_{CO} of ANBC in the presence of 100 ppm SO₂ at -1.0 and -1.3 V vs. RHE and in the presence of 1000 ppm SO₂ at -1.3 V vs. RHE is even slightly higher than the value in the case of pure CO₂, which is attributed to the competition between the HER and SO₂

reduction reactions. As a comparison, the Ag foil electrode is more sensitive to the presence of SO_2 impurities. Even 100 ppm SO_2 in the CO_2 stream decreases the FE_{CO} with 5% during a 1-hour test at -1.0 V vs. RHE (Figure S5.6d). The FE_{CO} and j_{CO} of Ag foil electrode in the presence of 1000 ppm and 100 ppm SO_2 are only similar to the pure CO_2 experiments when the potentials shift to -1.3 V vs. RHE. Therefore, it is clear that the ANBC electrode shows a higher tolerance to SO_2 impurities and exhibits a better CO_2RR performance than the Ag foil electrode. Furthermore, the CO_2RR performances on ANBC electrode or Ag foil electrode are co-dependent on the concentration of SO_2 and the applied potentials, as lower SO_2 concentrations and more negative potentials can help to reduce the negative effects.

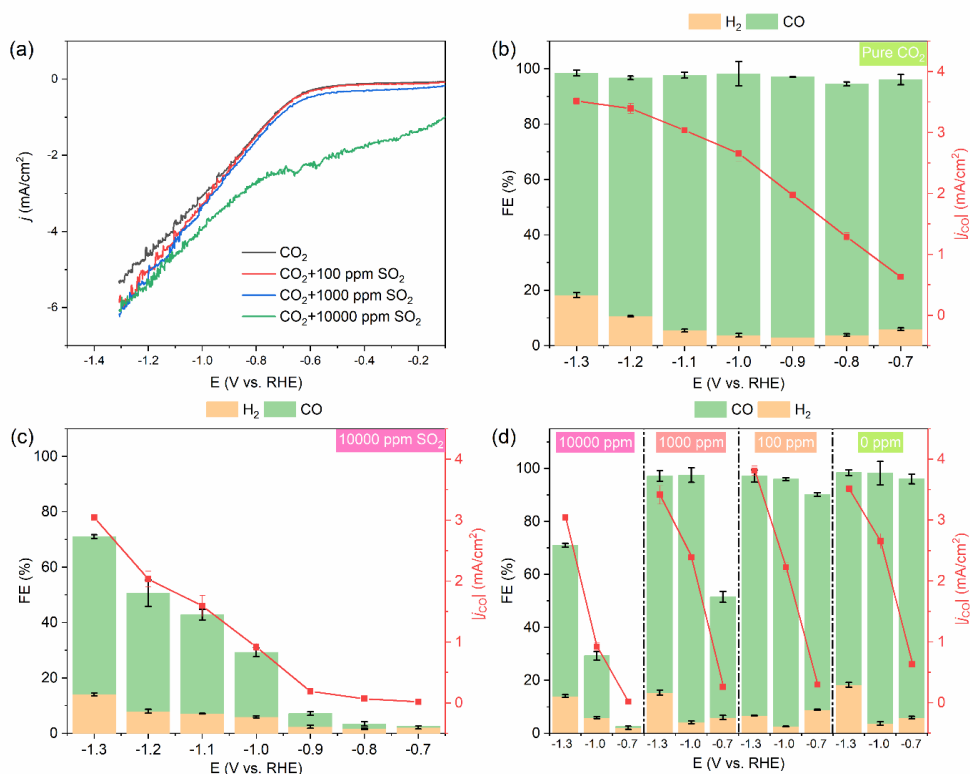


Figure 5.2 (a) LSV curves of the ANBC electrode without SO_2 and in the presence of different concentrations of SO_2 impurities; (b) Faradaic efficiency and partial current density toward CO for the ANBC electrode without SO_2 impurity from -0.7 to -1.3 V vs. RHE; (c) Faradaic efficiency and partial current density toward CO for the ANBC electrode in the presence of 10000 ppm SO_2 impurity from -0.7 to -1.3 V vs. RHE; (d) Faradaic efficiency and partial current density toward CO for the ANBC electrode in the presence of different concentrations of SO_2 impurities at -0.7, -1.0 and -1.3 V vs. RHE.

In addition, we carried out 8 h stability tests with pure CO₂ and CO₂ with 100 ppm SO₂ at -1.0 V vs. RHE. The FE_{CO} of ANBC shows an apparent decrease from 94% to 75% after 8 hours of continuous electrolysis with pure CO₂ (Figure 5.3a). Surprisingly, the ANBC electrode exhibits a stable FE_{CO} (above 85%) and FE_{H₂} (below 5%) within 8 hours of electrolysis in the presence of 100 ppm SO₂ (Figure 5.3b). Consistent with the results observed for 1-hour electrolysis, the presence of a low concentration of SO₂ has no serious effect on the CO₂RR performance of the ANBC electrode and helps to suppress the FE_{H₂} through competition with the HER. Similarly, the FE_{CO} of the Ag foil electrode shows a decreasing trend from 78% to 56% after 8 hours of measurement with pure CO₂ (Figure S5.7a). However, in the case of CO₂ with 100 ppm SO₂, different from the results from 1-hour electrolysis, the FE_{CO} of the Ag foil electrode shows a significant decrease (from 79% to 45%) during the longer electrolysis measurement (Figure S5.7b), which is attributed to the accumulation of impurities.

Considering that the concentration of SO₂ impurities in an actual flue gas can fluctuate, we evaluated the robustness of the ANBC electrode by modulating the reactant gas (CO₂ with 100 ppm SO₂ and pure CO₂) every 2 hours at -1.0 V vs. RHE. The ANBC electrode shows a strong tolerance to the gas feed changes, where the fluctuations in the total faradaic efficiency and FE_{CO} are almost negligible (Figure 5.3c). By contrast, the Ag foil electrode is more sensitive to changes in the reactant gas. The total faradaic efficiency and FE_{CO} in the case of pure CO₂ are higher than those in the presence of 100 ppm SO₂. Over time, a significant decline in the FE_{CO} can be clearly observed even in the case of pure CO₂ (Figure S5.7c). Corresponding to the above discussions, the ANBC electrode shows a longer stability and stronger robustness than the Ag foil electrode in the presence of 100 ppm SO₂ impurity.

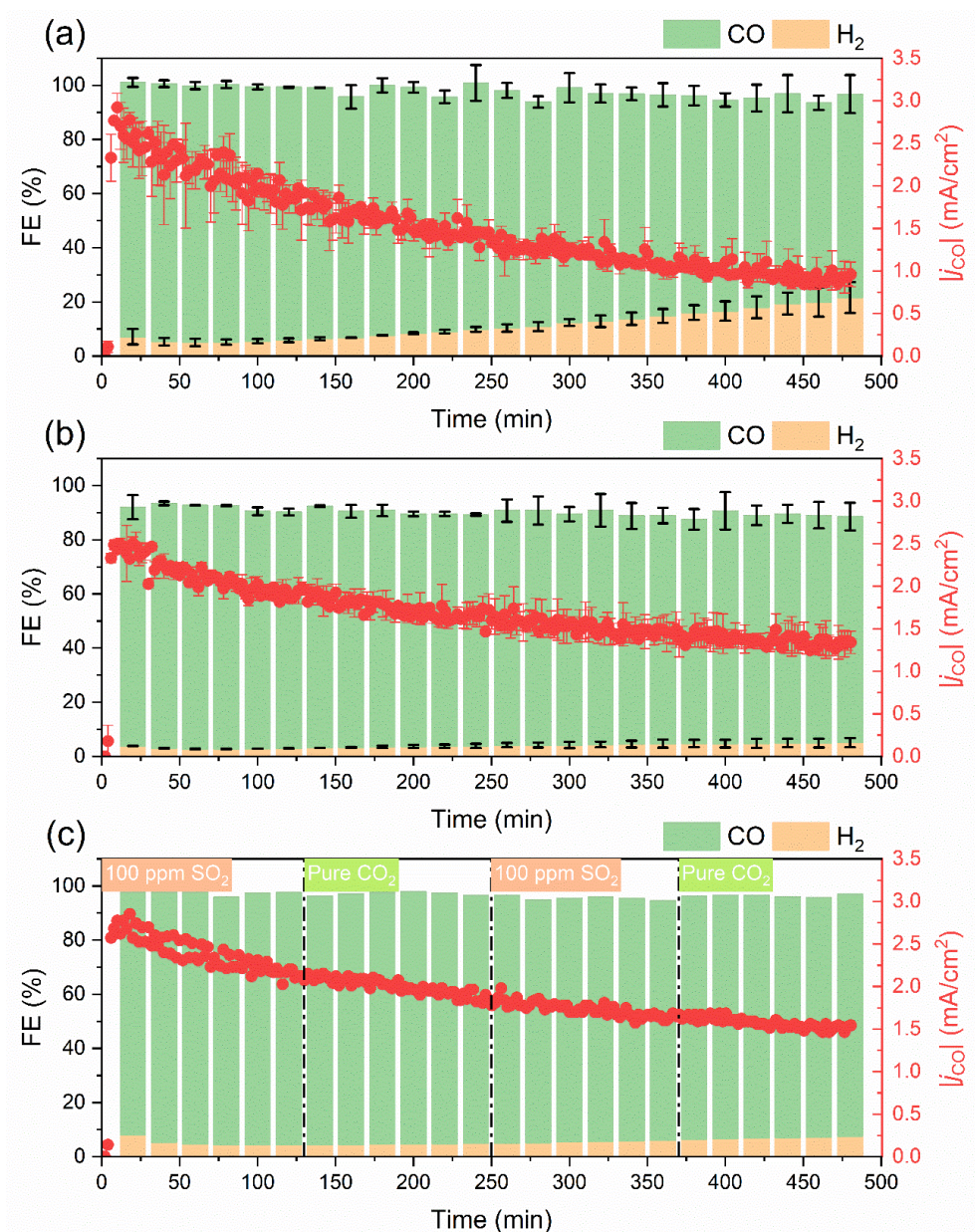


Figure 5.3 (a) 8-hour stability tests of ANBC electrode at -1.0 V vs. RHE in CO₂ saturated 0.1 M KHCO₃; (b) 8-hour stability tests of ANBC electrode at -1.0 V vs. RHE in CO₂ + 100 ppm SO₂ gas mixture saturated 0.1 M KHCO₃; (c) performance of CO₂ + 100 ppm SO₂ and pure CO₂ electrolysis over ANBC electrode at -1.0 V vs. RHE in 0.1 M KHCO₃ over 8 h, the gas feed is modulated every 2 hours.

To better understand the effect that SO_2 impurities have on the CO_2RR performance and the properties of ANBC electrodes, we carried out scanning electron microscopy (SEM) and X-ray photoelectron spectroscopy (XPS) characterizations to analyze the changes in surface microstructures and chemical composition of ANBC electrodes. The morphologies of the used ANBC electrodes (after 1 hour of electrolysis with different concentrations of SO_2 impurities) show no visible changes compared to the sample prior to testing (Figure 5.4a and Figure S5.8a). Further, pre- and post-reaction XPS measurements with the ANBC electrodes show an intensive peak at ~ 168.7 eV, with an atomic percentage of sulfur around 1.1 at. % for all electrodes. This peak is related to the sulfur containing functional groups incorporated in the Nafion binder (Figure 5.4b and Figure S5.8b).³³ In addition, even after 8 hours of continuous electrolysis with 100 ppm SO_2 at -1.0 V vs. RHE, the morphology and the atomic percentage of sulfur (1.08 at.%) of the ANBC electrode did not show significant changes (Figure S5.11). On the contrary, post-reaction SEM images of Ag foil electrodes in the presence of 10000 ppm SO_2 show pitting of the Ag foil electrode surface. This corrosion effect is diminished by reducing the SO_2 concentration or applying more negative potentials (Figure S5.9a and Figure S5.10a). Moreover, comparing the XPS results of the fresh Ag foil, the post-reaction Ag foil with pure CO_2 and the post-reaction Ag foil in the presence of different concentrations of SO_2 , clearly demonstrates the formation of sulfur-containing species on the Ag foil electrodes. The peak positions at 161.1 eV and 162.2 eV are assigned to the formation of silver sulfide (Ag_2S).³⁴ Additionally, trace amounts of sulfite (SO_3^{2-}) and sulfate (SO_4^{2-}) are detected.¹³ Higher concentrations of SO_2 and more positive potentials are more favorable for the formation of sulfur-containing species, especially Ag_2S (Figure S5.9b and Figure S5.10b). After 8 hours electrolysis with 100 ppm SO_2 at -1.0 V vs. RHE, the morphology of the Ag foil electrode was similar to a fresh electrode (Figure S5.12a). However, the sulfur content on the Ag foil significantly increased from 0.26 at.% (after 1h) to 4.25 at.% (after 8h), indicating the accumulation of sulfur-containing impurities on the Ag surface (Figure S5.12b). From these collective results, it is clear that SO_2 induced losses during the CO_2RR on ANBC mainly depend on the competition with SO_2 reduction, since no reconfigurations of the surface or inclusion of sulfur is observed. For the Ag foil electrode, besides the competition with SO_2 reduction, the formation and accumulation of silver sulfide surface species are important reasons for the loss of CO_2RR performance.

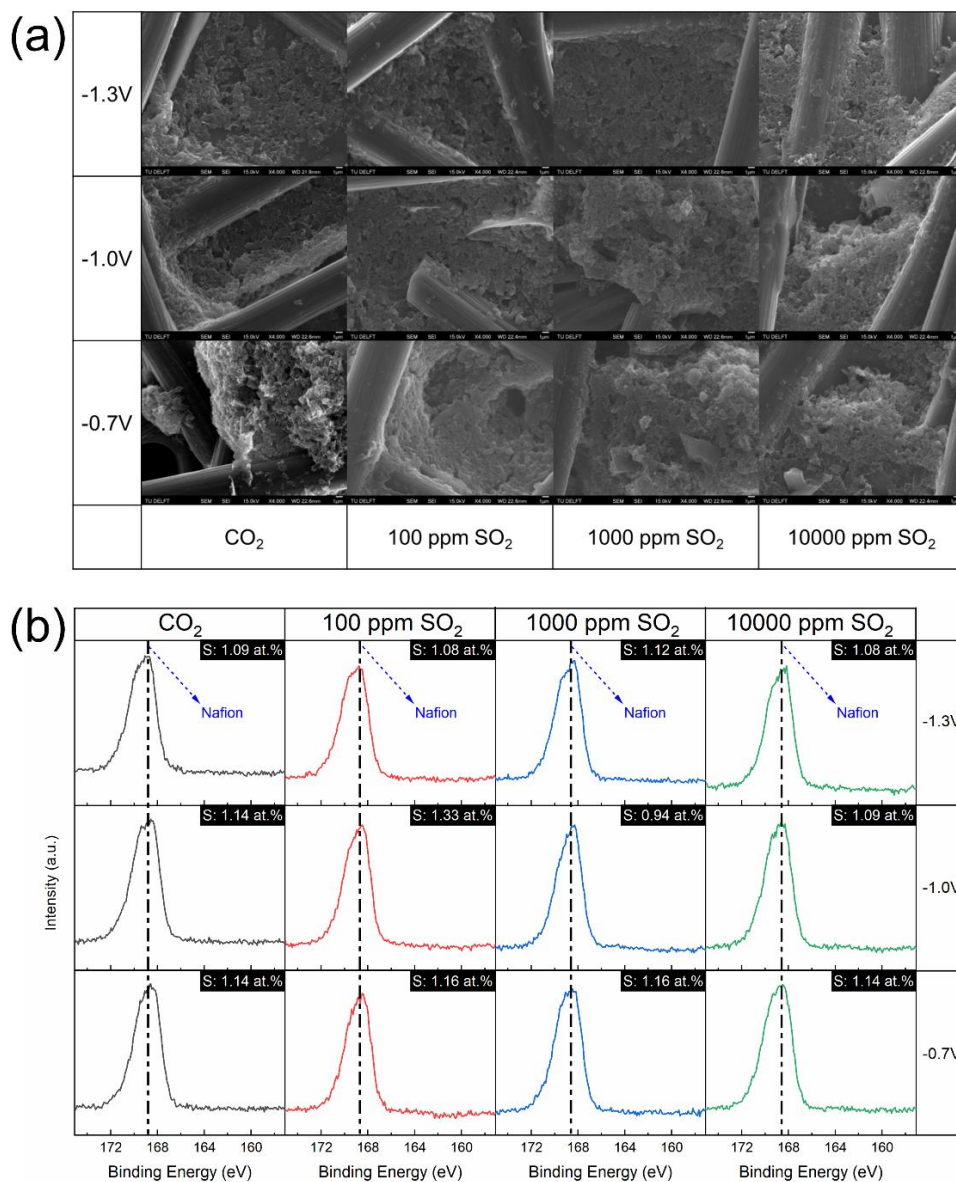


Figure 5.4 (a) SEM images and (b) S 2p XPS spectrum of ANBC electrodes after 1 h electrolysis in the presence of different concentration of SO₂ impurities and different potentials.

5.4 Conclusions

In summary, we carried out a systematic study to investigate the effects of SO_2 impurities on a self-made nitrogen-doped carbon catalyst and an Ag foil electrode (as a benchmark) for electrochemical CO_2 reduction to CO. The as-prepared ANBC catalyst achieves more than 90% faradaic efficiency toward CO from -0.8 to -1.1 V vs. RHE when feeding pure CO_2 . The presence of an extremely high concentration of SO_2 (10000 ppm) significantly reduces the CO_2RR performance as the SO_2 reduction becomes more preferential, whereas changes in the CO_2RR performances are almost negligible in the presence of 1000 and 100 ppm SO_2 impurities. Additionally, the ANBC catalyst shows stable FE_{CO} above 90% in an 8-hour stability measurement at -1.0 V vs. RHE with 100 ppm SO_2 impurity. The performance is even better than is the case with pure CO_2 , suggesting that the presence of a low concentration of SO_2 suppresses the FE_{H_2} through competition with the HER. In contrast, the Ag foil electrode is more sensitive to changes in the concentrations of SO_2 . The SEM and XPS results show that no SO_2 reduction generated sulfur-containing species are observed on the surface of the ANBC catalyst. However, the formation of silver sulfide, sulfate, and sulfite on the Ag foil electrode, as detected by XPS measurements, is likely responsible for the losses of CO_2RR performances. Overall, the ANBC catalyst exhibits a greater tolerance, longer stability and better robustness to SO_2 impurities than the Ag foil electrode for CO_2RR to CO, indicating that N-doped carbon catalysts are feasible catalysts for CO_2 reduction applications using SO_2 contaminated CO_2 feeds.

5.5 Supporting Information

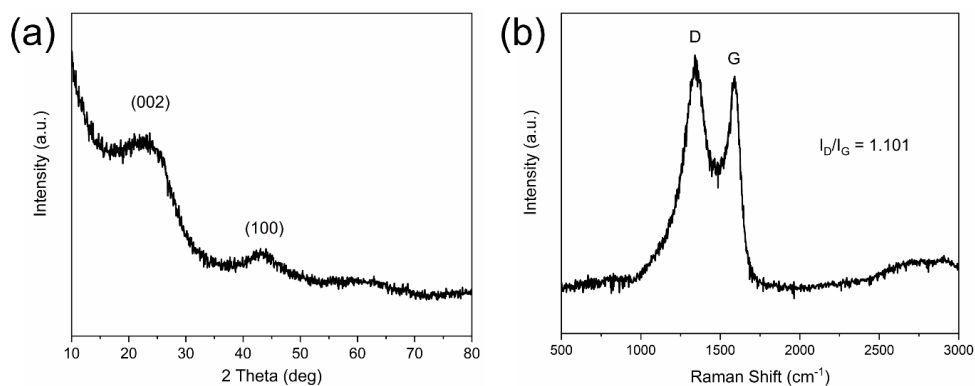


Figure S5.1 (a) XRD pattern and (b) Raman spectrum of the ANBC catalyst.

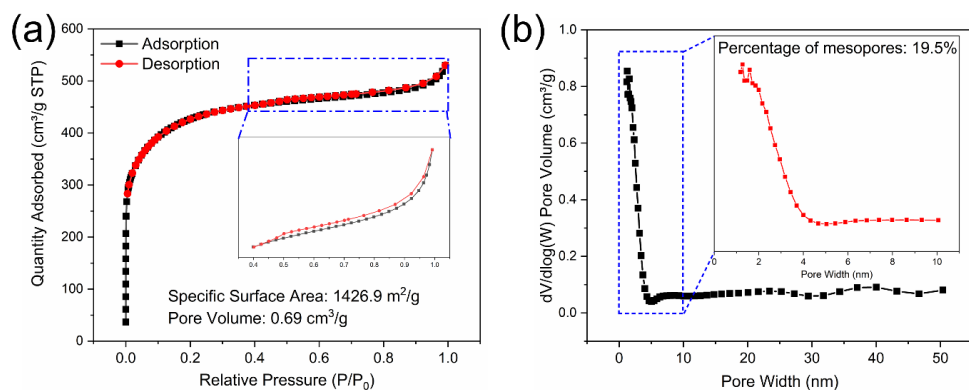


Figure S5.2 (a) N₂ adsorption-desorption isotherms and (b) Pore size distribution of the ANBC catalyst.

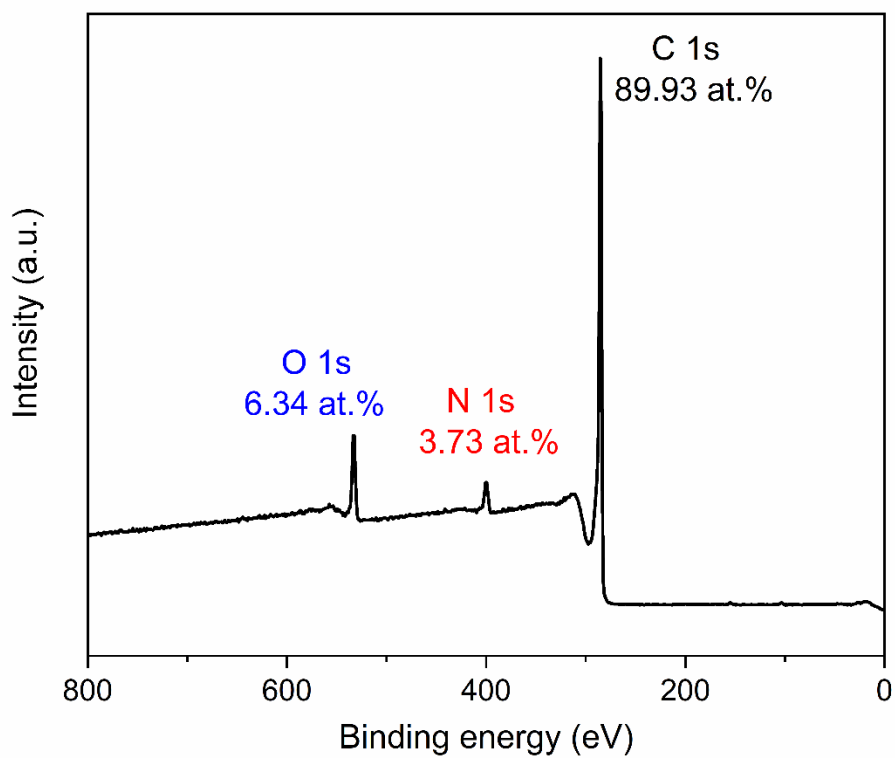


Figure S5.3 XPS survey spectrum of the ANBC catalyst.

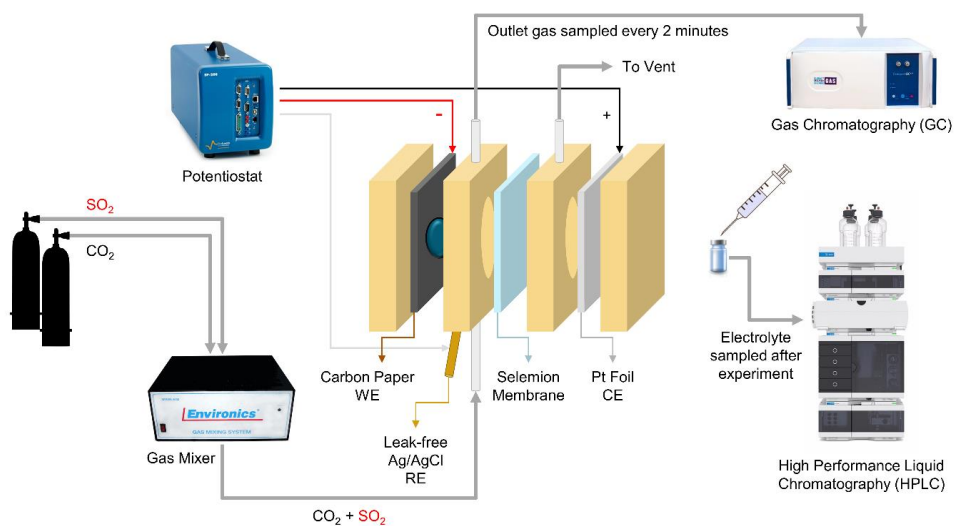


Figure S5.4 Schematic illustration of the electrochemical measurements system in this study.

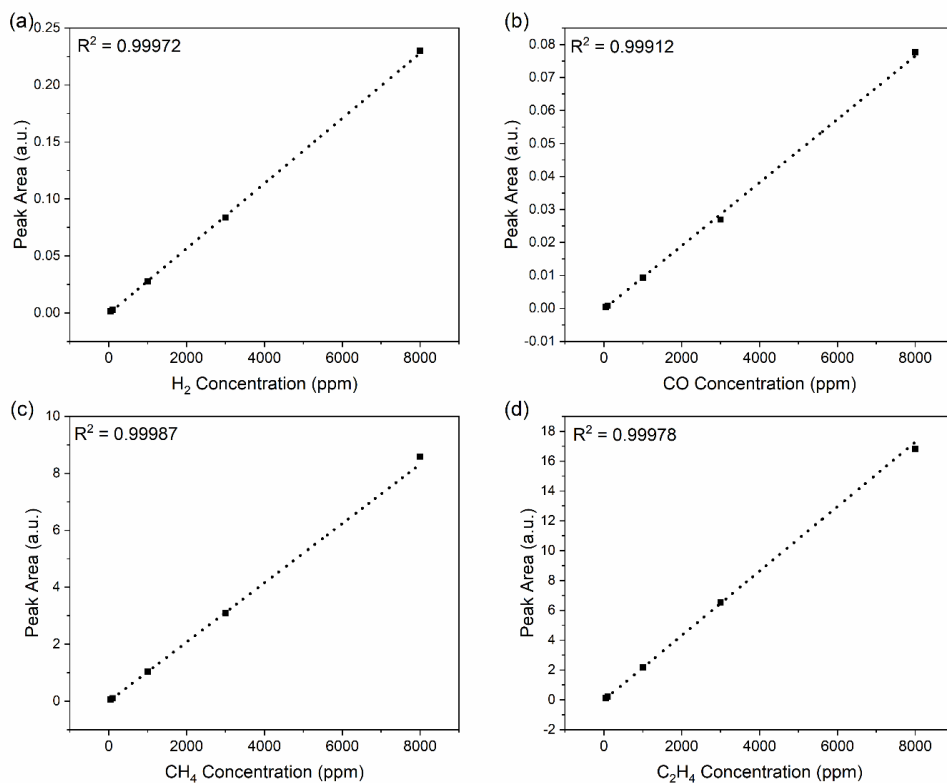


Figure S5.5 GC calibration curves for (a) H_2 , (b) CO , (c) CH_4 , (d) C_2H_4 .

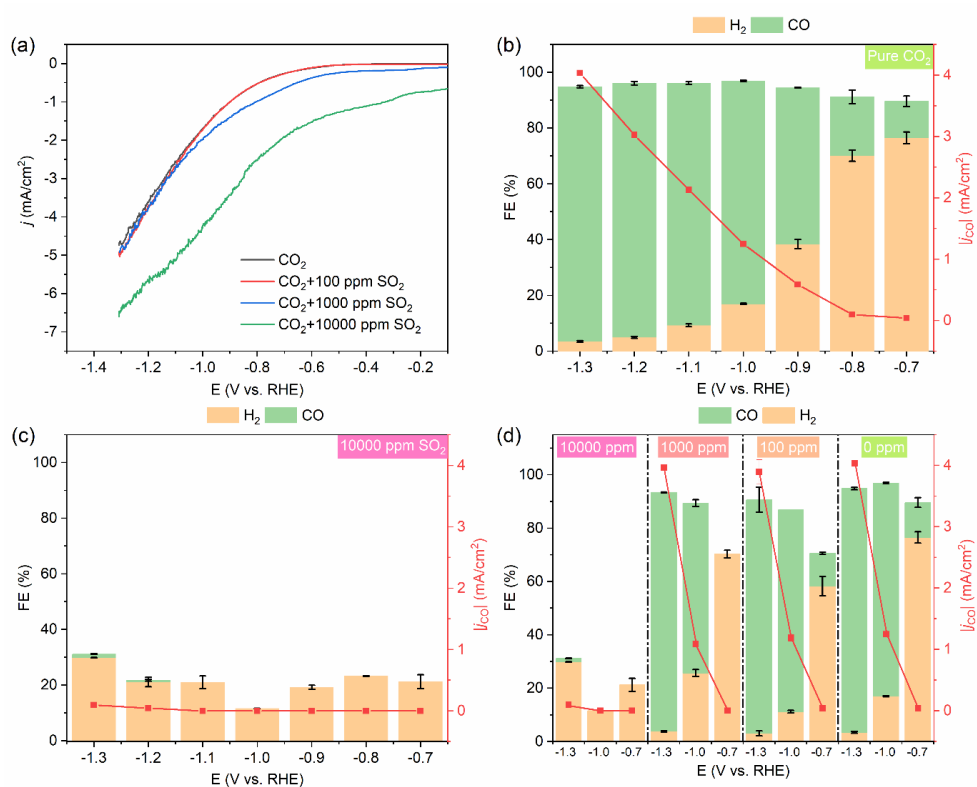


Figure S5.6 (a) LSV curves of the Ag foil electrode without SO₂ and in the presence of different concentrations of SO₂ impurities; (b) Faradaic efficiency and partial current density of CO for the Ag foil electrode without SO₂ impurity from -0.7 to -1.3 V vs. RHE; (c) Faradaic efficiency and partial current density of CO for the Ag foil electrode in the presence of 10000 ppm SO₂ impurity from -0.7 to -1.3 V vs. RHE; (d) Faradaic efficiency and partial current density of CO for the Ag foil electrode in the presence of different concentrations of SO₂ impurities at -0.7, -1.0 and -1.3 V vs. RHE.

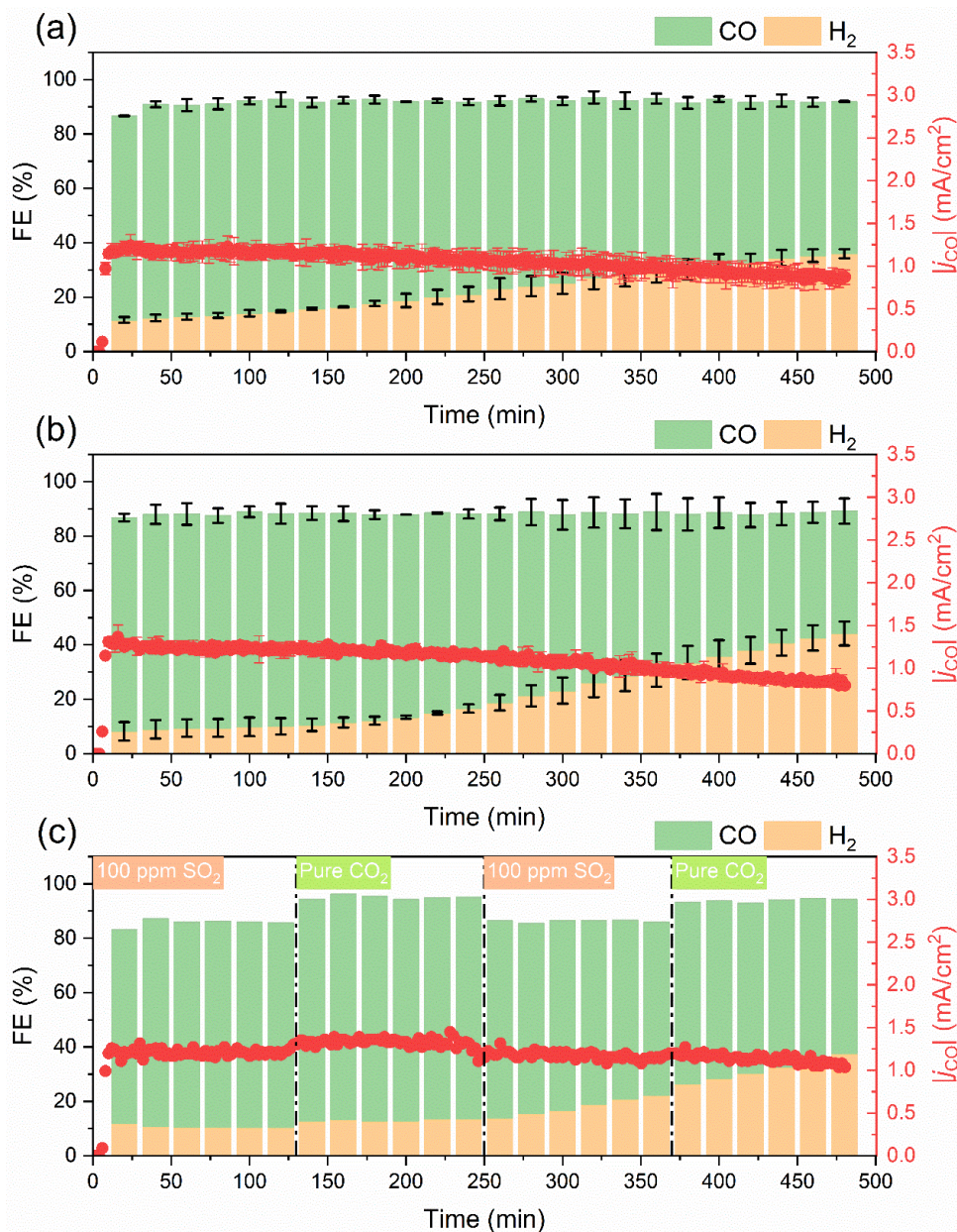


Figure S5.7 (a) 8-hour stability tests of Ag foil electrode at -1.0 V vs. RHE in CO₂ saturated 0.1 M KHCO₃; (b) 8-hour stability tests of Ag foil electrode at -1.0 V vs. RHE in CO₂ + 100 ppm SO₂ gas mixture saturated 0.1 M KHCO₃; (c) performance of CO₂ + 100 ppm SO₂ and pure CO₂ electrolysis over Ag foil electrode at -1.0 V vs. RHE in 0.1 M KHCO₃ over 8 h, the gas feed is modulated every 2 hours.

Supporting discussion about the concept of stability and robustness:

In contrast to the concept of stability, the robustness evaluation mainly focuses on “the ability of a system to resist change without adapting its initial stable configuration”. In this study, we evaluate the effect of the change in SO_2 concentration on ANBC and Ag foil electrodes in a continuous feed stream by modulating the gas composition. A catalyst can be marked as “robust” if it is capable of adapting to the changes in its operating conditions with minimal damage, alteration or loss of functionality.

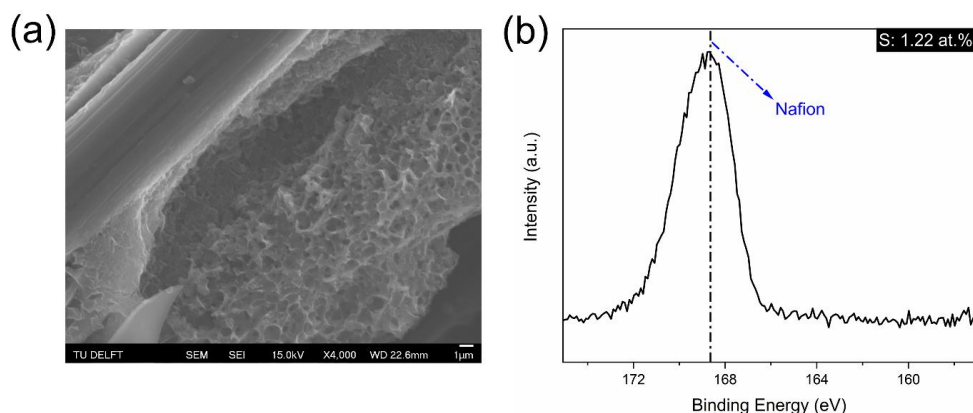


Figure S5.8 (a) SEM image and (b) S 2p XPS spectrum of fresh ANBC electrode.

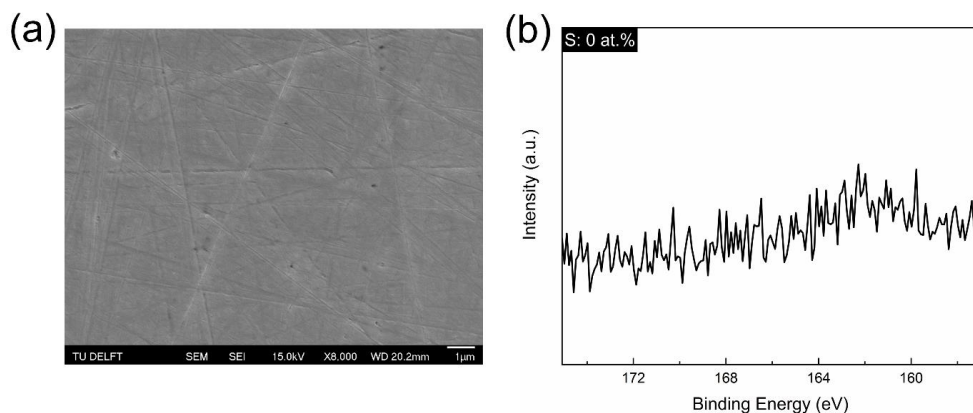


Figure S5.9 (a) SEM image and (b) S 2p XPS spectrum of fresh Ag foil electrode.

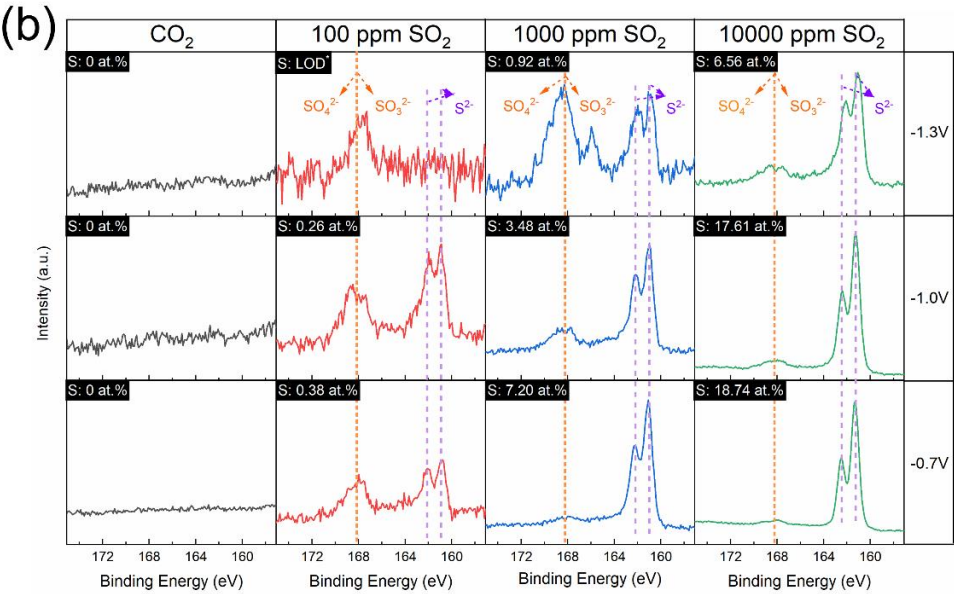
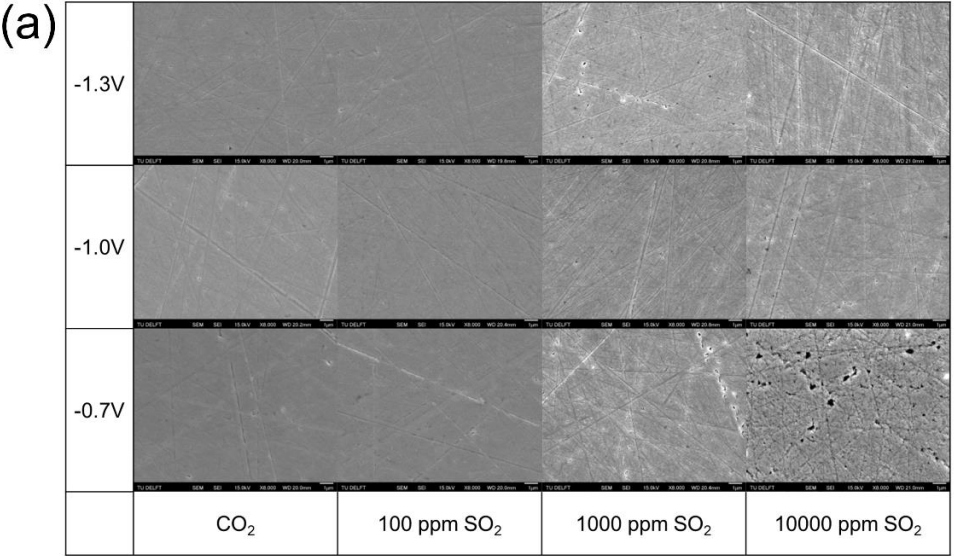


Figure S5.10 (a) SEM images and (b) S 2p XPS spectrum of Ag foil electrodes after 1 h electrolysis in the presence of different concentrations of SO₂ impurities and different potentials. (* LOD = Lower than detection limits)

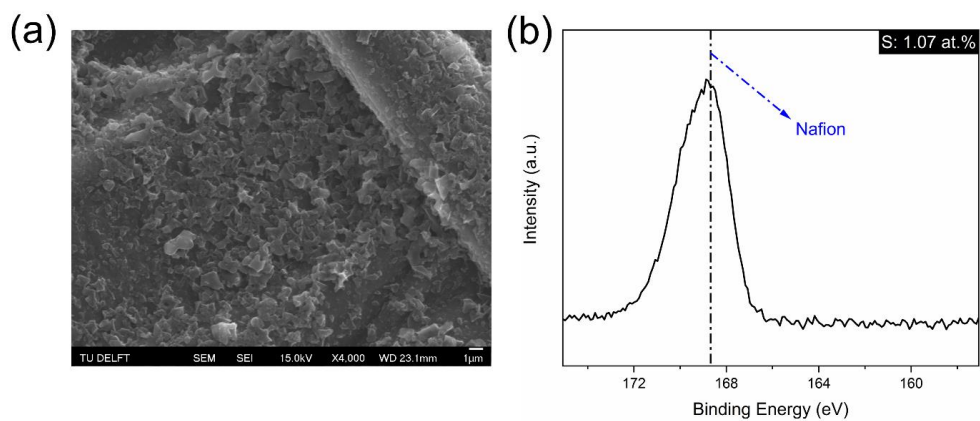


Figure S5.11 (a) SEM image and (b) S 2p XPS spectrum of ANBC electrode after 8 hours of continuous electrolysis with 100 ppm SO_2 at -1.0 V vs. RHE.

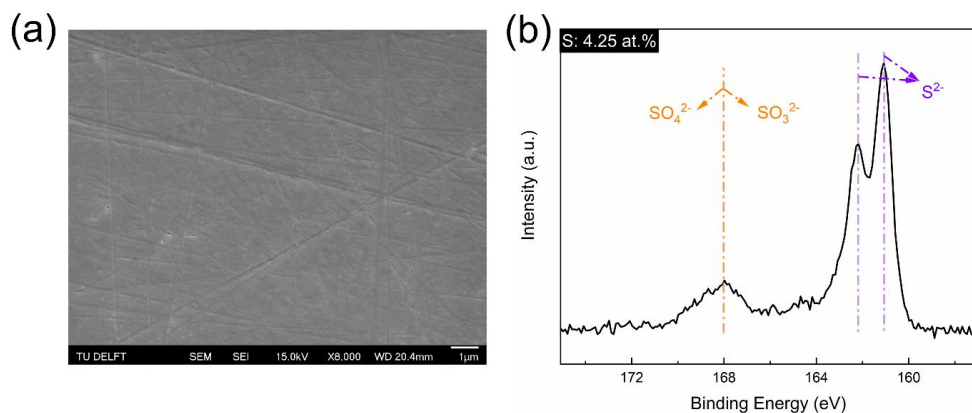


Figure S5.12 (a) SEM image and (b) S 2p XPS spectrum of Ag foil electrode after 8 hours of continuous electrolysis with 100 ppm SO_2 at -1.0 V vs. RHE.

Table S5.1 Standard reduction potentials for electrochemical CO₂ reduction to CO, H₂ evolution, and SO₂ reduction reactions.

Electrochemical reduction reactions	E° (V vs. RHE) at pH = 7
CO ₂ + 2H ⁺ + 2e ⁻ → CO + H ₂ O	-0.106
2H ⁺ + 2e ⁻ → H ₂	0
SO ₂ + 4H ⁺ + 4e ⁻ → S + 2H ₂ O	0.451
SO ₂ + 6H ⁺ + 6e ⁻ → H ₂ S + 2H ₂ O	0.347

Table S5.2 Gas mixtures for electrochemical measurements.

Gas cylinders	Gas mixtures for measurements	Total flow rate (sccm/min)	Recipes (sccm/min)		
			CO ₂	CO ₂ + 100 ppm SO ₂	CO ₂ + 10000 ppm SO ₂
CO ₂	CO ₂		10	0	0
CO ₂ + 100 ppm SO ₂	CO ₂ + 100 ppm SO ₂		0	10	0
CO ₂ + 10000 ppm SO ₂	CO ₂ + 1000 ppm SO ₂	10	9	0	1
	CO ₂ + 10000 ppm SO ₂		0	0	10

Table S5.3 The pH values of different gas mixtures saturated electrolytes.

	CO ₂	CO ₂ + 100 ppm SO ₂	CO ₂ + 1000 ppm SO ₂	CO ₂ + 10000 ppm SO ₂
Saturation time	15 min	15 min	15 min	15 min
Gas flow rate	10 sccm/min	10 sccm/min	10 sccm/min	10 sccm/min
pH	6.80	6.78	6.75	6.72

References

- (1) Kortlever, R.; Shen, J.; Schouten, K. J. P.; Calle-Vallejo, F.; Koper, M. T. M. Catalysts and Reaction Pathways for the Electrochemical Reduction of Carbon Dioxide. *J. Phys. Chem. Lett.* **2015**, *6*, 4073–4082.
- (2) Lawrence, K. R.; Kumar, A. S.; Asperti, S.; van den Berg, D.; Girichandran, N.; Kortlever, R. Advances in Electrochemical Carbon Dioxide Reduction Toward Multi-Carbon Products. In *Chemical Valorisation of Carbon Dioxide*; Stefanidis, G., Stankiewicz, A., Eds.; The Royal Society of Chemistry: London, 2022; pp 388–412.
- (3) Birdja, Y. Y.; Pérez-Gallent, E.; Figueiredo, M. C.; Göttle, A. J.; Calle-Vallejo, F.; Koper, M. T. M. Advances and Challenges in Understanding the Electrocatalytic Conversion of Carbon Dioxide to Fuels. *Nat. Energy* **2019**, *4*, 732–745.
- (4) De Luna, P.; Hahn, C.; Higgins, D.; Jaffer, S. A.; Jaramillo, T. F.; Sargent, E. H. What Would It Take for Renewably Powered Electrosynthesis to Displace Petrochemical Processes? *Science*. **2019**, *364*, eaav3506.
- (5) Zheng, T.; Jiang, K.; Wang, H. Recent Advances in Electrochemical CO₂-to-CO Conversion on Heterogeneous Catalysts. *Adv. Mater.* **2018**, *30*, 1802066.
- (6) Gabardo, C. M.; Seifitokaldani, A.; Edwards, J. P.; Dinh, C.-T.; Burdyny, T.; Kibria, M. G.; O'Brien, C. P.; Sargent, E. H.; Sinton, D. Combined High Alkalinity and Pressurization Enable Efficient CO₂ Electroreduction to CO. *Energy Environ. Sci.* **2018**, *11*, 2531–2539.
- (7) Möller, T.; Ju, W.; Bagger, A.; Wang, X.; Luo, F.; Ngo Thanh, T.; Varela, A. S.; Rossmeisl, J.; Strasser, P. Efficient CO₂ to CO Electrolysis on Solid Ni–N–C Catalysts at Industrial Current Densities. *Energy Environ. Sci.* **2019**, *12*, 640–647.
- (8) Zheng, T.; Jiang, K.; Ta, N.; Hu, Y.; Zeng, J.; Liu, J.; Wang, H. Large-Scale and Highly Selective CO₂ Electrocatalytic Reduction on Nickel Single-Atom Catalyst. *Joule* **2019**, *3*, 265–278.
- (9) Abdinejad, M.; Irtem, E.; Farzi, A.; Sassenburg, M.; Subramanian, S.; Iglesias van Montfort, H.-P.; Ripepi, D.; Li, M.; Middelkoop, J.; Seifitokaldani, A. CO₂ Electrolysis via Surface-Engineering Electrografted Pyridines on Silver Catalysts. *ACS Catal.* **2022**, *12*, 7862–7876.
- (10) Wang, H.; Liu, Y.; Laaksonen, A.; Krook-Riekkola, A.; Yang, Z.; Lu, X.; Ji, X. Carbon Recycling—An Immense Resource and Key to a Smart Climate Engineering: A Survey of Technologies, Cost and Impurity Impact. *Renew. Sustain. Energy Rev.* **2020**, *131*, 110010.

- (11) Legrand, U.; Apfel, U. P.; Boffito, D. C.; Tavares, J. R. The Effect of Flue Gas Contaminants on the CO₂ electroreduction to Formic Acid. *J. CO₂ Util.* **2020**, *42*, 101315.
- (12) Grim, R. G.; Huang, Z.; Guarnieri, M. T.; Ferrell, J. R.; Tao, L.; Schaidle, J. A. Transforming the Carbon Economy: Challenges and Opportunities in the Convergence of Low-Cost Electricity and Reductive CO₂ Utilization. *Energy Environ. Sci.* **2020**, *13*, 472–494.
- (13) Luc, W.; Ko, B. H.; Kattel, S.; Li, S.; Su, D.; Chen, J. G.; Jiao, F. SO₂-Induced Selectivity Change in CO₂ Electroreduction. *J. Am. Chem. Soc.* **2019**, *141*(25), 9902–9909.
- (14) Choi, B. U.; Tan, Y. C.; Song, H.; Lee, K. B.; Oh, J. System Design Considerations for Enhancing Electroproduction of Formate from Simulated Flue Gas. *ACS Sustain. Chem. Eng.* **2021**, *9*, 2348–2357.
- (15) Zhai, Y.; Chiachirelli, L.; Sridhar, N. Effect of Gaseous Impurities on the Electrochemical Reduction of CO₂ on Copper Electrodes. *ECS Trans.* **2009**, *19*, 1–13.
- (16) Ko, B. H.; Hasa, B.; Shin, H.; Jeng, E.; Overa, S.; Chen, W.; Jiao, F. The Impact of Nitrogen Oxides on Electrochemical Carbon Dioxide Reduction. *Nat. Commun.* **2020**, *11*, 5856.
- (17) House, K. Z.; Baclig, A. C.; Ranjan, M.; Van Nierop, E. A.; Wilcox, J.; Herzog, H. J. Economic and Energetic Analysis of Capturing CO₂ from Ambient Air. *Proc. Natl. Acad. Sci.* **2011**, *108*, 20428–20433.
- (18) Raksajati, A.; Ho, M. T.; Wiley, D. E. Techno-Economic Evaluation of CO₂ Capture from Flue Gases Using Encapsulated Solvent. *Ind. Eng. Chem. Res.* **2017**, *56*, 1604–1620.
- (19) Hu, C.; Dai, L. Doping of Carbon Materials for Metal-Free Electrocatalysis. *Adv. Mater.* **2019**, *31*, 1–17.
- (20) Vasileff, A.; Zheng, Y.; Qiao, S. Z. Carbon Solving Carbon's Problems: Recent Progress of Nanostructured Carbon-Based Catalysts for the Electrochemical Reduction of CO₂. *Adv. Energy Mater.* **2017**, *7*, 1–21.
- (21) Adegoke, K. A.; Maxakato, N. W. Electrochemical CO₂ Conversion to Fuels on Metal-Free N-Doped Carbon-Based Materials: Functionalities, Mechanistic, and Technoeconomic Aspects. *Mater. Today Chem.* **2022**, *24*, 100838.
- (22) Fu, S.; Li, M.; Asperti, S.; Jong, W. de; Kortlever, R. Unravelling the Effect of Activators Used in The Synthesis of Biomass-Derived Carbon Electrocatalysts on the Electrocatalytic Performance for CO₂ Reduction. *ChemSusChem* **2023**, *16*, e202202188.

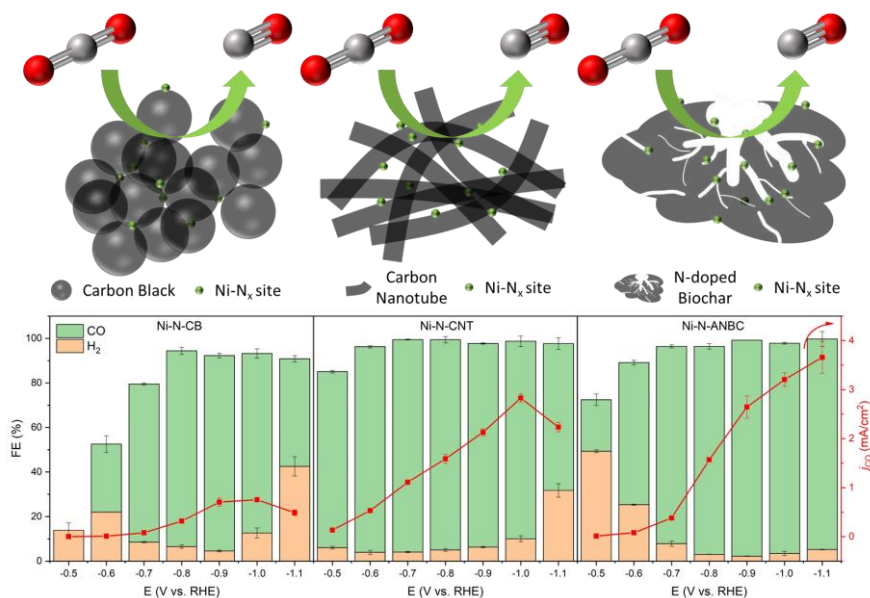
- (23) Gerber, I. C.; Serp, P. A Theory/Experience Description of Support Effects in Carbon-Supported Catalysts. *Chem. Rev.* **2019**, *120*, 1250–1349.
- (24) Feng, H.; Hu, H.; Dong, H.; Xiao, Y.; Cai, Y.; Lei, B.; Liu, Y.; Zheng, M. Hierarchical Structured Carbon Derived from Bagasse Wastes: A Simple and Efficient Synthesis Route and Its Improved Electrochemical Properties for High-Performance Supercapacitors. *J. Power Sources* **2016**, *302*, 164–173.
- (25) Daiyan, R.; Tan, X.; Chen, R.; Saputera, W. H.; Tahini, H. A.; Lovell, E.; Ng, Y. H.; Smith, S. C.; Dai, L.; Lu, X.; Amal, R. Electroreduction of CO₂ to CO on a Mesoporous Carbon Catalyst with Progressively Removed Nitrogen Moieties. *ACS Energy Lett.* **2018**, *3*, 2292–2298.
- (26) Zou, K.; Deng, Y.; Chen, J.; Qian, Y.; Yang, Y.; Li, Y.; Chen, G. Hierarchically Porous Nitrogen-Doped Carbon Derived from the Activation of Agriculture Waste by Potassium Hydroxide and Urea for High-Performance Supercapacitors. *J. Power Sources* **2018**, *378*, 579–588.
- (27) Li, F.; Xue, M.; Knowles, G. P.; Chen, L.; MacFarlane, D. R.; Zhang, J. Porous Nitrogen-Doped Carbon Derived from Biomass for Electrocatalytic Reduction of CO₂ to CO. *Electrochim. Acta* **2017**, *245*, 561–568.
- (28) Niu, J.; Shao, R.; Liu, M.; Zan, Y.; Dou, M.; Liu, J.; Zhang, Z.; Huang, Y.; Wang, F. Porous Carbons Derived from Collagen-Enriched Biomass: Tailored Design, Synthesis, and Application in Electrochemical Energy Storage and Conversion. *Adv. Funct. Mater.* **2019**, 1905095.
- (29) Liu, W. J.; Jiang, H.; Yu, H. Q. Emerging Applications of Biochar-Based Materials for Energy Storage and Conversion. *Energy Environ. Sci.* **2019**, *12*, 1751–1779.
- (30) Yan, C.; Jiang, X.; Yu, J.; Ding, Z.; Ma, L.; Su, T.; Wang, Y.; Wang, C.; Huang, G.; Xu, S. Waste to Wealth: Direct Utilization of Spent Materials for Electrocatalysis and Energy Storage. *Green Chem.* **2023**, *25*, 3816.
- (31) Harmon, N. J.; Wang, H. Electrochemical CO₂ Reduction in the Presence of Impurities: Influences and Mitigation Strategies. *Angew. Chemie Int. Ed.* **2022**, *61*, e202213782.
- (32) Chu, S.; Rashid, R. T.; Pan, Y.; Wang, X.; Zhang, H.; Xiao, R. The Impact of Flue Gas Impurities and Concentrations on the Photoelectrochemical CO₂ Reduction. *J. CO₂ Util.* **2022**, *60*, 101993.
- (33) Leverett, J.; Yuwono, J. A.; Kumar, P.; Tran-Phu, T.; Qu, J.; Cairney, J.; Wang, X.; Simonov, A. N.; Hocking, R. K.; Johannessen, B.; Dai, L.; Daiyan, R.; Amal, R. Impurity

Tolerance of Unsaturated Ni-N-C Active Sites for Practical Electrochemical CO₂ Reduction. *ACS Energy Lett.* **2022**, 7, 920–928.

(34) Ghafoor, S.; Ata, S.; Mahmood, N.; Arshad, S. N. Photosensitization of TiO₂ Nanofibers by Ag₂S with the Synergistic Effect of Excess Surface Ti³⁺ States for Enhanced Photocatalytic Activity under Simulated Sunlight. *Sci. Rep.* **2017**, 7, 1–10.

6

Ni-N-C catalysts for CO₂ electrochemical reduction to CO: The effects of carbon support



Abstract: Carbon-supported nickel and nitrogen co-doped (Ni-N-C) catalysts have been extensively studied as selective and active catalysts for CO₂ electroreduction to CO. Most studies have focused on adjusting the coordination structure of Ni-N_x active sites, while the impact of the carbon supports have often been overlooked. Herein, we synthesize a series of Ni-N-C catalysts on different carbon supports (carbon black, multi-walled carbon nanotubes, activated nitrogen-doped biochar) using a ligand-mediated method, and investigate the effect of the carbon supports on the electrocatalytic performance. All of the prepared Ni-N-C catalysts show good faradaic efficiencies (FE) toward CO production (up to ~90%). However, the onset potentials and current densities for CO production vary greatly. The agglomeration of carbon black (CB) leads to the coverage of Ni-N_x active sites on Ni-N-CB, thereby lowering the CO₂ reduction reaction (CO₂RR) activity. Ni-N-CNT, using carbon nanotubes (CNT), benefits from its wide pore size distribution and abundant surface Ni-N_x sites, leading to a high FE_{CO} (>91%) at low overpotentials. Moreover, Ni-N-CNT displays a high FE_{CO} over a large potential window. The narrow pore size and hierarchical structure of N-doped biochar (ANBC) confines part of the Ni-N_x sites in deeper pores, allowing Ni-N-ANBC to maintain excellent FE_{CO} (>92%) at more negative potentials than Ni-N-CB and Ni-N-CNT. This study demonstrates the importance of the carbon support for Ni-N-C catalysts and provides new insights into the design of efficient Ni-N-C catalysts for the CO₂RR.

6.1 Introduction

With the growing climate problems caused by excessive CO₂ emissions, the need for accelerating the deployment of carbon neutral energy and production technologies has become stronger.^{1,2} The electrochemical CO₂ reduction reaction (CO₂RR) powered by renewable electricity is a promising technology to convert waste CO₂ into chemicals and fuels. Thereby, the process can store surplus electricity from intermittent sources, such as wind and solar, into chemical bonds.^{3–7} Depending on the choice of catalysts, CO₂ can be reduced to CO,⁸ formate,⁹ CH₄,¹⁰ C₂H₄,¹¹ and oxygenated hydrocarbons. Among these products, CO is considered an attractive and competitive product.¹² The two-electrons transfer reduction of CO₂ to CO exhibits a relatively high product selectivity with lower energy costs.¹³ In addition, CO can be widely used in downstream chemical transformations, such as Fischer-Tropsch synthesis.¹⁴ However, due to the inevitable competition with the hydrogen evolution reaction (HER), the CO₂RR in aqueous electrolytes still faces challenges.¹⁵ Therefore, seeking active, efficient, stable and cost-effective catalysts remains an important challenge for the application of CO₂RR technology.

Recently, transition metal and nitrogen co-doped carbon materials, hereinafter referred to as M-N-C, were demonstrated as efficient catalysts for the CO₂RR.¹⁶ The M-N_x structures (a central metal coordinatively bound to a different amounts of N atoms) are the active sites for the CO₂RR.¹⁷ Many studies have reported that varying the central metal, such as Fe, Co, and Ni, leads to a different selectivity and activity for the CO₂RR.^{18–21} In particular, the coordinative Ni-N_x sites exhibit favorable energetics for CO₂ activation and reduction which results in a high CO faradaic efficiency. Möller et al. reported a Ni-N-C catalyst integrated in a gas diffusion electrode (GDE) electrolyzer and showed a stable performance with 85% faradaic efficiency and 200 mA/cm² partial current density toward CO over a 20 hours test, at an applied potential of -1.1 V vs. RHE.²² Zheng et al. used a Ni-N-C catalyst in a 10 × 10 cm membrane electrode assembly (MEA) system, which exhibited an average current of ~8 A and over 90% faradaic efficiency toward CO during 6 hours electrolysis at a cell voltage of 2.8 V.²³ In comparison to Ag and Au electrocatalysts, inexpensive Ni-N-C catalysts exhibit competitive performances and show great potential for large-scale application.

To further improve the catalytic performance and reveal the active sites and reaction mechanisms of Ni-N-C catalysts, many studies have adjusted the coordination structures of Ni-N_x sites.^{24,25} Surprisingly, Ni-N₄, Ni-3N (Ni coordinate with three nitrogen atoms), and Ni-VN₃ (V is coordination vacancy of Ni centers) have all been demonstrated as potential active sites, experimentally and theoretically.^{26–28} These studies show the complexity of the reaction mechanism of these catalysts. On the other hand, altering the morphology and pore structure of carbon materials is also considered to be an effective strategy to improve

the performance of Ni-N-C catalysts for CO₂RR. For instance, the Strasser group pointed out that “the reaction rate is not determined by the kinetics of the CO₂RR on the active site but rather to the CO₂ transport to those sites”.²⁹ Therefore, it is crucial to improve the accessibility of active sites by tuning the physicochemical properties (porosity, hydrophobicity, etc.) of carbon supports to enhance the catalytic performance of Ni-N-C catalysts. In the past few years, carbon black,²³ carbon nanotube,³⁰ graphene,³¹ and other carbon supports which were made from carbonization of different carbon precursors,^{32–36} were widely used to synthesize Ni-N-C catalysts for the CO₂RR and most of them show excellent performances. However, most of the existing studies mainly focus on the importance of the Ni-N_x sites, but overlook the contribution of the carbon supports. Therefore, the role of the properties of different carbon supports and the interaction between carbon support and Ni-N_x sites remain poorly understood. In addition, due to the diversity of catalyst preparation methods, reactor types and sizes, reaction parameter settings, etc., it is hard to deduce how the properties of different carbon supports affect the catalytic performance for the CO₂RR by simply comparing the results from published studies.³⁷ Overall, it is crucial to understand the influence of the carbon support properties on the performance of Ni-N-C catalysts, as it will help to further optimize the performance of Ni-N-C catalysts.

Here, we selected commercial carbon black (CB), multi-walled carbon nanotube (CNT), and a self-made activated N-doped biochar (ANBC) as different carbon supports to synthesize a series of Ni-N-C catalysts by a ligand-mediated method. In this study, we focus on analyzing the effect of the different carbon supports of Ni-N-C catalysts on the CO₂RR performance. In particular, the physicochemical properties of different carbon supports, such as hydrophobicity, surface roughness, porosity, the abundance of defects, and the distribution of active sites are comprehensively analyzed. All prepared Ni-N-C catalysts show roughly 90% FE_{CO}, but also exhibit significant differences in current densities. The agglomeration of carbon black for Ni-N-CB blocks Ni-N_x active sites and induces a poor CO₂RR activity. Ni-N-CNT shows more than 91% FE_{CO} from -0.6 to -0.8 V vs. RHE due to the wide pore size and abundant surface Ni-N_x active sites. In contrast, Ni-N-ANBC shows more than 93% FE_{CO} at more negative potentials (-0.8 to -1.1 V vs. RHE) owing to the larger specific surface area, smaller pore size, and hierarchical structures of N-doped biochar that help to confine part of the Ni-N_x active sites inside the pores.

6.2 Experimental Section

All chemicals were used as received without further purification. Aqueous solutions were prepared from ultrapure water (Milli-Q IQ 7000, 18.2 MΩ).

6.2.1 Synthesis of catalysts

Synthesis of ANBC: The activated N-doped biochar (ANBC) was prepared according to the procedure outlined in our previous study.³⁸ In brief, the ANBC was synthesized by a one-step pyrolysis method. 5 g of sugarcane bagasse powder, 10 g of urea and 15 g of NaOH (mass ratio: 1:2:3) were added into a crucible and mixed homogeneously. The mixture was transferred to a furnace, heated at 800 °C for 1 h with a ramping rate of 10 °C/min under a N₂ atmosphere (100 mL/min, 99.99%, Linde gas). Then the furnace was cooled to room temperature. The black powder collected after pyrolysis was dispersed in 1 M HCl for 4 h at 60 °C to remove the residual sodium containing salts and other impurities. After the acid wash, the black powder was filtered and rinsed with ultrapure water until it reached a neutral pH. Finally, the activated N-doped biochar was dried in an oven (105 °C) 12 h. The end product was denoted as ANBC.

Synthesis of Ni-N-C catalysts: The Ni-N-C catalysts were synthesized according to a ligand-mediated method reported by Yang et al. with slight modifications.³⁹ 8.3 mg nickel(II) acetate tetrahydrate (Sigma-Aldrich, 99.995%) and 23.2 mg 1,10-phenanthroline monohydrate (Sigma-Aldrich, 99%) were dispersed in 50 mL of methanol (VWR Chemical, 99.8%) and stirred for 20 minutes at room temperature. The molar ratio of Ni to the ligand was 1: 3.5. An excess of 1,10-phenanthroline was used to guarantee high dispersion of the metal centers to form Ni-N_x sites instead of Ni nanoclusters on the carbon supports. Subsequently, either 100 mg carbon black (Vulcan XC 72R) or multi-wall carbon nanotube (Sigma-Aldrich) or ANBC was added into the solution. The molar ratio of Ni to carbon is approximately 1: 250, and the calculated weight percentage of Ni is ~1.5 wt.%. Then the solution was heated at 60 °C for 4 h under continuous stirring. Afterward, the solution was transferred to a vacuum oven and heated at 60 °C for 12 h to evaporate the solvent. The obtained black solid was ground in a mortar and then transferred into an alumina crucible and placed in the middle of a tube furnace. The tube furnace was first purged with argon at a flow rate of 500 mL/min for 1 h to remove the air inside the tube, then heated to 600 °C with a ramping rate of 5 °C/min under an argon atmosphere (250 mL/min, 99.99%, Linde gas) and then held at 600 °C for 2 h. After cooling down to room temperature, the black powder was collected and ground one more time and the final products were designated as Ni-N-CB, Ni-N-CNT, and Ni-N-ANBC, respectively.

Synthesis of Ni-C catalysts: As a comparison, the Ni-C catalysts were prepared under the same procedure as Ni-N-C catalysts but without adding 1,10-phenanthroline monohydrate. The obtained products were recorded as Ni-CB, Ni-CNT, and Ni-ANBC, respectively.

6.2.2 Characterization

Scanning electron microscopy (SEM) images were taken on a JEOL JSM-6500F microscope with an acceleration voltage of 15 kV. Transmission electron microscopy (TEM) images were obtained using a JEOL JEM1400 microscope, operating at an acceleration voltage of 120 kV. Powder X-ray diffraction (XRD) patterns were measured with a Bruker AXS D2 Phaser diffractometer with Cu K α radiation ($\lambda = 0.15406$ nm), the scanning 2θ range was between 10° to 90° using a step length of 0.02° . X-ray photoelectron spectroscopy (XPS) measurements were carried out on a Thermo Scientific K-Alpha system using a monochromatic Al K α X-ray source (1486.6 eV). CasaXPS (Version 2.3.22PR1.0) was used for the further data analysis. Contact angle measurements were performed on a standard Goniometer setup (OCA25, DataPhysics Instruments, Germany) using the sessile drop method. For the static contact angle measurements, a 2 μ L droplet was dispensed onto the substrate using an automatic pipetting unit, the contact angle was photographed and measured by a goniometer software (SCA 20) automatically. For the dynamic contact angle measurements, a liquid-dispensing syringe was placed 5 mm above the substrate and a 10 μ L droplet was gently dispensed. Then the volume of the droplet was first increased from 10 μ L to 30 μ L and then decreased to 10 μ L at a rate of 0.16 μ L/s, which was controlled by an electronic dosing system. The increase-decrease procedure was carried out 2 times and the contact angle and the diameter of the drop base were recorded every second by SCA 20. All measurements were taken in ambient air and the temperature remained between 21 - 24 $^\circ$ C. N $_2$ adsorption-desorption isotherms were recorded at 77K using a Micromeritics TriStar II 3020 instrument. Samples were degassed at 300 $^\circ$ C for 15 h before measurement. Specific surface areas were determined by the Brunauer-Emmett-Teller (BET) method and pore size distribution were calculated using the Density Functional Theory (DFT) model. Raman spectra were recorded from 500 to 3000 cm^{-1} on a Horiba Scientific LabRAM HR Evolution Raman Spectroscopy system with an excitation wavelength of 514 nm. The content of Ni in the catalysts were measured by inductively coupled plasma optical emission spectroscopy (ICP-OES, Spectro Arcos).

6.2.3 Electrode preparation

Working electrodes were prepared by a drop casting method. 4 mg of catalyst was dispersed into a solvent mixture containing 950 μ L isopropanol and 50 μ L of 5% Nafion perfluorinated resin solution (Sigma-Aldrich). The mixture was sonicated for 1 h to obtain a homogeneous ink. Afterwards, 10 μ L of the catalyst ink was drop casted on a 1 cm^2 round shape carbon paper and thoroughly dried at room temperature. The catalyst loading was around 0.04 mg/cm^2 . A 25 mm \times 25 mm \times 1 mm platinum foil (99.9%, Mateck, Germany) was used as the counter electrode, which was cleaned by flame annealing at least 3 times to remove any possible impurities before use. A leak-free Ag/AgCl electrode (40 mm length,

Innovative instrument, USA) was used as reference electrode. The reference electrode was checked before every experiment by comparing with a master Ag/AgCl reference electrode (BASi, MF-2056, USA), which is never used for any experiments and kept in pristine working condition. Deviations between the tested reference electrode and master reference electrode were measured by an open circuit potential (OCP) test, where the deviation should always be lower than 5 mV.

6.2.4 Electrochemical measurement

All working electrodes were tested in a compact H-cell, similar to Lobaccaro et al.⁴⁰ Each compartment contained 1.8 mL of 0.1 M KHCO_3 as electrolyte and the cathode and anode chambers were separated by an anion-exchange membrane (Selemion AMV, AGC Engineering, Japan). Before each experiment, the electrolyte was purged with CO_2 for 15 minutes to obtain a CO_2 -saturated 0.1 M KHCO_3 electrolyte with pH = 6.8. Electrochemical measurements were carried out using a Biologic SP-200 potentiostat (Biologic, France). All measured potentials were converted to the reversible hydrogen electrode (RHE) scale according to the formula: $E \text{ (V vs. RHE)} = E \text{ (V vs. Ag/AgCl)} + 0.197 + 0.059 \times \text{pH}$. Linear sweep voltammetry (LSV) measurements were recorded in CO_2 -saturated (pH = 6.8) and Ar-saturated (pH = 8.3) 0.1 M KHCO_3 electrolytes at a scan rate of 5 mV/s. The electrochemically active surface areas (ECSA) of the electrodes were determined by measuring the double layer capacitance (C_{dl}), which were derived from cyclic voltammetry measurements with a scan rate at 5, 10, 25, and 50 mV/s in a potential window from 0.45 to 0.55 V vs. RHE. The C_{dl} was estimated by plotting the $\Delta j (j_a - j_c)/2$ at 0.50 V vs. RHE against the scan rates, where the slope of the plot gives the C_{dl} . Chronoamperometric electrolysis measurements (with iR compensation) were carried out at different applied potentials from -0.50 to -1.15 V vs. RHE and each potential was applied for 1 h. The cell resistance (R_s) was measured by applying a potentiostatic electrochemical impedance spectrometry (PEIS) test from 200 kHz to 100 mHz. The potentiostat can only compensate 85% of R_s automatically during the CO_2 RR measurements, thus the remaining 15% was corrected manually afterwards. During the chronoamperometry tests, CO_2 was purged continuously into the catholyte with a flow rate of 8 mL/min using a mass flow controller. The gaseous CO_2 reduction products were analyzed by an online gas chromatography every 2 minutes, using a CompactGC 4.0 (Global analyser solutions, The Netherlands) equipped with one flame ionization detector (FID) to analyze hydrocarbon compounds and two thermal conductivity detectors (TCD) to analyze CO and H_2 , respectively. The GC was calibrated using calibration gas cylinders (Linde gas Benelux B.V.) with five different concentrations of analytes (50, 100, 1000, 3000, and 8000 ppm) in CO_2 . The faradaic efficiencies (FEs) reported in this study for gas products were determined using the data collected from 42 min to 54 min, which show a more stable current and gas product composition. An aliquot of the catholyte was collected at the end of the CO_2 RR measurements and the liquid products were quantified using a high-performance liquid

chromatography (HPLC, Agilent 1260 Infinity), equipped with two Aminex HPX 87-H columns (Bio-Rad) placed in series. The column oven was maintained at a constant 60 °C, using a 1 mM H₂SO₄ aqueous solution as eluent with a steady flow of 0.6 mL/min and applying a refractive index detector (RID) for product detection.

6.3 Results and Discussions

6.3.1 Catalyst characterization

The morphologies and microstructures of Ni-N-C catalysts were visualized using scanning electron microscopy (SEM) and transmission electron microscopy (TEM). SEM images of Ni-N-C catalysts (Figure 6.1a, b and c) show interconnected nanoporous structures with multilevel channels. In the TEM images Ni-N-CB (Figure 6.1d) exhibits a representative nanosphere-stacked morphology of carbon black, Ni-N-CNT (Figure 6.1e) shows a structure of cross-linked multi-walled carbon nanotubes, and Ni-N-ANBC (Figure 6.1f) exhibits a crumpled nanosheet-like morphology. The absence of nickel clusters or nano particles in the TEM images suggests a uniform dispersion of Ni-N_x active sites over the catalysts. As comparison, a multitude of Ni nanoparticles can be observed over Ni-C catalysts (see Figure S6.1), indicating that 1,10-phenanthroline isolates Ni species effectively. The TEM image of pristine ANBC (Figure S6.1g) shows that no additional particulate contaminations exist on the self-made activated N-doped biochar.

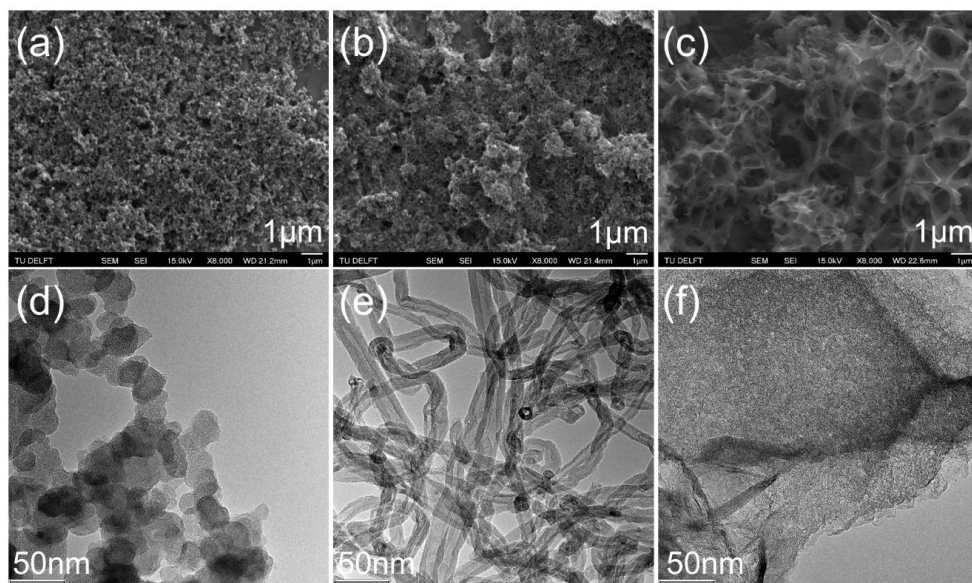


Figure 6.1 SEM images of (a) Ni-N-CB, (b) Ni-N-CNT, (c) Ni-N-ANBC, and TEM images of (d) Ni-N-CB, (e) Ni-N-CNT, (f) Ni-N-ANBC.

Figure 6.2a shows the X-ray diffraction (XRD) patterns of the prepared Ni-N-C catalysts. The two broad diffraction peaks located at around $2\theta = 25^\circ$ and 44° correspond to the (002), and (100) planes of graphitic carbon, respectively. Although the (200) crystal plane of NiO may overlap with the (100) plane of carbon at around $2\theta = 44^\circ$, no other obvious diffraction peaks of NiO can be observed. In contrast, the XRD patterns of Ni-C materials (Figure S6.2) show two additional diffraction peaks at around $2\theta = 37^\circ$ and 63° , which can be readily indexed as the (111) and (220) crystal planes of NiO.⁴¹ In addition, the XRD patterns of the pristine carbon materials (Figure S6.2) only display the feature peaks of graphitic carbon.

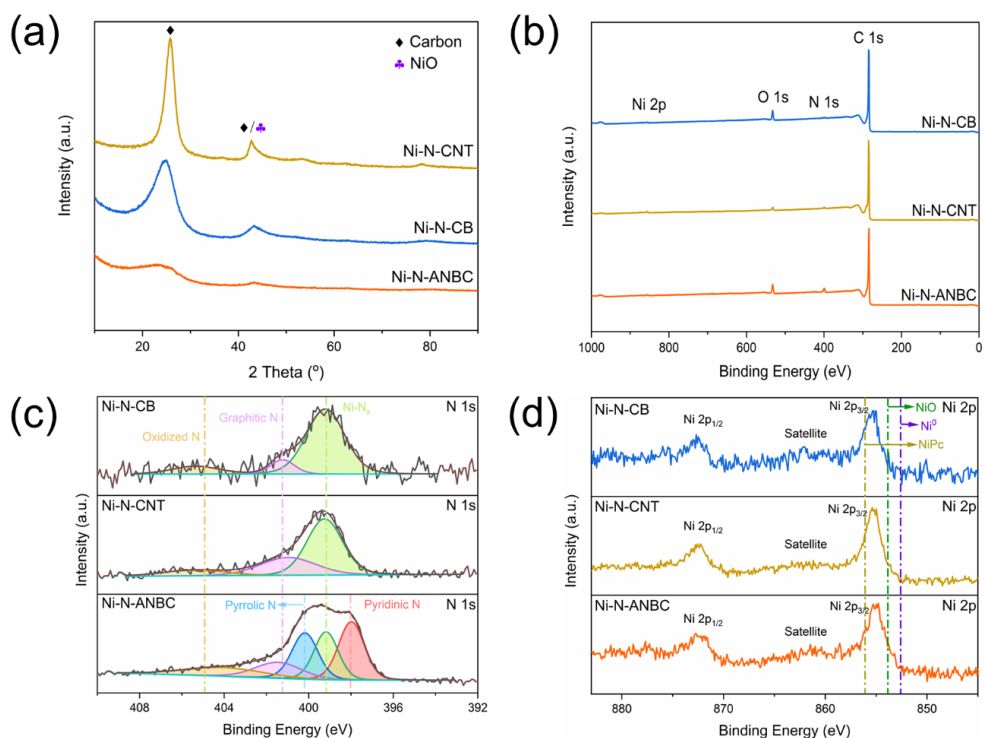


Figure 6.2 (a) XRD patterns, (b) XPS full survey, (c) High-resolution N 1s XPS spectra, (d) High-resolution Ni 2p XPS spectra of Ni-N-CB, Ni-N-CNT, and Ni-N-ANBC.

The chemical composition of Ni-N-C catalysts was investigated by X-ray photoelectron spectroscopy (XPS). The survey spectra (Figure 6.2b) reveal the presence of C, N, O and Ni. The high-resolution N 1s spectra (Figure 6.2c) can be deconvoluted into pyridinic N (~398.2 eV), Ni-N (~399.2 eV), pyrrolic N (~400.2 eV), graphitic N (~401.8 eV), and oxidized N (~404.7 eV).^{28,42} The Ni-N-CB and Ni-N-CNT samples are dominated by a Ni-N signal, which is in line with the results from Xi et al.⁴³ Since Ni-N-ANBC used N-doped biochar as a support, it shows a more complex N 1s spectrum which contains all N-containing species. The high-resolution Ni 2p spectra of Ni-N-C catalysts show the binding energy of Ni 2p_{3/2} at ~855 eV, which is lower than Ni²⁺ in nickel phthalocyanine (NiPc) (856 eV) but higher than Ni⁰ in Ni metal (852.6 eV), indicating that the valence state of the Ni species in Ni-N-C catalysts are between 0 and +2.^{44–46} The XPS spectra and chemical compositions of pristine carbon and Ni-C materials are summarized in Figure S6.3 and Table S6.1. The high-resolution N 1s spectra of CB and CNT indicate that no additional nitrogen was induced into the pristine carbon materials. Similarly, the high-resolution Ni 2p spectra of CB, CNT, and ANBC indicates that

no Ni-containing impurities existed in the pristine carbon supports. Remarkably, Ni-ANBC also features peaks of a Ni-N structure in the high-resolution N 1s spectrum (Figure S6.3h), which can be attributed partial coordination of N-containing defects on the surface of ANBC with free Ni^{2+} to form a stable Ni-N_x structure.⁴⁷

In summary, we have successfully synthesized a series of Ni-N-C catalysts on different carbon supports via a ligand-mediated method. No obvious Ni-containing nanoparticles are observed in Ni-N-C catalysts by TEM and XRD. Combining the analysis of XPS high-resolution N 1s and Ni 2p spectra, we confirm the prevalent presence of Ni-N_x moieties in all Ni-N-C catalysts. In addition, XRD and XPS characterization confirms that no apparent impurities originate from the pristine carbon supports. Therefore, any distinction in electrochemical performance for CO_2RR can be ascribed to carbon support-related factors.

6.3.2 Electrocatalytic performance

The electrocatalytic performance of Ni-N-C catalysts toward the CO_2RR were evaluated in a compact H-cell. Linear sweep voltammograms of the Ni-N-C catalysts in Ar-saturated and CO_2 -saturated 0.1 M KHCO_3 electrolytes are shown in Figure S6.4. All of the Ni-N-C catalysts exhibit a larger current density in a CO_2 -saturated electrolyte than in a Ar-saturated electrolyte, suggesting that the catalysts possess activity for the CO_2RR . The voltammograms of Ni-N-C catalysts in a CO_2 -saturated electrolyte are depicted in Figure 6.3a, and show that the CO_2 reduction onset potential of Ni-N-CNT is lower than that of Ni-N-CB and Ni-N-ANBC. As a comparison (Figure S6.4), Ni-CB and Ni-CNT have no activity for the CO_2RR whereas ANBC and Ni-ANBC show activity for the CO_2RR , which is attributed to contributions from the N-doped biochar.^{38,48}

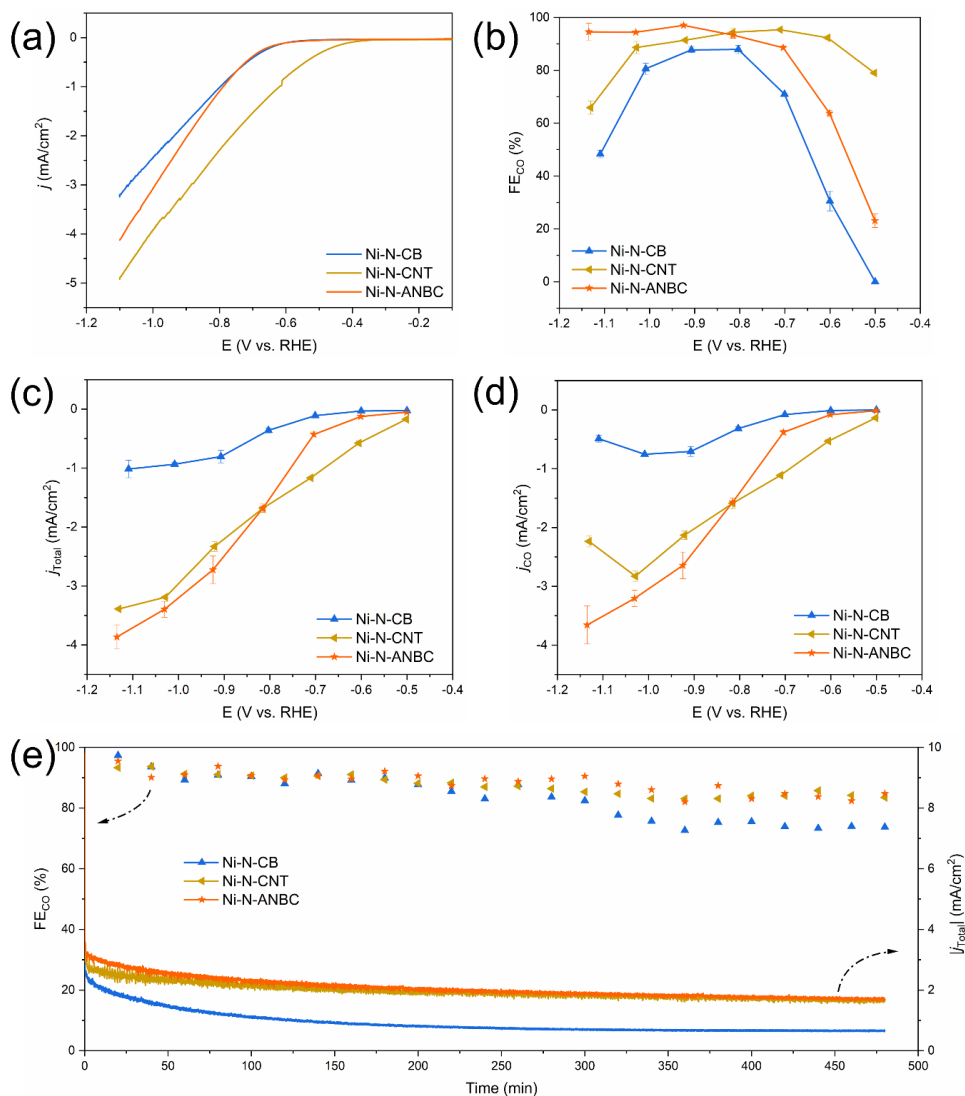


Figure 6.3 (a) Linear sweep voltammograms in a CO₂-saturated 0.1 M KHCO₃ electrolyte, (b) Faradaic efficiency toward CO, (c) Total current density and (d) Partial current density toward CO during CO₂ electrolysis in the same electrolyte at different potentials and (e) 8 h stability tests at -0.9 V vs. RHE of Ni-N-CB, Ni-N-CNT, and Ni-N-ANBC.

To further evaluate the catalytic performance of the Ni-N-C catalysts, chronoamperometry measurements are performed in a potential window from -0.5 V to -

1.15 V vs. RHE (with iR compensation). CO and H₂ are detected as dominant gaseous products while no liquid products were detected in the catholyte. The faradaic efficiencies (FE) toward CO for the different Ni-N-C catalysts are presented in Figure 6.3b. All of the Ni-N-C catalysts show a good FE_{CO} (up to ~90%) in different potential windows. In particular, the FE_{CO} of Ni-N-CB increases from -0.5 V to -0.8 V vs. RHE, reaches a maximum of 88% FE_{CO} at -0.8 V vs. RHE and then decreases from -0.8 V to -1.11 V vs. RHE. Ni-N-CNT shows a higher FE_{CO} than other samples from -0.5 V vs. RHE to -0.8 V vs. RHE. It maintains a good FE_{CO} (~90%) from -0.6 V to -1.03 V vs. RHE, with a decrease to 66% at -1.13 V vs. RHE. The FE_{CO} of Ni-N-ANBC exhibits an increasing trend from -0.5 V to -0.83 V vs. RHE and then reaches a high FE_{CO} (>90%, maximum 97% at -0.93 V vs. RHE) from -0.82 V to -1.15 V vs. RHE. According to the total current density (j_{Total}) (Figure 6.3c) and partial current density of CO (j_{CO}) (Figure 6.3d), Ni-N-CB shows a lower catalytic activity than the other samples over the entire potential window. Ni-N-CNT and Ni-N-ANBC exhibit a comparable catalytic activity, where Ni-N-CNT shows a higher j_{CO} from -0.5 V to -0.83 V vs. RHE and Ni-N-ANBC shows a higher j_{CO} from -0.83 V to -1.15 V vs. RHE. The faradaic efficiencies toward H₂ (FE_{H2}) and partial current densities toward H₂ (j_{H2}) of Ni-N-C catalysts are presented in Figure S6.5, with the FE_{H2} showing an opposite trend to that of FE_{CO} and Ni-N-ANBC showing the lowest j_{H2} values, indicating that it is least active for the hydrogen evolution reaction (HER). Additionally, Figure S6.6 summarizes the electrochemical performances for the CO₂RR of all prepared samples (Ni-N-C, Ni-C, and ANBC). It is clear that both Ni-CB and Ni-CNT have no catalytic activity for CO₂ reduction to CO, indicating that Ni nanoparticles have a preference for the HER over the CO₂RR. These results are consistent with previous reports from Boppella et al.⁴⁹ It is worth noting that the j_{CO} of ANBC and Ni-ANBC are lower than that of Ni-N-ANBC, even though the carbon support (N-doped biochar) also shows good faradaic efficiency toward CO, implying that the main activity of Ni-N-ANBC is provided by the Ni-N_x moieties on the ANBC instead of the N-doped biochar.

Long-term (8 h) stability measurements of Ni-N-C catalysts were performed at -0.9 V vs. RHE (Figure 6.3e). During the 8 h electrolysis tests, the FE_{CO} of Ni-N-CNT and Ni-N-ANBC decreases from ~90% to ~85%, while the FE_{CO} of Ni-N-CB decreases from ~90% to ~75%. The current density of all Ni-N-C catalysts exhibits a decreasing trend over the first 2 h and then maintains stable performance, which is in line with results published by Hu et al.¹⁹ In general, Ni-N-CNT and Ni-N-ANBC show a higher catalytic activity and longer stability during electrochemical CO₂ reduction than Ni-N-CB.

To study the structure-performance relationship of the Ni-N-C catalysts, several electrochemical characterizations were performed. The electrochemical active surface areas (ECSA) of all prepared samples were determined by measuring the electric double-layer capacitances (C_{dl}) (Figure S6.7). As shown in Figure 6.4a, Ni-N-ANBC (0.93 mF/cm²) shows a significantly larger C_{dl} value than Ni-N-CB (0.26 mF/cm²) and Ni-N-CNT (0.36 mF/cm²). The

C_{dl} values of these Ni-N-C catalysts are positively correlated with their specific surface areas which are calculated by N_2 adsorption-desorption measurements. However, their C_{dl} values do not show a clear correlation with their electrochemical performances. Although the C_{dl} values of Ni-N-CNT and Ni-N-ANBC show significant differences, they exhibit competitive electrocatalytic performances for CO_2RR . In addition, as shown in Figure S6.8, Ni-CB (0.26 mF/cm^2) shows a similar C_{dl} value as Ni-N-CB (0.27 mF/cm^2); Ni-CNT (0.33 mF/cm^2) shows a similar C_{dl} value as Ni-N-CB (0.36 mF/cm^2); ANBC (0.95 mF/cm^2) and Ni-ANBC (1.02 mF/cm^2) show similar C_{dl} values as Ni-N-ANBC (0.95 mF/cm^2). Despite the Ni-C samples showing no CO_2RR activity or less CO_2RR activity than the Ni-N-C catalysts, the C_{dl} values of the Ni-C samples are similar to those of the Ni-N-C catalysts, which indicates that the C_{dl} values are mainly dependent on the properties of carbon supports rather than the active sites. This means that not all electrochemically active sites are catalytically active for the CO_2RR . Therefore, in the case of porous carbon-based catalysts, we believe that ECSA-based calculations are not effective in comparing their catalytic performances.

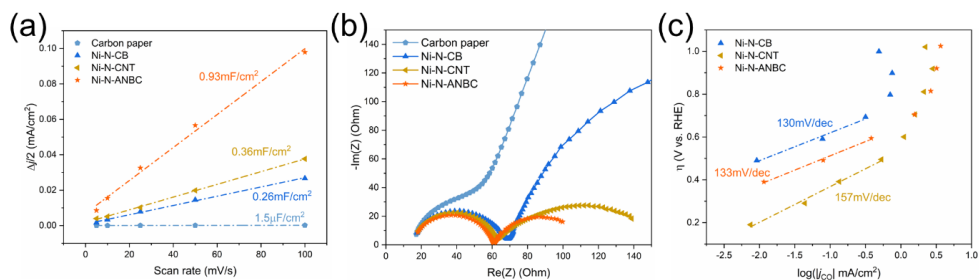


Figure 6.4 (a) Double layer capacitance, (b) Nyquist plots, and (c) Tafel plots of Ni-N-CB, Ni-N-CNT, and Ni-N-ANBC.

Furthermore, electrochemical impedance spectroscopy (EIS) measurements, depicted in Figure 6.4b, show that Ni-N-CNT and Ni-N-ANBC exhibit lower charge-transfer resistance than Ni-N-CB, which highlights their potential to accelerate electron transfer during the CO_2RR . Control measurements with the Ni-C samples (Figure S6.9) show similar charge-transfer resistances to that of the Ni-N-C catalysts, indicating that the charge-transfer resistances are determined by the properties of the carbon supports. The kinetics of the Ni-N-C catalysts are plotted in Tafel slopes (Figure 6.4c). The Tafel slope values of Ni-N-CB, Ni-N-CNT, and Ni-N-ANBC are calculated to be 130, 157, and 133 mV/dec , respectively. All of these values are close to the theoretical value of 118 mV/dec , implying that the prepared Ni-N-C catalysts exhibit a similar rate-determine step (RDS) toward CO_2RR , which is the single electron transfer to the adsorbed CO_2 to form a $CO_2^{\cdot-}$ intermediate.^{50–52}

Control experiments to verify whether the observed CO was produced from CO₂ were carried out in an Ar-saturated electrolyte at -0.9 V vs. RHE. As shown in Figure S6.10, the carbon paper used for electrode preparation shows a low catalytic activity and only produces H₂, in both CO₂-saturated and Ar-saturated electrolytes, suggesting that all of the CO₂RR activity is derived from the Ni-N-C catalysts. Performing chronoamperometry measurements with the Ni-N-C catalysts in an Ar-saturated electrolyte only leads to H₂ production, indicating that all of the produced CO originates from electrochemical CO₂ reduction and not from the decomposition of the carbon supports.

6.3.3 Factors behind the performance differences

The hydrophobicity and surface roughness of porous carbon electrocatalysts are considered to have a critical impact on their performance for the CO₂RR.⁵³ A more hydrophobic surface helps to inhibit the HER and thereby enhances the CO₂RR performance.⁵⁴ The surface roughness affects the residence time of gas bubbles on the electrode surface,⁵⁵ and bubbles with a larger size and longer residence time can partially cover the active sites resulting in a lower activity.⁵⁶ In this study, we carried out static contact angle measurements to evaluate the hydrophobicity of the Ni-N-C catalysts, with a larger contact angle indicating a higher hydrophobicity. Dynamic contact angle (advancing-receding contact angle) measurements were performed to evaluate the surface roughness of the drop-casted electrodes. In particular, as the electrode surface becomes rougher, the difference between the advancing contact angle and receding contact angle becomes larger, conversely, the difference in the diameter of the drop base becomes smaller. The results of hydrophobicity and surface roughness of Ni-N-C catalysts are depicted in Figure S6.11. All Ni-N-C catalysts exhibit similar contact angles at around 130° (Figure S6.11a and Table S6.2), indicating that they possess similar hydrophobicity. In addition, the difference between advancing and receding contact angles (Figure S6.11b) and the difference in diameters of the drop base (Figure S6.11c) of all Ni-N-C catalysts are almost negligible, suggesting that all of them show similar surface roughness. Although the different carbon-based supports show significant differences at the microscopic scale (Figure 6.1), they do not exhibit significant differences in macroscopic hydrophobicity and surface roughness. According to the above discussions, the effect of hydrophobicity and surface roughness of Ni-N-C catalysts on the differences of CO₂RR performances in this study is almost negligible.

The porous structures of carbon-based catalysts are favorable to the CO₂RR electrocatalytic performance.⁵⁷ Abundant porous structures provide a larger specific area and especially mesopores and macropores play an important role in enhancing the mass transfer and improving the accessibility of the active sites.⁵⁸ N₂ adsorption-desorption measurements were performed to determine the specific surface area and porosity of the prepared Ni-N-C catalysts. The N₂ adsorption-desorption isotherms of Ni-N-C catalysts are

shown in Figure 6.5a, with the curves of Ni-N-CB and Ni-N-CNT exhibiting a rapid increase at relatively high pressures ($P/P_0 > 0.8$), suggesting the presence of macropores. Additionally, Ni-N-CNT shows an apparent hysteresis loop ($0.8 < P/P_0 < 1.0$), indicating the existence of mesopores. On the contrary, Ni-N-ANBC exhibits a sharp uptake at relatively low pressures ($P/P_0 < 0.005$), revealing the predominant presence of micropores. The corresponding pore width distributions of Ni-N-C catalysts (Figure 6.5b), which are calculated by a density functional theory (DFT) model show similar results. The pore width of Ni-N-CB and Ni-N-ANBC are mainly centered at around 55 nm and 2 nm, respectively. However, the pore width distribution of Ni-N-CNT shows two intensive peaks located at around 35 nm and 55 nm. The specific surface areas of Ni-N-CB, Ni-N-CNT, and Ni-N-ANBC are calculated to be 171.4 m²/g, 173.3 m²/g, and 1053.5 m²/g, respectively. The percentage of meso-/macropores of Ni-N-CB, Ni-N-CNT, and Ni-N-ANBC are calculated as 94.4%, 99.0%, and 26.0%, respectively (Table S6.3). It is noteworthy that although Ni-N-CNT and Ni-N-ANBC show dramatic differences in specific surface area and the percentage of meso-/macropores, they exhibit competitive CO₂RR performances. This indicates that the contribution of micropores in carbon materials should not be underestimated. This is in line with the literature, where Estevez et al. reported that a higher percentage of micropores in carbon materials can enhance the CO₂ capture performance,⁵⁹ while Liu et al. synthesized a coal-based N-doped carbon catalysts for CO₂RR and pointed out that the spatial confinement effect of the micropores is beneficial for CO₂ converting to CO.⁶⁰ Furthermore, the N₂ adsorption-desorption isotherms, pore width distribution, and textural properties of pristine carbon materials and Ni-C samples are summarized in Figure S6.12 and Table S6.3. It can be clearly seen that the isotherms and pore width distributions of pristine carbon materials and Ni-C samples are similar to the Ni-N-C catalysts. Loading Ni or Ni-N_x onto the carbon support blocks part of the pores and leads to a decrease in specific surface area (Table S6.3), but does not change the main porosity of the carbon material itself. These results demonstrate that the ligand-mediated synthesis method for Ni-N-C catalysts does not affect the pristine porosity of the carbon supports.

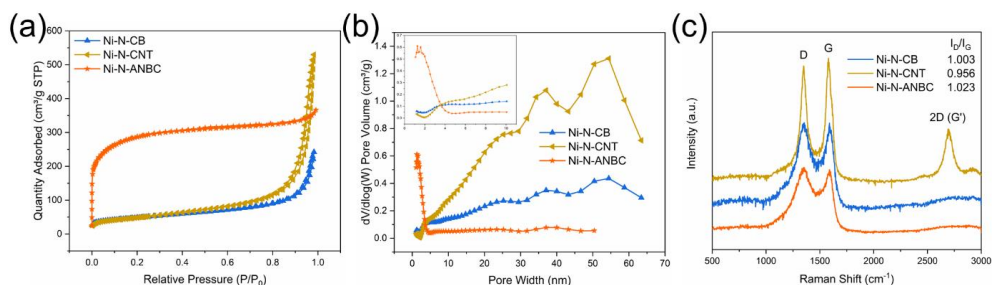


Figure 6.5 (a) N₂ adsorption-desorption isotherms, (b) Pore width distributions, (c) Raman spectra of Ni-N-CB, Ni-N-CNT, and Ni-N-ANBC.

Defects in carbon materials have been demonstrated to facilitate the adsorption and activation of CO₂, which are beneficial for CO₂RR performance.⁶¹ Hence, Raman spectroscopy is carried out to analyze the abundance of defects of Ni-N-C catalysts. As shown in Figure 6.5c, all of the materials show two peaks located at around 1350 cm⁻¹ and 1590 cm⁻¹ that can be assigned as the D band and G band of carbon materials. Additionally, Ni-N-CNT exhibits another distinct peak at around 2700 cm⁻¹, which can be attributed to the 2D band of graphitic carbon materials, indicating that Ni-N-CNT has a higher degree of graphitization. The I_D/I_G ratio reflects the abundance of defects in carbon materials. Among all Ni-N-C catalysts, Ni-N-ANBC (I_D/I_G = 1.023) exhibits more defects than Ni-N-CB (I_D/I_G = 1.003) and Ni-N-CNT (I_D/I_G = 0.956), which is attributed to the introduced nitrogen heteroatoms. Ni-N-CNT shows the lowest I_D/I_G value, indicating its high degree of graphitization. However, both Ni-N-ANBC and Ni-N-CNT show good performances toward the CO₂RR, suggesting that the contributions of defects in Ni-N-C catalysts to CO₂RR activity are almost negligible. It is important to note that several studies have demonstrated that the intrinsic defects in carbon materials show efficient catalytic activity for CO₂RR.^{62–64} However, most of the reported defect-rich carbon materials are generated by the removal of nitrogen heteroatoms from N-doped carbon via thermal treatment under an inert atmosphere.⁶⁵ Nonetheless, high temperatures can not completely remove the nitrogen heteroatoms and also facilitate carbon network rearrangements leading to a decrease in defects.^{66,67} Therefore, it is difficult to assess the contribution of defects in carbon supports of Ni-N-C catalysts to CO₂RR performance. Furthermore, the Raman spectra of pristine carbon materials and Ni-C samples are depicted in Figure S6.13. All of the Ni-N-C catalysts and Ni-C samples show lower I_D/I_G values than the pristine carbon materials, indicating that the additional annealing and introduction of other carbon sources (1,10 - phenanthroline) will decrease the abundance of defects in carbon supports and improve their degree of graphitization.

Apart from the contribution of porosity to the CO₂RR performance, the distribution of Ni-N_x active sites also has a crucial influence on the CO₂RR performances of Ni-N-C catalysts. This distribution is jointly affected by the morphology and porosity of different carbon supports.^{68,69} The Ni loadings of different Ni-N-C catalysts were measured by both X-ray photoelectron spectrometry (XPS) and inductively coupled plasma optical emission spectrometry (ICP-OES). For comparison, the XPS results in atomic percentages (at. %) were converted to weight percentages (wt. %). As shown in Figure 6.6a, the ICP-OES results indicate that all Ni-N-C catalysts show a similar Ni loading at around 1.1 wt.%, close to the intended Ni loading of 1.5 wt.%. However, XPS results demonstrate that the contents of Ni in Ni-N-CB, Ni-N-CNT, and Ni-N-ANBC are 0.24 wt. %, 0.51 wt. %, and 0.32 wt. %, respectively, which are lower than the results obtained by ICP-OES analysis. This difference attests that

part of the Ni-N_x active sites are confined inside the pores of different carbon supports and are therefore not detectable by XPS. Several studies report similar results.^{70,71} Since the penetration depth of XPS is limited and only reflects the Ni content on the surface of Ni-N-C catalysts,⁷² the results of XPS indicate that Ni-N-CNT exhibits more surface Ni-N_x active sites than Ni-N-CB and Ni-N-ANBC. Combining the different distributions of active sites, structural properties and electrochemical performances of Ni-N-C catalysts, we illustrate our findings in Figure 6.6b. Due to the agglomeration of carbon black nanospheres, parts of Ni-N_x sites are buried inside of the carbon particles. Therefore, the Ni-N-CB catalyst shows a lower CO₂RR performance than Ni-N-CNT and Ni-N-ANBC. On the contrary, due to the fiber-like, multilayered tubular structure of the multi-walled carbon nanotube, the Ni-N_x active sites cannot easily enter the interior of the carbon nanotube. By virtue of its abundant surface Ni-N_x active sites and wider pore size, Ni-N-CNT exhibits better CO₂RR performances than other Ni-N-C catalysts at relatively lower overpotentials. In contrast, Ni-N-ANBC has a hierarchical structure and a part of the Ni-N_x active sites are distributed in deeper and smaller pores. This leads to some Ni-N_x sites not being readily accessible and showing a poorer CO₂RR activity at more positive potentials. However, as the potential becomes more negative, the electrowetting helps to improve the accessibility of Ni-N_x active sites in the pores of the ANBC.⁷³ Consequently, this distribution of active sites allows the Ni-N-ANBC catalyst to maintain a good FE_{CO} (> 90%) and *j*_{CO} at more negative potentials.

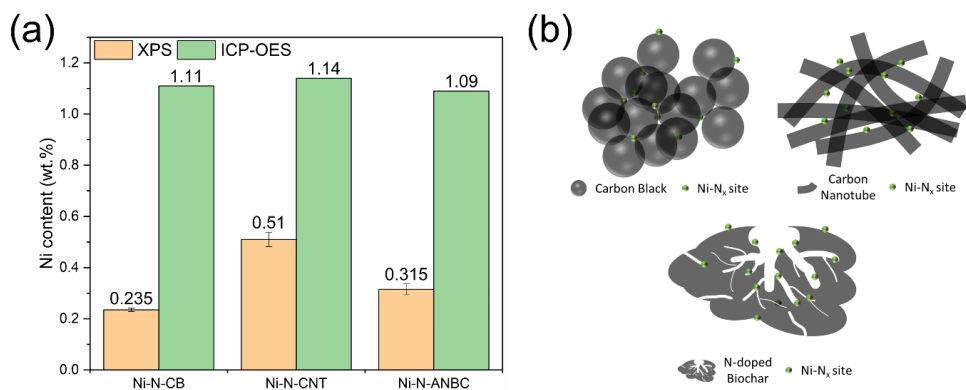


Figure 6.6 (a) The Ni content of Ni-N-CB, Ni-N-CNT, and Ni-N-ANBC quantified by XPS and ICP. (b) Schematic illustration of the distribution of actives of Ni-N-CB, Ni-N-CNT, and Ni-N-ANBC.

From the above discussions, we find that the CO₂RR performances of the Ni-N-C catalysts are highly dependent on the applied carbon supports. The agglomeration of carbon

black nanospheres covers several Ni-N_x active sites, which causes Ni-N-CB to show a relatively poor CO₂RR performance. Multi-walled carbon nanotubes display larger pore sizes than other carbon supports and the Ni-N_x active sites are mostly distributed on the surface of carbon nanotubes. This allows fast mass transfer of reactants to the active sites, thus enabling Ni-N-CNT to show excellent CO₂RR performance even at low overpotential. On the contrary, N-doped biochar shows a hierarchical structure with a large number of micropores, where part of the Ni-N_x active sites are confined in deeper and smaller pores. This enables Ni-N-ANBC to exhibit a great CO₂RR performance at more negative potentials. In general, we can therefore conclude that selecting a suitable carbon support is important to help Ni-N-C catalysts exhibit better CO₂RR performances.

6.4 Conclusions

We have successfully synthesized a group of Ni-N-C catalysts by using different carbon supports via a ligand-mediated method. We comprehensively studied the critical factors of carbon supports that govern the CO₂RR performances of the prepared Ni-N-C catalysts, which include hydrophobicity, surface roughness, porosity, the abundance of defects, and the distribution of active sites. All of the Ni-N-C catalysts exhibit similar hydrophobicity and surface roughness and show high faradaic efficiencies toward CO (ca. 90%) over different potential windows. However, their current densities show significant differences. The morphology and porosity of different carbon supports influence the distribution and accessibility of the Ni-N_x active sites. As a result, Ni-N-CB shows poorer CO₂RR performances that are attributed to the agglomeration of carbon black nanospheres which covers parts of Ni-N_x active sites. Ni-N-CNT displays a wider pore size and more Ni-N_x active sites on the carbon surface, which enables faster mass transfer of reactants to the Ni-N_x active sites, enabling the Ni-N-CNT to show a great FE_{CO} (>90%) and j_{CO} at lower overpotentials. The micropore-dominated N-doped biochar with hierarchical structures exhibits a larger specific surface area and smaller pore size, with a part of the Ni-N_x active sites confined in deeper and narrower pores. This pore architecture enables Ni-N-ANBC to maintain a good FE_{CO} even at more negative potentials. This study reveals the role of carbon support of Ni-N-C catalysts and presents the importance of selecting suitable carbon supports for Ni-N-C catalysts to exhibit excellent CO₂RR performance.

6.5 Supporting Information

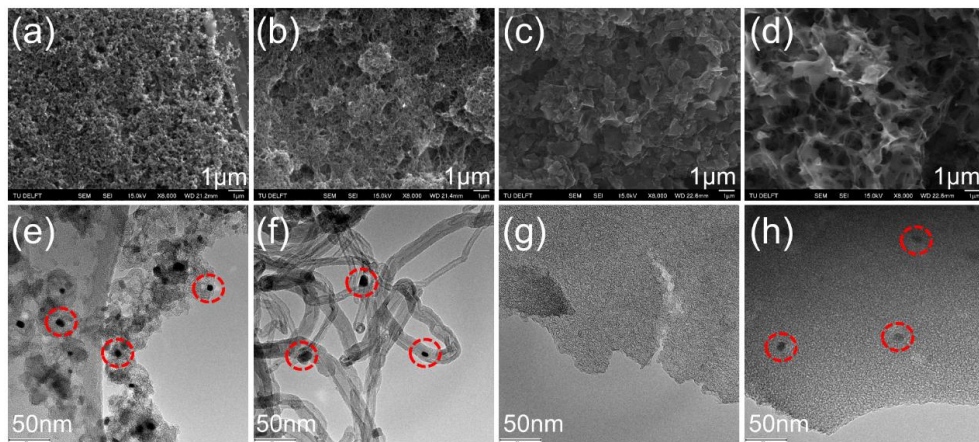


Figure S6.1 SEM images of (a) Ni-CB, (b) Ni-CNT, (c) ANBC, (d) Ni-ANBC and TEM images of (e) Ni-CB, (f) Ni-CNT, (g) ANBC, (h) Ni-ANBC.

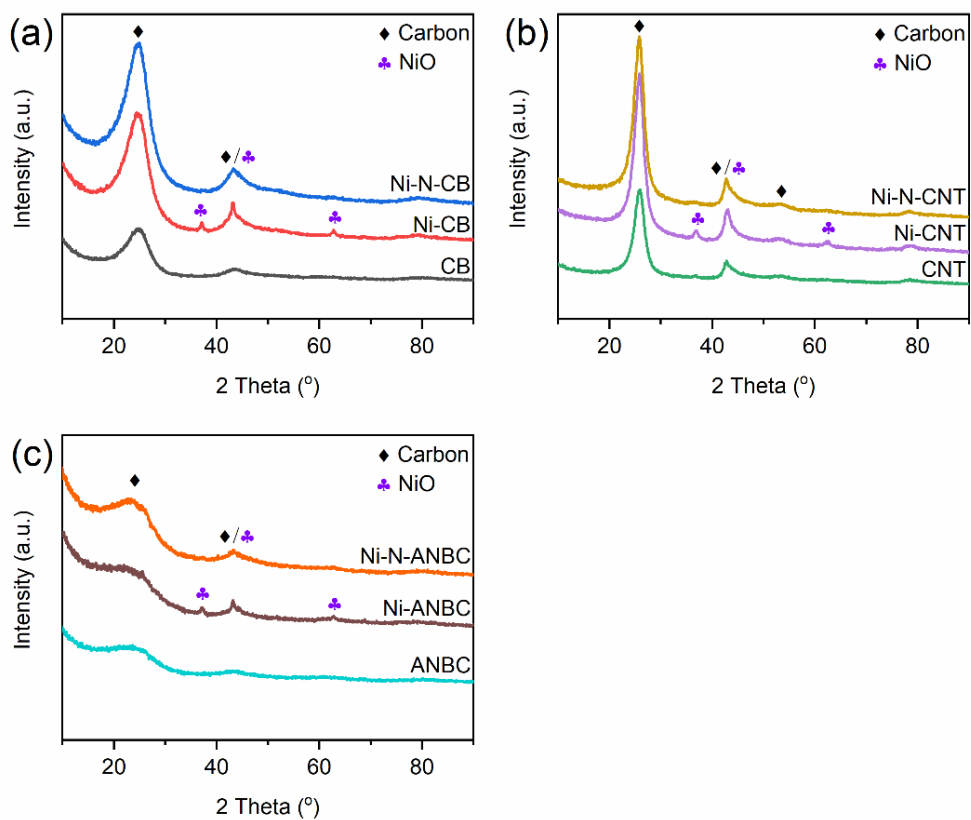


Figure S6.2 XRD patterns of (a) Carbon black-derived samples, (b) Multi-walled carbon nanotube-derived samples, (c) Activated N-doped biochar-derived samples.

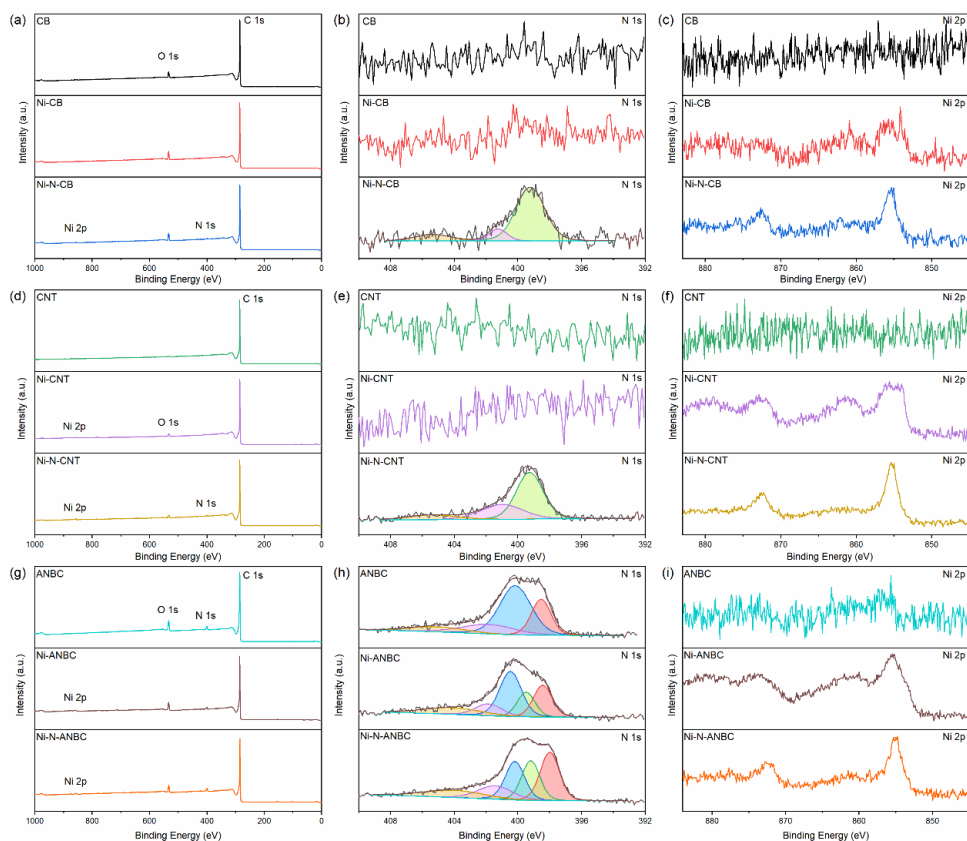


Figure S6.3 (a) XPS full survey, (b) High-resolution N1s spectra, (c) High-resolution Ni 2p spectra of carbon black-derived samples; (d) XPS full survey, (e) High-resolution N1s spectra, (f) High-resolution Ni 2p spectra of multi-walled carbon nanotube-derived samples; (g) XPS full survey, (h) High-resolution N1s spectra, (i) High-resolution Ni 2p spectra of activated N-doped biochar-derived samples.

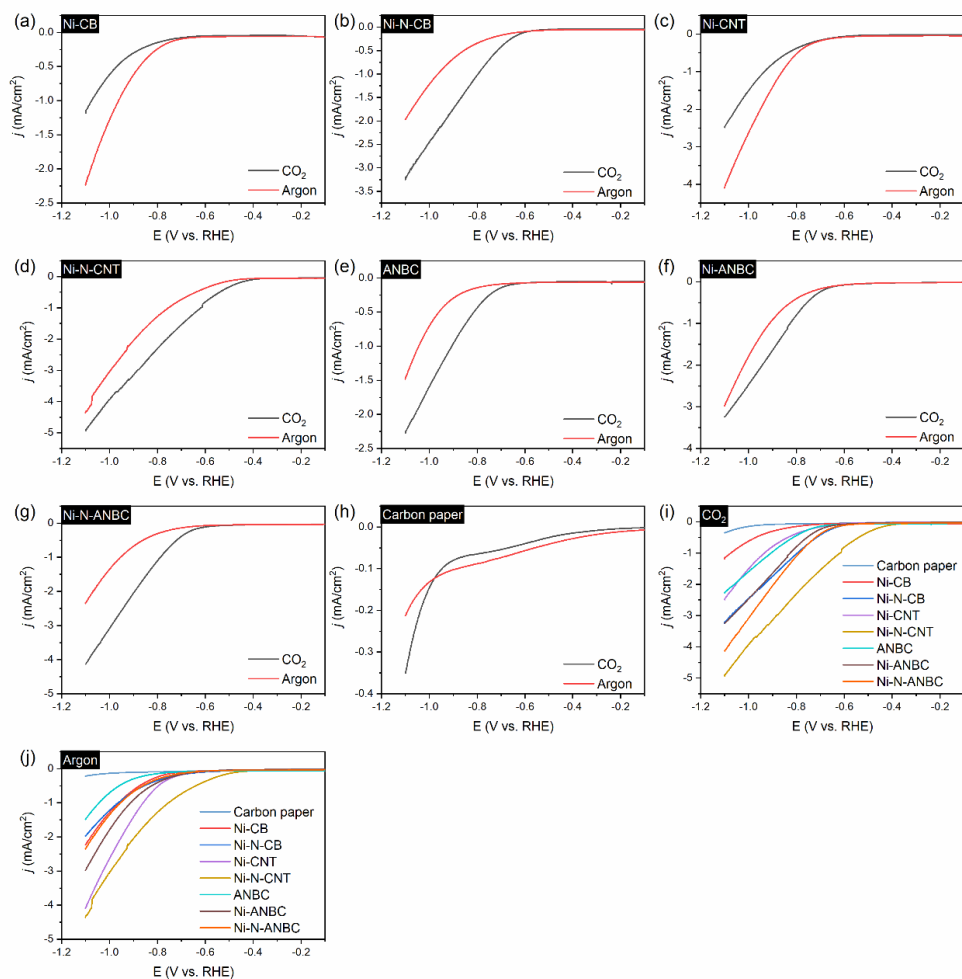


Figure S6.4 LSV curves of (a) Ni-CB, (b) Ni-N-CB, (c) Ni-CNT, (d) Ni-N-CNT, (e) ANBC, (f) Ni-ANBC, (g) Ni-N-ANBC, (h) carbon paper in CO₂-saturated and Ar-saturated 0.1 M KHCO₃ electrolytes; and (i) Comparisons of all samples in CO₂-saturated 0.1 M KHCO₃ electrolyte; (j) Comparisons of all samples in Ar-saturated 0.1 M KHCO₃ electrolyte.

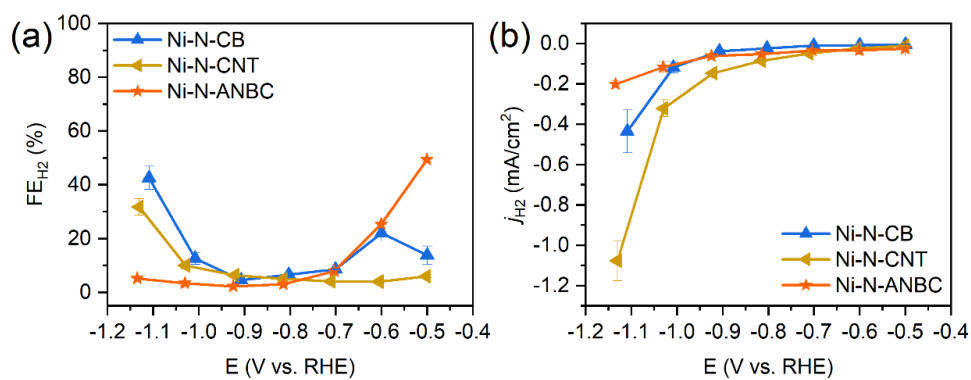


Figure S6.5 (a) Faradaic efficiency of H_2 , (b) Partial current density of H_2 of Ni-N-CB, Ni-N-CNT, and Ni-N-ANBC.

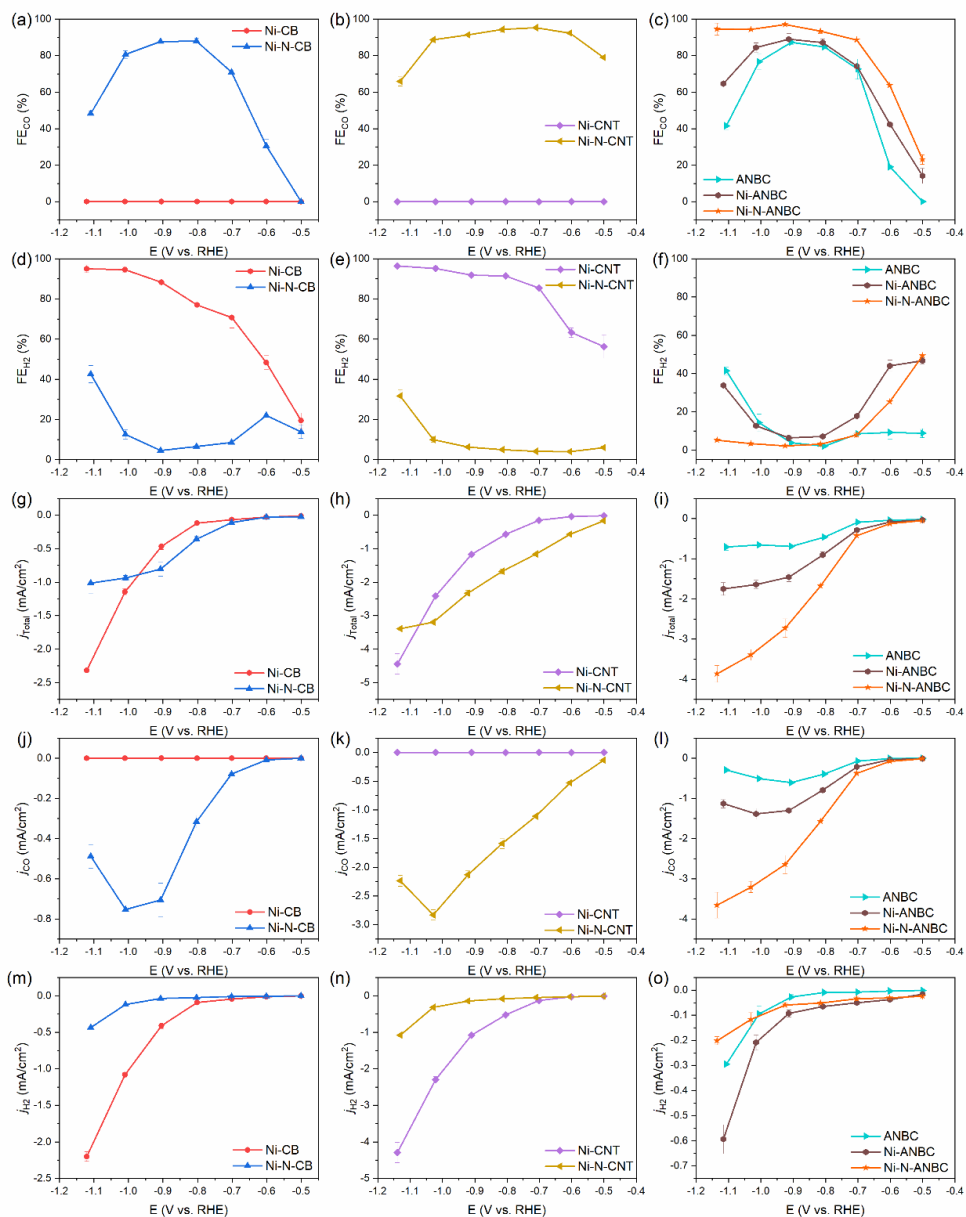


Figure S6.6 Faradaic efficiency of CO ((a), (b), (c)); Faradaic efficiency of H₂ ((d), (e), (f)) ; Total current density ((g), (h), (i)); Partial current density of CO ((j), (k), (l)); Partial current density of H₂ ((m), (n), (o)) of Ni-CB, Ni-N-CB, Ni-CNT, Ni-N-CNT, ANBC, Ni-ANBC, and Ni-N-ANBC.

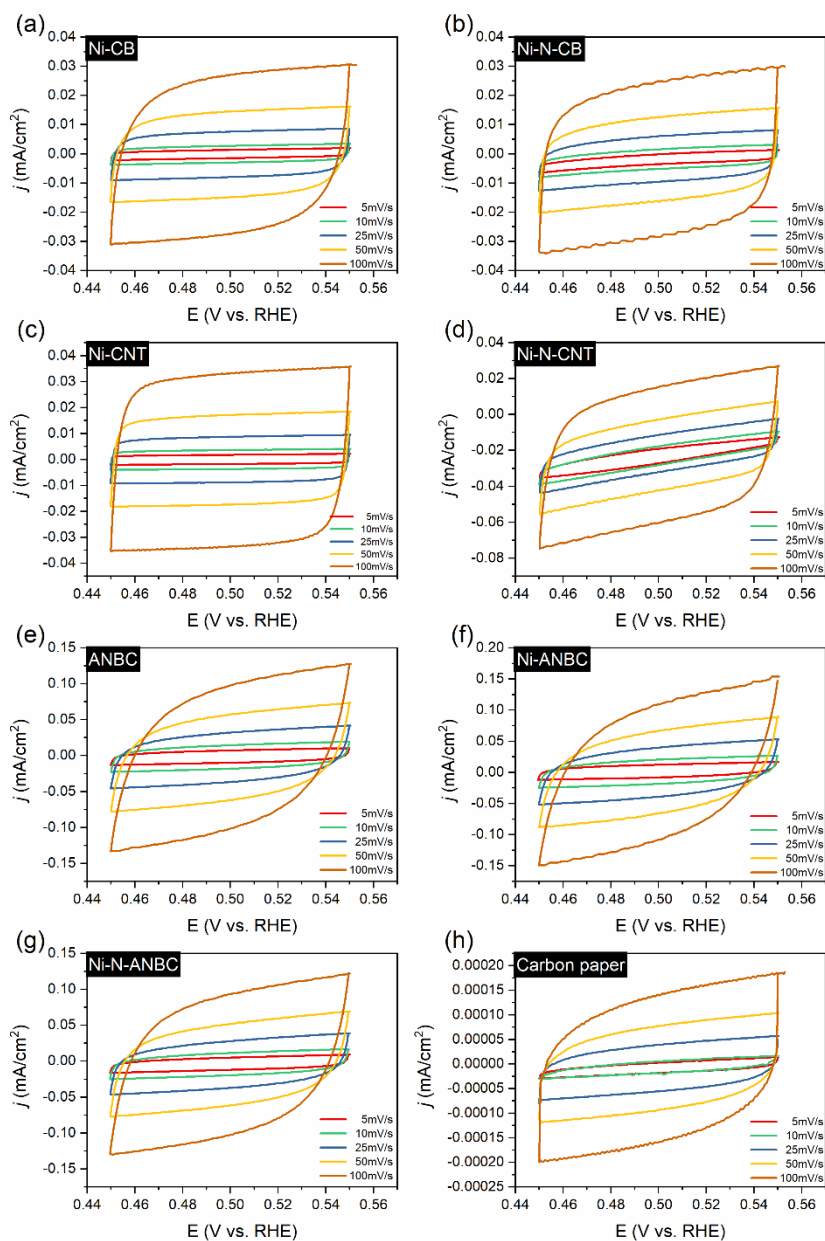


Figure S6.7 CVs of (a) Ni-CB, (b) Ni-N-CB, (c) Ni-CNT, (d) Ni-N-CNT, (e) ANBC, (f) Ni-ANBC, (g) Ni-N-ANBC and (h) Carbon paper from 0.45 to 0.55 V vs. RHE at various scan rates.

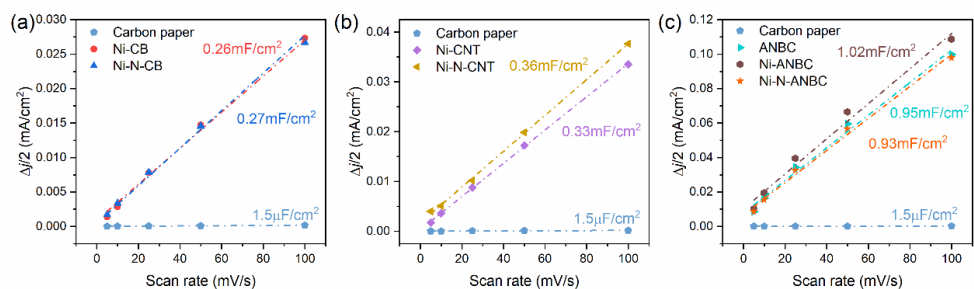


Figure S6.8 The double layer capacitance of (a) Ni-CB, and Ni-N-CB; (b) Ni-CNT, and Ni-N-CNT; (c) ANBC, Ni-ANBC, and Ni-N-ANBC.

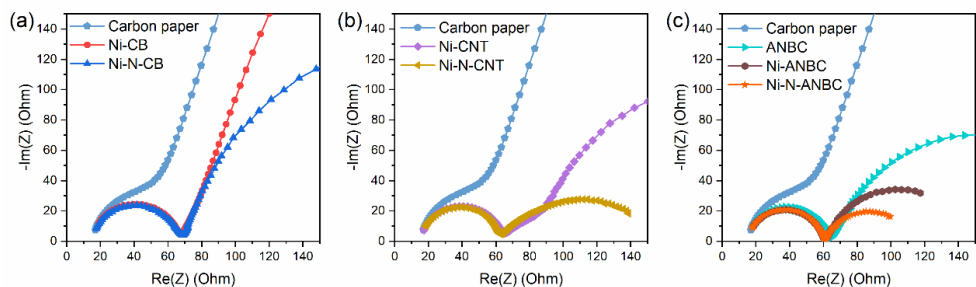


Figure S6.9 The Nyquist plots of (a) Ni-CB, and Ni-N-CB; (b) Ni-CNT, and Ni-N-CNT; (c) ANBC, Ni-ANBC, and Ni-N-ANBC.

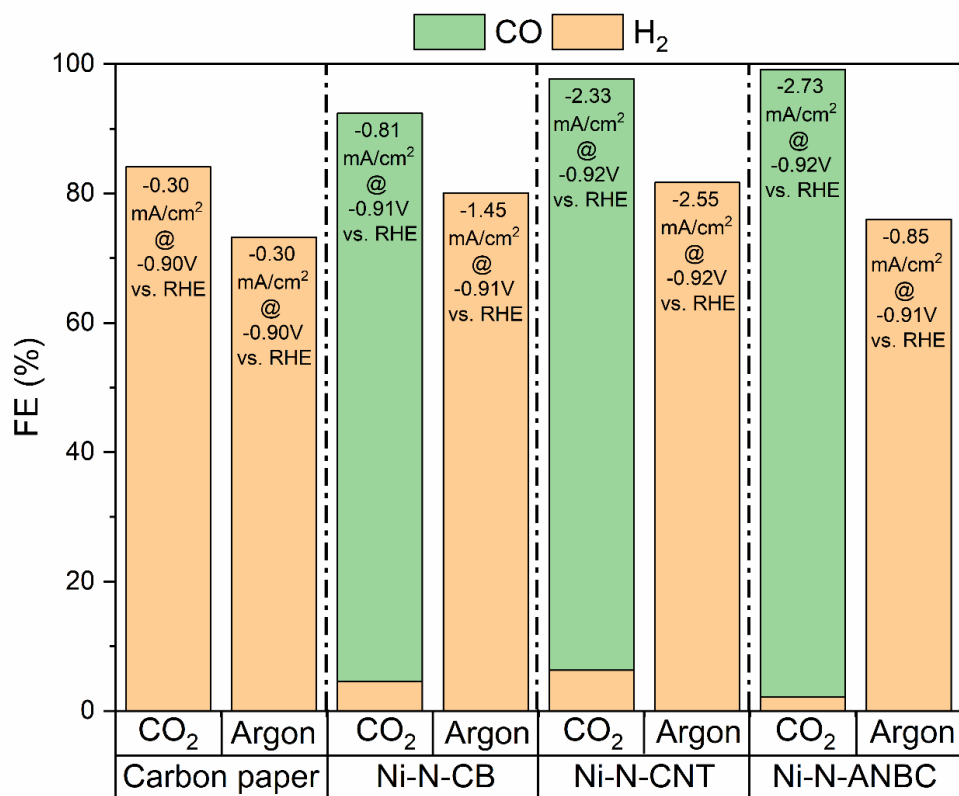


Figure S6.10 The control experiment of carbon paper and different Ni-N-C catalysts in CO₂-saturated and Ar-saturated 0.1 M KHCO₃ electrolyte at -0.9 V vs. RHE.

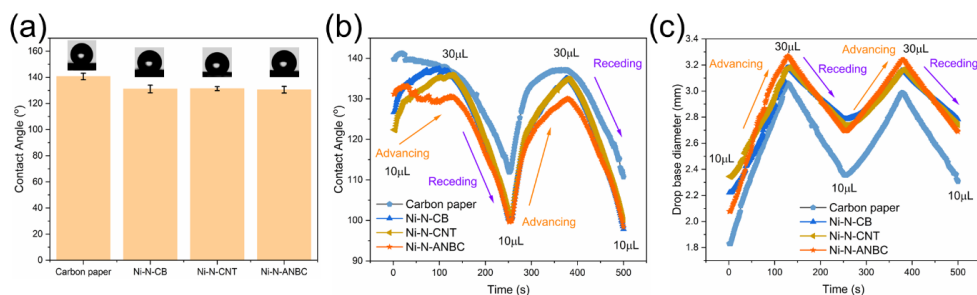


Figure S6.11 (a) Static contact angle, (b) Advancing and receding contact angle during the dynamic contact angle measurements, and (c) Drop base diameter during the dynamic contact angle measurements of Ni-N-CB, Ni-N-CNT, and Ni-N-ANBC.

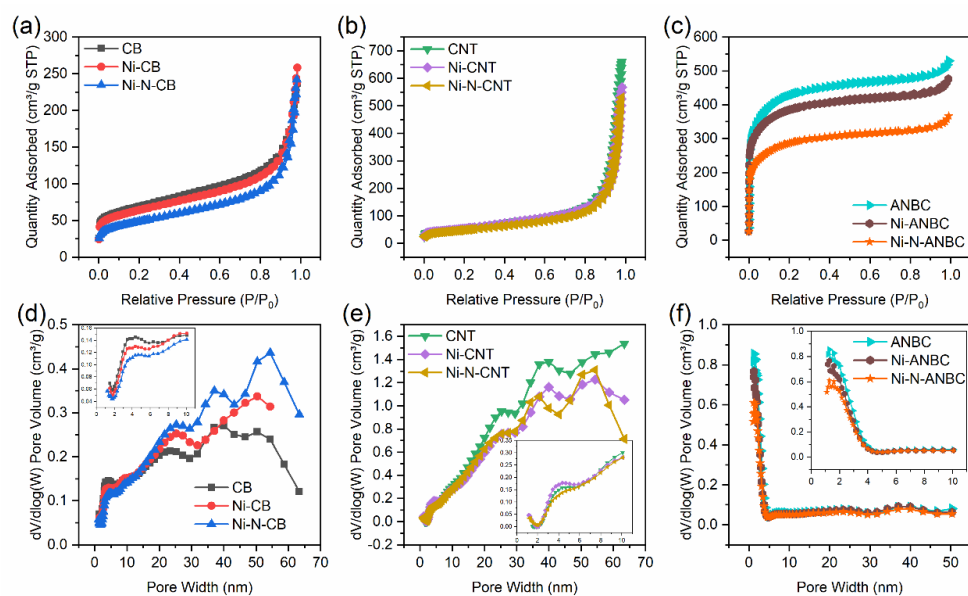


Figure S6.12 N₂ adsorption-desorption isotherms of (a) Carbon black-derived samples, (b) Multi-walled carbon nanotube-derived samples, (c) Activated N-doped biochar-derived samples; and Pore size distributions of (d) Carbon black-derived samples, (e) Multi-walled carbon nanotube-derived samples, (f) Activated N-doped biochar-derived samples.

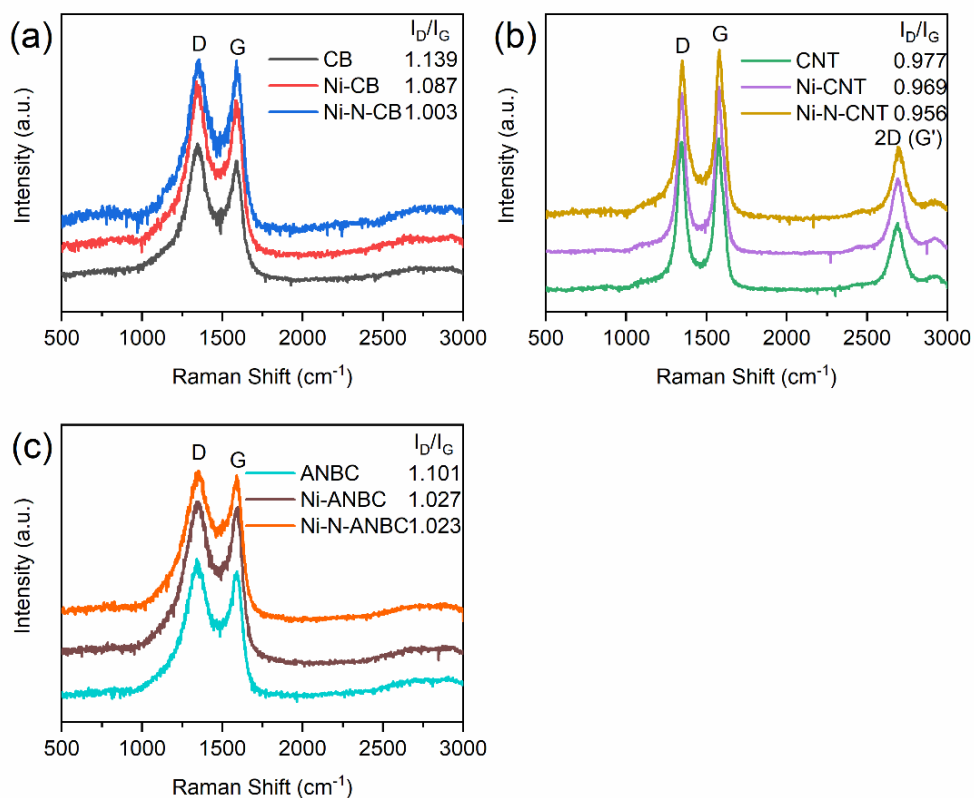


Figure S6.13 Raman spectra of (a) Carbon black-derived samples, (b) Multi-walled carbon nanotube-derived samples, (c) Activated N-doped biochar-derived samples.

Table S6.1 Surface elemental contents and N1s XPS data of different carbon catalysts

Samples	C	O	Ni	N	Pyridinic N(at.%)	Ni-Nx (at.%)	Pyrrolic N(at.%)	Graphitic N(at.%)	Oxidized N(at.%)
	(at.%)	(at.%)	(at.%)	(at.%)	~398.2eV	~399.2eV	~400.2eV	~401.8eV	~404.7eV
CB	96.78	3.22	-	-	-	-	-	-	-
Ni-CB	95.20	4.80	-	-	-	-	-	-	-
Ni-N-CB	94.90	4.47	0.05	0.58	-	77.42	-	10.75	11.83
CNT	99.63	0.37	-	-	-	-	-	-	-
Ni-CNT	98.16	1.79	0.05	-	-	-	-	-	-
Ni-N-CNT	97.52	1.84	0.11	0.53	-	59.23	-	29.65	11.12
ANBC	89.93	6.34	-	3.73	23.15	-	51.11	16.52	9.21
Ni-ANBC	91.89	5.57	0.22	2.32	21.74	16.00	36.58	11.52	14.16
Ni-N-ANBC	92.05	4.54	0.07	3.34	28.18	21.90	22.82	13.95	13.15

Table S6.2 Static contact angle data for the Ni-N-C samples

Sample	Contact angle (°)				
	Drop 1	Drop 2	Drop 3	Mean	Standard Deviation
Carbon paper	137.8	141.9	142.3	140.7	2.49
Ni-N-CB	134.4	129.7	129.1	131.1	2.90
Ni-N-CNT	132.7	129.7	131.6	131.3	1.52
Ni-N-ANBC	133.4	128.7	129.5	130.5	2.51

Table S6.3 Textural properties of different carbon-based samples

Samples	N ₂ adsorption/desorption					
	S _{BET}	V _{total} (P/P ₀ =0.99)	V _{micro}	V _{meso}	V _{meso} /V _t	D _{avg}
	m ² /g	cm ³ /g	cm ³ /g	cm ³ /g	%	nm
CB	245.2	0.367	0.041	0.326	88.82	6.0
Ni-CB	228.4	0.399	0.039	0.360	90.04	7.0
Ni-N-CB	171.4	0.374	0.021	0.353	94.40	8.8
CNT	186.4	1.023	0.010	1.013	99.00	21.9
Ni-CNT	186.1	0.879	0.008	0.871	99.13	18.9
Ni-N-CNT	173.3	0.821	0.008	0.813	99.03	18.9
ANBC	1426.9	0.738	0.555	0.183	24.85	2.1
Ni-ANBC	1420.1	0.821	0.617	0.204	24.88	2.3
Ni-N-ANBC	1053.5	0.553	0.409	0.144	26.04	2.1

References

- (1) Chu, S.; Cui, Y.; Liu, N. The Path towards Sustainable Energy. *Nat. Mater.* **2017**, *16* (1), 16–22.
- (2) Obama, B. The Irreversible Momentum of Clean Energy. *Science*. **2017**, *355* (6321), 126–129.
- (3) Kortlever, R.; Shen, J.; Schouten, K. J. P.; Calle-Vallejo, F.; Koper, M. T. M. Catalysts and Reaction Pathways for the Electrochemical Reduction of Carbon Dioxide. *J. Phys. Chem. Lett.* **2015**, *6* (20), 4073–4082.
- (4) Birdja, Y. Y.; Pérez-Gallent, E.; Figueiredo, M. C.; Göttle, A. J.; Calle-Vallejo, F.; Koper, M. T. M. Advances and Challenges in Understanding the Electrocatalytic Conversion of Carbon Dioxide to Fuels. *Nat. Energy* **2019**, *4* (9), 732–745.
- (5) Seh, Z. W.; Kibsgaard, J.; Dickens, C. F.; Chorkendorff, I. B.; Nørskov, J. K.; Jaramillo, T. F. Combining Theory and Experiment in Electrocatalysis: Insights into Materials Design. *Science*. **2017**, *355*, 6321.
- (6) De Luna, P.; Hahn, C.; Higgins, D.; Jaffer, S. A.; Jaramillo, T. F.; Sargent, E. H. What Would It Take for Renewably Powered Electrosynthesis to Displace Petrochemical Processes? *Science*. **2019**, *364* (6438), eaav3506.
- (7) Lawrence, K. R.; Kumar, A. S.; Asperti, S.; van den Berg, D.; Girichandran, N.; Kortlever, R. Advances in Electrochemical Carbon Dioxide Reduction Toward Multi-Carbon Products. In *Chemical Valorisation of Carbon Dioxide*; 2022; pp 388–412.
- (8) Jin, S.; Hao, Z.; Zhang, K.; Yan, Z.; Chen, J. Advances and Challenges for the Electrochemical Reduction of CO₂ to CO: From Fundamentals to Industrialization. *Angew. Chemie* **2021**, *133* (38), 20795–20816.
- (9) Van Daele, K.; De Mot, B.; Pupo, M.; Daems, N.; Pant, D.; Kortlever, R.; Breugelmans, T. Sn-Based Electrocatalyst Stability: A Crucial Piece to the Puzzle for the Electrochemical CO₂ Reduction toward Formic Acid. *ACS Energy Lett.* **2021**, *6* (12), 4317–4327.
- (10) Guan, A.; Chen, Z.; Quan, Y.; Peng, C.; Wang, Z.; Sham, T.-K.; Yang, C.; Ji, Y.; Qian, L.; Xu, X. Boosting CO₂ Electroreduction to CH₄ via Tuning Neighboring Single-Copper Sites. *ACS energy Lett.* **2020**, *5* (4), 1044–1053.
- (11) Dinh, C.-T.; Burdyny, T.; Kibria, M. G.; Seifitokaldani, A.; Gabardo, C. M.; De Arquer, F. P. G.; Kiani, A.; Edwards, J. P.; De Luna, P.; Bushuyev, O. S. CO₂ Electroreduction to Ethylene via Hydroxide-Mediated Copper Catalysis at an Abrupt Interface. *Science*. **2018**, *360* (6390), 783–787.

- (12) Zheng, T.; Jiang, K.; Wang, H. Recent Advances in Electrochemical CO₂-to-CO Conversion on Heterogeneous Catalysts. *Adv. Mater.* **2018**, *30* (48), 1802066.
- (13) Nguyen, D. L. T.; Kim, Y.; Hwang, Y. J.; Won, D. H. Progress in Development of Electrocatalyst for CO₂ Conversion to Selective CO Production. *Carbon Energy* **2020**, *2* (1), 72–98.
- (14) Hernández, S.; Farkhondeh, M. A.; Sastre, F.; Makkee, M.; Saracco, G.; Russo, N. Syngas Production from Electrochemical Reduction of CO₂: Current Status and Prospective Implementation. *Green Chem.* **2017**, *19* (10), 2326–2346.
- (15) Zhao, S.; Jin, R.; Jin, R. Opportunities and Challenges in CO₂ Reduction by Gold- and Silver-Based Electrocatalysts: From Bulk Metals to Nanoparticles and Atomically Precise Nanoclusters. *ACS energy Lett.* **2018**, *3* (2), 452–462.
- (16) Varela, A. S.; Ranjbar Sahraie, N.; Steinberg, J.; Ju, W.; Oh, H. S.; Strasser, P. Metal-Doped Nitrogenated Carbon as an Efficient Catalyst for Direct CO₂ Electroreduction to CO and Hydrocarbons. *Angew. Chemie - Int. Ed.* **2015**, *54* (37), 10758–10762.
- (17) Brimley, P.; Almajed, H.; Alsunni, Y.; Alherz, A. W.; Bare, Z. J. L.; Smith, W. A.; Musgrave, C. B. Electrochemical CO₂ Reduction over Metal-/Nitrogen-Doped Graphene Single-Atom Catalysts Modeled Using the Grand-Canonical Density Functional Theory. *ACS Catal.* **2022**, *12* (16), 10161–10171.
- (18) Ju, W.; Bagger, A.; Hao, G. P.; Varela, A. S.; Sinev, I.; Bon, V.; Roldan Cuenya, B.; Kaskel, S.; Rossmeisl, J.; Strasser, P. Understanding Activity and Selectivity of Metal-Nitrogen-Doped Carbon Catalysts for Electrochemical Reduction of CO₂. *Nat. Comm.* **2017**, *8*, 944.
- (19) Hu, X. M.; Hval, H. H.; Bjerglund, E. T.; Dalgaard, K. J.; Madsen, M. R.; Pohl, M. M.; Welter, E.; Lamagni, P.; Buhl, K. B.; Bremholm, M.; Beller, M.; Pedersen, S. U.; Skrydstrup, T.; Daasbjerg, K. Selective CO₂ Reduction to CO in Water Using Earth-Abundant Metal and Nitrogen-Doped Carbon Electrocatalysts. *ACS Catal.* **2018**, *8* (7), 6255–6264.
- (20) Pan, F.; Deng, W.; Justiniano, C.; Li, Y. Identification of Champion Transition Metals Centers in Metal and Nitrogen-Codoped Carbon Catalysts for CO₂ Reduction. *Appl. Catal. B Environ.* **2018**, *226*, 463–472.
- (21) Li, J.; Pršlja, P.; Shinagawa, T.; Martín Fernández, A. J.; Krumeich, F.; Artyushkova, K.; Atanassov, P.; Zitolo, A.; Zhou, Y.; García-Muelas, R.; López, N.; Pérez-Ramírez, J.; Jaouen, F. Volcano Trend in Electrocatalytic CO₂ Reduction Activity over Atomically Dispersed Metal Sites on Nitrogen-Doped Carbon. *ACS Catal.* **2019**, *9* (11), 10426–10439.

- (22) Möller, T.; Ju, W.; Bagger, A.; Wang, X.; Luo, F.; Thanh, T. N.; Varela, A. S.; Rossmeisl, J.; Strasser, P. Efficient CO₂ to CO Electrolysis on Solid Ni–N–C Catalysts at Industrial Current Densities. *Energy Environ. Sci.* **2019**, *12* (2), 640–647.
- (23) Zheng, T.; Jiang, K.; Ta, N.; Hu, Y.; Zeng, J.; Liu, J.; Wang, H. Large-Scale and Highly Selective CO₂ Electrocatalytic Reduction on Nickel Single-Atom Catalyst. *Joule* **2019**, *3* (1), 265–278.
- (24) Wang, Z.; Choi, J.; Xu, M.; Hao, X.; Zhang, H.; Jiang, Z.; Zuo, M.; Kim, J.; Zhou, W.; Meng, X. Optimizing Electron Densities of Ni–N–C Complexes by Hybrid Coordination for Efficient Electrocatalytic CO₂ Reduction. *ChemSusChem* **2020**, *13* (5), 929–937.
- (25) Mou, K.; Chen, Z.; Zhang, X.; Jiao, M.; Zhang, X.; Ge, X.; Zhang, W.; Liu, L. Highly Efficient Electroreduction of CO₂ on Nickel Single-atom Catalysts: Atom Trapping and Nitrogen Anchoring. *Small* **2019**, *15* (49), 1903668.
- (26) Li, X.; Bi, W.; Chen, M.; Sun, Y.; Ju, H.; Yan, W.; Zhu, J.; Wu, X.; Chu, W.; Wu, C. Exclusive Ni–N₄ Sites Realize near-Unity CO Selectivity for Electrochemical CO₂ Reduction. *J. Am. Chem. Soc.* **2017**, *139* (42), 14889–14892.
- (27) Yang, J.; Qiu, Z.; Zhao, C.; Wei, W.; Chen, W.; Li, Z.; Qu, Y.; Dong, J.; Luo, J.; Li, Z. In Situ Thermal Atomization to Convert Supported Nickel Nanoparticles into Surface-bound Nickel Single-atom Catalysts. *Angew. Chemie Int. Ed.* **2018**, *57* (43), 14095–14100.
- (28) Yan, C.; Li, H.; Ye, Y.; Wu, H.; Cai, F.; Si, R.; Xiao, J.; Miao, S.; Xie, S.; Yang, F.; Li, Y.; Wang, G.; Bao, X. Coordinatively Unsaturated Nickel-Nitrogen Sites towards Selective and High-Rate CO₂ Electroreduction. *Energy Environ. Sci.* **2018**, *11* (5), 1204–1210.
- (29) Varela, A. S.; Ju, W.; Bagger, A.; Franco, P.; Rossmeisl, J.; Strasser, P. Electrochemical Reduction of CO₂ on Metal-Nitrogen-Doped Carbon Catalysts. *ACS Catal.* **2019**, *9* (8), 7270–7284.
- (30) Niu, Y.; Zhang, C.; Wang, Y.; Fang, D.; Zhang, L.; Wang, C. Confining Chainmail-Bearing Ni Nanoparticles in N-doped Carbon Nanotubes for Robust and Efficient Electroreduction of CO₂. *ChemSusChem* **2021**, *14* (4), 1140–1154.
- (31) Jiang, K.; Siahrostami, S.; Zheng, T.; Hu, Y.; Hwang, S.; Stavitski, E.; Peng, Y.; Dynes, J.; Gangisetty, M.; Su, D. Isolated Ni Single Atoms in Graphene Nanosheets for High-Performance CO₂ Reduction. *Energy Environ. Sci.* **2018**, *11* (4), 893–903.
- (32) Jiang, K.; Siahrostami, S.; Akey, A. J.; Li, Y.; Lu, Z.; Lattimer, J.; Hu, Y.; Stokes, C.; Gangishetty, M.; Chen, G. Transition-Metal Single Atoms in a Graphene Shell as Active Centers for Highly Efficient Artificial Photosynthesis. *Chem* **2017**, *3* (6), 950–960.

- (33) Lu, P.; Yang, Y.; Yao, J.; Wang, M.; Dipazir, S.; Yuan, M.; Zhang, J.; Wang, X.; Xie, Z.; Zhang, G. Facile Synthesis of Single-Nickel-Atomic Dispersed N-Doped Carbon Framework for Efficient Electrochemical CO₂ Reduction. *Appl. Catal. B Environ.* **2019**, *241*, 113–119.
- (34) Jeong, H.-Y.; Balamurugan, M.; Choutipalli, V. S. K.; Jeong, E.; Subramanian, V.; Sim, U.; Nam, K. T. Achieving Highly Efficient CO₂ to CO Electroreduction Exceeding 300 MA Cm⁻² with Single-Atom Nickel Electrocatalysts. *J. Mater. Chem. A* **2019**, *7* (17), 10651–10661.
- (35) Yang, H.; Lin, Q.; Zhang, C.; Yu, X.; Cheng, Z.; Li, G.; Hu, Q.; Ren, X.; Zhang, Q.; Liu, J. Carbon Dioxide Electroreduction on Single-Atom Nickel Decorated Carbon Membranes with Industry Compatible Current Densities. *Nat. Commun.* **2020**, *11* (1), 593.
- (36) Li, H.; Li, H.; Wei, P.; Wang, Y.; Zang, Y.; Gao, D.; Wang, G.; Bao, X. Tailoring Acidic Microenvironments for Carbon-Efficient CO₂ Electrolysis over Ni-NC Catalyst in a Membrane Electrode Assembly Electrolyzer. *Energy Environ. Sci.* **2023**, *16*, 1502–1510.
- (37) Watkins, N. B.; Schiffer, Z. J.; Lai, Y.; Musgrave, C. B.; Atwater, H. A.; Goddard, W. A.; Agapie, T.; Peters, J. C.; Gregoire, J. M. Hydrodynamics Change Tafel Slopes in Electrochemical CO₂ Reduction on Copper. *ACS Energy Lett.* **2023**, *8* (5), 2185–2192.
- (38) Fu, S.; Li, M.; Asperti, S.; Jong, W. de; Kortlever, R. Unravelling the Effect of Activators Used in The Synthesis of Biomass-Derived Carbon Electrocatalysts on the Electrocatalytic Performance for CO₂ Reduction. *ChemSusChem* **2023**, *16*, e202202188.
- (39) Yang, H.; Shang, L.; Zhang, Q.; Shi, R.; Waterhouse, G. I. N.; Gu, L.; Zhang, T. A Universal Ligand Mediated Method for Large Scale Synthesis of Transition Metal Single Atom Catalysts. *Nat. Commun.* **2019**, *10* (1), 1–9.
- (40) Lobaccaro, P.; Singh, M. R.; Clark, E. L.; Kwon, Y.; Bell, A. T.; Ager, J. W. Effects of Temperature and Gas–Liquid Mass Transfer on the Operation of Small Electrochemical Cells for the Quantitative Evaluation of CO₂ Reduction Electrocatalysts. *Phys. Chem. Chem. Phys.* **2016**, *18* (38), 26777–26785.
- (41) Wei, Z.; Qiao, H.; Yang, H.; Zhang, C.; Yan, X. Characterization of NiO Nanoparticles by Anodic Arc Plasma Method. *J. Alloys Compd.* **2009**, *479* (1–2), 855–858.
- (42) Artyushkova, K.; Kiefer, B.; Halevi, B.; Knop-Gericke, A.; Schlögl, R.; Atanassov, P. Density Functional Theory Calculations of XPS Binding Energy Shift for Nitrogen-Containing Graphene-like Structures. *Chem. Commun.* **2013**, *49* (25), 2539–2541.
- (43) Xi, D.; Li, J.; Low, J.; Mao, K.; Long, R.; Li, J.; Dai, Z.; Shao, T.; Zhong, Y.; Li, Y.; Li, Z.; Loh, X. J.; Song, L.; Ye, E.; Xiong, Y. Limiting the Uncoordinated N Species in M–N_x Single-

Atom Catalysts toward Electrocatalytic CO₂ Reduction in Broad Voltage Range. *Adv. Mater.* **2021**, 2104090.

(44) Yang, H. Bin; Hung, S. F.; Liu, S.; Yuan, K.; Miao, S.; Zhang, L.; Huang, X.; Wang, H. Y.; Cai, W.; Chen, R.; Gao, J.; Yang, X.; Chen, W.; Huang, Y.; Chen, H. M.; Li, C. M.; Zhang, T.; Liu, B. Atomically Dispersed Ni(i) as the Active Site for Electrochemical CO₂ Reduction. *Nat. Energy* **2018**, 3 (2), 140–147.

(45) Li, Z.; He, D.; Yan, X.; Dai, S.; Younan, S.; Ke, Z.; Pan, X.; Xiao, X.; Wu, H.; Gu, J. Size-dependent Nickel-based Electrocatalysts for Selective CO₂ Reduction. *Angew. Chemie* **2020**, 132 (42), 18731–18736.

(46) Rong, X.; Wang, H.; Lu, X.; Si, R.; Lu, T. Controlled Synthesis of a Vacancy-defect Single-atom Catalyst for Boosting CO₂ Electroreduction. *Angew. Chemie* **2020**, 132 (5), 1977–1981.

(47) Ma, S.; Su, P.; Huang, W.; Jiang, S. P.; Bai, S.; Liu, J. Atomic Ni Species Anchored N-Doped Carbon Hollow Spheres as Nanoreactors for Efficient Electrochemical CO₂ Reduction. *ChemCatChem* **2019**, 11 (24), 6092–6098.

(48) Fu, S.; Li, M.; Jong, W. de; Kortlever, R. Tuning the Properties of N-Doped Biochar for Selective CO₂ Electroreduction to CO. *ACS Catal.* **2023**, 13, 10309–10323.

(49) Boppella, R.; Austeria, M.; Kim, Y.; Kim, E.; Song, I.; Eom, Y.; Praveen Kumar, D.; Balamurugan, M.; Sim, E.; Kim, H.; Kim, T. K. Pyrrolic N-Stabilized Monovalent Ni Single-Atom Electrocatalyst for Efficient CO₂ Reduction: Identifying the Role of Pyrrolic-N and Synergistic Electrocatalysis. *Adv. Funct. Mater.* **2022**, 32 (35), 2202351.

(50) Li, H.; Xiao, N.; Hao, M.; Song, X.; Wang, Y.; Ji, Y.; Liu, C.; Li, C.; Guo, Z.; Zhang, F.; Qiu, J. Efficient CO₂ Electroreduction over Pyridinic-N Active Sites Highly Exposed on Wrinkled Porous Carbon Nanosheets. *Chem. Eng. J.* **2018**, 351, 613–621.

(51) Kou, W.; Zhang, Y.; Dong, J.; Mu, C.; Xu, L. Nickel-Nitrogen-Doped Three-Dimensional Ordered Macro-/Mesoporous Carbon as an Efficient Electrocatalyst for CO₂ Reduction to CO. *ACS Appl. Energy Mater.* **2020**, 3 (2), 1875–1882.

(52) Liu, W.; Wei, S.; Bai, P.; Yang, C.; Xu, L. Robust Coal Matrix Intensifies Electron/Substrate Interaction of Nickel-Nitrogen (Ni-N) Active Sites for Efficient CO₂ Electroreduction at Industrial Current Density. *Appl. Catal. B Environ.* **2021**, 299, 120661.

(53) Hursán, D.; Samu, A. A.; Janovák, L.; Artyushkova, K.; Asset, T.; Atanassov, P.; Janáky, C. Morphological Attributes Govern Carbon Dioxide Reduction on N-Doped Carbon Electrodes. *Joule* **2019**, 3 (7), 1719–1733.

- (54) Lim, C.; Lee, W. H.; Won, J. H.; Ko, Y.; Kim, S.; Min, B. K.; Lee, K.; Jung, W. S.; Oh, H. Enhancement of Catalytic Activity and Selectivity for the Gaseous Electroreduction of CO₂ to CO: Guidelines for the Selection of Carbon Supports. *Adv. Sustain. Syst.* **2021**, *5* (12), 2100216.
- (55) Cao, B.-Y.; Chen, M.; Guo, Z.-Y. Effect of Surface Roughness on Gas Flow in Microchannels by Molecular Dynamics Simulation. *Int. J. Eng. Sci.* **2006**, *44* (13–14), 927–937.
- (56) Faber, M. S.; Dziedzic, R.; Lukowski, M. A.; Kaiser, N. S.; Ding, Q.; Jin, S. High-Performance Electrocatalysis Using Metallic Cobalt Pyrite (CoS₂) Micro-and Nanostructures. *J. Am. Chem. Soc.* **2014**, *136* (28), 10053–10061.
- (57) Ma, X.; Du, J.; Sun, H.; Ye, F.; Wang, X.; Xu, P.; Hu, C.; Zhang, L.; Liu, D. Boron, Nitrogen Co-Doped Carbon with Abundant Mesopores for Efficient CO₂ Electroreduction. *Appl. Catal. B Environ.* **2021**, *298*, 120543.
- (58) Sun, M.-H.; Huang, S.-Z.; Chen, L.-H.; Li, Y.; Yang, X.-Y.; Yuan, Z.-Y.; Su, B.-L. Applications of Hierarchically Structured Porous Materials from Energy Storage and Conversion, Catalysis, Photocatalysis, Adsorption, Separation, and Sensing to Biomedicine. *Chem. Soc. Rev.* **2016**, *45* (12), 3479–3563.
- (59) Estevez, L.; Barpaga, D.; Zheng, J.; Sabale, S.; Patel, R. L.; Zhang, J. G.; McGrail, B. P.; Motkuri, R. K. Hierarchically Porous Carbon Materials for CO₂ Capture: The Role of Pore Structure. *Ind. Eng. Chem. Res.* **2018**, *57* (4), 1262–1268.
- (60) Liu, W.; Qi, J.; Bai, P.; Zhang, W.; Xu, L. Utilizing Spatial Confinement Effect of N Atoms in Micropores of Coal-Based Metal-Free Material for Efficiently Electrochemical Reduction of Carbon Dioxide. *Appl. Catal. B Environ.* **2020**, *272*, 118974.
- (61) Wu, Q.; Yan, X.; Jia, Y.; Yao, X. Defective Carbon-Based Materials: Controllable Synthesis and Electrochemical Applications. *EnergyChem* **2021**, *3* (5), 100059.
- (62) Wu, Q.; Gao, J.; Feng, J.; Liu, Q.; Zhou, Y.; Zhang, S.; Nie, M.; Liu, Y.; Zhao, J.; Liu, F.; Zhong, J.; Kang, Z. A CO₂ Adsorption Dominated Carbon Defect-Based Electrocatalyst for Efficient Carbon Dioxide Reduction. *J. Mater. Chem. A* **2020**, *8* (3), 1205–1211.
- (63) Wang, W.; Shang, L.; Chang, G.; Yan, C.; Shi, R.; Zhao, Y.; Waterhouse, G. I. N.; Yang, D.; Zhang, T. Intrinsic Carbon-defect-driven Electrocatalytic Reduction of Carbon Dioxide. *Adv. Mater.* **2019**, *31* (19), 1808276.
- (64) Dong, Y.; Zhang, Q.; Tian, Z.; Li, B.; Yan, W.; Wang, S.; Jiang, K.; Su, J.; Oloman, C. W.; Gyenge, E. L.; Ge, R.; Lu, Z.; Ji, X.; Chen, L. Ammonia Thermal Treatment toward Topological

Defects in Porous Carbon for Enhanced Carbon Dioxide Electroreduction. *Adv. Mater.* **2020**, 32 (28), 2001300.

(65) Li, D.; Jia, Y.; Chang, G.; Chen, J.; Liu, H.; Wang, J.; Hu, Y.; Xia, Y.; Yang, D.; Yao, X. A Defect-Driven Metal-Free Electrocatalyst for Oxygen Reduction in Acidic Electrolyte. *Chem* **2018**, 4 (10), 2345–2356.

(66) Daiyan, R.; Tan, X.; Chen, R.; Saputera, W. H.; Tahini, H. A.; Lovell, E.; Ng, Y. H.; Smith, S. C.; Dai, L.; Lu, X.; Amal, R. Electroreduction of CO₂ to CO on a Mesoporous Carbon Catalyst with Progressively Removed Nitrogen Moieties. *ACS Energy Lett.* **2018**, 3 (9), 2292–2298.

(67) Ling, L.; Jiao, L.; Liu, X.; Dong, Y.; Yang, W.; Zhang, H.; Ye, B.; Chen, J.; Jiang, H. Potassium-Assisted Fabrication of Intrinsic Defects in Porous Carbons for Electrocatalytic CO₂ Reduction. *Adv. Mater.* **2022**, 34 (42), 2205933.

(68) Gupta, S.; Zhao, S.; Ogoke, O.; Lin, Y.; Xu, H.; Wu, G. Engineering Favorable Morphology and Structure of Fe-N-C Oxygen-reduction Catalysts through Tuning of Nitrogen/Carbon Precursors. *ChemSusChem* **2017**, 10 (4), 774–785.

(69) Ning, L.; Liao, S.; Li, H.; Tong, R.; Dong, C.; Zhang, M.; Gu, W.; Liu, X. Carbon-Based Materials with Tunable Morphology Confined Ni (0) and Ni-N_x Active Sites: Highly Efficient Selective Hydrogenation Catalysts. *Carbon* **2019**, 154, 48–57.

(70) Duarte, M.; Daems, N.; Hereijgers, J.; Arenas-Esteban, D.; Bals, S.; Breugelmans, T. Enhanced CO₂ Electroreduction with Metal-Nitrogen-Doped Carbons in a Continuous Flow Reactor. *J. CO₂ Util.* **2021**, 50, 101583.

(71) Xu, Y.; Liu, Y.; Cui, P.; Shang, N.; Wang, C.; Gao, Y. Stable Ni Catalyst Encapsulated in N-Doped Carbon Nanotubes for One-Pot Reductive Amination of Nitroarenes with Aldehydes. *Appl. Catal. A Gen.* **2021**, 622, 118230.

(72) Watts, J. F.; Wolstenholme, J. *An Introduction to Surface Analysis by XPS and AES*; John Wiley & Sons, 2019.

(73) Bienen, F.; Paulisch, M. C.; Mager, T.; Osiewacz, J.; Nazari, M.; Osenberg, M.; Ellendorff, B.; Turek, T.; Nieken, U.; Manke, I. Investigating the Electrowetting of Silver-based Gas-diffusion Electrodes during Oxygen Reduction Reaction with Electrochemical and Optical Methods. *Electrochem. Sci. Adv.* **2023**, 3 (1), e2100158.

7

Conclusions and Recommendations

7.1 Conclusions

In this dissertation, a series of biomass-derived N-doped carbon catalysts are synthesized for the electrochemical CO₂ reduction to CO. Sugarcane bagasse is selected as the feedstock owing to its large availability and easy accessibility. The abundant natural vascular fiber bundles in bagasse make it a good precursor to prepare porous carbon materials. A facile one-step pyrolysis method that combines the carbonization, activation, and N-doping simultaneously, is used. The effects of activators, carbonization temperatures, and additions of dopant used in the synthesis of N-doped biochar catalysts on the electrocatalytic performance for CO₂ reduction are systematically studied. The correlations between physicochemical properties and electrochemical CO₂RR performances of N-doped biochar catalysts are also comprehensively investigated. Moreover, one of the best N-doped biochar catalysts is selected for further applications. Overall, N-doped biochar exhibits better performance (selectivity, activity, and stability) than a silver foil electrode for electrochemical CO₂ reduction to CO, in the presence of 100 to 10000 ppm SO₂ impurities. N-doped biochar is also used as a carbon support to synthesize nickel-nitrogen-carbon (Ni-N-C) catalysts for CO₂RR. The as-prepared Ni-N-C catalyst on N-doped biochar shows more competitive CO₂RR performance than Ni-N-C catalysts on carbon black and carbon nanotubes. These studies provide new insights into the design, evaluation and utilization of N-doped biochar catalysts for electrochemical CO₂ reduction.

In Chapter 3, the influences of the type of activators used in the synthesis of N-doped biochar catalysts for the performance of electrochemical CO₂RR have been discussed. Six different activators of NaHCO₃, K₂CO₃, Mg₅(OH)₂(CO₃)₄, NaOH, KOH, and KHCO₃ are applied for preparing N-doped biochar catalysts via a standard synthesis procedure. Depending on the diversity of activation mechanisms, such as oxidation, etching and templating, the textural properties and surface chemistry of as-prepared catalysts exhibit massive differences, thus further resulting in significant differences in the electrochemical CO₂RR performance. The results demonstrate that the overall CO₂RR performance of the synthesized N-doped biochar catalysts is not only determined by the content of total N or specific N-containing species, but rather by the synergistic effect of the overall surface chemistry, the porosity and the degree of graphitization. Among these N-doped biochar catalysts, the sample activated by NaOH exhibits a good CO₂RR performance with 80% faradaic efficiency toward CO at -0.93 V vs. RHE, which is attributed to the proper N-doping content, large surface area and abundant pores with a relatively high mesoporosity and relatively high degree of graphitization.

In Chapter 4, NaOH is used as activator, and a series of N-doped biochar catalysts with different physicochemical properties are synthesized by tuning the carbonization temperature and N-doping level and used for the CO₂RR to analyze the structure-

performance relationship. In general, the N-doped biochar synthesized at higher carbonization temperatures (800 to 900 °C) shows a better performance. However, increasing the N-doping content does not efficiently improve the CO₂RR performance of N-doped biochar catalyst. The observed results suggest that neither the N-doping level nor the specific surface area is positively correlated to the observed CO₂RR performance of N-doped biochar catalysts, which is consistent with our previous results. A multivariate correlation analysis is established to evaluate the correlation between physicochemical properties and electrochemical CO₂RR performances of N-doped biochar. The results demonstrate that improving the surface hydrophobicity, the abundance of defects, and optimizing the porosity distribution of N-doped carbon can significantly improve the overall catalytic performance for CO₂ electrochemical reduction. Our data highlights the importance of a comprehensive analysis of the physicochemical properties of N-doped carbon catalysts for CO₂RR performance and enables the rational design of high-performance N-doped carbon catalysts for the CO₂RR in the future.

In Chapter 5, one of the most efficient N-doped biochar catalysts is selected as a catalyst for electrochemical CO₂ reduction to CO in the presence of varying concentrations of SO₂ impurities. The overall CO₂RR performance is co-dependent on the SO₂ concentrations and applied potential. The catalyst outperforms a silver foil electrode in the presence of SO₂, displaying a better CO₂RR performance, including a higher faradaic efficiency and current density to CO, stronger tolerance, stability and robustness to gaseous impurities. The presence of 10000 ppm SO₂ in a CO₂ stream significantly reduces the CO₂RR performance of N-doped biochar catalyst as the SO₂ reduction reaction becomes the dominant reaction. However, the changes in the CO₂RR performances are almost negligible in the presence of 1000 and 100 ppm SO₂ impurities. Additionally, it maintains over 90% faradaic efficiency toward CO during an 8-hour stability measurement at -1.0 V vs. RHE with 100 ppm SO₂ and shows a strong tolerance to the gas feed changes (the concentration of SO₂ fluctuates from 0 to 100 ppm) with negligible changes of the faradaic efficiency and current density of CO. SEM and XPS results indicate the absence of sulfur-containing species resulting from SO₂ reduction on the surface of N-doped biochar catalyst. These results suggest that N-doped carbon catalysts are feasible catalysts for CO₂ reduction applications using SO₂ contaminated CO₂ feeds.

In Chapter 6, a group of Ni-N-C catalysts are synthesized by using carbon black (CB), multi-walled carbon nanotubes (CNT), and activated nitrogen-doped biochar (ANBC) as carbon support via a ligand mediated method. The Ni-N-ANBC catalyst shows a maximum of 97% faradaic efficiency to CO at -0.93 V vs. RHE, which is better than Ni-N-CB catalyst (maximum 88% FE_{CO} at -0.8 V vs. RHE) and comparable to Ni-N-CNT catalyst (maximum 95% FE_{CO} at -0.7 V vs. RHE). In addition, the critical factors of carbon support that govern the CO₂RR performances of the prepared Ni-N-C catalysts, which include hydrophobicity, surface

roughness, porosity, the abundance of defects, and the distribution of active sites, are comprehensively investigated. As a result, the porosity of carbon supports and the distribution of Ni-N_x active sites are confirmed as the main factors that influence the CO₂RR performance of Ni-N-C catalysts. The micropore-dominated N-doped biochar with hierarchical structures exhibits a larger specific surface area and smaller pore size, with a part of the Ni-N_x active sites confined in deeper and narrower pores, enabling Ni-N-ANBC catalyst to maintain a good CO₂RR performance even at more negative potentials. This study reveals the role of the carbon support of Ni-N-C catalysts for electrochemical CO₂RR and presents the feasibility of using N-doped biochar as a more sustainable carbon support for the preparation of Ni-N-C catalysts.

In summary, N-doped biochar catalysts show a great potential to substitute the unsustainable fossil-based carbon catalysts for electrochemical CO₂ reduction to CO. It is possible to obtain an excellent catalyst with high selectivity, activity and stability by precisely modulating the porosity, surface wettability, abundance of defects, and other physicochemical properties of N-doped biochar material. Benefitting from the stability of carbon materials, N-doped biochar enables better performances than benchmarked metal catalysts even in harsh reaction conditions. Integrating the hierarchical structure of N-doped biochar with Ni-N_x active sites could further improve the catalytic performance of metal-free carbon catalysts for CO₂RR.

7.2 Recommendations

The unique properties of biomass-derived N-doped carbon catalysts, including large specific surface area, tunable porosity, abundant defects, and resistance to bases and acids, enable them to exhibit competitive performances for electrochemical CO₂ reduction to CO. Additionally, the cost-effectiveness, sustainability, and environmental friendliness of N-doped biochar catalysts make them viable alternatives to fossil-based carbon catalysts. However, the investigation on these N-doped biochar catalysts is still in its infancy. Many scientific and technological challenges have still to be addressed. The recommendations are listed below:

- It is not advisable to develop novel catalysts with high selectivity and activity for CO₂RR via screening of random combination of feedstocks, activators, dopants, and operation conditions, which is endless and meaningless. Efforts should be dedicated to reveal the synthesis-properties-performance correlations of N-doped biochar catalysts for CO₂RR, instead of showing off their exquisite nanostructures and impressive performances.

- The mechanisms of N-doped biochar formation need further investigation. Understanding the migration principles of N-containing species in gas, solid, and liquid products by Time of Flight Mass Spectrometer (TOFMS), Two-Dimensional Infrared Spectroscopy (2D-IR), etc., during the carbonization and functionalization processes, will be helpful to optimize the conditions for N-doped biochar preparation and to more precisely control the N-doping content and speciation.
- Chemical activators are widely used to enlarge the specific surface area and porosity of carbon materials. However, their corrosive effects during activation process on the equipment and the following acid wash processes exhibit negative impacts to the environment. Therefore, seeking green and eco-friendly activators for effective activation processes are highly desired, such as potassium acetate (CH_3COOK), hydroxyapatite ($\text{Ca}_5(\text{PO}_4)_3(\text{OH})$), etc.
- The chemical compositions of various biomass are significantly different. Therefore, improving the homogeneity of biomass-derived N-doped carbon materials through feedstock pretreatment (such as torrefaction, etc.), optimization of preparation conditions and other strategies (such as bio-refinery, etc.) is crucial to improve the reproducibility of catalyst performance.
- The active sites and reaction mechanisms for CO_2RR on N-doped carbon catalysts need to be further investigated. DFT is a powerful tool to reveal the active sites, while such often overly idealized models also make the results of DFT simulations controversial. The effects from micro environment around the active sites, such as ion concentration, surface wettability, should also be included into the simulation model.
- In addition, the deconvolution of high resolution XPS spectra is highly subjective, these should be very careful assessed when comparing XPS results from different research groups. Providing the detail information about the fitting of XPS spectra are highly encouraged.
- Integrating the N-doped biochar catalyst in a gas diffusion layer (GDL) or a gas diffusion electrode (GDE) will be an attractive topic. Using membrane electrode assembly (MEA) for high-throughput CO_2 electrochemical reduction to improve the reaction activity of N-doped biochar catalyst is also attractive and meaningful for future applications.
- Owing to the resistance to bases and acids of carbon materials, it is worthy to evaluate the performance of N-doped biochar catalysts for CO_2RR in the presence of other gas impurities, such as hydrogen sulfide (H_2S), carbonyl sulfide (COS),

nitrogen oxides (NO_x), nitrogen (N_2) and oxygen (O_2), etc. In addition, performing N-doped biochar catalysts for CO_2RR in acidic electrolytes is also attractive.

- Techno-economic analyses and life cycle assessment (LCA) studies of using biomass-derived N-doped carbon catalysts to substitute the fossil-based carbon catalysts for electrochemical CO_2 reduction to CO are highly desired.

Acknowledgements

Time flies. I almost reach to the end of my Ph.D. journey in TU Delft. It is an incredible, challenging and unforgettable experience in my life. Everything is so familiar to recall, as if it happened yesterday. I am profoundly grateful to all those who have helped me in the past four years. Without their invaluable support, guidance, and encouragement, I would not have been able to complete this dissertation.

First and foremost, I would like to express my deepest gratitude to my supervisors, **Prof. Dr. Ir. Wiebren de Jong** and **Dr. Ruud Kortlever**. Thank you for providing me such a great opportunity to TU Delft and working together with your team. You gave me enormous freedom to design experiments, verify interesting ideas and extend collaborations with others. You supported me to attend the ECCM winter school in Garderen and Electrochemistry winter school in Antwerp to develop my research skills. You also encouraged me to participate in domestic and international conferences to show my research progress. I appreciate your very kind comments after each biweekly progress meeting, such as “Thanks for your work, great job!”, which makes me become more confident. Your expertise, honesty, patience and humility have been instrumental in shaping my overall academic growth. I am grateful to you for your insightful guidance, valuable suggestions, and unwavering support throughout the entire process.

I would like to express my heartfelt appreciation to the members of my thesis committee, **Prof. Magda Titirici**, **Prof. Ruud van Ommen**, **Prof. Guido Mul**, **Dr. Lorenzo Botto** and **Dr. Marta Costa Figueiredo** for the invaluable feedback and constructive criticism, which have significantly enriched this work.

I would also like to thank all of the technicians supporting my research. I am not able to complete my project without your help. **Ing. Michel van den Brink**, thank you for your management of the lab and especially for your help on the ICP measurements. You are the most responsible and hardworking technician I had ever seen in TU Delft. I am always proud to say that “I feel happy because we have Michel, I feel sad because we only have Michel”. **Ing. Kees Kwakernaak**, thanks for your training on the SEM-EDX measurement. I always got some good comments on my SEM images from my friends and I think that should be attributed to the skills you taught me in the past few years. **Willy Rook**, thank you for helping me carry out the N₂ adsorption-desorption measurement. I am impressed by your expertise. I learned a lot of details about the analysis of N₂ adsorption-desorption results. **Ruud Hendrikx**, I appreciate your help on the XRD characterization. You are always fast-response and always give me a very professional characterization report. My special appreciation also

goes to the supporting staff for the help and assistance in the daily work: **Eveline van der Veer, Rob van den Boogaard, Leslie van Leeuwen, and Dr. Maryam Alimoradi Jazi.**

I am deeply indebted to my colleagues and lab mates who provided a supportive and inspiring atmosphere throughout the journey. **Ming Li**, I could not imagine how hard will my life be without your help in the past four years. I appreciate your patience and dedication to the operation and analysis of TEM and XPS measurements. You are a reliable collaborator for scientific research and an impeccable friend for daily life. I learned a lot from your attitude to life and you gave me sufficient positive energy to overcome my blue moment. **Dr. Marilia Pupo**, thanks for your training in using the compact H-cell at the beginning of my project. **Daniël van den Berg**, I really enjoy the discussions about the cultural differences with you. **Hengameh Farahmandazad**, thank you for letting me use your silver electrodes. **Simone Asperti**, I appreciate your strict and critical attitude to research, especially for the leak-free Ag/AgCl reference electrode. **Nandalal Girichandran**, I enjoy the time with you at Antwerp. **Asvin Sajeev Kumar**, my friend, I appreciate your work in building the setup for the impurities-containing experiments, and I enjoy the discussions with you. **Boaz Izelaar**, thank you for helping me prepare the Ni-N-C catalysts and TEM measurements. I enjoy the time with you at Noordwijkerhout and Prague. **Aleksandra Kaminska**, you bring a lot of joy to our office, I feel very relaxed when we share gossip together (Ahahaha). **Katherine Rochon Lawrence**, thanks for your suggestions on the spray coating of gas diffusion electrodes and your responsibility for HPLC. **Iris Burgers**, I enjoy the time we play football together in X. **Dr. Ahmed Mohsen Ismail**, thanks for your training in preparing the gas diffusion electrodes and using the MEA cell for electrochemical CO₂ reduction. I learned a lot of fundamental knowledge of electrochemistry from you. **Min Li**, thank you for helping me carry out the N₂ adsorption-desorption measurements. I am also grateful to my colleagues from the Large-Scale Energy Storage group: **Dr. Sevgi Polat, Dr. Hamid Gilvari, Dr. Andrea Mangel Raventos, Mara del Grosso, Christos Tsekos, Katherine Encalada Flores and Sohan Phadke.**

My sincere thanks go to my dear friends at TU Delft: **Dr. Liangyuan Wei, Dr. Xuan Tao, Dr. Wenze Guo, Dr. Bin Fang, Dr. Teng Dong, Dr. Zac Leong, Dr. An Zhao, Dr. Jian Wang, Haoyu Li, Rong Fan, Mengmeng Zhang, Qi An, Heng Li, Pingping Cui, Willy Huang, Qingfeng Tong, Tiange Yuan, Mengran Li, Qianyi Chen, and Ziyu Li.** Thank you all for sharing your experience and positive energy with me. Your encouragement and kind words motivated me to overcome many challenges in the past four years. I feel lucky that I am surrounded by so many talented and warmhearted friends. In the past four years, we made mooncakes, dumplings, and hotpots together and shared them with each other, we enjoyed delicious cuisines together in Delft, Den Haag, Rotterdam, etc. I will never forget these happy moments we spent together. I would also like to extend my gratitude to my friends out of Delft. **Muyi Zhang**, thank you for visiting me from Sweden during your vacation. You are my

role model. Your attitude to research and life have been a constant source of motivation for me. **Fujing Ma**, thank you for visiting me from France during your summer school. The white wine you brought from Bordeaux is fantastic! **Haoyu Xiao** and **Zihao Liu**, my young brothers, thank you for bringing my ID card and gifts from China and hosting me in Groningen and Giethoorn. We had a great time together and I feel really relaxed with you guys. I learned a lot from your optimistic attitude toward life, which helped me to mitigate my negative energy and overcome obstacles in my most hard time. Many thanks to my friends **Yujie Wang**, **Haolan Zhou**, **Hao Sun**. It is a great pleasure to be friends with you for so many years. We are far away with each other but I still feel your support and encouragement during moments of self-doubt.

I would like to thank my master's supervisor **Prof. Haiping Yang** and bachelor's supervisor **Prof. Enchen Jiang**. I even couldn't start my Ph.D. without your supervision and encouragement. You taught me how to develop my research skills, and most importantly, you also taught me how to be a good person. You encouraged me to explore the possibilities of my life and inspired me to experience multi-culture in a broader world. I am getting more confident to face challenges in my future life.

I would also like to extend my gratitude to the **China Scholarship Council (CSC)**, whose financial support made this research possible.

Last but not least, I offer my deepest appreciation and love to **my parents** and **my girlfriend**. Your continuous unconditional love and encouragement supported me to complete my studies over the past four years. You always urge me to relax and not worry too much about the future. Thank you for standing by me in all of my pursuits and inspiring me to follow my dreams.

I am thankful to **everyone** who has contributed to this significant milestone in my life.

Shilong Fu

Delft, The Netherlands

2023.11

Curriculum vitae

Shilong Fu

- 11-11-1992 Born in Luoyang, China
- 2012-2016 **B.Sc. in Energy and Environmental Systems Engineering**
Faculty of Material and Energy
South China Agriculture University, Guangzhou, China
Supervisor: Prof. Enchen Jiang
- 2015-2016 **Research Assistant**
Guangzhou Institute of Energy Conversion, Guangzhou, China
Chinese Academy of Sciences
- 2016-2019 **M.Sc in New Energy Technology and Engineering**
State Key Laboratory of Coal Combustion
China-EU Institute for Clean and Renewable Energy
Huazhong University of Science and Technology, Wuhan, China
Supervisor: Prof. Haiping Yang
- 2017-2018 **M.Sc in Energy (Double master degree)**
MINES ParisTech
Université Paris Sciences et Lettres, Paris, France
- 2018-2018 **Visiting Student**
Mid Sweden University, Sundsvall, Sweden
Supervisor: Prof. Wennan Zhang
- 2019-2023 **Ph.D. in Process and Energy**
Faculty of Mechanical Engineering
Delft University of Technology, Delft, The Netherlands
Thesis: Renewable for Sustainable: Using Biomass-derived Carbon for
Electrochemical CO₂ Reduction
Supervisor: Prof. Wiebren de Jong, Dr. Ruud Kortlever

List of Publications

Journal Articles - Within the scope of the dissertation:

1. **Shilong Fu**, Ming Li, Simone Asperti, Wiebren de Jong, Ruud Kortlever. Unravelling the Effect of Activators used in The Synthesis of Biomass-Derived Carbon Electrocatalysts on the Electrocatalytic Performance for CO₂ Reduction. *ChemSusChem*, 2023, 16, e202202188.
2. **Shilong Fu**, Ming Li, Wiebren de Jong, Ruud Kortlever. Tuning the Properties of N-Doped Biochar for Selective CO₂ Electroreduction to CO. *ACS Catalysis*, 2023, 13, 10309-10323.
3. **Shilong Fu**, Asvin Sajeev Kumar, Ming Li, Wiebren de Jong, Ruud Kortlever. Electrochemical CO₂ Reduction in the Presence of SO₂ Impurities on a Nitrogen-doped Carbon Electrocatalyst. *Submitted*.
4. **Shilong Fu**, Boaz Izelaar, Ming Li, Qi An, Min Li, Wiebren de Jong, Ruud Kortlever. Ni-N-C catalysts for CO₂ electrochemical reduction to CO: The effects of carbon support. *Submitted*.
5. **Shilong Fu**, Wiebren de Jong, Ruud Kortlever. Recent Progress of Biomass-derived Nitrogen-doped Carbon Materials as Electrocatalysts. *In preparation*.

Journal Articles – Outside the scope of the dissertation:

6. **Shilong Fu**, Yingquan Chen, Haiping Yang. Research Advances in Methanation Catalysts for Bio-Syngas. *Journal of Shenyang Agricultural University*, 2017, 04, 488-496. (In Chinese)
7. Jun Zou, Japhet Oladipo, **Shilong Fu**, Amal Al-Rahbi, Haiping Yang, Chunfei Wu, Ning Cai, Paul Williams, Hanping Chen. Hydrogen production from cellulose catalytic gasification on CeO₂/Fe₂O₃ catalyst. *Energy Conversion and Management*, 2018, 171, 241-248.
8. Ming Li, **Shilong Fu**, Saeed Saedy, Aparna Rajendrakumar, Frans Tichelaar, Ruud Kortlever, J. Ruud van Ommen. Nanostructuring Pt-Pd Bimetallic Electrocatalysts for CO₂ Reduction Using Atmospheric Pressure Atomic Layer Deposition. *ChemCatChem*, 2022, 14, e202200949
9. Daniël van den Berg, Boaz Izelaar, **Shilong Fu**, Ruud Kortlever. The effect of surface conditions on the electrochemical CO₂ reduction performance of bimetallic AuPd electrocatalysts. *Catalysis Science & Technology*, 2023, DOI: 10.1039/D3CY01411H.

10. Ming Li, Saeed Saedy, **Shilong Fu**, Teise Stellema, Ruud Kortlever, J. Ruud van Ommen. Enhancing the durability of Pt nanoparticles for water electrocatalysis using ultrathin SiO₂ layers. *Submitted*.
11. **Shilong Fu**, Ming Li, Asvin Sajeev Kumar, Wiebren de Jong, Ruud Kortlever. The impact of sulfur-containing gaseous impurities on electrochemical CO₂ reduction on a nickel-nitrogen-carbon catalyst. *In preparation*.
12. Asvin Sajeev Kumar, **Shilong Fu**, Saeed Saedy, Ahmed Mohsen Ismail, Mahinder Ramdin, J. Ruud van Ommen, Wiebren de Jong, Ruud Kortlever. Effect of sulphur-based gaseous contaminants on electrochemical CO₂ reduction to C₂+ products. *In preparation*.
13. Min Li, Jinghan Zhao, **Shilong Fu**, Ahmed Mohsen Ismail, Ruud Kortlever, Atsushi Urakawa. Polymer Modified Ru Nanoparticles Catalyst Boost Electroreduction of Nitrate to Ammonia in Water-fed PEM Cell. *In preparation*.

Oral Presentations:

1. **Shilong Fu**, Ming Li, Simone Asperti, Wiebren de Jong, Ruud Kortlever. Unravelling the effect of activators used in the synthesis of biomass-derived carbon electrocatalysts on the electrocatalytic performance for CO₂ reduction. 1st Regional Meeting of the International Society of Electrochemistry, 15th - 19th, August, 2022, Prague, Czech Republic.
2. **Shilong Fu**, Boaz Izelaar, Ming Li, Qi An, Min Li, Wiebren de Jong, Ruud Kortlever. Ni-N-C catalysts for CO₂ electrochemical reduction to CO: The effect of carbon supports. 24th Netherlands Catalysis and Chemistry Conference, 6th - 8th, March, 2023, Noordwijkerhout, The Netherlands.

Poster Presentations:

1. **Shilong Fu**, Ming Li, Wiebren de Jong, Ruud Kortlever. Electrocatalytic CO₂ reduction on biomass-derived N-doped carbon materials. 23rd Netherlands Catalysis and Chemistry Conference, 9th - 11th, May, 2022, Noordwijkerhout, The Netherlands.
2. **Shilong Fu**, Asvin Sajeev Kumar, Ming Li, Wiebren de Jong, Ruud Kortlever. Electrochemical CO₂ Reduction in the Presence of SO₂ Impurities on a Nitrogen-doped Carbon Electrocatalyst. 74th Annual International Society of Electrochemistry Meeting, 3rd - 8th, September, 2023, Lyon, France. **(Best Poster Prize)**

